Tracking the origin of volatile depletion in the Earth with indium

Deze Liu

Thèse préparée à l'institut de physique du globe de Paris

Université Paris Cité

École doctorale Sciences de la Terre et de l'environnement
et physique de l'Univers STEP'UP N°560
IPGP - Cosmochimie, astrophysique et géophysique expérimentale

Tracking the origin of volatile depletion in the Earth with indium

par **Deze Liu**

Thèse de doctorat de Sciences de la Terre et de l'environnement

dirigée par
Frédéric Moynier
Et par **Julien Siebert**

présentée et soutenue publiquement le
15 décembre 2022

devant un jury composé de:

Martin Bizzarro (Professeur, Université de Copenhague)	Rapporteur
Bernard Charlier (Associate Prof, Université de Liége)	Rapporteur
Laurette Piani (Chargé de recherche, Université de Lorraine)	Examinatrice
Celia Dalou (Chargé de recherche, Université de Lorraine)	Examinatrice
Bénédicte Menez (Professeur, Université Paris Cité)	Examinatrice
Frédéric Moynier (Professeur, Université Paris Cité)	Directeur de thèse
Julien Siebert (Professeur, Université Paris Cité)	Co-directeur de thèse

Abstract

The accretion history and the nature of the building blocks of the Earth are still highly debated. The elemental and isotopic compositions of moderately volatile elements (MVEs) of the Earth and meteorites can give important insights in these issues. In general, the abundance of lithophile MVEs in the bulk silicate Earth (BSE) exhibit a log-linear depletion pattern (compared to solar composition) along with the 50% condensation temperature (T_C^{50}), while the siderophile MVEs show an additional depletion due to the metal-silicate partitioning during the Earth's core-formation processes. However, indium (In) is an exception as its abundance is over-abundant in the BSE compared to elements of similar volatility and siderophility. This overabundance can be explained as the results of: 1) an over-estimated volatility of In under nebular environment; 2) a late delivery of CI-like materials, known as the heterogeneous accretion, which describes that the Earth's accretion started from volatile-depleted materials and followed by a late accretion of volatile-rich materials. To explain the overabundance of In, the late-accretion model requires either a) In behaved as a lithophile element under the Earth's core-formation conditions or b) the precursor materials of proto-Earth carried an enrichment in In compare to known meteorites. Therefore, studying the behavior of In during the volatilization process and metal-silicate partitioning processes can give an insight to the over-abundance of In in the BSE, and further provide implications to the origin of the depletion of MVEs and the building blocks of the Earth.

In this dissertation, I applied experimental approaches to study the volatility and siderophility of In, developed a method for high precision In isotopic analysis on natural rocks and analyzed the In isotopic composition of the Earth's rocks and chondrites. The study on the volatility of In focuses on the vaporization process of silicate melt-vapor system. The evaporation experiments of In were performed on a silicate melt of basaltic composition and under a variety of temperatures and oxygen fugacities. Combine with our experimental data and current quantification approach of elemental volatility for

vapor-melt system, the volatility of In during evaporation process was quantified in this thesis. The results exhibit a significantly lower volatility of In in vapor-melt evaporation system, in comparison with its volatility in nebular environment, indicating the overabundance of In as the result of non-nebular environment. The partitioning behavior of In between metal and silicate was studied with a variety of metal-silicate segregation experiments which were performed in piston cylinder, multi-anvil and diamond anvil cell, spanning a wide range of pressure-temperature conditions (~ 2 to 50 GPa, ~ 1700 to 4000 K), covering the P-T conditions from the early accretion stage to the final deep magma ocean. According to the experimental results, In does not behave as a lithophile element throughout the Earth's core-formation conditions, instead a significant fraction partitioned into the core during the Earth's accretion. I used these results to demonstrate that the In Earth's budget has two sources: early accreted precursor materials lost less In by evaporation as previously thought due to the lower volatility of In as previously thought and late delivered carbonaceous-like volatile-rich materials. The In isotopic compositions of a series of terrestrial rock samples from basalt to rhyolite were reported here. The indium isotopic compositions of these samples show insignificant isotopic fractionations within the current analytical uncertainty, which reflect the constant oxidation sate and limited variations of coordination number of In during fractional crystallization. Based on the basalts collected from different tectonic settings, we propose the first estimation for the In isotopic composition of the Eath's mantle (δ^{115}In = -0.02 ± 0.19‰, 2SD, n = 10). Furthermore, a resolvable In isotopic fractionation was found in S-free metal-silicate experimental samples, while the presence of sulfur was observed to decrease the fractionation. Given the discrepancy of the isotopic fractionation on S-bearing/free samples, as well as the estimated partition coefficients DIn, the upper and lower bound of the In isotopic composition of the bulk Earth (BE) can be assessed. Extrapolating the regressed parameters to the base of the magma ocean (~ 40 – 50 GPa, 3200 ~ 3900 K), the upper bound of BE is identical with BSE, and the lower bound is ~ -0.08 ± 0.15‰,

which overlapped with the In isotopic composition of the BSE within the current analytical precision.

Key words: Indium, evaporation, volatile elements, metal-silicate partitioning, isotopic fractionation, late accretion, core formation.

Résumé

L'histoire de l'accrétion et la nature des éléments constitutifs de la Terre font encore l'objet d'un grand débat. Les compositions élémentaires et isotopiques des éléments modérément volatils (MVE) de la Terre et des météorites peuvent fournir des informations importantes sur ces questions. En général, l'abondance des MVE lithophiles dans la partie silicatée de la Terre (BSE) présente un modèle d'appauvrissement log-linéaire (par rapport à la composition solaire) avec la température de 50% condensation (T_c^{50}), tandis que les MVE sidérophiles présentent un appauvrissement supplémentaire dû à la partition métal-silicate pendant les processus de formation du noyau terrestre. Cependant, l'indium (In) est une exception car son abondance est surabondante dans l'ESB par rapport aux éléments de volatilité et de sidérophilie similaires. Cette surabondance peut être expliquée comme les résultats de : 1) une volatilité surestimée de l'In dans l'environnement nébulaire ; 2) un apport tardif de matériaux de type CI, connue sous le nom d'accrétion hétérogène, qui décrit que l'accrétion de la Terre a commencé à partir de matériaux appauvris en volatilité et a été suivie par une accrétion tardive de matériaux riches en volatils. Pour expliquer la surabondance de l'In, le modèle d'accrétion tardive exige soit a) que l'In se comporte comme un élément lithophile dans les conditions de formation du noyau terrestre, soit b) que les matériaux précurseurs de la proto-Terre soient enrichis en In par rapport aux météorites connues. Par conséquent, l'étude du comportement de l'In pendant le processus de volatilisation et les processus de partition métal-silicate peut donner un aperçu de la surabondance de l'In dans l'ESB, et fournir des informations sur l'origine de l'appauvrissement des MVE de la Terr**e.**Dans cette thèse, j'ai appliqué des

approches expérimentales pour étudier la volatilité et la sidérophilie de l'In, développé une méthode d'analyse isotopique de l'In à haute précision sur des roches naturelles et analysé la composition isotopique de l'In des roches terrestres et des chondrites. L'étude sur la volatilité de l'In se concentre sur le processus de vaporisation du système silicate liquide-vapeur. Les expériences d'évaporation de l'In ont été réalisées sur un silicate fondu de composition basaltique et sous une variété de températures et de fugacités d'oxygène. En combinant nos données expérimentales et l'approche actuelle de quantification de la volatilité élémentaire pour le système vapeur-liquide, la volatilité de l'In pendant le processus d'évaporation a été quantifiée dans cette thèse. Les résultats montrent une volatilité significativement plus faible de l'In dans le système d'évaporation liquide-vapeur, en comparaison avec sa volatilité dans l'environnement nébulaire, indiquant la surabondance de l'In comme résultat de l'environnement non-nébulaire. Le comportement de partage de l'In entre le métal et le silicate a été étudié à l'aide d'une variété d'expériences de ségrégation métal-silicate qui ont été réalisées dans un piston-cylindre, une cellule multi-enclumes et une cellule à enclume de diamant, couvrant une large gamme de conditions de pression-température (~ 2 à 50 GPa, ~ 1700 à 4000 K), recouvrant les conditions P-T du stade précoce d'accrétion à l'océan magmatique profond final. D'après les résultats expérimentaux, l'In ne se comporte pas comme un élément lithophile dans les conditions de formation du noyau de la Terre, mais une fraction significative s'est ségrégé dans le noyau pendant l'accrétion de la Terre. J'ai utilisé ces résultats pour démontrer que le bilan d'In de la Terre a deux sources : les matériaux précurseurs accrétés précocement ont perdu moins d'In par évaporation qu'on ne le pensait jusqu'à présent, en raison de la volatilité plus faible de l'In démontré lors de nos experiences, et les matériaux riches en volatils de type carboné livrés tardivement. Les compositions isotopiques de l'In d'une série d'échantillons de roches terrestres allant du basalte à la rhyolite ont été rapportées ici. Les compositions isotopiques de l'indium de ces échantillons montrent des fractionnements isotopiques insignifiants dans les limites de l'incertitude analytique actuelle, ce qui reflètent l'état

d'oxydation constant et les variations limitées du nombre de coordination de l'In pendant la cristallisation fractionnée. Sur la base des basaltes collectés dans différents contextes tectoniques, nous proposons la première estimation de la composition isotopique en In du manteau terrestre (δ^{115}In = -0,02 ± 0,19‰, 2SD, n = 10). En outre, un fractionnement isotopique d'In a été trouvé dans les échantillons expérimentaux métal-silicate sans S, tandis que la présence de soufre diminue le fractionnement. Compte tenu de la divergence du fractionnement isotopique sur les échantillons avec ou sans S, ainsi que des coefficients de partage estimés DIn, les limites supérieures et inférieures de la composition isotopique de l'In dans la Terre peuvent être évaluées. En extrapolant les paramètres régressés jusqu'à la base de l'océan magmatique (~ 40 - 50 GPa, 3200 ~ 3900 K), la limite supérieure de BE est identique à celle de l'ESB, et la limite inférieure est de ~ -0,08 ± 0,15‰, ce qui recouvre la composition isotopique en In de l'ESB avec la précision analytique actuelle.

Mots clés: Indium, évaporation, éléments volatils, partage métal-silicate, fractionnement isotopique, accrétion terrestre.

Résumé substantiel

L'origine des éléments constitutifs de la Terre, ainsi que l'histoire de l'accrétion de la Terre sont des sujets fondamentaux pour comprendre la formation de la Terre. Cependant, la différenciation du noyau et les processus ignés de formation des roches de la croûte terrestre posent des problèmes majeurs pour répondre à ces questions. En tant que matériaux résiduels du système solaire primitif, les météorites primitives ont été considérées comme des analogues des matériaux de construction de la Terre. Néanmoins, les compositions élémentaires et isotopiques de la Terre ne peuvent pas être complètement associées à un seul type de météorite connu, ce qui implique la complexité des blocs de construction de la Terre. En comparaison avec les météorites primitives, en particulier les chondrites CI, connues pour leur composition chimique proche de la composition moyenne du système solaire (à l'exception de certains éléments très volatils tels que H, C, N, etc.), la Terre est considérablement appauvrie en éléments volatils (à la fois modérément et fortement volatils), alors que l'origine de l'appauvrissement en éléments volatils est encore mal comprise. Certaines hypothèses classiques ont tenté d'expliquer l'appauvrissement en éléments volatils comme étant le résultat soit 1) d'une condensation incomplète de la nébuleuse solaire, où les éléments volatils du système solaire interne ont été emportés par le jeune Soleil, soit 2) de la perte par évaporation des matériaux précurseurs de la Terre. De plus, de plus en plus de preuves provenant d'anomalies isotopiques (par exemple Ca, Ni, Ti, Cr, Zn, etc.), de la composition isotopique d'éléments volatils (par exemple Ag, Zn, Cu, Rb, H, etc.), ainsi que de modèles de formation de noyaux ont suggéré l'existence de matériaux riches en éléments volatils de type carboné qui auraient été livrés à la Terre au cours de sa phase d'accrétion tardive, et auraient constitué une source importante du bilan des éléments volatils de la Terre. Ces résultats soulignent l'importance des éléments volatils pour retracer les blocs de construction de la Terre et l'histoire de l'accrétion, et ont donc été choisis comme objectif de cette thèse.

Comme mentionné plus haut, la Terre est appauvrie en éléments volatils, et l'étendue

de leur appauvrissement dans la masse silicatée de la Terre (BSE) peut être quantifiée en la normalisant par rapport aux chondrites CI (à savoir les abondances normalisées CI, -Mg ci-après). Les abondances normalisées CI, -Mg des éléments lithophiles modérément volatils (MVE) de la Terre présentent une corrélation log-linéaire avec la température de condensation de 50 %, qui est une échelle de température généralement utilisée pour représenter la volatilité des éléments dans des conditions nébulaires, ce qui indique que l'appauvrissement des MVE de la Terre est le résultat de processus de volatilité, par exemple l'évaporation et/ou la condensation. De plus, les MVE sidérophiles présentent un appauvrissement supplémentaire par rapport aux éléments lithophiles en raison de leur séquestration pendant le processus de formation du noyau terrestre. Dans cette thèse, l'accent est mis sur un élément unique, l'indium (In), qui est à la fois un élément modérément volatil et sidérophile (ESV), dont l'abondance normalisée CI, -Mg se situe au-dessus de la "tendance à l'épuisement" définie par les ESV lithophiles, et qui a donc été considéré comme "surabondant" dans l'ESB. Cette caractéristique unique permet à la composition élémentaire et isotopique de l'In d'être façonnée à la fois par des processus " liés à la volatilité " et par le processus de formation du noyau, et la connaissance de l'origine de la surabondance de l'In peut donc donner un aperçu de l'origine de l'épuisement des éléments volatils de la Terre.

Des études antérieures ont fourni quelques explications possibles de sa surabondance : 1) volatilité surestimée au cours d'un événement de perte de volatilité ; 2) l'indium peut se comporter comme un élément lithophile dans les conditions de formation du noyau terrestre car le coefficient de partage élémentaire est fonction des conditions physico-chimiques (par exemple, la pression, la température, les compositions en métaux et en silicates). Cependant, les travaux détaillés sur la volatilité et la sidérophilie de l'indium sont rares et sont donc étudiés dans cette thèse. La volatilité et la sidérophilie de l'In ont été étudiées à l'aide d'une série d'expériences d'évaporation et d'expériences de partition métal-silicate, afin de mieux comprendre les comportements géochimiques de l'In pendant la perte volatile sur les matériaux de construction de la Terre et le processus

de formation du noyau, respectivement. Ces approches expérimentales de pétrologie nous permettent de quantifier les comportements géochimiques de l'indium dans des conditions physico-chimiques données (par exemple, température, pression, composition de la masse fondue, etc.), et de prédire les compositions élémentaires et isotopiques de l'indium au cours de l'accrétion de la Terre et de la formation du noyau. En outre, les isotopes de l'indium peuvent également constituer un traceur robuste, car les isotopes de l'indium peuvent être utilisés pour déterminer la composition élémentaire de l'indium.

Afin d'appliquer le système des isotopes de l'In pour suivre l'origine de l'épuisement des volatiles et les matériaux de construction potentiels de la Terre, une méthode de détermination des isotopes de l'In de haute précision sur les roches a été développée dans cette thèse, et le fractionnement isotopique de l'In pendant la différenciation ignée a été discuté plus en détail. D'après la composition isotopique de l'In mesurée sur les roches terrestres, la composition isotopique de la Terre silicatée, ainsi que celle de la Terre extrapolée à partir des résultats expérimentaux sur les métaux-silicates, sont estimées sur la base des meilleurs résultats analytiques actuels.

La volatilité de l'In a été étudiée via une série d'expériences d'évaporation réalisées à des températures (1573 à 1773 K) et des fO2 (-10 à -0,68 en unités logarithmiques) variables. La volatilité des éléments est fortement gouvernée par la fugacité de l'oxygène du milieu environnant, et les variations de fO2 peuvent également modifier les volatilités relatives entre les différents éléments. Par conséquent, pour l'échelle de température traditionnelle, la température de condensation de 50 %, qui a été estimée sur la base de l'hypothèse de conditions nébulaires (par exemple, logfO2 = -14, 10-4 bar), son application pour quantifier la volatilité élémentaire devrait être soumise à cette condition environnementale. Cependant, pour la perte de volatils qui a lieu sur le silicate fondu pendant l'évaporation, l'état redox environnemental pourrait être différent des conditions nébulaires, avec un état plus oxydatif, comme cela a été observé dans les chondres et les calculs théoriques pour l'évaporation sur le silicate fondu naturel. Ces

observations impliquent que la température de condensation de 50 % est peut-être inadaptée pour prédire la volatilité des éléments pendant le processus d'évaporation du système vapeur-fonte. Cette hypothèse a été confirmée par les résultats des expériences d'évaporation dans les études précédentes et dans cette thèse. Les résultats expérimentaux de l'In ont indiqué une volatilité plus faible de l'In par rapport à d'autres MVE avec une température de condensation voisine de 50 % (par exemple, le Cd), suggérant une température d'évaporation de 1 % (c'est-à-dire que 1 % d'un élément spécifique s'est évaporé de la phase condensée à la phase vapeur et a atteint l'équilibre) comme une échelle de température plus appropriée dans un système vapeur-fusion pendant l'évaporation. En utilisant cette nouvelle échelle de température, l'In n'est en fait pas " surabondant " dans la BSE, et permet un déficit supplémentaire par le processus de formation du noyau, ce qui indique que les matériaux de construction de la Terre ont très probablement perdu leurs MVE dans des conditions oxydatives " non nébulaires ", et ont donc conservé plus d'In que ce qui est attendu des conditions nébulaires.

Une série d'expériences de partition métal-silicate a été menée pour étudier le comportement de partition de l'In en fonction de la température, de la pression, de la composition de la masse fondue, de la fugacité de l'oxygène et des éléments légers dans les phases métalliques. Les conditions expérimentales couvraient une large gamme de pression (2 ~ 51 GPa) et de température (1600 ~ 4000 K), allant de la taille proche des planétésimaux aux conditions finales de pression-température de la base d'un océan magmatique profond. Les effets de S et Si sur le partage de l'In ont été examinés plus en détail par leurs expériences de dopage respectives. Nos résultats expérimentaux suggèrent un effet négligeable de la pression et de la température sur le partitionnement de l'In, alors que les effets des éléments légers, S et Si, ont été observés, en particulier Si, dont la présence dans les phases métalliques peut diminuer significativement le partitionnement de l'In. De plus, on a observé que les effets de S et Si sur In dépendent à la fois de la température et de la pression, et la validité des paramètres d'interaction

régressés de εIn-S et εIn-Si a été examinée avec les expériences P-T les plus élevées. Des scénarios d'accrétion homogène et trois scénarios d'accrétion hétérogène possibles (basés sur les différentes trajectoires d'évolution de la fugacité de l'oxygène) ont été modélisés, et leurs résultats ont tous donné un coefficient de partage final DIn de 3 ~ 5, indiquant le noyau comme un réservoir important du bilan d'In de la Terre. Cette estimation est cohérente avec les modèles antérieurs d'accrétion tardive qui suggéraient que des matériaux riches en volatilité de type CI avaient été délivrés à la Terre avant que la formation du noyau ne cesse. En outre, les résultats modélisés indiquent également une sidérophilie plus élevée de l'In par rapport au Cd dans toutes les conditions de formation du noyau, ce qui est contraire au rapport In/Cd normalisé par l'IC dans l'ESB, ce qui plaide contre l'accrétion tardive de matériaux de type IC ayant une abondance relative identique d'In et de Cd comme seule source du bilan d'In de la Terre. Au contraire, le bilan d'In de la Terre provient plus probablement du mélange de deux sources: (1) les matériaux de type CI accrétés tardivement (derniers 10 % de la masse terrestre); (2) les matériaux précurseurs de la proto-Terre accrétés au cours de la phase principale d'accrétion (c'est-à-dire les premiers 90 % de la masse terrestre), qui devraient contenir des quantités substantielles d'In et beaucoup moins de Cd. Cette hypothèse est cohérente avec la faible volatilité de l'In dans des conditions oxydatives " non nébuleuses ", ce qui implique que l'épuisement de la volatilité des matériaux précurseurs accrétés au début s'est produit dans de telles conditions.

La première méthode de détermination des isotopes de l'In, ainsi que les compositions isotopiques de l'In des roches terrestres sont rapportées dans cette thèse. La méthode de détermination isotopique de l'In, comprenant la purification de l'In par chromatographie sur colonne et la mesure isotopique sur spectromètre de masse, a été développée à l'Institut de Physique du Globe de Paris (IPGP). Cette méthode chimique peut éliminer efficacement les éléments de la matrice et les interférences isobares (Sn et Cd) presque complètement, et peut retourner la composition isotopique In des échantillons de roche avec une reproductibilité externe de ~0.12‰ (2SD). Les compositions isotopiques en

In d'une série d'échantillons de roches, y compris les géostandards BHVO-2, BCR-2, GSP-2, et des échantillons Afar/Islande dont les types de roches vont du basalte à la rhyolite ont été rapportés ici. Les compositions isotopiques de l'indium de ces échantillons montrent des fractionnements isotopiques insignifiants dans le cadre de l'incertitude analytique actuelle, qui peuvent être expliqués comme les résultats d'un état d'oxydation constant et des variations limitées du nombre de coordination de In pendant la cristallisation fractionnée. Les basaltes analysés provenant de différents contextes géologiques ont été observés avec une composition isotopique en In presque homogène dans le niveau actuel d'incertitude analytique, et donc, la première estimation pour la composition isotopique en In du manteau (δ115In = -0,02 ± 0,19‰, 2SD, n = 10) est suggérée. Par ailleurs, la composition isotopique en In des échantillons des expériences de partitionnement métal-silicate a également été analysée afin d'étudier le fractionnement isotopique en In au cours de la ségrégation métal-silicate. Les résultats analytiques montrent un fractionnement isotopique résoluble dans les échantillons sans soufre, où l'isotope In le plus lourd est enrichi dans les phases silicatées. En outre, la présence de soufre dans les phases métalliques peut diminuer le fractionnement isotopique de l'In, probablement en raison de la liaison covalente In-S plus forte que la liaison métallique In-Fe, dans laquelle la première peut enrichir plus d'isotopes lourds. Compte tenu de la divergence du fractionnement isotopique sur les échantillons porteurs/sans S, ainsi que des coefficients de partage estimés DIn, les limites supérieures et inférieures de la composition isotopique de l'In de la terre en vrac (BE) peuvent être évaluées. En extrapolant les paramètres régressés à la base de l'océan magmatique (~ 40 - 50 GPa, 3200 ~ 3900 K), la limite supérieure de la BE est identique à l'ESB, et la limite inférieure est de ~ -0.08 ± 0.15‰, ce qui correspond à la composition isotopique de l'In dans l'ESB avec la précision analytique actuelle.

Ces travaux de recherche ont fait progresser nos connaissances sur le comportement géochimique de l'indium, et nous ont permis de mieux comprendre l'origine de la " surabondance " d'indium dans la BSE, et ont également permis de comprendre l'origine

de l'épuisement des matières volatiles de la Terre et le moment où ces matières volatiles sont livrées à la Terre.

Acknowledgements

There are so many people who have given me so much warmth and help during my time at IPGP, and I am so grateful to them. Firstly, I would like to thank my advisors, Frederic Moynier and Julien Siebert, who have spent so much time teaching me and sharing their knowledge and insights with me to enable me to get into the field. I am very grateful to them for their help and very glad to work with them at IPGP for the past four years.

I am very thankful to Paolo A. Sossi for too many things, thank him for sharing his time and experiment experiences with me, and thank him for providing many important suggestions. I would like to thank Edith Kubik for her training on the high pressure experiments, and sharing her precious experiences with me. I thank Yan Hu for her warmhearted help in mass spectrometer lab, and appreciate many discussions with her. I am grateful to Edward Inglis, Shengyu Tian, Wei Dai, Gabriel Devos for their so much help in clean lab. I thank Nicolas Wehr for his tecnique assitance in piston-cilinder lab and evaporation lab. I am grateful to Pascale Louvat, Pierre Burckel, Dimitri Rigoussen, Tu-Han Luu, Pamela Gutiérrez for their help in clean lab and mass spectrometer labs. I thank Stephan Borensztajn for his tecnique assitance with SEM. I thank Michel Fialin and Nicolas Rividi for their assistance with the electron microprobe. I deeply thank the fellow graduate students, post-docs and faculty members in CAGE and other teams at IPGP for their warm help and share in both science and life.

Finally, I would like to thank my parents for their support and care. I appreciate all my friends in Paris who have brought me so much happiness.

Contents

Chapter 1. Introduction

1.1 The formation of the Earth

The solar system formed 4567.30 ± 0.16 Ma ago (Connelly et al., 2012), from the collapse of a cold1 dense molecular cloud and following the formation of the solar nebula and the proto-Sun (e.g., Burkhardt et al., 2008; Dauphas and Chaussidon, 2011). The molecular cloud is an interstellar cloud, which is mainly composed of hydrogen and helium in molecular state, which were produced during the Big Bang, as well as a a minor percentage (~ 2%) of heavier elements (atom mass heavier than H and He) which were the products of nucleosynthesis processes occurred on other stars (e.g., Faure and Mensing, 2007 and references therein). As the cloud reached a high enough density, it started to collapse due to its self-gravitation, then the solar nebula and proto-Sun formed, and the latter is located at center the solar system. Derived by the conservation of angular momentum, the proto-Sun started its growth process and accreted most of the materials from the solar nebula. The proto-Sun started to emit strong solar winds, and blow away much of the remaining nebular gas from the inner solar system to the outer side of solar system. Volatiles such as water, carbon oxide, ammonia condensed at ~ 5 astronomical units (AU) from the Sun, which is also known as snow line or ice line (Cieza et al., 2016; Kennedy and Kenyon, 2008). These volatiles were captured by those gas giants located in the outer solar system, e.g., Jupiter and Saturn. Although the warmer temperature in inner solar system prevented the condensation of volatiles, the remaining materials formed rocky planets in this area, like the Earth, Mars, Mercury (also known as terrestrial planets).

For the study of the history of the Earth, which material(s) composed the building blocks of the Earth, and when/how did these materials accreted to the Earth are fundamental questions. As mentioned above, the accretion of the Earth may start from

the remaining materials after the formation of the Sun in inner solar system. However, the signatures of both elemental and isotopic signatures of the Earth suggest a more complex accretion history instead of a single source material as the building blocks (e.g., Braukmuller et al., 2019; Johansen et al., 2015; Johansen et al., 2021; Kruijer et al., 2020; Kubik et al., 2021b; Nanne et al., 2019; Piani et al., 2020; Pringle and Moynier, 2017; Savage et al., 2022; Schiller et al., 2018; Schiller et al., 2020; Sossi et al., 2019; Sossi et al., 2016; Sossi et al., 2018b; Sossi et al., 2022; Van Kooten et al., 2021; Wänke and Dreibus, 1988; Wänke et al., 1984). The accretion history and the building blocks of the Earth is still debated, and will be the key point on which this dissertation focuses on. An introduction of the hypothesis of the Earth's building blocks and accretion history are provided in the following sections.

1.2 Hypothesis of the building blocks of the Earth

Due to the Earth's differentiation process such as core-formation and mantle-crust differentiation, the direct approach to study the building materials from the proto-Earth is difficult. Therefore, the studies of Earth's building blocks focus on the meteorites, which are the remnant materials following planets' accretion, and these meteoritic materials can be seen as a major sources of planets' building blocks.

Chondrites are the meteorite type that did not experience differentiated and melting process, and therefore preserved the most primitive signatures of the early solar system. Depending on the mineralogy and chemical compositions, chondrites can be further divided into carbonaceous chondrite, enstatite chondrite and ordinary chondrite. Carbonaceous chondrites (C-type chondrite, CC) were named from their higher carbon contents in comparison with other chondrites, their chemical compositions, more specifically the CI-chondrites, have a similar composition as the Sun (except for the highly volatiles like H, He and N), and therefore are typically used as the referenced materials of the average chemical composition of the solar system (e.g., McDonough and Sun, 1995; Palme and O'Neill, 2014). Enstatite chondrites (E-type chondrites, EC),

are named from their abundant mineral phase, enstatite. The E-type chondrites are characterized as the most reduced chondrites among the meteorite collections with an oxygen fugacity ~ 6 to 8 units below iron-wüstite buffer (ΔIW- 6 to -8) (Fogel et al., 1989), whereas carbonaceous chondrites are typically seen as the oxidized chondrites (ΔIW- 2 to -3) (e.g., Righter et al., 2016). Ordinary chondrite (O-type chondrite, OC) are the most common chondrites, and hence named as 'ordinary', ordinary chondrites are also known for their high abundance of chondrules, which are seen as the products of high-temperature process (i.e., relevant with evaporation or condensation process). The redox state of ordinary chondrite is between carbonaceous chondrite and enstatite chondrite (Righter et al., 2016).

Non-chondrite can be further divided into achondrites, iron and stony-iron meteorites, and planetary meteorites which are considered from Mars and Moon. Non-chondrites typically have experienced melting process or came from differentiated telluric bodies; therefore, their compositions can provide an insight into accretion and evolution history of differentiated bodies in early solar system.

Over the past several decades, the building blocks of the Earth were studied by comparing the Earth's chemical compositions with the primitive materials sampled by meteorites. However, numerous studies have shown that the elemental and isotopic characteristics of the Earth cannot be explained by any single known meteorite collection. In 1970s, Clayton et al. (1976) analyzed the oxygen isotopic compositions of the Earth and a wide variety of meteorites, and found that the oxygen isotopic composition of the Earth was different from carbonaceous chondrites (named as CCs and here after) and ordinary chondrites (OCs) but with similarities with enstatite chondrites (ECs). However, ECs are silicon-rich and highly reduced materials, their elemental abundances are not in agreement with the estimated composition of bulk Earth, instead the latter exhibits more similarities with carbonaceous chondrites (e.g., Allègre et al., 1995; McDonough and Sun, 1995).

Studies on nucleosynthetic isotope anomalies also shed a light on the reservoirs of

the Earth's building materials. Nucleosynthetic isotope anomaly refers to the mass-independent isotopic variations that observed on the Earth and meteorites. These anomalies are suggested to arise from pre-solar grains, which carried the isotopic signatures of fusion reactions in the core of massive stars and/or explosive nucleosynthesis process (Clayton, 2003), and were not further entirely homogenized during the accretion in proto-planetary disc (Clayton, 1982). Therefore, nucleosynthetic isotope anomaly can be used as important tracers to study the heterogeneity of materials in solar system. Recent studies on the isotopic system with nucleosynthetic isotope anomalies (e.g., Ti, Cr, Mo, Nd, Fe, Zn) proposed a 'non-carbonaceous-carbonaceous' (NC-CC) chondrites difference for the Earth's building materials (Budde et al., 2019; Kruijer et al., 2020; Nanne et al., 2019; Savage et al., 2022; Schiller et al., 2018; Schiller et al., 2020; Trinquier et al., 2007; Trinquier et al., 2009). This model suggested that the Earth's building materials were formed by the mixing of CC and NC-like materials, as the Earth's isotopic anomalies fall intermediate between CC and NC. A pebble accretion model is consistent with the observed nucleosynthetic isotope anomalies of the Earth. This model suggests that the Earth primarily accreted from the pebbles of millimeter-size NC materials, possibly chondrule-like materials, and the CC-like materials delivered to the Earth during a later stage (Johansen et al., 2015; Johansen et al., 2021; Schiller et al., 2020). Alternatively, enstatite chondrites exhibit the closest isotopic composition to the Earth and thus were suggested as the primary building blocks of the Earth (e.g., Javoy et al., 2010). Nonetheless, regardless of enstatite chondrites or carbonaceous chondrites, their abundances of many MVEs are significantly more abundant than in the Earth (McDonough and Sun, 1995; Palme and O'Neill, 2014), indicating the existence of a volatile depletion mechanism during the nebular and/or post-nebular environment. The origin of the volatile depletion process is still not clear and debated (e.g., Albarede, 2009; Norris and Wood, 2017). Therefore, to study the Earth's building materials and accretion history, it is crucial to know the origin of the Earth's volatile depletion and further place constraints on the environmental conditions

during which volatile depletion occurred, and this is the major object of this thesis.

1.3 The depletion of volatile elements in the Earth

In comparison with carbonaceous chondrites, the Earth's highly volatile and moderately volatile elements abundances are significantly depleted (Albarede, 2009; Braukmüller et al., 2019; Marty, 2012; Marty and Yokochi, 2006; McDonough and Sun, 1995; Palme and O'Neill, 2014; Piani et al., 2020; Wasson and Kallemeyn, 1988). Figure. 1-1 shows the CI, -Mg normalized elemental abundances of the Earth plotted against 50% condensation temperature (T_C^{50}), defined as the temperature at which half of the elements initially in vapor and condensed to solid state at nebular conditions (10^{-4} bar, $\log fO_2 = -14$) (Lodders, 2003; Wood et al., 2019), which exhibit a flat pattern for the refractory lithophile elements and a log-linear depleted pattern for the lithophile moderately volatile elements (volatility intermediate between Mg-silicate and FeS, named as MVEs hereafter). The additional depletion of siderophile MVEs are caused by the Earth's core-formation processes. Over the past several decades, many studies report on the origin of the Earth's volatile depletion, however, the mechanisms for this volatile depletion are still unclear to date. Some major on-debate topics focus on the following points: 1) whether the building materials experienced vaporization processed and thus lost their volatile elements; 2) which type of meteorite-like materials constitute the Earth's building materials, like carbonaceous chondrites/enstatite chondrites/ordinary chondrite, and when and how did these materials lose their volatiles; 3) whether there is a late-added volatile-rich materials delivered to the Earth, and if so, when did these materials arrived the Earth, and how much did they contribute to the Earth's present volatile budgets? Surrounding these questions, there are a few hypotheses that have been proposed to explain the origin of the Earth's volatile depletion:

1) Incomplete condensation of MVEs from solar nebula. hypothesis describes that the energetic radiation blown from the young Sun drive gas phases away from condensed

phases before which the temperature decreased to the values that most of volatile condensed, and therefore separated volatile elements from refractory elements, resulting in an incomplete condensation of volatile elements in the planetary building materials (e.g., Albarede, 2009; Vollstaedt et al., 2020).

2) The vaporization loss on the building materials of the Earth e.g., Ringwood (1966). Numerous experimental studies have observed that evaporation process on silicate melt can lead to the loss of volatile elements (e.g., Norris and Wood, 2017; Richter, 2004; Richter et al., 2002; Sossi et al., 2019). Furthermore, this evaporation-induced volatile loss may also fractionate isotopes, and leave an enrichment of heavier isotopes in evaporated residue (Sossi et al., 2020; Wimpenny et al., 2019; Yu et al., 2003). In comparison with chondrites, the Earth has a heavier isotopic composition of Si (Moynier et al., 2020; Pringle et al., 2014), Fe (Sossi et al., 2016) and Mg (Hin et al., 2017), which suggest that evaporation processes may have played an important role on shaping the Earth's chemical composition.

3) A mixing sources of Earth's MVEs budgets. Different from Si, Fe and Mg, which are typically considered as less volatile elements, the isotopic compositions of MVEs in the Earth were not observed with resolvable heavier isotopic than chondrites, for example, Ag (Schönbächler et al., 2010), Cu (Mahan et al., 2018c; Savage et al., 2015), S (Suer et al., 2017a), Zn (Mahan et al., 2018a; Sossi et al., 2018b) and Sn (Kubik et al., 2021b). These studies observed that the Earth's isotopic compositions of MVEs were not resolvable with the range of carbonaceous chondrites, and hence suggested the carbonaceous chondrites as an important source of Earth's MVEs budget. Furthermore, the Earth's budgets of MVEs are modelled as the results of the mixing of carbonaceous chondrites and volatile depleted materials (Schönbächler et al., 2010; Wänke and Dreibus, 1988; Wänke et al., 1984), and this hypothesis is also favored in this dissertation. Moreover, the contribution fraction and chemical composition of each end-member (CC-like, NC-like) materials, as well as the volatile depletion mechanisms (timing, pressure, temperature, oxygen fugacity etc.) are still unclear.

There are some different approaches that have been applied to study the contribution of each building materials accreted by the Earth. Highly siderophile elements (HSEs), in particular platinum group elements (PGEs) are known for their high iron-affinity, according to the partitioning coefficient results from metal-silicate experiments, the concentrations of HSEs in the bulk silicate Earth (BSE) should be nearly zero. However, this phenomenon is not observed in the BSE, instead, the CI, -Mg normalized abundances of these HSEs exhibit a flat pattern along with their T_C[50] (Palme and O'Neill, 2014). This additional amounts of HSEs were explained as the results of a late-added CI-like with ~ 0.5 % of Earth's mass which arrived the Earth after the core-formation ceased, and therefore without further equilibrium between core and mantle, and avoid sequestration into the core and this hypothesis is also known as 'late veneer' model (O'Neill et al., 1995). This estimated CC-like materials contribution fraction is also consistent with the ratios and abundances of S, Se and Te in Earth's mantle (Wang and Becker, 2013). Marty (2012)'s study on the highly volatiles (water, carbon and noble gases) suggested ~2 % Earth mass materials CI or CM-like materials were required to satisfy the present highly volatile composition in BSE. On the other hand, Piani et al. (2020) showed that enstatite chondrite could be an important component of the Earth's highly volatile budget, and further found a ~ 4% contribution from CI-like volatile rich materials to the surficial hydrogen inventory, and ~ 15% contribution to the surficial nitrogen inventory. Studies on oxygen isotopes and metal-silicate experiments on MVEs suggested a fraction of ~ 4 % Earth's mass of CI-like materials (Albarede et al., 2013; Ballhaus et al., 2013a). Recent studies from Braukmüller et al. (2018) and Braukmuller et al. (2019) provided an high precision dataset for the concentrations of MVEs in carbonaceous chondrites and they observed a 'hockey-stick' volatile depletion pattern among different types of carbonaceous chondrites and the Earth, and further suggested ~ 10-15 wt.% CI-like materials delivered to the Earth before core formation process ceased. Warren (2011) combined the observed nucleosynthetic isotope anomalies on ε^{54}Cr (Trinquier et al., 2007), ε^{50}Ti

(Trinquier et al., 2009) and $\Delta^{17}O$ (Clayton et al., 1976) from early published studies and provided an estimation of ~ 24 wt.% (up to ~32 wt.%) of CC-like materials accreted to the Earth, while Dauphas et al. (2014) proposed a mixture of 2 % of CC-like materials, 7% of OC-like materials and 91% of EC-like materials could best match the Earth's nucleosynthetic isotope anomalies. Studies on the Ca (Schiller et al., 2018) and Fe anomalies (Schiller et al., 2020) suggested ~ 60% of Earth mass accreted via the pebbles of NC-like materials, possibly ureilite and/or chondrule-like materials that seen as the representative early inner disk materials, and followed a later delivered CC-like materials with ~ 40% Earth mass. A simulation of the pebble accretion model in Johansen et al. (2021) further supported this 'two-generation' pebble model, as well as the fraction of NC and CC components, and they also suggested the 'early generation' pebbles could be crucial carrier of Earth's water and carbon. Zn isotopic anomalies suggest that the Earth accreted from primary NC-like materials (~ 94%) and a late-accreted ~ 6% of CC-like materials (Savage et al., 2022; Steller et al., 2022). Recent studies on the dichotomy of Mo, Ni also supports the existence of later-delivered CC-like materials to the Earth (Budde et al., 2019; Nanne et al., 2019).

Although there are some different models already tried to provide constraints on Earth's building components, as mentioned above, the results predicted between models cannot be well matched, and therefore more evidences are still required, and this is the main purpose of this dissertation. In this dissertation, a moderately volatile element, indium (In), was used as the tracer for the tracking the origin of volatile depletion in the Earth. The studies of In are conducted in different aspects, including experimental approaches (evaporation experiments and metal-silicate segregation experiments) and isotopic analyses. The introduction of In is provided in the next section.

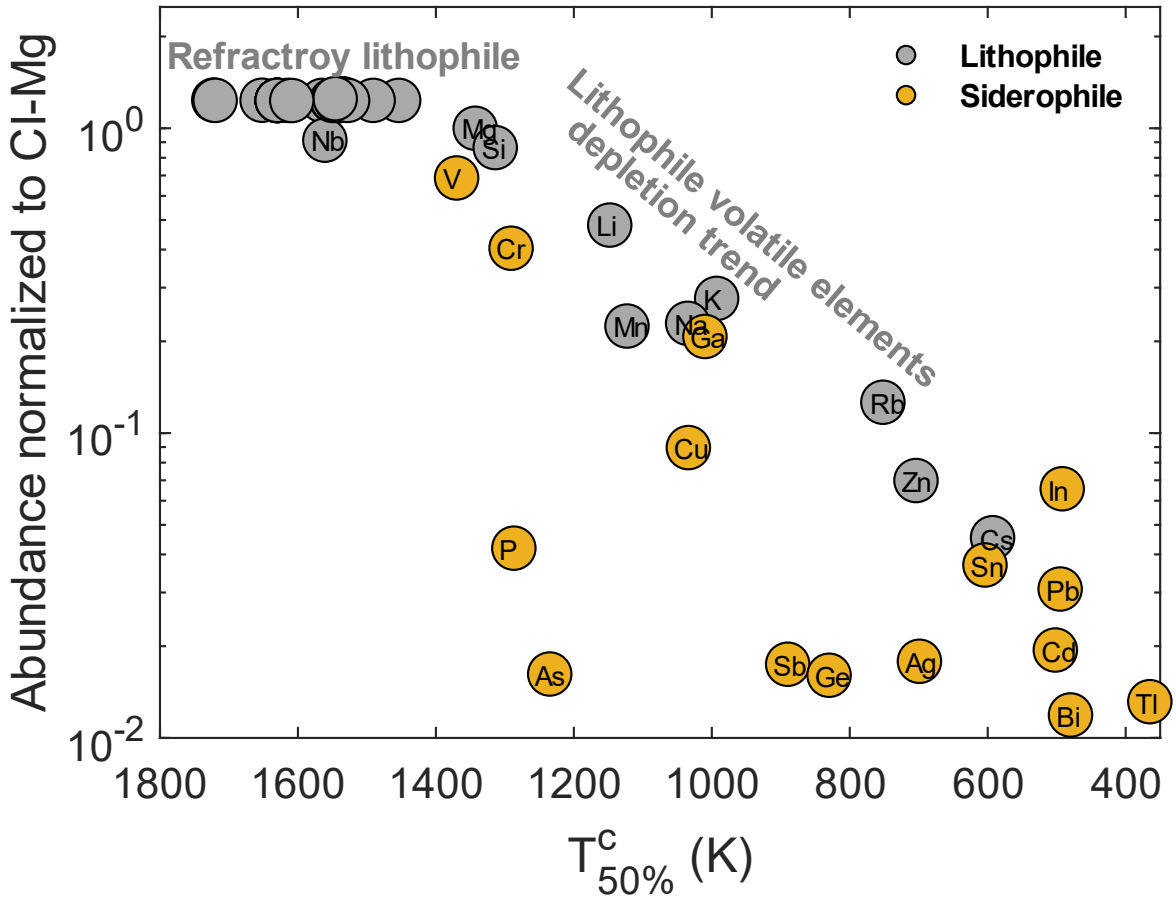

Figure. 1-1 Abundances of representative volatile and refractory elements in the BSE normalized to CI chondrites and Mg vs. T_c^{50}. Elemental abundance of BSE and CI chondrite from Palme and O'Neill. (2014) and references therein; The abundance of In is taken from the current estimate of Wang et al. (2016); T_c^{50} from Wood et al. (2019). The refractory lithophile elements such as Ca, Ti, Sc, Zr and rare earth elements (REE) have higher T_c^{50} than Mg, and exhibit a flat pattern. The lithophile volatile elements display a near log-linear depletion along with T_c^{50}. As both volatile and siderophile element, the abundance of In in the BSE is similar as Zn, which is lithophile element and T_c^{50} markedly higher than In (~ 200 K)

1.4 Indium, an important tracer of the volatile depletion processes

Indium (In) is a trace element with a low abundance in the BSE, from ~ 11 ppb to 18 ppb according to different estimations (McDonough and Sun, 1995; Wang et al., 2015; Witt-Eickschen et al., 2009; Yi et al., 2000). As described in section 1.4, most of the lithophile MVEs follow the near log-linear depletion pattern along with T_C^{50}, a typical temperature scale used to quantify elemental volatility in nebular environment. However, In is an exception in comparison with this depletion pattern. In has a T_C^{50} of 536 K (Lodders, 2003) or 492 K (Wood et al., 2019), indicating it is a moderately to highly volatile elements during the condensation of a nebular gas. Moreover, In is also a siderophile (iron-affinity) element, implying an additional sequestration into the core during the Earth's core-formation can be expected. However, as both a volatile and a siderophile element, In falls over the depletion trend which is defined by the lithophile MVEs as shown in Figure.1-1, indicating that In is apparently over-abundant in the BSE. The origin for this overabundance of In, is still unclear. Several hypotheses have been proposed (Braukmuller et al., 2019; Norris and Wood, 2017; Wang et al., 2016b; Witt-Eickschen et al., 2009) to explain this overabundance, and can be summarized as: 1) heterogenous distribution of In in the Earth's mantle (and therefore a wrong estimation of the In concentration of the mantle), however this hypothesis is not favored in their study as it is not likely that only In would be heterogeneously distributed in the Earth's mantle, while other neighboring elements with similar behavior would be not ; 2) inappropriate use of the temperature scale T_C^{50}, which only described the elemental volatility under nebular environment and does not reflect evaporation under oxidative conditions; 3) additional In brought by the volatile-rich materials during Earth's accretion, i.e. late accretion; 4) The precursor materials of proto-Earth have already contained an anomalously high amount of In compared to other MVEs (unlikely). Although these hypotheses have been proposed, the studies on the geochemical characteristics of In are still scarce, and hindered the understanding of the origin of In

in the Earth. In view of the unique characteristics of In as mentioned above, the understanding of its origin can also give an insight to the accreted building materials and history of the Earth.

In this dissertation, the three aspects, volatility, siderophility and isotopic signatures of In were studied. The knowledge of volatility, siderophility are expected to provide the context to understand the potential depletion mechanisms of In during the Earth's accretion, including evaporation/condensation process of building materials, core-formation process during Earth's formation. In isotopic geochemical behavior (during evaporation and core formation), as well as the In isotopic composition in bulk silicate Earth and bulk Earth (meteorites) is also reported as a fundamental work for the future application of In isotopes system for tracking the potential building materials of the Earth. An introduction of each aspect is described in the following sections.

1.4.1. The volatility of In during evaporation process in a vapor-melt system.

The elemental volatilities are traditionally quantified with the temperature scale, T_C^{50} (Lodders, 2003; Wood et al., 2019). This temperature scale was estimated according to the nebular conditions, which correspond to total pressure in 10^{-4} bar and oxygen fugacity of $\log fO_2 = -14$ (Lodders, 2003; Wood et al., 2019) and therefore described the elemental volatility in nebular environment. However, as the evolution of solar nebula, the environmental conditions also changed along with the temporal and spatial variations. For instance, Mn/Na ratios can be used to compare the oxygen fugacity during which the volatile depletion occurred, because the relative volatilities between Mn and Na are sensitive to oxygen fugacity, in which Na can be more volatile than Mn as the increase of oxygen fugacity (O'Neill and Palme, 2008; Siebert et al., 2018). The Mn/Na ratios of differentiated bodies such as howardite-eucrite-diogenite (HED) parent bod, angrite parent body, Mars and Moon are observed to be higher than chondrites, indicating a more oxidizing conditions existed during which their formation and/or volatile loss via evaporation/condensation processes (Siebert et al., 2018). Furthermore, the different Mn/Na ratios observed in chondrules also suggested a variable oxygen fugacity environment during the early solar system, even before the

dissipation of nebular gas (Mahan et al., 2018b; Wang et al., 2017).

Oxygen fugacity is an important parameter which governs the elemental volatility (shown in Figure. 1-2), and can result in a significant deviation of elemental relative volatilities between neighboring elements with similar T_C^{50} (e.g., Norris and Wood, 2017). Therefore, the application of T_C^{50} for representing elemental volatility should be strictly limited for the nebular conditions, otherwise, the assumptions based on this temperature scale may bring in incorrect assessment (Sossi and Fegley, 2018; Sossi et al., 2019). Based on this observation, a new temperature scale, was proposed by Sossi et al (2019), to quantify elemental volatilities under higher oxygen fugacity and total pressure than nebular conditions, and can give an insight to elemental volatility under the scenarios like planetary accretion and/or chondrule-formation.

Inspired by Norris and Wood (2017) and Sossi et al. (2019), a series of evaporation experiments were conducted on the melt of basaltic composition, under variable temperature and oxygen fugacities in this dissertation, and the volatility of In in the evaporation process was quantified followed the approach derived in Sossi et al. (2019). The results and relevant discussions are provided in **Chapter 2**.

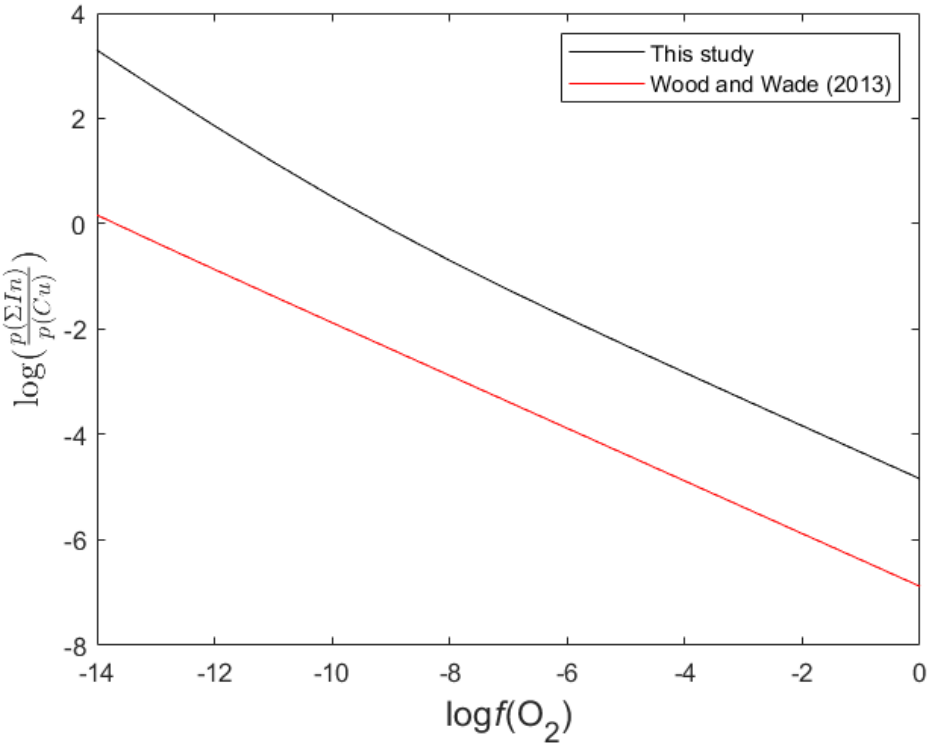

Figure. 1-2 The relative volatility of In and Cu plot as a function of oxygen fugacity. The relative volatility between In and Cu is expressed to be the ratio of Cu (g) and sum of partial pressure of In (g) and In_2O(g) from vaporization reactions:

$$CuO_{0.5}(l) = Cu\ (g) + \frac{1}{4}O_2(g)$$

$$InO_{1.5}(l) = In\ (g) + \frac{3}{4}O_2(g)$$

$$In_2O\ (g) = 2In(g) + \frac{1}{2}O_2(g)$$

Thermodynamic data of pure substances of Cu is from Barin and Platzki (1989). The black line represents the ratio of $p(\sum In)/p(Cu)$ varying with oxygen fugacity in this study, where using the modified equilibrium constant (K^*_{In}) of In that described in Chapter 2, while K^*_{Cu} is calculated from pure substances and activity coefficient $\gamma_{CuO_{0.5}}$ at 1573K, extrapolated from Wood and Wade (2013). The red line shows the calculated ratio of $p(\sum In)/p(Cu)$ by using the activity coefficients of $InO_{1.5}$ ($\gamma_{InO_{1.5}} = 0.008$ at 1573K) extrapolated from Wood and Wade (2013). concentration of $CuO_{0.5}$ and $InO_{1.5}$ in melt are assumed to be 1 wt.%, which are close to our experimental conditions. Regardless the different activity coefficients that are relevant with melt composition, both studies exhibit varying relative volatilities between In and Cu. Our results show that pIn/pCu is unity at ~ log$f$O$_2$ = -9 at 1573 K which is consistent with the observed relative volatility of Cu and In from Sossi et al., 2019 and Chapter 2, suggesting elemental relative volatilities are strongly governed by oxygen fugacity.

1.4.2. The siderophility of In.

In is a siderophile element, and hence the Earth's core-formation process could sequestrate part of In into the core (Ballhaus et al., 2013a; Mann et al., 2009; Righter et al., 2017; Righter et al., 2018a; Steenstra et al., 2020; Wang et al., 2016a; Wood et al., 2014b). However, this process depends on the siderophility (iron-affinity) of In and the effects of temperature, pressure, melt composition, oxygen fugacity and light elements (e.g., S, Si) in metallic phases, as the elemental partitioning coefficient (noted as D, the ratio of elemental molar fraction between metal and silicate) are controlled by these physical-chemical conditions.

Therefore, the estimation of the In abundance in the Earth's core and a further estimation of bulk In budget in the Earth requires the knowledge of the siderophility of In and how these parameters influence In's partitioning coefficient under the Earth's core-formation process. However, the experimental studies on the partitioning of In are still limited and most of these experiments were performed at low pressure-temperature conditions, which hindered the study on the In's partitioning during Earth's core-formation. Moreover, the Earth's core contains various light elements such as S, Si, O, C and N (e.g., Dalou et al., 2017; McDonough, 2003; Siebert et al., 2013; Suer et al., 2017a), and the light elements in metallic phases can have strong effect on the partitioning (e.g., Steenstra et al., 2020; Wood et al., 2014b), and this effect can be quantified with the term interaction parameter (noted as $\varepsilon_M^{S/Si}$, which describes the effects from S or Si on the partitioning of element M, a detailed description and application of $\varepsilon_M^{S/Si}$ can be found in Ma (2001)). Recent experimental studies have reported a strong effect of Si on the partitioning of In between metal and silicate (Righter et al., 2017; Righter et al., 2018a; Steenstra et al., 2020), indicating the existence of Si in the core may strongly influence the abundance of In in the core. Furthermore, Steenstra et al. (2020) also observed a significant pressure-dependent $\varepsilon_M^{S/Si}$ on In, and the similar pressured-dependent interaction parameters between light elements and MVEs such as Sn, Bi, Tl are also observed in recent studies (Kubik et al., 2021a; Kubik et al., 2021b; Steenstra et al., 2020), suggesting that the application of

extrapolated interaction parameters of In and S or Si from low-pressure experiments may result in incorrect estimation of the In concentration in the core. However, the results of $\varepsilon_M^{S/Si}$ estimated from higher pressure are still scarce, in particular pressure more than 5 GPa and/or 13-15 GPa, known as the structure transition pressure range (Fei et al., 1997; Fei et al., 2000; Morard et al., 2007; Sanloup et al., 2011; Shibazaki et al., 2015)), and lack of the re-examination by the experiments conducted under the final Earth's core-formation conditions, and this is one of the goals in this dissertation.

In this dissertation, a series of metal-silicate experiments were performed under a wide range of *P-T* conditions (from 2 to 50 GPa, ~ 1600 to 4000 K), which approached the whole *P-T* conditions corresponding to the Earth's core-formation process (e.g., Siebert et al., 2012; Siebert et al., 2011). The effects of S and Si on the partitioning of In were also discussed. Based on the dataset in this dissertation and literatures, the evolution of the partitioning model of In during the Earth's accretion, as well as a further discussion on the sources of Earth's In budget, are provided in **Chapter 4**.

1.4.3. Indium isotopic composition of the Earth and future application.

Chondrites, as the remnant solid materials of early Solar System, are expected to preserve the signatures of the building materials of planets. Therefore, as introduced in section 1.3, comparing the Earth's isotopic composition with chondritic isotopic composition, provide important information to the Earth's building materials and accretion stages. As a moderately volatile element, the isotopic composition of In of the Earth carries the signature of each constituted component of the Earth. In other words, if the dominant In budget came from the late-delivered CI-like materials such as 'hockey stick' model that was proposed by Braukmuller et al. (2019), the Earth's In isotopic composition should therefore inherit a carbonaceous chondritic isotopic composition. Conversely, if the volatile depletion pattern of the Earth was only shaped by the evaporation-induced volatile loss, and if such evaporation process further caused kinetic isotopic fractionation, the Earth's In isotopic composition may therefore exhibit a heaver isotopic composition compared with chondrites due to the evaporated residue as the building materials. Alternatively, although most evaporation experiments

conducted under high vacuum produce kinetic isotopic fractionation (e.g., Yu et al., 2003), the isotopic fractionation during the evaporation process that occurred under non-ideal conditions (e.g., higher total pressure, higher gas density) could be strongly suppressed by the low mass transport rate over evaporation surface in a vapor-melt system (Richter et al., 2002; Richter et al., 2007; Sossi et al., 2020; Wimpenny et al., 2019). Given these potential hypotheses on the Earth's volatile origin and depletion, In isotopes can be expected as an useful tracer that recorded the footprint of these processes. However, the knowledge of In isotopes, for example, their geochemical behavior and potential fractionation during igneous differentiation process, as well as In isotopic composition in the bulk silicate Earth and bulk Earth, is still poorly understood, and hence is required before it could be used as the tracer of the Earth's building blocks and timing/origin of the volatile depletion. A brief introduction of In isotopic geochemistry is provided below, more detailed results and discussions can be found in **Chapter 3** (the In isotope determination method and In isotopic composition in terrestrial rocks) and **Chapter 4** (In isotopic fractionation between silicate and metal segregation).

In has two naturally occurring isotopes, ^{113}In (~ 4.28 %) and ^{115}In (~ 95.72%), in which ^{113}In is a stable isotope, and ^{115}In is radioactive isotope (β-decay to ^{115}Sn) with a very long half-life of 4.41×10^{14} years (Pfeiffer et al., 1979) and therefore can be approximated seen as a stable isotope. In is dominantly hosted in pyroxene and olivine in mafic rocks, and biotite and amphibole in felsic rocks. In is a moderately incompatible element, and has a concentration ~ 0.05 ppm in continental crust and ~ 0.08 ppm in oceanic crust, lower concentration in mantle (~ 0.01 ppm) (Arevalo Jr and McDonough, 2010; Palme and O'Neill, 2014; Rudnick et al., 2003; Witt-Eickschen et al., 2009). The In isotopic compositions in natural samples are still poorly understood and the relevant studies on the In isotopic geochemistry is scarce. Therefore, an object of this dissertation is developing the determination method including chemical purification and analytical method of In isotopes, and obtained a dataset of the isotopic compositions of the Earth's rocks. Furthermore, considering that a potential isotopic

fractionation of In may occurred during metal-silicate segregation process, as already observed on Fe (Shahar et al., 2015), nitrogen (Dalou et al., 2019), Sn (Kubik et al., 2021b), Si (Moynier et al., 2020), the isotopic composition of a series of metal-silicate experimental samples were also analyzed in this dissertation.

1.5 Experimental and analytical technique

In this section, a brief introduction of the experimental apparatuses (evaporation experiments and metal-silicate experiments) is provided, as well as the operational principles of the analytical instruments for elemental and isotopic compositions including mass spec and electron probe, and backscatter/secondary electron.

1.5.1 Apparatus of evaporation and metals-silicate experiments

Evaporation experiments were performed with a gas-mixing atmosphere-control tube furnace. The furnace tube is made of alumina with a size of 70-cm-long, 4.2 cm of diameter (Sossi et al., 2020). The oxygen fugacities during experiments were buffered by the mixing of CO and CO_2 at a fixed total gas flow rate (200 standard cubic centimeters per minute, *sccm*). The ratio of CO and CO_2 was adjusted using four MKS G-series mass flow controllers. The experimental temperature was measured by a type B thermocouple ($Pt_{94}Rh_6/Pt_{70}Rh_{30}$, measured uncertainty ± 0.5%), which is located less than 1 cm above the sample beads, providing a precise measurement of the temperature within the ~4 cm-long hotspot in the furnace. The furnace tube was isolated from outside by a steel ball valve. During the running of experiments, the valve is closed to prevent the potential fluctuations of oxygen fugacity, once the heating procedure was complete, the value was then opened manually, and samples then quickly drop-quenched into the Milli-Q (18.2 Ω) deionized water.

Metal-silicate segregation experiments were performed with three different high-pressure apparatuses including piston-cylinder, multi-anvil and diamond-anvil-cell presses, allowing to perform the high-pressure experiments from ~ 2 GPa up to 50 GPa. The piston-cylinder apparatus used hydraulic rams as the pressure-generation equipment, and a graphite furnace was placed into pressure media for heating samples.

Experiments performed on piston-cylinder all had the same pressure conditions (2GPa), and the pressure calibration used the approach described in Perkins and Newton (1981). Sample powder was filled in a MgO capsule and used cylindrical talc-pyrex/$BaCO_3$ pressure medium depending on the temperature choices. Multi-anvil press was used for the experiments that performed under the pressure range ~ 7 to 20 GPa. Multi-anvil apparatus also used hydraulic press as the pressure source, and a few tool-steel anvils and tungsten carbide cubic were equipped in hydraulic press which allows to provide a higher P-T conditions (up to 3000 K and 30 GPa). The single crystal MgO was used as capsule and MgO + Cr_2O_3 (5%) was used as pressure media. Pressure calibration was performed according to the transition of Bi, quartz-coesite and coesite-sishovite (Lloyd, 1971; Rubie, 1999; Yagi et al., 1987; Yagi and Akimoto, 1976). Diamond-anvil-cell (DAC) apparatus was used for the experiments that conducted under the highest P-T conditions (~ 50 GPa and 4000 K). Re gaskets were drilled and used for the sample chamber. The sample assembly consisted metal layer and silicate layer, in which metal mixture was placed into a two-layer of silicate glass. The pressure was achieved by pushing the two diamond anvils together, and its value was determined by diamond Raman spectroscopy at room temperature and after heating procedure. The heating was achieved via a fiber laser.

1.5.2 Multi - instrument analyses of element and isotope

The elemental concentration analyses were conducted on electron microprobe analysis (EPMA), laser-ablation inductively-coupled-plasma mass spectrometry (LA-ICP-MS) and Quadrupole inductively-coupled-plasma mass spectrometry (Q-ICP-MS), while isotopic analyses were performed on multi-collector inductively-coupled-plasma mass spectrometry (MC-ICP-MS). EPMA can be used to analyze the elemental composition on the sample surface, as well as the appearance information and spatially chemical compositional differences. There different functions can be achieved via X-rays (elemental composition analyses), secondary electrons (surface image) and back-scatter electrons (spatially chemical composition differences), and all of these electrons and X-rays are generated by the interaction between sample surface and excited

electrons from an electron source that equipped on the EPMA system. When the emitted electrons interact with the sample which is composed of different elemental species, the produced X-rays are also with different wavelength due to the influences of different species. Then these X-rays can be detected and analyzed with the coupled wavelength dispersive spectrometers (WDS) and/or energy dispersive spectrometers (EDS), allowing the chemical compositional analyses on the sample surface. Simultaneously, secondary electrons can be sensed and reconstructed to provide an appearance of the sample surface, and back-scatter electrons can provide an image that reflects the chemical compositional differences on the sample surface because the heavier elements can generate backscatter electrons more efficiently, and result in a brighter area in the backscatter electrons image (BSE), the same operational principle is also applied on scan electron microscopy (SEM).

Although the designs of the sample-introduction system/collector/ion-separation system have significant differences, the basic operational principle of these mass spectrometers (Q-ICP-MS, LA-ICP-MS and MC-ICP-MS) are similar. Briefly, samples are introduced into the system, and then ionized by inductively coupled plasma source, generated positively-charged particles, then these cations are accelerated in an electrical potential gradient, and then enter magnetic field. In magnetic field, cations can be further separated according to their different ratios of ion's mass (m) and formal charge (z), m/z, and are finally detected and analyzed by collectors. The differences of these mass spectrometers, for example, Q-ICP-MS uses quadrupole to separate cations with different m/z ratios and collected these cations in a continuous time and therefore can measure the elemental concentrations of a broad mass range (typically Li to U), while MC-ICP-MS uses a curved magnetic field which can let low m/z cations pass through a more curved path and *vice versa*, this design allows the separated ion beams to be simultaneously detected and measured by Faraday cups, and hence can provide a high-precision measurement of isotopic compositions.

References

Albarede, F. (2009) Volatile accretion history of the terrestrial planets and dynamic implications. Nature 461, 1227-1233.

Albarede, F., Ballhaus, C., Blichert-Toft, J., Lee, C.-T., Marty, B., Moynier, F. and Yin, Q.-Z. (2013) Asteroidal impacts and the origin of terrestrial and lunar volatiles. Icarus 222, 44-52.

Allègre, C.J., Poirier, J.-P., Humler, E. and Hofmann, A.W. (1995) The chemical composition of the Earth. Earth and Planetary Science Letters 134, 515-526.

Arevalo Jr, R. and McDonough, W.F. (2010) Chemical variations and regional diversity observed in MORB. Chem. Geol. 271, 70-85.

Ballhaus, C., Laurenz, V., Münker, C., Fonseca, R.O.C., Albarède, F., Rohrbach, A., Lagos, M., Schmidt, M.W., Jochum, K.-P., Stoll, B., Weis, U. and Helmy, H.M. (2013) The U/Pb ratio of the Earth's mantle—A signature of late volatile addition. Earth and Planetary Science Letters 362, 237-245.

Barin, I. and Platzki, G. (1989) Thermochemical data of pure substances. Wiley Online Library.

Braukmüller, N., Wombacher, F., Funk, C. and Münker, C. (2019) Earth's volatile element depletion pattern inherited from a carbonaceous chondrite-like source. Nature Geoscience 12, 564-568.

Braukmüller, N., Wombacher, F., Hezel, D.C., Escoube, R. and Münker, C. (2018) The chemical composition of carbonaceous chondrites: Implications for volatile element depletion, complementarity and alteration. Geochimica et Cosmochimica Acta 239, 17-48.

Braukmuller, N., Wombacher, F., Funk, C. and Munker, C. (2019) Earth's volatile element depletion pattern inherited from a carbonaceous chondrite-like source. Nature Geoscience 12, 564-+.

Budde, G., Burkhardt, C. and Kleine, T. (2019) Molybdenum isotopic evidence for the late accretion of outer Solar System material to Earth. Nature Astronomy 3, 736-741.

Burkhardt, C., Kleine, T., Bourdon, B., Palme, H., Zipfel, J., Friedrich, J.M. and Ebel, D.S. (2008) Hf–W mineral isochron for Ca, Al-rich inclusions: age of the solar system and the timing of core formation in planetesimals. Geochimica et

Cosmochimica Acta 72, 6177-6197.

Cieza, L.A., Casassus, S., Tobin, J., Bos, S.P., Williams, J.P., Perez, S., Zhu, Z., Caceres, C., Canovas, H., Dunham, M.M., Hales, A., Prieto, J.L., Principe, D.A., Schreiber, M.R., Ruiz-Rodriguez, D. and Zurlo, A. (2016) Imaging the water snow-line during a protostellar outburst. Nature 535, 258-261.

Clayton, D. (1982) Cosmic chemical memory-a new astronomy. Quarterly Journal of the Royal Astronomical Society 23, 174.

Clayton, D. (2003) Handbook of Isotopes in the Cosmos.

Clayton, R.N., Onuma, N. and Mayeda, T.K. (1976) A classification of meteorites based on oxygen isotopes. Earth and Planetary Science Letters 30, 10-18.

Connelly, J.N., Bizzarro, M., Krot, A.N., Nordlund, Å., Wielandt, D. and Ivanova, M.A. (2012) The absolute chronology and thermal processing of solids in the solar protoplanetary disk. Science 338, 651-655.

Dalou, C., Füri, E., Deligny, C., Piani, L., Caumon, M.-C., Laumonier, M., Boulliung, J. and Edén, M. (2019) Redox control on nitrogen isotope fractionation during planetary core formation. Proceedings of the National Academy of Sciences 116, 14485-14494.

Dalou, C., Hirschmann, M.M., von der Handt, A., Mosenfelder, J. and Armstrong, L.S. (2017) Nitrogen and carbon fractionation during core-mantle differentiation at shallow depth. Earth and Planetary Science Letters 458, 141-151.

Dauphas, N. and Chaussidon, M. (2011) A perspective from extinct radionuclides on a young stellar object: the Sun and its accretion disk. arXiv preprint arXiv:1105.5172.

Dauphas, N., Chen, J.H., Zhang, J., Papanastassiou, D.A., Davis, A.M. and Travaglio, C. (2014) Calcium-48 isotopic anomalies in bulk chondrites and achondrites: Evidence for a uniform isotopic reservoir in the inner protoplanetary disk. Earth and Planetary Science Letters 407, 96-108.

Faure, G. and Mensing, T. (2007) Introduction to planetary science. Springer.

Fei, Y., Bertka, C.M. and Finger, L.W. (1997) High-pressure iron-sulfur compound,

Fe3S2, and melting relations in the Fe-FeS system. Science 275, 1621-1623.

Fei, Y., Li, J., Bertka, C.M. and Prewitt, C.T. (2000) Structure type and bulk modulus of Fe3S, a new iron-sulfur compound. American Mineralogist 85, 1830-1833.

Fogel, R.A., Hess, P.C. and Rutherford, M.J. (1989) Intensive parameters of enstatite chondrite metamorphism. Geochimica et Cosmochimica Acta 53, 2735-2746.

Hin, R.C., Coath, C.D., Carter, P.J., Nimmo, F., Lai, Y.-J., Pogge von Strandmann, P.A.E., Willbold, M., Leinhardt, Z.M., Walter, M.J. and Elliott, T. (2017) Magnesium isotope evidence that accretional vapour loss shapes planetary compositions. Nature 549, 511-515.

Javoy, M., Kaminski, E., Guyot, F., Andrault, D., Sanloup, C., Moreira, M., Labrosse, S., Jambon, A., Agrinier, P. and Davaille, A. (2010) The chemical composition of the Earth: Enstatite chondrite models. Earth and Planetary Science Letters 293, 259-268.

Johansen, A., Low, M.-M.M., Lacerda, P. and Bizzarro, M. (2015) Growth of asteroids, planetary embryos, and Kuiper belt objects by chondrule accretion. Science Advances 1, e1500109.

Johansen, A., Ronnet, T., Bizzarro, M., Schiller, M., Lambrechts, M., Nordlund, Å. and Lammer, H. (2021) A pebble accretion model for the formation of the terrestrial planets in the Solar System. Science Advances 7, eabc0444.

Kennedy, G.M. and Kenyon, S.J. (2008) Planet formation around stars of various masses: the snow line and the frequency of giant planets. The Astrophysical Journal 673, 502.

Kruijer, T.S., Kleine, T. and Borg, L.E. (2020) The great isotopic dichotomy of the early Solar System. Nature Astronomy 4, 32-40.

Kubik, E., Siebert, J., Blanchard, I., Agranier, A., Mahan, B. and Moynier, F. (2021a) Earth’s volatile accretion as told by Cd, Bi, Sb and Tl core–mantle distribution. Geochimica et Cosmochimica Acta 306, 263-280.

Kubik, E., Siebert, J., Mahan, B., Creech, J., Blanchard, I., Agranier, A., Shcheka, S. and Moynier, F. (2021b) Tracing Earth's Volatile Delivery With Tin. Journal of

Geophysical Research: Solid Earth 126, e2021JB022026.

Lloyd, E.C. (1971) Accurate Characterization of the High-pressure Environment: Proceedings. US National Bureau of Standards.

Lodders, K. (2003) Solar system abundances and condensation temperatures of the elements. The Astrophysical Journal 591, 1220.

Ma, Z. (2001) Thermodynamic description for concentrated metallic solutions using interaction parameters. Metallurgical and Materials Transactions B 32, 87-103.

Mahan, B., Moynier, F., Beck, P., Pringle, E.A. and Siebert, J. (2018a) A history of violence: Insights into post-accretionary heating in carbonaceous chondrites from volatile element abundances, Zn isotopes and water contents. Geochimica et Cosmochimica Acta 220, 19-35.

Mahan, B., Moynier, F., Siebert, J., Gueguen, B., Agranier, A., Pringle, E.A., Bollard, J., Connelly, J.N. and Bizzarro, M. (2018b) Volatile element evolution of chondrules through time. Proceedings of the National Academy of Sciences 115, 8547-8552.

Mahan, B., Siebert, J., Blanchard, I., Badro, J., Kubik, E., Sossi, P. and Moynier, F. (2018c) Investigating Earth's Formation History Through Copper and Sulfur Metal-Silicate Partitioning During Core-Mantle Differentiation. Journal of Geophysical Research-Solid Earth 123, 8349-8363.

Mann, U., Frost, D.J. and Rubie, D.C. (2009) Evidence for high-pressure core-mantle differentiation from the metal–silicate partitioning of lithophile and weakly-siderophile elements. Geochimica et Cosmochimica Acta 73, 7360-7386.

Marty, B. (2012) The origins and concentrations of water, carbon, nitrogen and noble gases on Earth. Earth and Planetary Science Letters 313, 56-66.

Marty, B. and Yokochi, R. (2006) Water in the early Earth. Reviews in Mineralogy and Geochemistry 62, 421-450.

McDonough, W. (2003) 2.15–Compositional model for the earth’s core. Treatise on geochemistry, 547-568.

McDonough, W.F. and Sun, S.-S. (1995) The composition of the Earth. Chem. Geol.

120, 223-253.

Morard, G., Sanloup, C., Fiquet, G., Mezouar, M., Rey, N., Poloni, R. and Beck, P. (2007) Structure of eutectic Fe–FeS melts to pressures up to 17 GPa: implications for planetary cores. Earth and Planetary Science Letters 263, 128-139.

Moynier, F., Deng, Z., Lanteri, A., Martins, R., Chaussidon, M., Savage, P. and Siebert, J. (2020) Metal-silicate silicon isotopic fractionation and the composition of the bulk Earth. Earth and Planetary Science Letters 549, 116468.

Nanne, J.A., Nimmo, F., Cuzzi, J.N. and Kleine, T. (2019) Origin of the non-carbonaceous–carbonaceous meteorite dichotomy. Earth and Planetary Science Letters 511, 44-54.

Norris, C.A. and Wood, B.J. (2017) Earth's volatile contents established by melting and vaporization. Nature 549, 507.

O'Neill, H.S.C., Dingwell, D., Borisov, A., Spettel, B. and Palme, H. (1995) Experimental petrochemistry of some highly siderophile elements at high temperatures, and some implications for core formation and the mantle's early history. Chem. Geol. 120, 255-273.

O'Neill, H.S.C. and Palme, H. (2008) Collisional erosion and the non-chondritic composition of the terrestrial planets. Philosophical Transactions of the Royal Society A: Mathematical, Physical and Engineering Sciences 366, 4205-4238.

Palme, H. and O'Neill, H. (2014) Cosmochemical Estimates of Mantle Composition. Planets, Asteriods, Comets and The Solar System, Volume 2 of Treatise on Geochemistry . Edited by Andrew M. Davis. Elsevier.

Perkins, D. and Newton, R. (1981) Charnockite geobarometers based on coexisting garnet—pyroxene—plagioclase—quartz. Nature 292, 144-146.

Pfeiffer, L., Mills Jr, A.P., Chandross, E. and Kovacs, T. (1979) Beta spectrum of In 115. Physical Review C 19, 1035.

Piani, L., Marrocchi, Y., Rigaudier, T., Vacher, L.G., Thomassin, D. and Marty, B. (2020) Earth's water may have been inherited from material similar to enstatite chondrite meteorites. Science 369, 1110-1113.

Pringle, E.A. and Moynier, F. (2017) Rubidium isotopic composition of the Earth, meteorites, and the Moon: Evidence for the origin of volatile loss during planetary accretion. Earth and Planetary Science Letters 473, 62-70.

Pringle, E.A., Moynier, F., Savage, P.S., Badro, J. and Barrat, J.-A. (2014) Silicon isotopes in angrites and volatile loss in planetesimals. Proceedings of the National Academy of Sciences 111, 17029-17032.

Richter, F.M. (2004) Timescales determining the degree of kinetic isotope fractionation by evaporation and condensation. Geochimica et Cosmochimica Acta 68, 4971-4992.

Richter, F.M., Davis, A.M., Ebel, D.S. and Hashimoto, A. (2002) Elemental and isotopic fractionation of Type B calcium-, aluminum-rich inclusions: experiments, theoretical considerations, and constraints on their thermal evolution. Geochimica et Cosmochimica Acta 66, 521-540.

Richter, F.M., Janney, P.E., Mendybaev, R.A., Davis, A.M. and Wadhwa, M. (2007) Elemental and isotopic fractionation of Type B CAI-like liquids by evaporation. Geochimica et Cosmochimica Acta 71, 5544-5564.

Righter, K., Nickodem, K., Pando, K., Danielson, L., Boujibar, A., Righter, M. and Lapen, T. (2017) Distribution of Sb, As, Ge, and In between metal and silicate during accretion and core formation in the Earth. Geochimica et Cosmochimica Acta 198, 1-16.

Righter, K., Pando, K., Marin, N., Ross, D., Righter, M., Danielson, L., Lapen, T. and Lee, C. (2018) Volatile element signatures in the mantles of Earth, Moon, and Mars: Core formation fingerprints from Bi, Cd, In, and Sn. Meteorit. Planet. Sci. 53, 284-305.

Righter, K., Sutton, S.R., Danielson, L., Pando, K. and Newville, M. (2016) Redox variations in the inner solar system with new constraints from vanadium XANES in spinels. American Mineralogist 101, 1928-1942.

Ringwood, A.E. (1966) Chemical evolution of the terrestrial planets. Geochimica et Cosmochimica Acta 30, 41-104.

Rubie, D. (1999) Characterising the sample environment in multianvil high-pressure experiments. Phase Transitions 68, 431-451.

Rudnick, R., Gao, S., Holland, H. and Turekian, K. (2003) Composition of the continental crust. The crust 3, 1-64.

Sanloup, C., Van Westrenen, W., Dasgupta, R., Maynard-Casely, H. and Perrillat, J.-P. (2011) Compressibility change in iron-rich melt and implications for core formation models. Earth and Planetary Science Letters 306, 118-122.

Savage, P.S., Moynier, F. and Boyet, M. (2022) Zinc isotope anomalies in primitive meteorites identify the outer solar system as an important source of Earth's volatile inventory. Icarus 386, 115172.

Savage, P.S., Moynier, F., Chen, H., Shofner, G., Siebert, J., Badro, J. and Puchtel, I.S. (2015) Copper isotope evidence for large-scale sulphide fractionation during Earth's differentiation. Geochem. Perspect. Lett. 1, 53-63.

Schönbächler, M., Carlson, R., Horan, M., Mock, T. and Hauri, E. (2010) Heterogeneous accretion and the moderately volatile element budget of Earth. Science 328, 884-887.

Schiller, M., Bizzarro, M. and Fernandes, V.A. (2018) Isotopic evolution of the protoplanetary disk and the building blocks of Earth and the Moon. Nature 555, 507-510.

Schiller, M., Bizzarro, M. and Siebert, J. (2020) Iron isotope evidence for very rapid accretion and differentiation of the proto-Earth. Science advances 6, eaay7604.

Shahar, A., Hillgren, V.J., Horan, M.F., Mesa-Garcia, J., Kaufman, L.A. and Mock, T.D. (2015) Sulfur-controlled iron isotope fractionation experiments of core formation in planetary bodies. Geochimica et Cosmochimica Acta 150, 253-264.

Shibazaki, Y., Kono, Y. and Fei, Y. (2015) Microscopic structural change in a liquid Fe-C alloy of~ 5 GPa. Geophysical Research Letters 42, 5236-5242.

Siebert, J., Badro, J., Antonangeli, D. and Ryerson, F.J. (2012) Metal-silicate partitioning of Ni and Co in a deep magma ocean. Earth and Planetary Science Letters 321, 189-197.

Siebert, J., Badro, J., Antonangeli, D. and Ryerson, F.J. (2013) Terrestrial accretion under oxidizing conditions. Science, 1227923.

Siebert, J., Corgne, A. and Ryerson, F.J. (2011) Systematics of metal–silicate partitioning for many siderophile elements applied to Earth's core formation. Geochimica et Cosmochimica Acta 75, 1451-1489.

Siebert, J., Sossi, P.A., Blanchard, I., Mahan, B., Badro, J. and Moynier, F. (2018) Chondritic Mn/Na ratio and limited post-nebular volatile loss of the Earth. Earth and Planetary Science Letters 485, 130-139.

Sossi, P.A. and Fegley, B. (2018) Thermodynamics of Element Volatility and its Application to Planetary Processes, in: King, P., Fegley, B., Seward, T. (Eds.), High Temperature Gas-Solid Reactions in Earth and Planetary Processes. Mineralogical Soc Amer & Geochemical Soc, Chantilly, pp. 393-459.

Sossi, P.A., Klemme, S., O'Neill, H.S.C., Berndt, J. and Moynier, F. (2019) Evaporation of moderately volatile elements from silicate melts: Experiments and theory. Geochimica et Cosmochimica Acta.

Sossi, P.A., Moynier, F., Treilles, R., Mokhtari, M., Wang, X. and Siebert, J. (2020) An experimentally-determined general formalism for evaporation and isotope fractionation of Cu and Zn from silicate melts between 1300 - 1500 °C and 1 bar. Geochimica et Cosmochimica Acta.

Sossi, P.A., Nebel, O. and Foden, J. (2016) Iron isotope systematics in planetary reservoirs. Earth and Planetary Science Letters 452, 295-308.

Sossi, P.A., Nebel, O., O'Neill, H.S.C. and Moynier, F. (2018) Zinc isotope composition of the Earth and its behaviour during planetary accretion. Chem. Geol. 477, 73-84.

Sossi, P.A., Stotz, I.L., Jacobson, S.A., Morbidelli, A. and O'Neill, H.S.C. (2022) Stochastic accretion of the Earth. Nature Astronomy, 1-10.

Steenstra, E.S., Seegers, A.X., Putter, R., Berndt, J., Klemme, S., Matveev, S., Bullock, E.S. and van Westrenen, W. (2020) Metal-silicate partitioning systematics of siderophile elements at reducing conditions: A new experimental database. Icarus 335, 113391.

Steller, T., Burkhardt, C., Yang, C. and Kleine, T. (2022) Nucleosynthetic zinc isotope anomalies reveal a dual origin of terrestrial volatiles. Icarus 386, 115171.

Suer, T.-A., Siebert, J., Remusat, L., Menguy, N. and Fiquet, G. (2017) A sulfur-poor terrestrial core inferred from metal–silicate partitioning experiments. Earth and Planetary Science Letters 469, 84-97.

Trinquier, A., Birck, J.-L. and Allegre, C.J. (2007) Widespread 54Cr heterogeneity in the inner solar system. The Astrophysical Journal 655, 1179.

Trinquier, A., Elliott, T., Ulfbeck, D., Coath, C., Krot, A.N. and Bizzarro, M. (2009) Origin of nucleosynthetic isotope heterogeneity in the solar protoplanetary disk. Science 324, 374-376.

Van Kooten, E., Schiller, M., Moynier, F., Johansen, A., Haugbølle, T. and Bizzarro, M. (2021) Hybrid accretion of carbonaceous chondrites by radial transport across the Jupiter barrier. The Astrophysical Journal 910, 70.

Vollstaedt, H., Mezger, K. and Alibert, Y. (2020) Carbonaceous chondrites and the condensation of elements from the Solar Nebula. The Astrophysical Journal 897, 82.

Wänke, H. and Dreibus, G. (1988) Chemical composition and accretion history of terrestrial planets. Philosophical Transactions of the Royal Society of London. Series A, Mathematical and Physical Sciences 325, 545-557.

Wänke, H., Dreibus, G. and Jagoutz, E. (1984) Mantle chemistry and accretion history of the Earth, Archaean geochemistry. Springer, pp. 1-24.

Wang, H., Weiss, B.P., Bai, X.-N., Downey, B.G., Wang, J., Wang, J., Suavet, C., Fu, R.R. and Zucolotto, M.E. (2017) Lifetime of the solar nebula constrained by meteorite paleomagnetism. Science 355, 623-627.

Wang, Z. and Becker, H. (2013) Ratios of S, Se and Te in the silicate Earth require a volatile-rich late veneer. Nature 499, 328.

Wang, Z., Becker, H. and Wombacher, F. (2015) Mass Fractions of S, Cu, Se, Mo, Ag, Cd, In, Te, Ba, Sm, W, Tl and Bi in Geological Reference Materials and Selected Carbonaceous Chondrites Determined by Isotope Dilution ICP-MS. Geostandards

and Geoanalytical Research 39, 185-208.

Wang, Z., Laurenz, V., Petitgirard, S. and Becker, H. (2016a) Earth's moderately volatile element composition may not be chondritic: Evidence from In, Cd and Zn. Earth and Planetary Science Letters 435, 136-146.

Wang, Z.C., Laurenz, V., Petitgirard, S. and Becker, H. (2016b) Earth's moderately volatile element composition may not be chondritic: Evidence from In, Cd and Zn. Earth and Planetary Science Letters 435, 136-146.

Warren, P.H. (2011) Stable-isotopic anomalies and the accretionary assemblage of the Earth and Mars: A subordinate role for carbonaceous chondrites. Earth and Planetary Science Letters 311, 93-100.

Wasson, J.T. and Kallemeyn, G.W. (1988) Compositions of chondrites. Phil. Trans. R. Soc. Lond. A 325, 535-544.

Wimpenny, J., Marks, N., Knight, K., Rolison, J.M., Borg, L., Eppich, G., Badro, J., Ryerson, F.J., Sanborn, M. and Huyskens, M.H. (2019) Experimental determination of Zn isotope fractionation during evaporative loss at extreme temperatures. Geochimica et Cosmochimica Acta 259, 391-411.

Witt-Eickschen, G., Palme, H., O'neill, H.S.C. and Allen, C.M. (2009) The geochemistry of the volatile trace elements As, Cd, Ga, In and Sn in the Earth's mantle: new evidence from in situ analyses of mantle xenoliths. Geochimica et Cosmochimica Acta 73, 1755-1778.

Wood, B.J., Kiseeva, E.S. and Mirolo, F.J. (2014) Accretion and core formation: The effects of sulfur on metal–silicate partition coefficients. Geochimica et Cosmochimica Acta 145, 248-267.

Wood, B.J., Smythe, D.J. and Harrison, T. (2019) The condensation temperatures of the elements: A reappraisal. American Mineralogist 104, 844-856.

Yagi, T., Akaogi, M., Shimomura, O., Suzuki, T. and Akimoto, S.I. (1987) In situ observation of the olivine - spinel phase transformation in Fe2SiO4 using synchrotron radiation. Journal of Geophysical Research: Solid Earth 92, 6207-6213.

Yagi, T. and Akimoto, S.-I. (1976) Direct determination of coesite-stishovite transition by in-situ X-ray measurements. Tectonophysics 35, 259-270.

Yi, W., Halliday, A.N., Alt, J.C., Lee, D.C., Rehkämper, M., Garcia, M.O., Langmuir, C. and Su, Y. (2000) Cadmium, indium, tin, tellurium, and sulfur in oceanic basalts: Implications for chalcophile element fractionation in the Earth. Journal of Geophysical Research: Solid Earth 105, 18927-18948.

Yu, Y., Hewins, R.H., Alexander, C.M.O.D. and Wang, J. (2003) Experimental study of evaporation and isotopic mass fractionation of potassium in silicate melts. Geochimica et Cosmochimica Acta 67, 773-786.

Chapter 2. Origin of moderately volatile element depletion on differentiated bodies: insights from the evaporation of indium from silicate melts

Deze Liu[1*], Frédéric Moynier[1], Julien Siebert[1,2], Paolo A. Sossi[1, 3], Yan Hu[1], Edith Kubik[1]

1. Université Paris Cité, Institut de Physique du Globe de Paris, 1 Rue Jussieu, 75005 Paris, France
2. Institut Universitaire de France, Paris, France.
3. Institute of Geochemistry and Petrology, ETH Zürich, Sonneggstrasse 5, CH-8092 Zürich, Switzerland

This chapter has been previously published as Liu et al. (2018). Origin of moderately volatile element depletion on differentiated bodies: insights from the evaporation of indium from silicate melts, Geochimica et Cosmochimica Acta., doi: 10.1016/j.gca.2022.09.043

Abstract

In comparison with the Sun and CI chondrites, moderately volatile elements (MVEs) are depleted in terrestrial planets and other small, rocky differentiated bodies in the inner solar system. The abundances of most MVEs in the bulk silicate Earth (BSE) fall on a trend that defines a near log-linear decrease with their 50% nebular condensation temperature (T_c^{50}). This temperature scale has traditionally been used to infer elemental volatility during planetary formation and accretion, however, indium (In) deviates from this correlation. Despite being a siderophile element that could have been depleted by core formation, In is overabundant for its calculated T_c^{50} in the BSE, as well as in the silicate portions of other small bodies (e.g., Moon and Vesta). This overabundance of In indicates that T_c^{50}, calculated under nebular conditions, may not be applicable to planetary evaporation that occurs at much higher oxygen fugacity (fO_2) and pressure than nominal nebular conditions. Here, we conduct a series of evaporation experiments for basaltic melts to quantify the volatility of In under conditions relevant to planetary

evaporation. Our results show that, when using the evaporation temperature (T_e^1, refers to the temperature at which 1% of element *i* has evaporated from liquid to gas phase under equilibrium) as the volatility scale, the abundances of volatile elements, including In, of the Moon and Vesta display a progressive depletion with increasing volatility (decreasing T_e^1). This smooth depletion pattern contrasts with the overabundance of In shown on the T_c^{50} scale, suggesting that volatile depletion on small bodies occurred under non-nebular environment instead of during nebular condensation. On the other hand, the volatile element composition of the BSE (including In) could be explained by integrating i) early accreted precursor materials of the proto-Earth that underwent volatile loss under conditions more oxidizing than those of the solar nebula with ii) late added volatile-rich materials.

Keywords: Indium; Evaporation experiment; Silicate melt; Volatile depletion

1. Introduction

Moderately volatile elements (MVEs) are the elements with volatility between S and the major components (Si, Mg and Fe) (Palme and O'Neill, 2014). The abundances of these MVEs in CI chondrites are similar to that in the solar photosphere. In contrast, they are variably depleted in the silicate portions of differentiated asteroids and planets, notably Earth and the Moon (e.g., Palme et al., 1988; O'Neill and Palme, 2008; Sossi and Fegley, 2018). These depletions can occur during nebular processes (e.g., incomplete condensation from the gas, Albarede, 2009; Morbidelli et al., 2020; Vollstaedt et al., 2020) and/or planetary (i.e., post-nebular) processes, for example, evaporative loss during accretion or differentiation on their bodies or precursor materials (Pringle et al., 2014; Hin et al., 2017; Norris and Wood, 2017; Ivanov et al., 2022). The volatility of a MVE changes in response to different physical and chemical conditions associated with nebular versus post-nebular processes.

The 50% condensation temperature (T_c^{50}) is a widely used volatility scale applicable to solar nebular conditions, and it refers to the temperature at which half the mass of an element is condensed from a gas of solar composition at equilibrium (Larimer, 1967).

Differentiated telluric bodies display coherent elemental abundance patterns with T_c^{50} as shown in Fig. 1. Specifically, refractory lithophile elements with high T_c^{50} have near-chondritic relative abundances, therefore displaying a flat relative abundance pattern with T_c^{50}. By contrast, lithophile MVEs with T_c^{50} between 1250 and 650 K show concomitant decreases in relative abundance with T_c^{50}, which is referred to as a volatility trend. In contrast to lithophile elements, siderophile elements are further depleted by core-formation and thus their relative abundances are lower than those defined by the volatility trend.

Indium (In) is a moderately to highly volatile element as characterized by its low T_c^{50} (536 K in Lodders, 2003 or 492 K in Wood et al., 2019), and does not follow the volatility trend defined by lithophile MVEs in the BSE. Given that In is a siderophile element, a greater depletion of In in the BSE is expected due to its sequestration into Earth's core. Contrary to this expectation, however, In lies above the volatility trend (*cf.* Witt-Eickschen et al. 2009). When compared to Zn, which has a higher T_c^{50} (704 K, Wood et al., 2019) and is less siderophile and chalcophile (Wood et al., 2014), In has a similar or even higher CI-normalized abundance in both terrestrial planets such as Earth (Palme and O'Neill, 2014), Mars (Taylor, 2013) and smaller telluric bodies like the Moon (Hauri et al., 2015) and Vesta (Steenstra et al., 2019, Sossi et al., 2022). This ubiquitous overabundance of In observed across a range of planetary bodies provides strong grounds to reject a single nebular process as the origin of the volatile depletion in inner solar system planets. Therefore, post-nebular processes must have occurred, which include late added material to the planetary mantle, evaporation on precursor parent bodies, or collisional erosion (Norris and Wood, 2017; O'Neill and Palme, 2008; Wang and Becker, 2013; Wang et al., 2016; Allibert et al., 2021).

Post-nebular processes take place after the nebular gas has dispersed. As such, evaporation and condensation are expected to have occurred at higher total pressures and more oxidized conditions (O'Neill and Palme, 2008; Visscher and Fegley Jr., 2013) than under nebular conditions (an H_2-rich atmosphere at nominal pressures of ~10^{-4} bar). Given the substantial change in thermodynamic conditions and consequently elemental

volatility, T_c^{50} may not be a suitable volatility scale to describe the totality of planetary accretion processes. This contention is supported by previous evaporation experiments of Norris and Wood (2017) that conducted in the vapor-silicate melt system at fixed temperature and pressure (1300°C, 1 bar) but variable oxygen fugacity from 2.3 logarithmic units below Fe–FeO buffer (iron-wüstite, ΔIW-2.3) to Ni–NiO buffer (ΔNNO). They found that In evaporated at a rate comparable to that of Zn, which differs from their relative volatilities inferred from T_c^{50}, where In is much more volatile than Zn. Furthermore, In was found to be much less volatile than Tl and Cd, despite their similar T_c^{50}. Norris and Wood (2017) explained the relatively more volatile nature of In by the high partial pressures of H_2S and H_2O in the nebula gas, which stabilize In-bearing species in the gas phase (InS, In_2S and InOH) and hence increase its volatility under nebular conditions with respect to Zn.

The differing volatility of In under nebular versus post-nebular conditions provides motivation for the development of a mechanism that predicts element volatility under non-nebular conditions. Sossi et al. (2019) derived a theoretical framework to quantify elemental volatility during evaporation of silicate melt based on Hertz-Knudsen-Langmuir (HKL) theory (Hertz, 1882; Knudsen, 1909; Langmuir, 1916; Richter et al., 2002) and proposed a new volatility scale calibrated by the evaporation temperature of elements in a vapor-melt system. Sossi et al. (2019) performed evaporation experiments on a range of MVEs to determine elemental volatility at 1 bar and variable temperature and oxygen fugacity (fO_2) conditions in the absence of H_2. However, In was not investigated in their study, which hinders our understanding of its overabundance on the T_c^{50} volatility scale and volatile loss during planetary processes.

To assess the volatility of In in a vapor-melt system, we conduct evaporation experiments on In_2O_3 and ZnO-doped basaltic melt composition in CO-CO_2 gas mixing furnace at 1 bar. We quantify the amount of In remaining in the quenched glasses as a function of temperature and fO_2. This allows us to infer the speciation of In in the gas phase and to determine its evaporation temperature based on the empirically theoretical framework described in Sossi et al. (2019). Our new results along with published

elemental volatility data provide critical insights into the origin of volatile depletion of the Earth and smaller differentiated bodies.

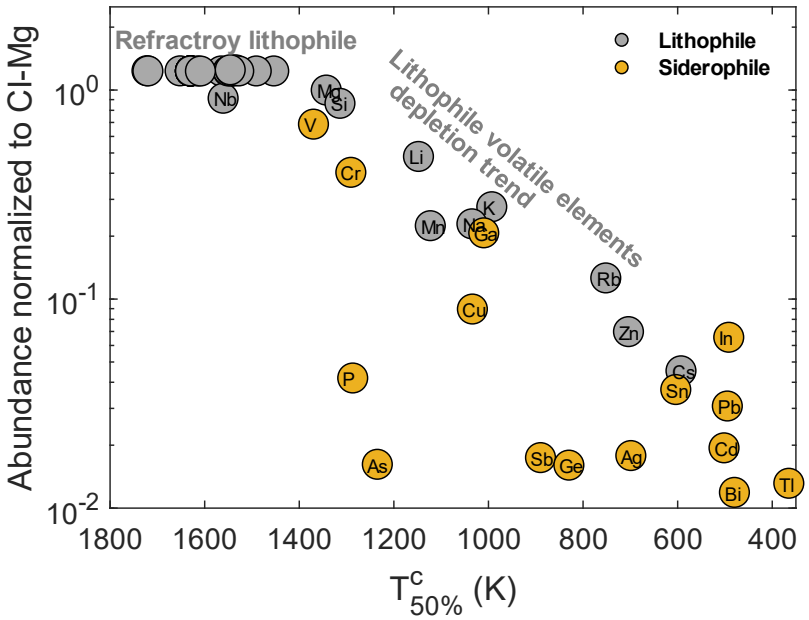

Fig. 1 Abundances of representative volatile and refractory elements in the BSE normalized to CI chondrites and Mg vs. T_c^{50}. Elemental abundance of BSE and CI chondrite from Palme and O'Neill. (2014) and references therein; The abundance of In is taken from the current estimate of Wang et al. (2016); T_c^{50} from Wood et al. (2019). The refractory lithophile elements such as Ca, Ti, Sc, Zr and rare earth elements (REE) have higher T_c^{50} than Mg, and exhibit a flat pattern. The lithophile volatile elements display a near log-linear depletion along with T_c^{50}. As both volatile and siderophile element, the abundance of In in the BSE is similar as Zn, which is lithophile element and T_c^{50} is markedly higher than In (~ 200 K)

2. Method

2.1 Sample preparation and evaporation experiments

Basaltic glasses are used as starting materials for the experiments, including a natural mid-ocean ridge basalt (MORB) glass and a synthetic glass in the FeO^T-CaO-MgO-Al_2O_3-SiO_2 (FCMAS) system (detailed compositions are listed in Table S1). Fresh MORB chips were selected carefully to avoid any alteration product. The synthetic FCMAS mixture was made by mixing reagent-grade oxide powders, except that Ca was added as carbonate ($CaCO_3$). These powders were preserved in a laboratory oven (set to 140℃) to avoid the influence of adsorbed water on weighing. The mixed powders

were ground with pestle and mortar under ethanol to make them as homogenous as possible, then the ethanol was dried down on a hotplate at 100℃. This step was repeated three times. Then this mixture was decarbonated at 950℃ for 16 h with a box furnace in air condition. Reagent-grade indium oxide (In_2O_3, ~1 wt. %) was then added to the MORB and FCMAS powders. ZnO powder (~ 1 wt.%) was also added to allow a direct comparison with previous studies.

The powder mixtures were then put in Pt crucibles and heated to be completely molten at 1400℃ for 30 min in air, and then quenched into water to form glass. This step was designed to ensure that In_2O_3 and ZnO were fully dissolved in the silicate melt to prevent unexpected evaporative loss of In_2O_3 or ZnO in pure oxide state during the following evaporation experiments. The measured In concentrations of synthetic mixtures~ 3% lower than the calculated initial concentration (Table. S1), which may indicate a minor loss to Pt crucible/evaporation loss and/or uncertainty on powder weighting or concentration analysis. The measured and calculated Zn concentrations are nearly identical. The following calculations used the measured concentration in synthetic MORB and FCMAS glasses as the initial compositions. Then, the synthetic basaltic glass mixtures were ground to a fine-grained and homogeneous powder in an agate mortar in preparation for further evaporation experiments. For each experiment, ~50 mg of pulverized glass was mixed into a slurry with polyethylene oxide (10,000 molecular weight) and then loaded onto a metallic wire. Two types of wires (Pt and Re wire) were used for evaporation experiments, of which Pt wire was used for the samples that performed at- or above $\log(fO_2) > -6$, while Re wire was used under more reducing conditions ($\log(fO_2) < -6$). This choice was dictated by the different solubilities of In into Pt and Re wire, where In is observed to significantly alloy with the Pt wire as fO_2 decreases, while negligible In was detected in the Re wire (see section 3.2 and Supplementary materials). However, solid Re metal wire is unstable with respect to its gaseous oxides above $\sim\log(fO_2) > -6$, restricting its use under these conditions. The total amounts of In in the metallic wire were assessed by analyzing the solutions that produced by dissolving whole wires after removal of the silicate part (results see

Supplementary materials, Fig. S2).

The oxygen fugacity of each experiment was buffered by CO-CO_2 gas mixing in a GERO atmosphere-controlled furnace at IPGP (furnace tube size: 70-cm-long, diameter: 4.2 cm; Sossi et al. 2020), and the ratio of CO_2 and CO was adjusted using four MKS G-series mass flow controllers. The log(fO_2) investigated here ranged from -10 to -0.68 (air) at different temperatures (1300°C, 1400°C and 1500°C). The total gas flow rate of all the gas-mixing experiments was fixed to 200 standard cubic centimeters per minute (sccm, *ca*. 0.24 cm/s) to eliminate the effect of thermal diffusion on fluctuations in the ratio of CO/CO_2 (Darken and Gurry, 1945) and potential variations in evaporation rate induced by variable gas flow rates. Conditions (T, fO_2 and duration) of experiments are listed in Table S2. A type B thermocouple ($Pt_{94}Rh_6/Pt_{70}Rh_{30}$, measured uncertainty ± 0.5%) is located less than 1 cm above the sample beads, providing a precise measurement of the temperature within the ~4 cm-long hotspot in the furnace. Before sample introduction, CO and CO_2 gases were fluxed through the alumina tube furnace for 10 min to ensure a homogeneous and stable oxygen fugacity that prevents unwanted evaporative loss of In due to fluctuations in fO_2 to occur. The samples were held at the set temperature for a duration of either 30 or 60 minutes. The bottom of the furnace alumina tube was isolated from outside by a steel ball valve. This valve was closed during heating to prevent potential fluctuations of oxygen fugacity. Once the evaporation experiment was complete, the valve was quickly opened manually, and sample subsequently drop-quenched into Milli-Q (18.2 Ω) deionized water.

After performing the first experiment, In was observed to build up on the walls of the alumina tube due to condensation, which could lead to unexpected contamination of the samples during heating. To estimate this potential contamination, blank experiments were performed with In-undoped pure MORB powders (see section 3.1).

2.2 Chemical analyses of the samples

Trace element concentrations of the quenched run products were measured with a Quadrupole Inductively-Coupled Plasma Mass Spectrometer (Q-ICP-MS) at the

Institut de Physique du Globe de Paris. The glass samples were removed from the metal wires carefully and ground into powders. The sample powders were dissolved in mixed acids by 1ml HNO_3 (16M) and 3ml HF (28M) in Savillex® standard PFA Teflon vials. The Teflon vials were closed and heated on a hotplate at 130°C for 2 days. The samples were dried at 100°C and re-dissolved in 2ml aqua regia at 130°C for 24h to remove insoluble fluorides. The samples were dried down again and redissolved in 6M HCl at 130°C for 18h. Samples were finally dissolved in 5ml 0.5M HNO_3 for 24h before ICP-MS measurements. The metal (Pt and Re) wires were also analyzed to quantify the amount of In loss by diffusion into the wire. They were dissolved in 3ml aqua regia for 24h, then dried and re-dissolved in 2ml 0.5N HNO_3 before measurements.

A set of ICP-MS standard solutions in 2 % v/v HNO_3 were used as calibration standards (0.01 to 20 ppm for major elements, 0.1 to 200 ppb for typical trace elements, and 0.01 to 200 ppb for In). Scandium and Re were used as internal standards to correct for matrix effects and mass bias of the instrument. For the Re wires, only Sc was used as an internal standard. A basalt geostandard BHVO-2 was analyzed to test the accuracy of the results, and giving an In concentration of 82 ppb (RSD = 1.5%), which is consistent with the reported values on ID-ICP-MS (82 to 87 ppb) from GEOREM (http://georem.mpch-mainz.gwdg.de/).

2.3 Electron probe micro-analysis for elemental zoning of In

Four samples that used the MORB mixture were run at 1300°C for 60 min at variable fO_2 (-10 to -0.68), to test for compositional heterogeneity. Samples were mounted in epoxy, polished to their largest cross sections and then analyzed with a CAMECA SX Five electron probe micro-analysis (EPMA) at CAMPARIS service (Sorbonne University). Operating conditions of the probe were set to a 20 KeV accelerating voltage and 10 nA beam current for the analyses on Na, Mg, Si, Al, K, Ca, Fe and 20 KeV, 200 nA were set for the analyses on P, S, Mn, In and Ti. Standards used for In_2O_3 is an alloy of In and P; albite for Na_2O; diopside for MgO, SiO_2 and CaO; orthopyroxene for K_2O and Al_2O_3; pyrite for FeO and S; Mn-Ti oxide for MnO and

TiO_2. Detection limit of In is ~ 160 ppm. Elemental zoning was assessed through profile mode analysis with a beam size of 30 μm and 15 to 20 analytical points were collected along the radius from the center to the rim of a glass bead. The final point was typically placed at < 30 μm from the edge of the bead. No crystalline phases were observed in our quenched glass beads.

3. Results

3.1 Evaluation of In contamination

To determine the extent of In and Zn contamination of the liquid silicate beads from the furnace, 16 blank experiments were conducted over the course of this study with temperature varying from 1300℃ to 1500℃ and fO_2 ($\log(fO_2)$) ranging from -10 to -0.68) for 1 hour on undoped MORB powders. Each blank sample was generally performed following the experiments using doped samples and were performed under the same experimental conditions. The concentration of In in the blank samples is observed to correlate with temperature and fO_2. Higher temperature and more reduced conditions lead to an increased contamination ratio of In (see supplementary information Table. S3 and Fig. S1). For example, a blank run at 1500℃ and $\log(fO_2)$ = -10 for 1 hour, is measured to contain ~ 3 ppm of In, while the doped sample (~ 1 wt.% of initial In) performed under the same conditions has ~7 ppm of In left in the residual glass. The ratio of blank/sample is therefore nearly 50%. Considering the higher contribution from contamination for the experiments performed at 1500℃ and $\log(fO_2)$ =-10 ~ -8, these conditions were not included for the discussion, other than to show that In concentration in the glasses of these experiments is essentially nil with respect to the initial quantity (~ 1 wt. % In).

3.2 In loss to metal wire

Under the imposed oxygen fugacities and temperatures in the furnace (down to $\log fO_2$ = -10, ~ ΔIW+1 to -1 from 1300℃ to 1500℃), In is assumed to exist as $InO_{1.5}$

in the melt (see section 3.4), and its solubility in metal increases with decreasing fO_2 by a reaction of $InO_{1.5}$ (silicate melt) = In (metal) + $3/4O_2$ (gas) (*e.g.,* Mann et al. 2009). After removal of the glass, the entirety of the remaining wire was dissolved to quantify the amount of In dissolved in metal. The amount of In dissolved in Re wire was found to be negligible (3 ~ 30 ng) compared to an initial doped amount of ~ 500 μg in the experiments. In comparison, Pt wires are observed to contain variably more In (from 4 to 120 μg) depending on experimental temperature and fO_2 (see supplementary information Table. S4 and Fig. S2). The solubility of In into Pt wire increases significantly at higher temperature and lower fO_2 (see supplementary information). For instance, an experiment performed under 1500°C and $\log(f(O_2)) = -5.01$ for 30 min, In dissolved into the Pt wire accounts for approximately 24% of that in the initial doping amount. Given the excessive In loss (> 20%) to the Pt wire for experiments conducted at 1500°C and $\log(f(O_2)) = -5 \sim -4$, their run products are not included in data fitting and relevant discussion. The Zn migration to wire is insignificant at our experimental conditions (≤1% for all experiments).

3.3 Elemental zoning

The rate of In loss from the melt surface during evaporation is presumably affected by the rate of In diffusion through the silicate. When diffusion is much slower than evaporation, the extent of evaporative In loss is limited by the diffusion rate, resulting in a radial zonation in In concentration in the glass bead. In contrast, should the diffusion rate exceed the evaporation rate, then In is transported sufficiently quickly to the melt surface to allow for continuous In loss by evaporation, and thus In should be homogeneously distributed in the glass bead.

To examine the spatial distribution of In in the glasses, a few replicates of MORB mixture were performed under the lowest temperature 1300°C, 60 min and variable fO_2 (-10, -8, -3.44 and -0.68). The In concentrations of these replicates were measured by EPMA. In Sossi et al. (2019), elemental zoning was observed only in their lowest temperature (1300°C) and most reduced ($\log fO_2 = -10$) run products, whereas run

products performed under higher temperature (1400°C, 1500°C and 1550°C), all MVEs were homogeneously distributed in the glass regardless of the oxygen fugacity under which they were synthesized. This observation implies that the increase of diffusion rate is faster than that of the evaporation rate with the increase of temperature given the experimental oxygen fugacity (fO_2 = -10 to -0.68) and ferrobasaltic melt composition. This suggests that elemental zoning is more likely to be present in samples performed under the lowest temperature and therefore the 1300°C-series were chosen to test the potential zoning. Moreover, the samples with the fastest evaporation rate (log fO_2= -8 to -10, 1400°C and 1500°C) were not used for fitting, as discussed in section 3.1.

Our results on these samples do not exhibit significant concentration gradient from center to rim, and suggest a near-homogeneous distribution of In (Fig. S3). Therefore, it is reasonable to assume that the influence of diffusivity is negligible at all conditions investigated in this study. However, there is still no available diffusion data of In, the diffusion limit on other melt compositions such as rhyolitic or dacitic melts would require further experimental tests.

3.4 In concentration and data fitting

The initial In concentration in both synthetic starting materials (mixtures of MORB and FCMAS) is ~ 0.96 wt.% (concentration for elemental In). The In concentration in fresh MORB is generally less than 0.1 ppm (Yi et al., 2000), which is negligible compared to the doped amount of In (~ 1 wt.% In_2O_3). For the glassy run products, the final In concentrations after evaporation vary from 12 ppm (DLF 04) to ~ 9700 ppm (DLF 02, see Table. S1) depending on different T and fO_2 conditions of experiments.

The extent of In depletion is expressed by the molar fraction of In in the evaporated residue, i.e., the sample glasses, relative to that in the starting materials. Here, we make the approximation that the ratio of molar fraction of In between evaporated residue and initial value (X_i^t/X_i^0) is equal to their ratio of concentration (C_i^t/C_i^0) due to lack of other abundant volatile components. Hence, In depletion can be expressed as:

$$\frac{X_i^t}{X_i^0} \approx \frac{C_i^t}{C_i^0} \quad (1)$$

where X_i^t and X_i^0refer to the fraction of element *i* at time *t* and the initial fraction of *i*, respectively, and C_i^t and C_i^0 represent the concentration of *i* at time *t* and the initial concentration, respectively.

The extent of depletion of In is related to its volatility and the specific physical conditions during an evaporation process. The volatility of In increases with increasing temperature and decreasing fO_2, which is consistent with the behavior of most MVEs such as Zn, Ge, Pb and Cu reported in previous studies (Norris and Wood 2017, Sossi et al. 2019). Sossi et al. (2019) provided a framework to assess elemental volatility based on the empirical application of the HKL equation for the evaporation on silicate melt. For a congruent dissociative evaporation reaction with single oxidation in liquid and multiple in gas, the volatility of an element, *i*, can be described by the following equation:

$$\frac{X_i^t}{X_i^0} = \exp\left(-\left(1-\frac{P_i}{P_{i,sat}}\right)\left(\frac{K_a^*}{f(O_2)^{\frac{n_a}{4}}}+\frac{K_b^*}{f(O_2)^{\frac{n_b}{4}}}\right)\frac{3M}{r\rho}\sqrt{\frac{1}{2\pi M_i RT}}(t-t_0)\right) \quad (2)$$

In this equation, K^* the modified equilibrium constant of a vaporization reaction, is defined as $K^* = \alpha_e \gamma_e^\infty K$. *a* and *b* refer to the different vaporization reactions (see below). α_e refers to the evaporation coefficient, representing the fraction of molecules that strike the vapor-liquid interface and change phases from their initial liquid state with respect to that expected for an ideal, Maxwell-Boltzmann gas. For an evaporation process occurring under ideal conditions, α_e can be taken as unity, i.e., α_e = 1. However, the value of α_e in an experimental and/or natural evaporation system could deviate from unity due to the influences from many factors, for example, temperature discrepancy between liquid and vapor interface, surface properties of melt, impurities at interface (Persad and Ward, 2016; Sossi and Fegley, 2018), which makes α_e difficult to determine *a priori*. The factor γ_e^∞ refers to activity coefficient of an element *e* in a given silicate melt at infinite dilution, and the studies on γ_e^∞ of indium in ferrobasaltic melt are still scarce to date. Given the uncertainties of both α_e and γ_e^∞,

Sossi et al. (2019) and Zhang et al. (2021) used the product of α_e and γ_e^{∞} as unknown and fit the value of K^* without assuming an individual value of α_e or γ_e^{∞}. Based on their experimental results, Sossi et al. (2019) suggested that the α_e values among different MVEs were all close to unity under their experimental conditions (1573K to 1823K, 1 bar; the same conditions are applied in this study); Zhang et al. (2021) calculated the values of $\alpha_e\gamma_e^{\infty}$ of evaporation experiments on basaltic and chondrule-like compositions, and observed a good consistence of $\alpha_e\gamma_e^{\infty}$ in the literature. The apparent discrepancy of a factor ~1000 to the experiments of Sossi et al. (2019) derives from the fact that Zhang et al. (2021) neglected to include the factor $1\text{-}P_i/P_{i,sat}$ (taken to be 0.001 in Sossi et al. 2019) when comparing their experiments performed under vacuum (and hence $1\text{-}P_i/P_{i,sat} \sim 1$) to those performed at 1 bar (Sossi et al. 2019). When this correction is included, the agreement is consistent among these studies.

In this study, the same approach was followed to fit K^*. The symbols P_i and $P_{i,sat}$ represent the partial pressure and equilibrium pressure, respectively, of the gas species of In presented in the experiments. Sossi et al. (2019) assumed a value of $P_i/P_{i,sat}$ = 0.999 for fitting the value of K^* and calculating the elemental evaporation temperature. The subsequent experimental calibration by Sossi et al. (2020) suggested that $P_i/P_{i,sat}$ =0.996 is a more appropriate value. To compare with the results in this study, K^* and evaporation temperature of elements reported in Sossi et al. (2019) are re-calculated with $P_i/P_{i,sat}$ =0.996. The fO_2 is the oxygen fugacity in bar; r is the radius of sample glass bead, which is typically ~1.6-1.7 mm, and is set be ~0.00165 m; ρ is the density of basaltic glass (2750 kg/m^3); n, is the electron number in reaction; M and M_i are the molar masses (kg/mol) of the basaltic glass bead and evaporated stable gas species, respectively. R is the gas constant (8.3145 J/K^{-1}.mol^{-1}); T is the experimental temperature in Kelvin. The symbol t_0 marks the time at which volatiles start to evaporate, an empirically-determined quantity that approximately relates to the thermal equilibrium time since insertion, recorded once temperature reached 99% of the set temperature (typically < 4 min), and t indicates experiment duration (in seconds) from insertion to quenching. The value of $t\text{-}t_0$ was maintained at either 30 min or 60 min in

this study.

The number of electrons exchanged, n, in a given vaporization reaction depends on the dominant melt species and that in the gas produced during evaporation. Here we assume In occurring as trivalent cation (In^{3+}) in melt over the fO_2 imposed in this study (air to ΔIW-2). This assumption is based on the estimated valence state of In in metal-silicate segregation experiments (e.g., Righter et al., 2017; Steenstra et al., 2020), which performed mostly under more reducing conditions than in this study (~ΔIW-1 to -5). The generated stable gas species of In are not known *a priori*, and there are three possible species including In (g), InO (g) and In_2O (g) (Lamoreaux et al., 1987). Assuming these species to be the vaporization products of In from the melt, the vaporization reactions can be written as following:

$$InO_{1.5}(l) = In\ (g) + 0.75O_2\ (g)\ (3.1)$$

$$InO_{1.5}(l) = InO\ (g) + 0.25O_2\ (g)\ (3.2)$$

$$2InO_{1.5}(l) = In_2O\ (g) + O_2\ (g)\ (3.3)$$

The equilibrium constants (K) of these equations can be expressed as:

$$K(3.1) = \frac{p_{In} {fO_2}^{3/4}}{a_{InO_{1.5}}}$$

$$K(3.2) = \frac{p_{InO} {fO_2}^{1/4}}{a_{InO_{1.5}}}$$

$$K(3.3) = \frac{p_{In_2O} fO_2}{{a_{InO_{1.5}}}^2}$$

Where p refers to partial pressure of corresponding gas species; $a_{InO1.5}$ refers to the activity of $InO_{1.5}$ in the silicate melt. Thermodynamic data taken from Lamoreaux et al. (1987) to calculate the relative stabilities of the three gas species at fixed T (1400 °C) and P (1 bar) with variable fO_2. Among these three gas species, In (g) is observed to be dominant under most of our experimental conditions (Fig.2). The ratio p_{In}/p_{InO} is proportional to $1/f(O_2)^{1/2}$, suggesting that In (g) should be more stable at low $f(O_2)$ (Fig.2a); p_{In}/p_{In2O} is proportional to $f(O_2)^{1/2}/ a_{InO1.5}$, indicating that In_2O (g) can be more stable at reducing conditions (Fig.2a) provided $a_{InO1.5}$ is high. However, if $a_{InO1.5}$ is

diluted (e.g., from 0.01 to 0.001), p_{In}/p_{In2O} can exceed 1, resulting in In (g) remaining as the dominant gas species within the range of experimental fO_2 (Fig.2b). In addition, when taking into account the equilibrium reactions between gas species as following:

$$InO\ (g) = In\ (g) + 0.5\ O_2\ (g) \quad (3.4)$$

$$In_2O\ (g) = 2In\ (g) + 0.5\ O_2\ (g) \quad (3.5)$$

the ratio of partial pressure of gas species can be expressed as:

$$\frac{p_{In}}{p_{InO}} = \frac{K(3.4)}{p_{O_2}^{\frac{1}{2}}} \quad (3.6)$$

$$\frac{p_{In}^{\ 2}}{p_{In_2O}} = \frac{K(3.5)}{p_{O_2}^{\frac{1}{2}}} \quad (3.7)$$

The relative stability of each gas species is shown in Fig.2c and d, where In (g) is still the dominant gas species at the experimental conditions. We find that InO (g) is only stable under very oxidizing conditions (near- or above the fO_2 of air at 1400 °C) and hence is assumed to be negligible in our experiments. In_2O (g) can be stable at the most reducing experiments. However, due to the low concentration of In in nature (~ usually below 200 ppb), $a_{InO1.5}$ is several orders of magnitude lower than in the experimental system, hence p_{In2O} is likely negligible during natural evaporation processes and only In (g) is likely to be present.

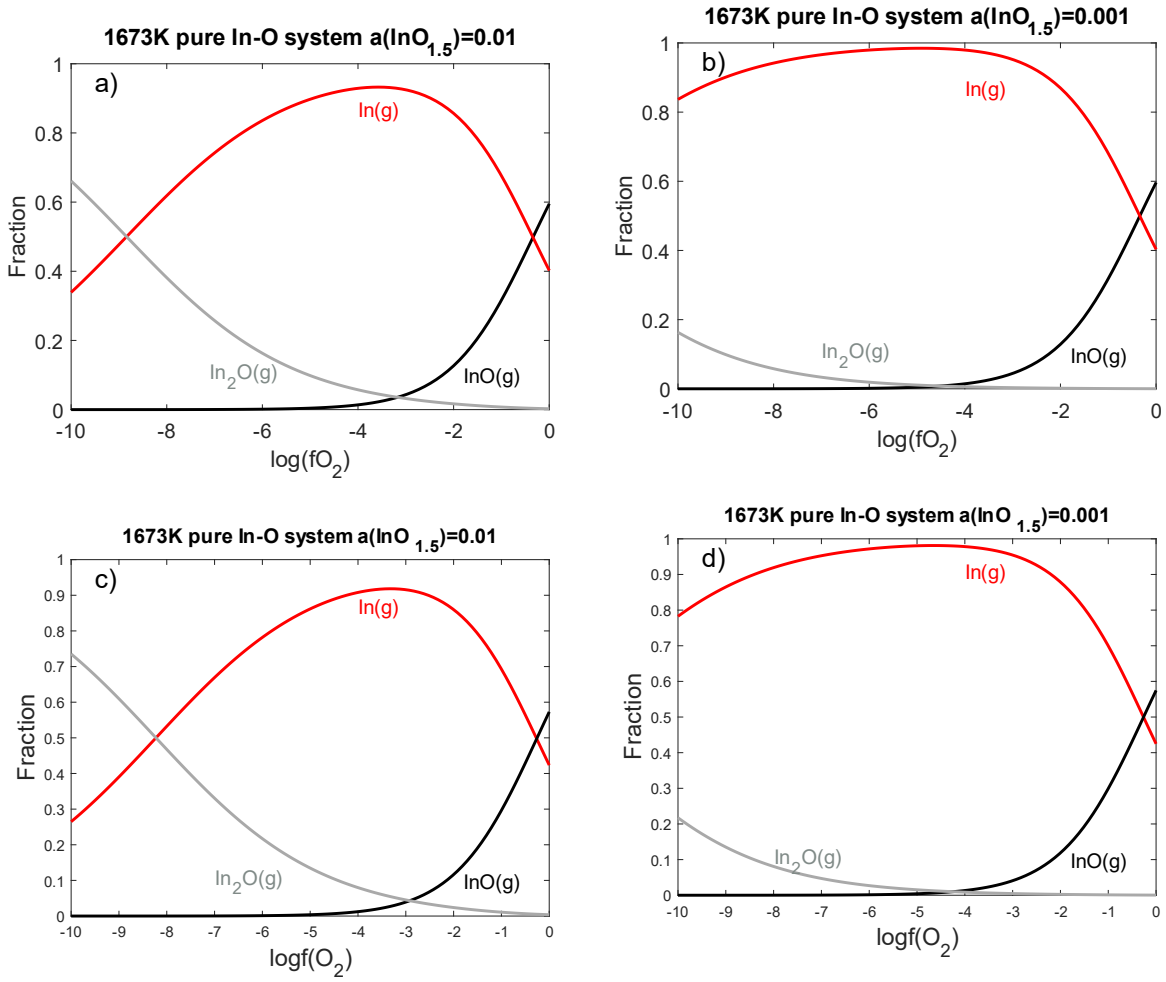

Fig.2 The relative stability of gas species InO (g) and In_2O (g) and In (g) are displayed as a function of log(fO_2) at 1673K and a) a(InO1.5) = 0.01; b) a(InO1.5) = 0.001; The thermodynamic data are taken from Lamoreaux et all. (1987). InO (g) is only stable at the most oxidizing condition (air condition). In_2O (g) is negligible at oxidizing conditions and can become more stable as decrease of fO_2. Moreover, In_2O (g) is proportional to $a(InO1.5)^2$ (Eq. 3.3), thus lower a(InO1.5) can decrease the relative stability of In_2O (g) significantly. Fig.2 c and d further take into account the equilibrium between gas phases (see discussion in section 3.4

Therefore, we assume that both In (g) and In_2O (g) are stable under our experimental conditions. Considering p_{In2O} and p_{In} are dependent variables (Eq. 3.10), the modified equilibrium constant (K*(3.3)) of reaction (3.3) is calculated by combining reaction (3.1) and (3.7). Reaction (3.5) is assumed to be ideal gas reaction under our experimental conditions (1573 K to 1773 K), substituting thermodynamic data of the gas species from Lamoreaux et al. (1987). Therefore, K*(3.3) is determined by K*(3.1) and K (3.5), can be expressed as:

$$K_{3.3}^{*} = \frac{(K_{3.1}^{*})^2}{K_{3.5}} \quad (3.8)$$

Using Eq. 2 to fit the data, the correlation of X_i^t/X_i^0 and fO_2 is consistent with the 3 and 4-electrons reactions (Fig. 3). For the evaporation experiment of Zn, Sossi et al. (2019) suggested that Zn remains as divalent cation (Zn^{2+}) in melt, and only has one stable gas species Zn (g), and hence corresponding to a 2-electrons reaction (n = 2). Our experimental results of Zn evaporation are similar to those reported in Sossi et al. (2019), exhibiting good reproducibility on evaporation experiments. The fitted results are shown in Fig. 3.

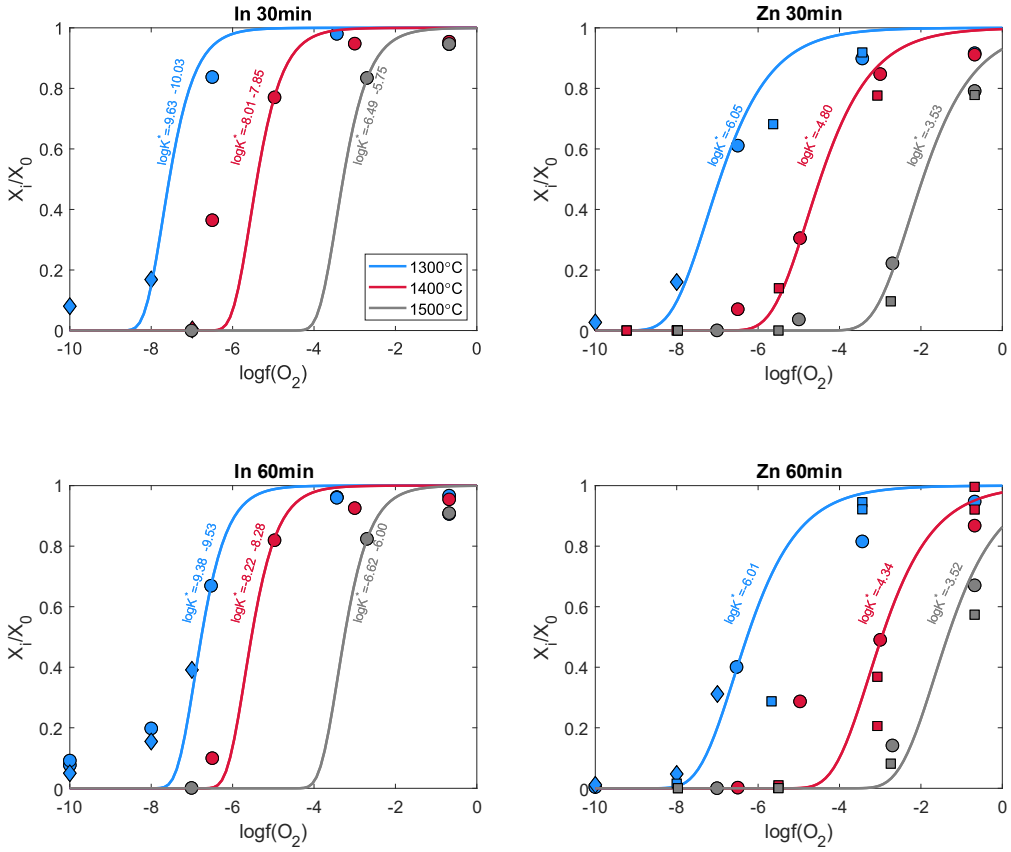

Fig. 3 The fraction of In and Zn remaining in the sample gas is displayed as a function of $logf(O_2)$. Figures show the experiments performed for 30 min and 60 min at variable temperature (1300°C to 1500°C), respectively. Both In-series are fit by non-linear least squares approach according to the reactions: InO1.5(l) = In(g) + 3/4O_2 and 2InO1.5(l) = In_2O(g) + O_2. Zn-series are fit according to reaction: ZnO(l) = Zn(g) + 1/2 O_2 (g). The modified equilibrium constants (log(K*)) are marked in figures. The circle symbols represent the experiments performed on synthetic MORB mixture; the diamond symbols represent the experiments on synthetic FCMAS mixture. The square symbols in Zn-series are the data points from Sossi et al. (2019), plotted as an comparison, where 60 min points are directly taken from their dataset, 30 min points are calculated from their 15min data points with Eq.2.

4. Discussion

The experiments presented here were performed under controlled physical conditions (T, P, fO_2) on basaltic silicate melts that were derived from both natural and synthetic rocks. The activity coefficients of trace elements, such as In, may change at varying silicate melt compositions (Holzheid et al. 1997, O'Neill and Eggins. 2002), which may lead to different volatility behavior than that inferred here using a basaltic composition (Wood and Wade 2013). Here, we assume that the basaltic melts (FCMAS and MORB) used in the experiments are representative of natural magmatic liquids, and we discuss elemental volatilities with respect to these compositions. Our experiments, performed in the absence of H_2 (g) and at atmospheric total pressure, are relevant to the assessment of elemental volatility during post-nebular processes that occurred at much higher fO_2 and total pressure than the H_2-dominant solar nebular environment (10^{-4} bar).

4.1 Elemental volatility and evaporation temperature

Volatile loss during evaporation is constrained by the physical conditions (T, P, fO_2 and silicate composition) of the system. Sossi et al. (2019) provided a new volatility scale based on elemental evaporation temperature, which can be used to quantify the elemental volatility in this study. For a congruent dissociative evaporation, the evaporation temperature ($T_{e,i}^{f}$) can be expressed as following:

$$T_{e,i}^{f} = \frac{-\Delta A_i^*}{\left(R\left(\frac{n}{4} ln fO_2 + lnP_T + ln\frac{f_i^{vap}}{f_i^{lid}}\right) - \Delta B_i^*\right)} \quad (4.1)$$

The symbols f_i^{vap} and f_i^{lid} represent the fractions of element i in the gas and in the liquid respectively and sum up to 1. P_T is the total pressure of experiment, and is equal to 1 bar in this study. The quantity n refers to the electron number in vaporization reaction (e.g., Eq 3.1), given the low abundance of In in nature (~ 0.1 ppm), In (g) is

considered as the dominant gas species during evaporation (see section 3.4), corresponding to $n = 3$. The derivation of Eq. 4.1 can be found in Sossi et al. (2019). To compare our data with published data directly, the evaporation temperature is also set to 1% evaporation temperature that refers to the temperature at which 1% of element i has evaporated from liquid to gas phase under equilibrium, and calculated at $\log(fO_2)$= -10 and -5, respectively (noted as $T_{e,i}^{1,-10}$ and $T_{e,i}^{1,-5}$) corresponding to values near the ΔIW buffer ($\log fO_2$ = -10 at 1650 K) and near ΔFMQ (Fayalite-Magnetite-Quartz) buffer ($\log fO_2$ = -5 at 1750 K) for representative MVEs like Na, K, Zn, Cu, Rb and In. ΔA_i^* and ΔB_i^* refer to the enthalpy and entropy of experimental vapor-melt reaction, calculated from the modified equilibrium constant K^* by converting to Gibbs free energies:

$$\Delta G^* = -RTlnK^* \quad (4.2)$$

Combining with the value of K^* defined in section 3.4 (which is different from that calculated in the pure oxide system), ΔG^* is calculated to describe the Gibbs free energy for the non-ideality of trace element dissolution in silicate melt (i.e., γ_e^∞) and the deviation of the evaporation coefficient, which may vary with temperature (Sossi et al., 2019). Therefore, the estimation of ΔG^* in this study is constrained by melt composition and experimental P-T conditions (1 bar, 1573K to 1773K). Then, ΔA_i^* and ΔB_i^* can be calculated by the Gibbs-Helmholtz equation:

$$\Delta G^* = \Delta A^* - T\Delta B^* \quad (4.3)$$

where, ΔG^* is a linear function of absolute temperature, T. ΔA_i^* is the intercept of the line, $-\Delta B_i^*$ is its slope on an Ellingham diagram (Fig. 4).

The T_c^{50} of a given element is estimated for condensation of a gas of solar composition from thermodynamic data combined with their solution properties in condensing phases. In comparison, $T_{e,i}^f$ is assessed from the thermodynamic properties (e.g., enthalpy and entropy) of the relevant vaporization reaction in a two-phase (liquid, vapor) system determined from the results of evaporation experiments. Therefore, $T_{e,i}^f$ can be seen as a direct approach to quantify elemental volatility during evaporation.

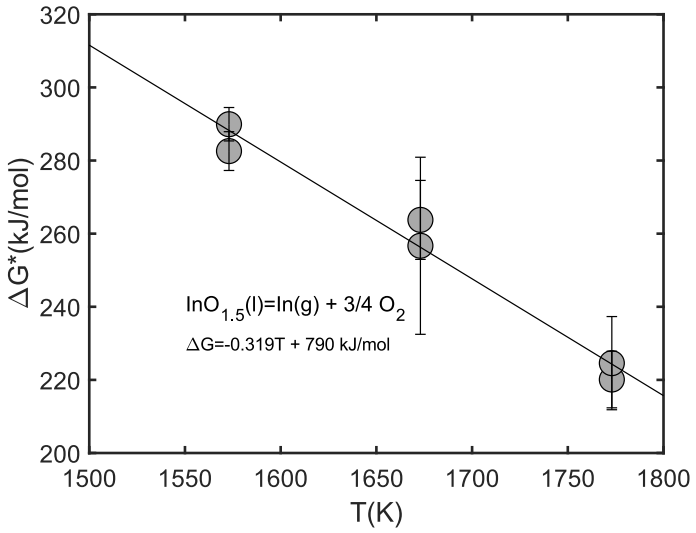

Fig. 4 $\Delta G^*$is plotted as a function of temperature. ΔA^* and ΔB^* can be calculated with Eq. 4.3, the regressed $\Delta A^* = 791 \pm 87$ kJ/mol; $\Delta B^* = 319 \pm 52$ J/mol. Substitute ΔA^* and ΔB^* into Eq. 4.1, the evaporation temperature can be estimated, $T_{e,In}^{-10}$ = 1578 ± 15 K; $T_{e,In}^{-5} = 1841 \pm 29$ K.

For most volatile elements such as Na, K, Rb and Zn, $T_{e,i}^{f}$ from a ferrobasaltic melt correlates with T_c^{50}, because these elements tend to condense into silicate minerals (Sossi et al., 2019). However, $T_{e,i}^{f}$ of In is not consistent with the correlation defined by other elements (Fig. 5), which shows that In is relatively less volatile compared to that which would be expected from its nebular condensation temperature. This observation confirms that the relative volatility of In in the vapor-melt system, an analogue of molten silicate mantles, is significantly lower than its volatility at nebular conditions, as also proposed by Norris and Wood (2017). These authors argued that the predominant gas species of In in the solar nebula is $InCl^0$, given the CI chondritic abundances of Clay et al. (2017), allowing it to remain in the gas phase until Cl condenses (T_c^{50} ~ 470 K). This destabilizes $InCl^0$, promoting its condensation into troilite as InS at the same temperature. Sossi and Fegley (2018), using the CI chondrite abundances of Lodders (2003), determine In^0 as the prevailing gas species, but also obtain similar condensation temperatures. Nevertheless, the fact that In condenses into sulfide from the solar nebula, as opposed to silicate melt for planetary evaporation,

leads to the large discrepancy between T_c^{50} and T_e (see also Sossi et al. (2019)).

In contrast to other highly volatile elements, whose T_c^{50} <500 K, the evaporation temperature of In ($T_{e,In}^{1,-10} = 1578 \pm 15\ K;\ T_{e,In}^{1,-5} = 1841 \pm 29\ K$) is higher than Zn ($T_{e,Zn}^{1,-10} = 1466 \pm 8\ K;\ T_{e,Zn}^{1,-5} = 1679 \pm 2\ K$) whose $T_c^{50} = 704\ K$ (Wood et al., 2019). Therefore, the CI-, Mg-normalized abundance of In in the BSE may be expected to approach that of Zn, should planetary evaporation have been the predominant cause of volatile depletion. Indeed, their CI-, Mg-normalized abundances in the BSE are observed to be similar, where ~ 0.070 for Zn, ~ 0.066 or 0.1 for In, depending on different estimations (Witt-Eickschen et al., 2009; Palme and O'Neill, 2014; Wang et al., 2016). Nevertheless, as In is a siderophile element, core formation on differentiated bodies should be considered when calculating the In budget in bulk planetary bodies (*i.e.,* core + mantle). The influence of core-formation on the compositions of both the Earth and small differentiated planetary bodies (Moon and Vesta) is discussed below.

Table. 1 50% condensation temperature and evaporation temperature of MVEs at variable fO_2.

Element	$T_c^{50}\ (K)$	$T_{e,i}^{1,-10}\ (K)$	SD	$T_{e,i}^{1,-5}\ (K)$	SD
Ge	830	1469	12	1664	3
Zn	704	1466	8	1679	2
Rb	752	1594	15	1762	7
Cu	1034	1619	10	1892	22
K	993	1688		2091	
Ga	1010	1741	1	2044	5
Na	1035	1752		2096	
Li	1148	1888		2120	
Cr*	1291	2155		2096	
Mg*	1343	2090		2138	
Mn*	1123	1974		2339	
Fe*	1338	2033		2394	
In	492	1578	15	1841	29

50% condensation temperature is taken from Wood et al. (2019).

Elements with '*' symbols, their evaporation temperature are calculated with the thermodynamic properties of pure oxide system. The evaporation temperature and uncertainties of the other elements is re-calculated from the thermodynamic data in

Sossi et al. (2019) with the assumption that $\frac{P_i}{P_i^{sat}} = 0.996$.

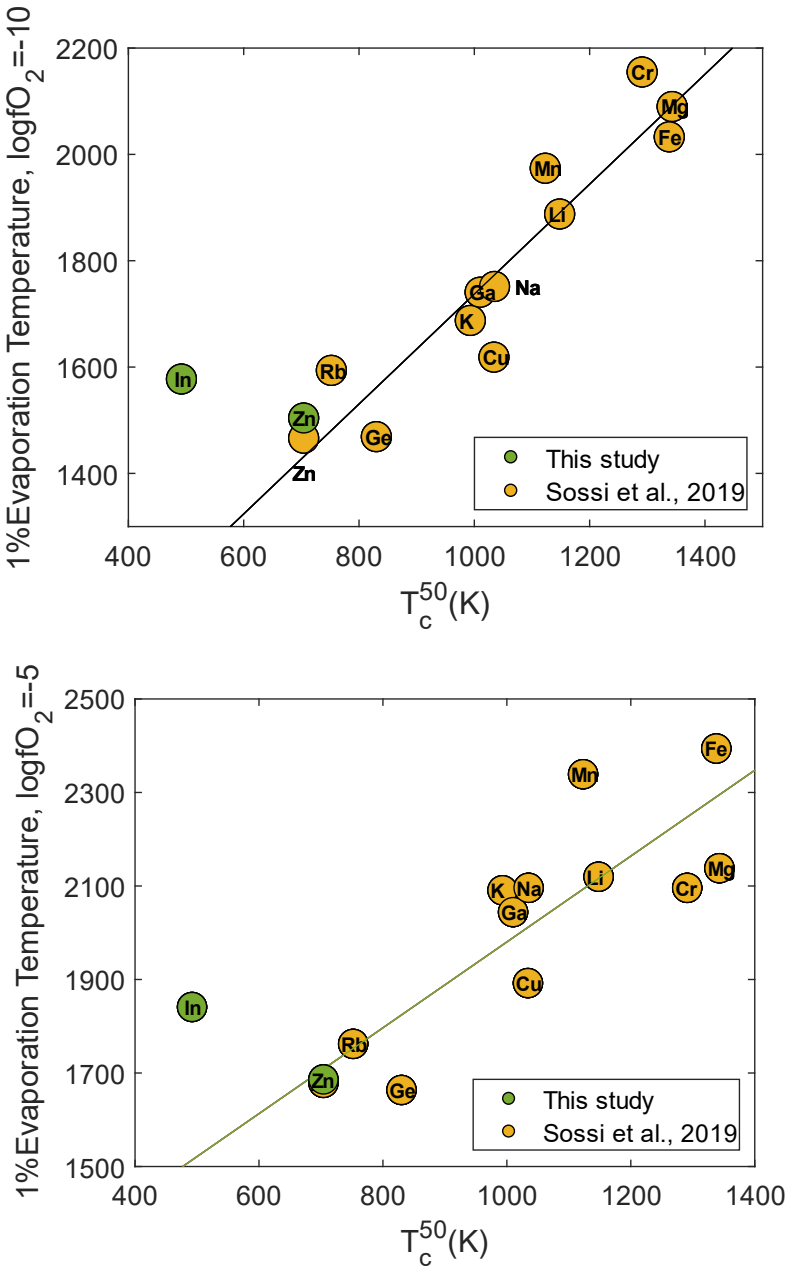

Fig. 5 The 1% evaporation temperature is plotted against 50% condensation temperature from Wood et al, (2019). The error bars are within the symbol size. The yellow cycles data is recalculated from Sossi et al. (2019), and provide in Table.1; In and Zn in this study is shown as green symbols. The results of Zn in this study have good consistency with previous Zn data in Sossi et al. (2019). The evaporation temperature and condensation temperature show a clear correlation for most of MVEs, while In is significantly higher than the trend which regressed by the other MVEs, which indicate In less volatile during evaporation of vapor-melt system.

4.2 The origin of overabundance of In in the BSE

The overabundance of In in the BSE was attributed to a heterogeneous accretion model of the Earth (e.g., Braukmüller et al., 2019). This model proposes that the Earth was accreted primarily from volatile depleted materials, followed by the delivery of volatile-rich materials whose MVEs are present in CI-chondritic relative abundances during the last 10-20 % accretion of Earth's mass before core formation ceased (*e.g.,* Wänke et al., 1984; Rubie et al. 2011). This hypothesis finds support in previous studies on MVEs and their isotopes, including Ag (Schönbächler et al., 2010), Cu (Savage et al., 2015; Mahan et al., 2018a), S (Suer et al., 2017), Zn (Mahan et al., 2018b), and Sn (Kubik et al., 2021). However, whether these late-added volatile-rich materials are the sufficient sources to explain the whole Earth's In budget, or in other words, whether the early accreted materials still carry a considerable amount of In, require further discussion.

The late added volatile-rich materials are suggested to have a CI-like constant-abundance plateau for elements with $T_c^{50} < 750$ K such as In, Zn and Cd (Braukmüller et al., 2019). In this case, assuming the entire budget for these 'plateau-abundance' elements in the Earth brought by these late-accreted materials, given the on-going core-formation process, their relative abundance in the BSE should follow the order of their partition coefficients (D) between core and mantle. The partition coefficients between core-forming metal and the overlying molten silicate mantle are primarily affected by *P-T*, fO_2, and abundances of light elements in the metallic phase. Metal-silicate equilibration experiments reveal that In generally has a higher tendency to partition into the metallic phase than do Zn and Cd ($D_{In} > D_{Cd} > D_{Zn}$) regardless of temperature and pressure conditions (Mann et al., 2009; Ballhaus et al., 2013; Wood et al., 2014; Wang et al., 2016; Righter et al., 2017; Righter et al., 2018). However, this observation is inconsistent with the CI, -Mg normalized abundances of In, Zn and Cd in BSE, where In is present at levels similar to Zn, and higher than Cd (e.g., Palme and O'Neill., 2014). Although the presence of light elements like S and Si can play a role on the partitioning

coefficient, they should not result in In becoming less siderophile than Cd and Zn, given the current estimation of the S content of Earth's core (~ 2 wt.%, Dreibus and Palme, 1996; Suer et al., 2017) and Si (~ 2 to 10 wt.%, Malavergne et al., 2004; Siebert et al., 2013; Badro et al., 2015; Rubie et al., 2015; for further discussion see Supplementary materials, Fig. S4 and S5). In order to accommodate these observations, the precursor materials of the proto-Earth are required to have higher CI-, Mg normalized abundance of In than Cd, thereby counteracting the greater depletion of In expected during core formation. To achieve this, In must have behaved in less volatile manner than Cd, as observed in our evaporation experiments on silicate melt.

Here, and in the previous study of Norris and Wood. (2017), we find that In is less volatile than Zn (see Fig. 3 and Fig. 5) and Cd during silicate melt evaporation. However, Cd was observed to be too volatile to have measurable content in most of the samples in Sossi et al. (2019), making it impossible to assess its 1% evaporation temperature from their experiments alone. This contrasts with the higher volatility of In than Zn and Cd during nebular condensation (e.g., Wood et al., 2019). Using the T_e[1] volatility scale calibrated in our study, the BSE abundance of In now falls below the volatility trend defined by other MVEs (Fig. 6), meaning it is no longer overabundant in the BSE. This observation permits the additional loss of In to the core during its formation, and suggests In depletion occurred on building blocks of the Earth (i.e., precursor materials of proto-Earth) were set by silicate melt evaporation rather than nebular condensation. Additionally, enrichments in the heavier isotopes of Si (Pringle et al., 2014; Moynier et al., 2020), Fe (Sossi et al. 2016) and Mg (Hin et al., 2017) in the Earth relative to chondrites are also taken as evidence for evaporation-induced volatile loss on the precursor materials of the Earth. Therefore, the In budget in the Earth would be suggested as a mixture of i) late added volatile-rich materials and ii) precursor materials of the proto-Earth with considerable quantities of In owing to its limited volatile depletion under non-nebular conditions.

The In isotopic compositions of Earth and chondrites will be a useful test to the various scenarios as discussed above. If Earth's In budget is derived from late-added chondritic

materials or non-vaporized precursors, the In isotopic composition of the Earth should be similar to those of chondrites. Alternatively, if the precursor materials experienced partial evaporation, the In isotope composition of the Earth would be expected to record these event(s). However, the isotopic fractionation reflects the physical-chemical conditions under which evaporation occurred, namely, the total pressure, gas composition/density and species of evaporated gas, which can suppress the extent of fractionation, and possibly result in insignificant isotopic fractionation (e.g., Young et al., 2019; Sossi et al., 2020). Furthermore, given the siderophile behavior of In, isotope fractionation during metal-silicate segregation also requires consideration when estimating the isotopic composition of In of the bulk Earth. Future studies of In isotopic compositions of terrestrial samples and chondrites, and isotope fractionation during metal-silicate partitioning are required.

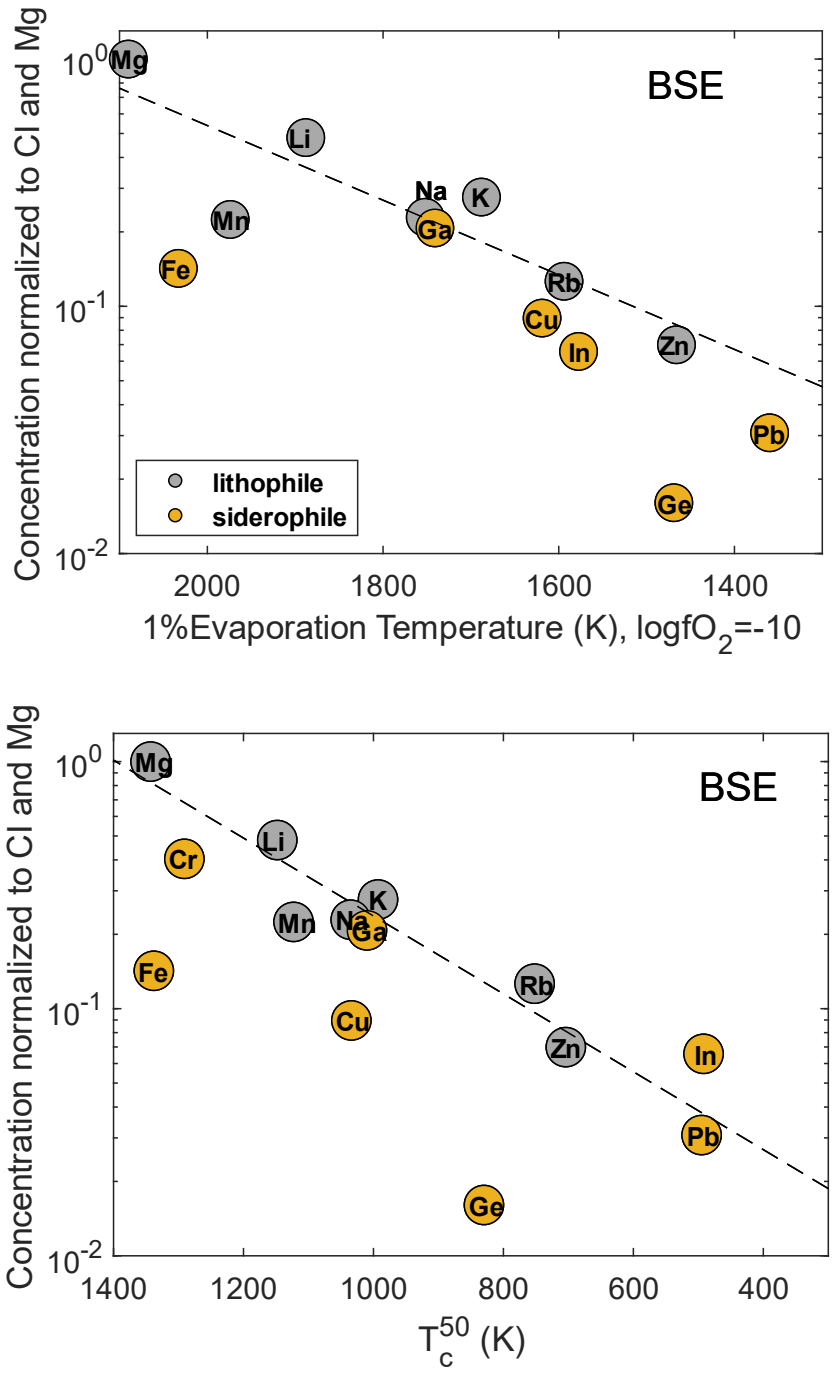

Fig. 6. The CI-Mg normalized elemental abundances in the BSE plot as a function of evaporation temperature and 50% condensation temperature, respectively. When using the new evaporation temperature scale, In falls below the volatility trend defined by other lithophile volatile elements due to core formation process and does not show overabundance in the BSE.

4.3 Moon and Vesta: implications for smaller differentiated bodies

Atmospheric loss is most likely to occur during the early stages of accretion of the

proto-Earth, after which Earth's gravity field is sufficiently large to prevent the effective loss of volatile components. These chemical and isotopic signatures of evaporation during early-stage accretion could be entirely or partially overprinted by late-added volatile-rich materials. By contrast, partial evaporation is more likely to generate volatile depletion among smaller telluric bodies with lower masses and escape velocities (*cf.* Pringle et al. 2014*;* Hin et al. 2017; Young et al. 2019; Benedikt et al. 2020, Sossi et al., 2022). In support of this assertion, smaller bodies show evidence of post-nebular volatile depletion. Most notably, the Mn/Na ratios of Mars, the Moon, Vesta and angrite parent bodies are higher than chondritic values (O'Neill and Palme, 2008; Siebert et al., 2018). Isotopic evidence from MVEs also supports that planetary volatilization is the dominant mechanism for volatile depletion. Moderately volatile elements in lunar samples, like Zn (Kato et al., 2015; Paniello et al., 2012a; Van Kooten et al., 2020), Ga (Kato and Moynier, 2017, Wimpenny et al., 2022), Rb (Pringle and Moynier, 2017; Nie and Dauphas, 2019), and K (Wang and Jacobsen, 2016; Tian et al., 2020) are enriched in the heavier isotopes, which indicate volatile loss by an evaporation process. A similar trend of heavy isotope enrichment is found for other volatile depleted bodies (e.g., Vesta and the angrite parent body) (Paniello et al., 2012b; Wang et al., 2012; Pringle et al., 2014; Pringle and Moynier, 2017).

Evaporation that caused the depletion in MVEs of small bodies likely occurred under a vapor-liquid environment, because mass transport in the solid-state is too slow relative to atmospheric cooling timescales to cause wholescale depletion of rocky bodies (*e.g.,* Bower et al. 2019). In these settings, the evaporation temperature is likely a more relevant scale of element volatilities than is the T_c^{50}. The abundances of lithophile elements in the Moon correlate well (R^2 = 0.94) with their respective evaporation temperatures (Fig. 7). Furthermore, assuming the Moon was formed from a BSE-like precursor (e.g., Ringwood, 1986), the BSE-Mg normalized abundance of In in the bulk silicate Moon (BSM) falls slightly below the volatile depletion trend defined by other lithophile MVEs, which implies limited In partitioning into the small lunar core. This conclusion is in agreement with the volatilities of MVEs calculated by Gibbs Free

Energy minimization incorporating activity coefficients of metal oxide species into a BSE-like silicate melt in *FactSage* (Ivanov et al. 2022). These authors argue that the chemical signature of the Moon may have been inherited from two distinct stages of condensation at both high (~4000 K) and low (~2000 K), each time at pressures higher (>0.1 bar) and oxygen fugacities (~near the Fayalite-Magnetite-Quartz buffer) significantly higher than those in the solar nebula. Although these authors did not consider In in their calculations, this scenario is broadly consistent with the physicochemical conditions proposed here.

The amount of In that resides in the lunar core can be estimated from published metal-silicate experiment data. Righter et al. (2017) estimated 1 ppb In in the lunar mantle and 4.5 ppb In the bulk Moon using a remarkably high D_{In} of ~ 200 determined in their experiments. This D value is more than an order of magnitude higher than other reported values under similar P-T-fO_2 conditions (e.g., Mann et al., 2009; Wood et al., 2014; Ballhaus et al., 2013). Mann et al. (2009) obtained D_{In} of 11 to 15 under 2 GPa and ~ 2000 K, ΔIW –1.5, similar to the D_{In} of 3~12 reported by Ballhaus et al. (2013) under 1.5 GPa, 1800 ~ 2100 K and ΔIW –1.5 ~ -2.1. These P-T conditions are comparable to those estimated for lunar core formation (~ 5 GPa, 2200 K and ΔIW-2; Rai and van Westrenen, 2014), and the median value of reported D_{In} of ~12 (Mann et al., 2009; Ballhaus et al. 2013) is used here to estimate In concentration in lunar core. An earlier estimate by O'Neill (1991) suggests that the bulk Moon contains 0.4 ppb In, based on the assumption of a volatile-free proto-Moon acquired its volatile inventory by ~ 4 wt.% H-chondrite late veneer. This estimate is slightly lower than the In concentration of 1.6 ppb estimated from lunar volcanic glass (Hauri et al., 2015). Assuming that the BSM with 1.6 ppb In (Hauri et al., 2015) is homogeneously and fully equilibrated with the lunar core that accounts for 1.5% of the Moon's mass (Weber et al., 2011), the In abundance of the bulk Moon is calculated to be 1.9 ppb. This means that BSM is the dominant reservoir of In.

The mantle of Vesta is known to be depleted in MVEs (Mittlefehldt, 2015; Steenstra et al., 2019), yet the origin of this depletion is still poorly understood. The super-

chondritic Mn/Na ratio of HED meteorites implies that evaporative loss may have occurred under non-nebular conditions. The isotopically light Cr in eucrites also suggests evaporation of Cr under relatively high fO_2, possibly during a magma ocean (Zhu et al., 2019). The CI-Mg normalized abundances of MVEs, particularly of In and Zn, in the Vestan mantle also correlate well with the evaporation temperature (Fig. 7). The smooth decrease in MVE abundance with evaporation temperature observed for the Moon and Vesta strongly supports an evaporation-induced volatile depletion, and suggests that T_e^1 is a more suitable volatility scale for thermodynamic processes occurring in a post-nebular environment.

The significantly different volatility of In under nebular and non-nebular conditions makes the In/Zn ratio an useful indicator of the conditions under which MVE depletion of a planetary body occurred. Under nebular conditions, In is more volatile than Zn ($T_c^{50}$of In < $T_c^{50}$of Zn), and thus volatile-depleted materials would be characterized by In/Zn <1. Under non-nebular conditions, In becomes less volatile than Zn (T_e^1 of In > T_e^1 of Zn), and planetary evaporation should give rise to residues with In/Zn ≥ 1. Therefore, the observed higher relative abundance of In than Zn in the lunar and Vestan mantle indicates a non-nebular origin of their MVEs (Fig.7). The isotopic composition of In in differentiated and undifferentiated meteorites should also shed light on whether partial evaporation or condensation was associated with volatile loss, and if so, under what conditions. Hence, future studies of the In isotope composition of achondritic meteorites is required.

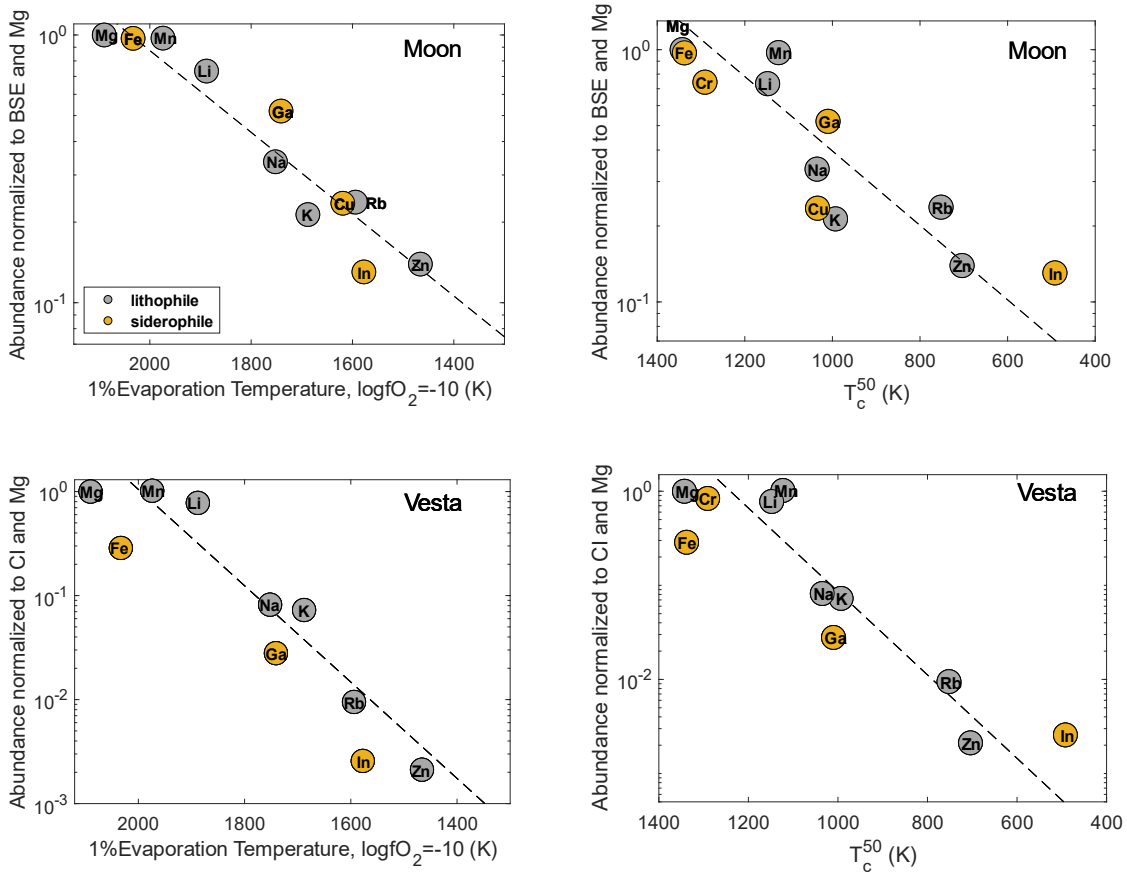

Fig. 7 The BSE, -Mg normalized abundances of bulk silicate Moon (BSM) and CI, -Mg normalized Vesta (BSV) are plotted against 1% evaporation temperature at $logf(O_2) = -10$ and 50% condensation temperature. The abundance of BSM is from Hauri et al. (2015) and BSE from Palme and O'Neill. (2014). Vesta data from Sossi et al., 2022 and references therein. These elemental abundances are provided in supplementary materials. Both normalized elemental abundances in the BSM and BSV show a near log-linear with the new evaporation temperature scale.

5. Conclusion

Indium is both a siderophile and a volatile element in a cosmochemical context. However, when considering its T_c^{50} , it is overabundant in the BSE compared to other MVEs. Here we show that the T_c^{50} is not suitable for assessing elemental volatility for evaporation processes that occurred under oxidizing planetary conditions and that a new scale is required. In this study, we have performed a series of evaporation experiments and calculated the evaporation temperature of In ($T_{e,i}^{1,-10}$ =1578 ± 15 K) using the empirically theoretical framework developed in Sossi et al. (2019). This evaporation temperature indicates a significantly lower relative volatility of In with respect to other MVEs compared to the 50% condensation temperature scale. Our results suggest that the volatile depletion of small bodies, like the Moon and Vesta, were controlled by volatilization processes under more oxidizing conditions than the solar nebula. Combining published partitioning data (with the limitation that all experiments were performed at pressure conditions lower than that relevant to Earth's core formation), we suggest that the present Earth's In budget consists of two components, the considerable amount of In carried by the early precursor materials and the subsequent complement from CI-like materials during late-accretion stage.

Acknowledgements

The authors very kindly thank Associated Editor Bernard Charlier, reviewer Bernard Wood and another two anonymous reviewers for their constructive suggestions. for handling this paper. D. L. thanks the China Scholarship Council (CSC) for a PhD fellowship. D.L appreciate Pierre Burckel for the analysis on ICP-MS at IPGP. D.L and J.S thank Daniel R. Neuville for the synthesis of starting materials at IPGP. D.L thanks Nicolas Wehr for the technique assistance on evaporation experiments. This work was partly supported by the IPGP analytical platform PARI, Ile-de-France SESAME Grants 12015908, DIM ACAV+, the ERC grant 101001282 (METAL), and Labex UnivEarth (FM).

References

Albarede, F. (2009). "Volatile accretion history of the terrestrial planets and dynamic implications." Nature **461**(7268): 1227-1233.

Allibert, L., Charnoz, S., Siebert, J., Jacobson, S.A. and Raymond, S.N. (2021) Quantitative estimates of impact induced crustal erosion during accretion and its influence on the Sm/Nd ratio of the Earth. Icarus 363, 114412.

Armytage, R., Georg, R., Williams, H. and Halliday, A. (2012) Silicon isotopes in lunar rocks: Implications for the Moon's formation and the early history of the Earth. Geochimica et Cosmochimica Acta 77, 504-514.

Badro, J., Brodholt, J.P., Piet, H., Siebert, J. and Ryerson, F.J. (2015) Core formation and core composition from coupled geochemical and geophysical constraints. Proceedings of the National Academy of Sciences 112, 12310-12314.

Ballhaus, C., Laurenz, V., Münker, C., Fonseca, R.O.C., Albarède, F., Rohrbach, A., Lagos, M., Schmidt, M.W., Jochum, K.-P., Stoll, B., Weis, U. and Helmy, H.M. (2013) The U/Pb ratio of the Earth's mantle—A signature of late volatile addition. Earth and Planetary Science Letters 362, 237-245.

Benedikt, M., Scherf, M., Lammer, H., Marcq, E., Odert, P., Leitzinger, M. and Erkaev, N.V. (2020) Escape of rock-forming volatile elements and noble gases from planetary embryos. Icarus 347, 113772.

Bower, D.J., Kitzmann, D., Wolf, A.S., Sanan, P., Dorn, C. and Oza, A.V. (2019) Linking the evolution of terrestrial interiors and an early outgassed atmosphere to astrophysical observations. Astronomy & Astrophysics 631, A103.

Braukmüller, N., Wombacher, F., Funk, C. and Münker, C. (2019) Earth's volatile element depletion pattern inherited from a carbonaceous chondrite-like source. Nature Geoscience 12, 564-568.

Clay, P.L., Burgess, R., Busemann, H., Ruzié-Hamilton, L., Joachim, B., Day, J.M. and Ballentine, C.J. (2017) Halogens in chondritic meteorites and terrestrial accretion. Nature 551, 614-618.

Darken, L.S. and Gurry, R. (1945) The system iron-oxygen. I. The wüstite field and related equilibria. Journal of the American Chemical Society 67, 1398-1412.

Dreibus, G. and Palme, H. (1996) Cosmochemical constraints on the sulfur content in the Earth's core. Geochimica et Cosmochimica Acta 60, 1125-1130.

Hauri, E.H., Saal, A.E., Rutherford, M.J. and Van Orman, J.A. (2015) Water in the Moon's interior: Truth and consequences. Earth and Planetary Science Letters 409, 252-264.

Hertz, H. (1882) Ueber die Verdunstung der Flüssigkeiten, insbesondere des Quecksilbers, im luftleeren Raume. Annalen der Physik 253, 177-193.

Hin, R.C., Coath, C.D., Carter, P.J., Nimmo, F., Lai, Y.-J., Pogge von Strandmann, P.A.E., Willbold, M., Leinhardt, Z.M., Walter, M.J. and Elliott, T. (2017) Magnesium isotope evidence that accretional vapour loss shapes planetary compositions. Nature 549, 511-515.

Holzheid, A., H. Palme and S. Chakraborty (1997). "The activities of NiO, CoO and FeO in silicate melts." Chemical Geology **139**(1-4): 21-38.

Ivanov, D., Fitoussi, C. and Bourdon, B. (2022) Trace element volatility and the conditions of liquid-vapor separation in the proto-lunar disk. Icarus 386, 115143.

Kato, C. and Moynier, F. (2017) Gallium isotopic evidence for extensive volatile loss from the Moon during its formation. Science advances 3, e1700571.

Kato, C., Moynier, F., Valdes, M.C., Dhaliwal, J.K. and Day, J.M.D. (2015) Extensive volatile loss during formation and differentiation of the Moon. Nature Communications 6, 7617.

Knudsen, M. (1909) Die Gesetze der Molekularströmung und der inneren Reibungsströmung der Gase durch Röhren. Annalen der Physik 333, 75-130.

Kubik, E., Siebert, J., Mahan, B., Creech, J., Blanchard, I., Agranier, A., Shcheka, S. and Moynier, F. (2021) Tracing Earth's Volatile Delivery With Tin. Journal of Geophysical Research: Solid Earth 126, e2021JB022026.

Lamoreaux, R.H., Hildenbrand, D.L. and Brewer, L. (1987) High-Temperature Vaporization Behavior of Oxides II. Oxides of Be, Mg, Ca, Sr, Ba, B, Al, Ga, In, Tl, Si, Ge, Sn, Pb, Zn, Cd, and Hg. Journal of Physical and Chemical Reference Data 16, 419-443.

Langmuir, I. (1916) The Evaporation, Condensation and Reflection of Molecules and the Mechanism of Adsorption. Physical Review 8, 149-176.

Larimer, J.W. (1967) Chemical fractionations in meteorites—I. Condensation of the elements. Geochimica et Cosmochimica Acta 31, 1215-1238.

Lodders, K. (2003) Solar system abundances and condensation temperatures of the elements. The Astrophysical Journal 591, 1220.

Mann, U., Frost, D.J. and Rubie, D.C. (2009) Evidence for high-pressure core-mantle differentiation from the metal-silicate partitioning of lithophile and weakly-siderophile elements. Geochimica Et Cosmochimica Acta 73, 7360-7386.

Mahan, B., Siebert, J., Blanchard, I., Badro, J., Kubik, E., Sossi, P. and Moynier, F. (2018a) Investigating Earth's Formation History Through Copper and Sulfur Metal-Silicate Partitioning During Core-Mantle Differentiation. Journal of Geophysical Research-Solid Earth 123, 8349-8363.

Mahan, B., Siebert, J., Blanchard, I., Borensztajn, S., Badro, J. and Moynier, F. (2018b) Constraining compositional proxies for Earth's accretion and core formation through high pressure and high temperature Zn and S metal-silicate partitioning. Geochimica et Cosmochimica Acta 235, 21-40.

Malavergne, V., Siebert, J., Guyot, F., Gautron, L., Combes, R., Hammouda, T., Borensztajn, S., Frost, D. and Martinez, I. (2004) Si in the core? New high-pressure and high-temperature experimental data. Geochimica et Cosmochimica Acta 68, 4201-4211.

Mittlefehldt, David W. "Asteroid (4) Vesta: I. The howardite-eucrite-diogenite (HED) clan of meteorites." Geochemistry 75.2 (2015): 155-183.

Morbidelli, A., Libourel, G., Palme, H., Jacobson, S.A. and Rubie, D.C. (2020) Subsolar Al/Si and Mg/Si ratios of non-carbonaceous chondrites reveal planetesimal formation during early condensation in the protoplanetary disk. Earth and Planetary Science Letters 538, 116220.

Moynier, F., Deng, Z., Lanteri, A., Martins, R., Chaussidon, M., Savage, P. and Siebert, J. (2020) Metal-silicate silicon isotopic fractionation and the composition of the bulk Earth. Earth and Planetary Science Letters 549, 116468.

Nie, N.X. and Dauphas, N. (2019) Vapor Drainage in the Protolunar Disk as the Cause for the Depletion in Volatile Elements of the Moon. The Astrophysical Journal Letters 884, L48

Norris, C.A. and Wood, B.J. (2017) Earth's volatile contents established by melting and vaporization. Nature 549, 507.

O'Neill, H.S.C. (1991) The origin of the Moon and the early history of the Earth—A chemical model. Part 2: The Earth. Geochimica et Cosmochimica Acta 55, 1159-1172.

O'Neill, H. S. C. and S. M. Eggins (2002). The effect of melt composition on trace element partitioning: an experimental investigation of the activity coefficients of FeO, NiO, CoO, MoO_2 and MoO_3 in silicate melts. Chemical Geology 186(1-2): 151-181.

O'Neill, H.S.C. and Palme, H. (2008) Collisional erosion and the non-chondritic composition of the terrestrial planets. Philosophical Transactions of the Royal Society A: Mathematical, Physical and Engineering Sciences 366, 4205-4238.

Palme, H., Larimer, J. and Lipschutz, M. (1988) Moderately volatile elements. Meteorites and the early solar system, 436-461.

Palme, H. and O'Neill, H. (2014) Cosmochemical Estimates of Mantle Composition. Planets, Asteriods, Comets and The Solar System, Volume 2 of Treatise on Geochemistry. Edited by Andrew M. Davis. Elsevier.

Paniello, R.C., Day, J.M. and Moynier, F. (2012a) Zinc isotopic evidence for the origin of the Moon. Nature 490, 376-379.

Paniello, R.C., Moynier, F., Beck, P., Barrat, J.-A., Podosek, F.A. and Pichat, S. (2012b) Zinc isotopes in HEDs: Clues to the formation of 4-Vesta, and the unique composition of Pecora Escarpment 82502. Geochimica et Cosmochimica Acta 86, 76-87.

Persad, A.H. and Ward, C.A. (2016) Expressions for the Evaporation and Condensation Coefficients in the Hertz-Knudsen Relation. Chemical Reviews 116, 7727-7767.

Pringle, E.A. and Moynier, F. (2017) Rubidium isotopic composition of the Earth, meteorites, and the Moon: Evidence for the origin of volatile loss during planetary accretion. Earth and Planetary Science Letters 473, 62-70.

Pringle, E.A., Moynier, F., Savage, P.S., Badro, J. and Barrat, J.-A. (2014) Silicon isotopes in angrites and volatile loss in planetesimals. Proceedings of the National Academy of Sciences 111, 17029-17032.

Rai, N. and van Westrenen, W. (2014) Lunar core formation: New constraints from metal-silicate partitioning of siderophile elements. Earth and Planetary Science Letters 388, 343-352.

Richter, F.M., Davis, A.M., Ebel, D.S. and Hashimoto, A. (2002) Elemental and isotopic fractionation of Type B calcium-, aluminum-rich inclusions: experiments, theoretical considerations, and constraints on their thermal evolution. Geochimica et Cosmochimica Acta 66, 521-540.

Ricolleau, A., Fei, Y.W., Corgne, A., Siebert, J. and Badro, J. (2011) Oxygen and silicon contents of Earth's core from high pressure metal-silicate partitioning experiments. Earth and Planetary Science Letters 310, 409-421.

Righter, K., Nickodem, K., Pando, K., Danielson, L., Boujibar, A., Righter, M. and Lapen, T. (2017) Distribution of Sb, As, Ge, and In between metal and silicate during accretion and core formation in the Earth. Geochimica et Cosmochimica Acta 198, 1-16.

Righter, K., Pando, K., Marin, N., Ross, D., Righter, M., Danielson, L., Lapen, T. and Lee, C. (2018) Volatile element signatures in the mantles of Earth, Moon, and Mars: Core formation fingerprints from Bi, Cd, In, and Sn. Meteorit. Planet. Sci. 53, 284-305.

Ringwood, A. (1986) Terrestrial origin of the Moon. Nature 322, 323-328.

Rubie, D.C., Frost, D.J., Mann, U., Asahara, Y., Nimmo, F., Tsuno, K., Kegler, P., Holzheid, A. and Palme,

H., (2011). Heterogeneous accretion, composition and core–mantle differentiation of the Earth. Earth and Planetary Science Letters, 301(1-2), pp.31-42.

Rubie, D.C., Jacobson, S.A., Morbidelli, A., O'Brien, D.P., Young, E.D., de Vries, J., Nimmo, F., Palme, H. and Frost, D.J. (2015) Accretion and differentiation of the terrestrial planets with implications for the compositions of early-formed Solar System bodies and accretion of water. Icarus 248, 89-108.

Savage, P.S., Moynier, F., Chen, H., Shofner, G., Siebert, J., Badro, J. and Puchtel, I.S. (2015) Copper isotope evidence for large-scale sulphide fractionation during Earth's differentiation. Geochem. Perspect. Lett. 1, 53-63.

Schönbächler, M., Carlson, R., Horan, M., Mock, T. and Hauri, E. (2010) Heterogeneous accretion and the moderately volatile element budget of Earth. Science 328, 884-887.

Siebert, J., Badro, J., Antonangeli, D. and Ryerson, F.J. (2013) Terrestrial accretion under oxidizing conditions. Science, 1227923.

Siebert, J. and Shahar, A. (2015) An Experimental Geochemistry Perspective on Earth's Core Formation. The Early Earth: Accretion and Differentiation 212, 103-121.

Siebert, J., Sossi, P.A., Blanchard, I., Mahan, B., Badro, J. and Moynier, F. (2018) Chondritic Mn/Na ratio and limited post-nebular volatile loss of the Earth. Earth and Planetary Science Letters 485, 130-139.

Sossi, P.A. and Fegley Jr, B. (2018) Thermodynamics of element volatility and its application to planetary processes. Reviews in Mineralogy and Geochemistry 84, 393-459.

Sossi, P.A., Klemme, S., O'Neill, H.S.C., Berndt, J. and Moynier, F. (2019) Evaporation of moderately volatile elements from silicate melts: Experiments and theory. Geochimica et Cosmochimica Acta. 260, 204-231.

Sossi, P.A., Nebel, O. and Foden, J. (2016) Iron isotope systematics in planetary reservoirs. Earth and Planetary Science Letters 452, 295-308.

Sossi, P.A., Nebel, O., O'Neill, H.S.C. and Moynier, F. (2018) Zinc isotope composition of the Earth and its behaviour during planetary accretion. Chem. Geol. 477, 73-84.

Sossi, P.A., Stotz, I.L., Jacobson, S.A., Morbidelli, A. and O'Neill, H.S.C. (2022) Stochastic accretion of the Earth. Nature Astronomy, 1-10.

Steenstra, E., Rai, N., Knibbe, J., Lin, Y. and van Westrenen, W. (2016) New geochemical models of core formation in the Moon from metal–silicate partitioning of 15 siderophile elements. Earth and Planetary Science Letters 441, 1-9.

Steenstra, E.S., Dankers, D., Berndt, J., Klemme, S., Matveev, S. and van Westrenen, W. (2019) Significant depletion of volatile elements in the mantle of asteroid Vesta due to core formation. Icarus 317, 669-681.

Steenstra, E.S., Seegers, A.X., Putter, R., Berndt, J., Klemme, S., Matveev, S., Bullock, E.S. and van Westrenen, W. (2020) Metal-silicate partitioning systematics of siderophile elements at reducing conditions: A new experimental database. Icarus 335, 113391.

Suer, T.-A., Siebert, J., Remusat, L., Menguy, N. and Fiquet, G. (2017) A sulfur-poor terrestrial core inferred from metal–silicate partitioning experiments. Earth and Planetary Science Letters 469, 84-97.

Taylor, G.J. (2013) The bulk composition of Mars. Geochemistry 73, 401-420.

Tian, Z., Jolliff, B.L., Korotev, R.L., Fegley Jr, B., Lodders, K., Day, J.M., Chen, H. and Wang, K. (2020)

Potassium isotopic composition of the Moon. Geochimica et Cosmochimica Acta 280, 263-280.

Van Kooten, E.M., Moynier, F. and Day, J.M. (2020) Evidence for transient atmospheres during eruptive outgassing on the Moon. The Planetary Science Journal 1, 67.

Visscher, C. and Fegley Jr, B. (2013) Chemistry of impact-generated silicate melt-vapor debris disks. The Astrophysical Journal Letters 767, L12.

Vollstaedt, H., Mezger, K. and Alibert, Y. (2020) Carbonaceous Chondrites and the Condensation of Elements from the Solar Nebula. The Astrophysical Journal 897, 82.

Wade, J. and Wood, B. (2005) Core formation and the oxidation state of the Earth. Earth and Planetary Science Letters 236, 78-95.

Wang, K., Moynier, F., Dauphas, N., Barrat, J.-A., Craddock, P. and Sio, C.K. (2012) Iron isotope fractionation in planetary crusts. Geochimica et Cosmochimica Acta 89, 31-45.

Wang, K. and Jacobsen, S.B. (2016) Potassium isotopic evidence for a high-energy giant impact origin of the Moon. Nature 538, 487-490.

Wang, Z. and Becker, H. (2013) Ratios of S, Se and Te in the silicate Earth require a volatile-rich late veneer. Nature 499, 328.

Wang, Z., Laurenz, V., Petitgirard, S. and Becker, H. (2016) Earth's moderately volatile element composition may not be chondritic: Evidence from In, Cd and Zn. Earth and Planetary Science Letters 435, 136-146.

Wänke, H., G. Dreibus, and E. Jagoutz. "Mantle chemistry and accretion history of the Earth." In Archaean geochemistry, pp. 1-24. Springer, Berlin, Heidelberg, 1984.

Weber, R.C., Lin, P.-Y., Garnero, E.J., Williams, Q. and Lognonné, P. (2011) Seismic detection of the lunar core. science 331, 309-312.

Wood, B.J., Kiseeva, E.S. and Mirolo, F.J. (2014) Accretion and core formation: The effects of sulfur on metal–silicate partition coefficients. Geochimica et Cosmochimica Acta 145, 248-267.

Wimpenny, J., Borg, L. and Sio, C.K.I. (2022) The gallium isotopic composition of the Moon. Earth and Planetary Science Letters 578, 117318.

Witt-Eickschen, G., Palme, H., O'neill, H.S.C. and Allen, C.M. (2009) The geochemistry of the volatile trace elements As, Cd, Ga, In and Sn in the Earth's mantle: new evidence from in situ analyses of mantle xenoliths. Geochimica et Cosmochimica Acta 73, 1755-1778.

Wood, B.J. and Wade, J. (2013) Activities and volatilities of trace components in silicate melts: a novel use of metal–silicate partitioning data. Contributions to Mineralogy and Petrology 166, 911-921.

Wood, B.J., Smythe, D.J. and Harrison, T. (2019) The condensation temperatures of the elements: A reappraisal. American Mineralogist 104, 844-856.

Yi, W., Halliday, A.N., Alt, J.C., Lee, D.C., Rehkämper, M., Garcia, M.O., Langmuir, C. and Su, Y. (2000) Cadmium, indium, tin, tellurium, and sulfur in oceanic basalts: Implications for chalcophile element fractionation in the Earth. Journal of Geophysical Research: Solid Earth 105, 18927-18948.

Young, E., Shahar, A., Nimmo, F., Schlichting, H., Schauble, E., Tang, H. and Labidi, J. (2019) Near-equilibrium isotope fractionation during planetesimal evaporation. Icarus 323, 1-15.

Zhang, Z.J., Nie, N.X., Mendybaev, R.A., Liu, M.-C., Hu, J.J., Hopp, T., Alp, E.E., Lavina, B., Bullock, E.S. and McKeegan, K.D. (2021) Loss and isotopic fractionation of alkali elements during diffusion-limited evaporation from molten silicate: Theory and experiments. ACS Earth and Space Chemistry 5, 755-784.

Zhu, K., Sossi, P.A., Siebert, J. and Moynier, F. (2019) Tracking the volatile and magmatic history of Vesta from chromium stable isotope variations in eucrite and diogenite meteorites. Geochimica et Cosmochimica Acta 266, 598-610.

Supplementary tables

Table. S1 The chemical composition of starting materials

wt. %	MORB mixture	FCMAS mixture
SiO_2[a]	49.61	38.30
Al_2O_3	14.44	10.44
MgO	7.75	14.87
FeO	9.35	16.93
CaO	13.00	16.98
TiO_2	1.00	-
MnO	0.18	-
Na_2O	2.05	-
K_2O	0.18	-
ppm (measured)		
In	9648	9631
Zn	10151	10591
ppm (calculated)		
In[b]	9947	9893
Zn[b]	10046	10198

Both elemental concentration of synthetic MORB and FCMAS mixtures are analyzed by Q-ICP-MS.

a: The concentration of SiO_2 is approximated as total (100 wt.%) subtract the sum of concentration of other major elements.

b: The calculated concentration of In and Zn of initial mixing powders of MORB and FCMAS. Concentrations were calculated by the weighing amounts.

Table. S2 Experimental conditions and indium and zinc concentration of samples.

Run	T (℃)	t-t_0 (min)	log$f$O$_2$	Metal wire	In concentration (wt.%)	Zn concentration (wt.%)
DLG-26	1300	30	-0.68	Pt	0.89	0.92
DLG-25	1300	60	-0.68	Pt	0.91	0.95
DLG-28	1300	30	-3.44	Pt	0.92	0.90
DLG-27	1300	60	-3.44	Pt	0.91	0.82
DLG-29	1300	30	-6.5	Re	0.79	0.61
DLG-30	1300	60	-6.53	Re	0.63	0.40
DLG-42	1300	60	-10	Re	0.07	0.00
DLG-01	1400	30	-0.68	Pt	0.87	0.80
DLG-04	1400	30	-0.68	Pt	0.90	0.92
DLG-02	1400	60	-0.68	Pt	0.90	0.87
DLG-12	1400	30	-3	Pt	0.89	0.85
DLG-13	1400	60	-3	Pt	0.87	0.49
DLG-17	1400	60	-4.97	Pt	0.78	0.29
DLG-16	1400	30	-4.97	Pt	0.73	0.31
DLG-34	1400	30	-6.5	Re	0.34	0.07
DLG-39	1400	60	-6.99	Re	0.09	0.00
DLG-07	1500	30	-0.68	Pt	0.89	0.80
DLG-05	1500	60	-0.68	Pt	0.86	0.67
DLG-10	1500	30	-2.7	Pt	0.73	0.22
DLG-11	1500	60	-2.7	Pt	0.72	0.14
DLG-20	1500	30	-5	Pt	0.41	0.04
DLG-22	1500	60	-5	Pt	0.21	0.01
DLG-37	1500	30	-7.01	Re	0.01	0.00
DLG-40	1500	60	-7.01	Re	0.00	0.00
DLF-02	1300	30	-3.44	Pt	0.97	0.00
DLF-03	1300	60	-6.96	Re	0.37	0.33
DLF-01	1400	60	-6.99	Re	0.00	0.00
DLF-04	1300	30	-8	Re	0.16	0.17
DLF-05	1300	60	-8	Re	0.15	0.05
DLF-06	1300	30	-10	Re	0.08	0.03
DLF-07	1300	60	-10	Re	0.05	0.01
MORB					0.96	1.01
FCMAS					0.96	1.06

The DLG-series samples used synthetic MORB mixture as starting materials. DLF-series samples used synthetic FCMAS as starting materials.

Table. S3 The In concentration in blank runs and ratios of furnace contamination

Run	T (°C)	logfO_2	t-t_0 (min)	In [Blank] ppm	Blank/Remnant (%)	Zn [Blank] ppm	Blank/Remnant (%)
Blk_1300_10	1300	-10	60	1.4	0.2	17	40.6
Blk_1300_8_1	1300	-8	60	3.2	0.2	5.2	1.0
Blk_1300_8_2	1300	-8	60	5.9	0.3	0.7	0.2
Blk_1300_6	1300	-6.5	60	4.7	0.1	3.7	0.1
Blk_1300_3	1300	-3.44	60	21.3	0.2	54.0	0.7
Blk_1300_air	1300	-0.68	60	68.7	0.8	80.0	0.8
Blk_1400_10	1400	-10	60	7.0	7.0	11.9	n.a.
Blk_1400_6	1400	-6.5	60	4.7	0.1	<blk	-
Blk_1400_3	1400	-3	60	31.7	0.4	32.3	0.7
Blk_1400_air	1400	-0.68	60	80.5	0.9	66.0	1.3
Blk_1500_10	1500	-10	60	3.3	48.3	<blk	-
Blk_1500_8	1500	-8	60	3.6	13.9	39.6	n.a.
Blk_1500_6	1500	-6.5	60	2.9	21.8	<blk	-
Blk_1500_5	1500	-5.07	60	60.1	2.9	<blk	-
Blk_1500_2	1500	-2.7	60	145.8	2.0	14.9	1.0
Blk_1500_air	1500	-0.68	60	338.0	3.9	19.7	0.3

Table. S4 The concentration of Fe, Zn and In in metal wire

Experimental conditions				Concentration in wire						Wire/Initial addition % (50mg MORB mixture)					
T (°C)	logfO_2	t-t_0 (min)	wire	Fe wt.%	SD	Zn ppm	SD	In ppm	SD	Fe	SD	Zn	SD	In	SD
1300	-0.68	30	Pt	0.06	0.00	0.22	-	302.9	0.1	0.40	0.00	0.00	-	1.52	0.00
1300	-3.44	30	Pt	0.07	0.00	<blk	-	774.1	1.1	0.49	0.00	<blk	-	3.89	0.00
1300	-6.5	30	Re	0.01	0.00	<blk	-	1.1	0.1	0.04	0.00	<blk	-	0.01	0.00
1300	-7.99	30	Re	0.00	0.00	<blk	-	1.1	0.1	0.02	0.00	<blk	-	0.01	0.00
1300	-10	30	Re	0.00	0.00	<blk	-	0.1	0.0	0.02	0.00	<blk	-	0.00	0.00
1400	-0.68	30	Pt	0.06	0.00	<blk	-	185.9	0.4	0.41	0.00	<blk	-	0.93	0.00
1400	-3	30	Pt	0.15	0.00	1.11	-	1266.3	5.6	1.04	0.00	0.01	-	6.37	0.00
1400	-4.97	30	Pt	0.22	0.00	<blk	-	1606.8	12.3	1.48	0.01	<blk	-	8.08	0.00
1400	-4.97	60	Pt	0.25	0.01	344.80	10.9	2124.9	42.7	1.70	0.05	1.70	0.05	10.68	0.00
1400	-6.5	30	Re	0.01	0.00	<blk	-	0.1	0.0	0.09	0.00	<blk	-	0.00	0.00
1400	-8	30	Re	0.00	0.00	<blk	-	0.2	0.0	0.02	0.00	<blk	-	0.00	0.00
1400	-10	30	Re	0.03	0.00	<blk	-	0.2	0.0	0.20	0.00	<blk	-	0.00	0.00
1500	-0.68	30	Pt	0.05	0.00	0.54	0.21	171.1	1.4	0.34	0.00	0.00	0.00	0.86	0.00
1500	-2.7	30	Pt	0.22	0.01	4.28	0.54	1528.7	16.0	1.52	0.04	0.00	0.00	7.68	0.00
1500	-3.99	30	Pt	0.47	0.00	2.32	0.38	4903.3	13.2	3.22	0.03	0.00	0.00	24.65	0.00
1500	-4	60	Pt	0.62	0.00	<blk	-	3548.2	13.5	4.25	0.02	<blk	-	17.84	0.00
1500	-5.02	30	Pt	0.60	0.01	2.63	0.39	4759.9	5.3	4.12	0.06	0.01	0.00	23.93	0.00
1500	-5.07	60	Pt	0.19	0.00	<blk	-	1171.6	1.5	1.29	0.01	<blk	-	5.89	0.00
1500	-6.5	30	Re	0.01	0.00	<blk	-	1.0	0.1	0.07	0.00	<blk	-	0.01	0.00
1500	-8	30	Re	0.00	0.00	<blk	-	0.0	0.0	0.03	0.00	<blk	-	0.00	0.00
1500	-10	30	Re	0.03	0.00	<blk	-	0.1	0.0	0.18	0.00	<blk	-	0.00	0.00

The contents of Fe, Zn and In represents their amounts in whole wire of each experiment and measured on Q-ICP-MS. The wire concentration is estimated by assuming a wire mass ~ 25mg. The 'wire/initial addition' is calculated by assuming the initial addition of Fe, In and Zn from 50mg synthetic MORB-mixture, dividing the measured total amounts by this assumed addition.

Table. S5 Concentration results for zoning tests.

T=1300°C, logfO_2= -0.68, 60 min

Run	points	Mg	2SD	Al	2SD	Ca	2SD	Fe	2SD	Si	2SD	Na	2SD
M3_3	1	4.90	0.48	7.65	0.31	8.56	0.00	7.33	0.58	23.44	0.42	1.49	0.41
M3_3	2	4.97	0.47	7.71	0.30	8.82	0.00	7.12	0.56	23.33	0.41	1.62	0.41
M3_3	3	4.79	0.47	7.72	0.30	8.81	0.00	7.16	0.56	23.55	0.41	1.52	0.41
M3_3	4	4.75	0.46	7.70	0.30	8.67	0.00	7.18	0.56	23.44	0.41	1.63	0.42
M3_3	5	4.85	0.47	7.77	0.30	8.65	0.00	6.97	0.55	23.50	0.41	1.65	0.42
M3_3	6	4.74	0.48	7.76	0.31	8.69	0.00	7.04	0.57	23.46	0.42	1.64	0.43
M3_3	7	4.75	0.46	7.74	0.30	8.80	0.00	7.05	0.56	23.54	0.41	1.61	0.42
M3_3	8	4.75	0.46	7.73	0.30	8.75	0.00	7.05	0.56	23.42	0.41	1.54	0.41
M3_3	9	4.82	0.48	7.78	0.31	8.52	0.00	7.12	0.58	23.41	0.42	1.62	0.44
M3_3	10	4.76	0.48	7.73	0.31	8.77	0.00	7.05	0.57	23.37	0.42	1.55	0.43
M3_3	11	4.88	0.49	7.77	0.31	8.74	0.00	7.29	0.58	23.58	0.42	1.71	0.44
M3_3	12	4.93	0.49	7.77	0.31	8.82	0.00	7.07	0.58	23.45	0.42	1.56	0.43
M3_3	13	4.85	0.48	7.70	0.31	8.75	0.00	7.19	0.58	23.45	0.42	1.62	0.44
M3_3	14	4.85	0.48	7.77	0.31	8.76	0.00	7.19	0.58	23.43	0.42	1.71	0.44
M3_3	15	4.69	0.46	7.66	0.30	8.71	0.00	7.18	0.56	23.51	0.41	1.66	0.42
Mean		4.82		7.73		8.72		7.13		23.46		1.61	
2SD		0.16		0.08		0.18		0.20		0.13		0.13	
Run	points	K	2SD	P	2SD	S	2SD	Mn	2SD	In	2SD	Ti	2SD
M3_3	1	0.15	0.10	0.11	0.01	0.01	0.01	0.13	0.02	0.89	0.05	0.65	0.02
M3_3	2	0.15	0.10	0.11	0.01	0.01	0.01	0.14	0.02	0.91	0.05	0.65	0.02
M3_3	3	0.15	0.10	0.11	0.01	0.01	0.01	0.14	0.02	0.93	0.05	0.65	0.02
M3_3	4	0.17	0.10	0.11	0.01	0.01	0.01	0.14	0.02	0.91	0.05	0.65	0.02
M3_3	5	0.15	0.10	0.11	0.01	0.02	0.01	0.14	0.02	0.92	0.05	0.65	0.02
M3_3	6	0.16	0.10	0.11	0.01	0.01	0.01	0.14	0.02	0.90	0.05	0.65	0.02
M3_3	7	0.13	0.10	0.11	0.01	0.00	0.01	0.13	0.02	0.87	0.05	0.66	0.02
M3_3	8	0.15	0.10	0.11	0.01	0.01	0.01	0.14	0.02	0.86	0.05	0.65	0.02
M3_3	9	0.14	0.10	0.11	0.01	0.01	0.01	0.14	0.02	0.85	0.05	0.65	0.02
M3_3	10	0.16	0.10	0.11	0.01	0.01	0.01	0.14	0.02	0.86	0.05	0.65	0.02

M3_3	11	0.16	0.10	0.11	0.01	0.01	0.01	0.14	0.02	0.86	0.05	0.65	0.02
M3_3	12	0.16	0.10	0.11	0.01	0.01	0.01	0.14	0.02	0.81	0.05	0.63	0.02
M3_3	13	0.15	0.10	0.11	0.01	0.01	0.01	0.14	0.02	0.83	0.05	0.65	0.02
M3_3	14	0.18	0.11	0.11	0.01	0.01	0.01	0.13	0.02	0.82	0.05	0.65	0.02
M3_3	15	0.16	0.10	0.11	0.01	0.01	0.01	0.14	0.02	0.82	0.05	0.65	0.02
Mean		0.15		0.11		0.01		0.14		0.87		0.65	
2SD		0.02		0.00		0.01		0.01		0.08		0.01	

T=1300°C, logfO_2= -3.44, 60 min

Run	points	Mg	2SD	Al	2SD	Ca	2SD	Fe	2SD	Si	2SD	Na	2SD
M6	1	4.82	0.49	7.65	0.31	8.66	0.87	7.16	0.58	23.47	0.42	1.58	0.43
M6	2	4.82	0.49	7.71	0.31	8.64	0.87	7.14	0.58	23.47	0.42	1.69	0.45
M6	3	4.83	0.48	7.72	0.31	8.72	0.88	6.88	0.57	23.51	0.42	1.61	0.43
M6	4	4.78	0.48	7.71	0.31	8.85	0.89	7.25	0.58	23.69	0.42	1.65	0.44
M6	5	4.93	0.49	7.66	0.31	8.90	0.89	7.13	0.58	23.56	0.42	1.79	0.45
M6	6	4.89	0.49	7.68	0.31	8.87	0.89	7.16	0.58	23.39	0.42	1.65	0.44
M6	7	4.87	0.49	7.66	0.31	8.68	0.87	7.21	0.58	23.36	0.42	1.64	0.43
M6	8	4.84	0.49	7.68	0.31	8.84	0.89	7.19	0.58	23.50	0.42	1.62	0.43
M6	9	4.87	0.49	7.72	0.31	8.75	0.88	7.12	0.58	23.37	0.42	1.63	0.43
M6	10	4.95	0.49	7.78	0.31	8.90	0.89	7.12	0.58	23.45	0.42	1.78	0.45
M6	11	4.77	0.48	7.71	0.31	8.89	0.89	6.92	0.57	23.27	0.42	1.66	0.44
M6	12	4.99	0.49	7.68	0.31	8.97	0.90	7.12	0.58	23.44	0.42	1.71	0.45
M6	13	4.84	0.49	7.62	0.31	8.98	0.90	7.25	0.59	23.50	0.42	1.59	0.43
M6	14	4.88	0.49	7.62	0.31	8.60	0.87	7.07	0.58	23.37	0.42	1.67	0.44
M6	15	4.86	0.48	7.64	0.31	8.82	0.88	6.96	0.57	23.48	0.42	1.59	0.43
M6	16	4.80	0.47	7.68	0.30	8.90	0.88	7.10	0.56	23.56	0.41	1.71	0.43
M6	17	4.91	0.49	7.76	0.31	8.71	0.87	7.13	0.58	23.52	0.42	1.68	0.44
M6	18	4.79	0.48	7.77	0.31	8.92	0.89	7.02	0.57	23.52	0.42	1.59	0.43
M6	19	4.78	0.47	7.72	0.30	8.89	0.88	7.00	0.56	23.60	0.41	1.71	0.43
M6	20	4.88	0.47	7.69	0.30	8.84	0.87	7.11	0.56	23.51	0.41	1.62	0.42

Mean		4.86		7.69		8.82		7.10		23.48		1.66	
2SD		0.12		0.09		0.22		0.20		0.19		0.12	
Run	points	K	2SD	P	2SD	S	2SD	Mn	2SD	In	2SD	Ti	2SD
M6	1	0.17	0.11	0.12	0.01	0.01	0.01	0.14	0.02	0.90	0.05	0.65	0.02
M6	2	0.18	0.11	0.12	0.01	0.01	0.01	0.14	0.02	0.91	0.05	0.66	0.02
M6	3	0.15	0.10	0.11	0.01	0.00	0.01	0.14	0.02	0.92	0.05	0.65	0.02
M6	4	0.13	0.10	0.12	0.01	0.00	0.01	0.14	0.02	0.93	0.05	0.66	0.02
M6	5	0.14	0.11	0.11	0.01	0.00	0.01	0.14	0.02	0.92	0.05	0.65	0.02
M6	6	0.17	0.11	0.12	0.01	0.00	0.01	0.14	0.02	0.95	0.05	0.66	0.02
M6	7	0.12	0.10	0.12	0.01	0.01	0.01	0.14	0.02	0.95	0.05	0.66	0.02
M6	8	0.12	0.10	0.11	0.01	0.01	0.01	0.14	0.02	0.96	0.05	0.65	0.02
M6	9	0.15	0.10	0.11	0.01	0.00	0.01	0.14	0.02	0.96	0.05	0.65	0.02
M6	10	0.15	0.10	0.11	0.01	0.00	0.01	0.14	0.02	0.96	0.05	0.65	0.02
M6	11	0.14	0.10	0.11	0.01	0.01	0.01	0.14	0.02	0.96	0.05	0.65	0.02
M6	12	0.13	0.10	0.11	0.01	0.00	0.01	0.14	0.02	0.97	0.05	0.66	0.02
M6	13	0.15	0.10	0.11	0.01	0.00	0.01	0.14	0.02	0.98	0.05	0.65	0.02
M6	14	0.15	0.11	0.11	0.01	0.00	0.01	0.14	0.02	0.97	0.05	0.65	0.02
M6	15	0.15	0.10	0.11	0.01	0.01	0.01	0.14	0.02	0.98	0.05	0.65	0.02
M6	16	0.15	0.10	0.11	0.01	0.00	0.01	0.14	0.02	1.00	0.05	0.65	0.02
M6	17	0.14	0.10	0.11	0.01	0.00	0.01	0.14	0.02	0.99	0.05	0.66	0.02
M6	18	0.18	0.11	0.11	0.01	0.00	0.01	0.14	0.02	1.01	0.05	0.65	0.02
M6	19	0.15	0.10	0.11	0.01	0.00	0.01	0.14	0.02	1.00	0.05	0.66	0.02
M6	20	0.18	0.10	0.11	0.01	0.00	0.01	0.13	0.02	1.01	0.05	0.65	0.02
Mean		0.15		0.11		0.00		0.14		0.96		0.65	
2SD		0.04		0.00		0.00		0.00		0.07		0.01	

T=1300°C, logfO_2= -8, 60 min

Run	points	Mg	2SD	Al	2SD	Ca	2SD	Fe	2SD	Si	2SD	Na	2SD
M5	1	5.06	0.48	7.87	0.30	9.04	0.89	7.07	0.56	23.95	0.41	1.63	0.42
M5	2	4.96	0.48	7.88	0.30	8.83	0.87	7.20	0.56	23.89	0.41	1.54	0.41

M5	3	4.92	0.47	7.86	0.30	8.82	0.87	7.24	0.57	23.71	0.41	1.55	0.41
M5	4	4.93	0.47	7.88	0.30	8.98	0.88	7.22	0.57	23.79	0.41	1.57	0.41
M5	5	4.84	0.47	7.80	0.30	9.09	0.89	7.08	0.56	23.79	0.41	1.58	0.41
M5	6	4.90	0.47	7.84	0.30	8.84	0.87	7.18	0.56	23.96	0.41	1.65	0.42
M5	7	4.81	0.48	7.83	0.31	8.87	0.89	7.18	0.58	23.86	0.42	1.51	0.42
M5	8	4.95	0.49	7.82	0.31	8.97	0.90	7.04	0.57	23.82	0.42	1.59	0.43
M5	9	4.85	0.47	7.83	0.30	8.95	0.88	7.26	0.57	23.87	0.41	1.56	0.41
M5	10	4.72	0.48	7.04	0.29	8.31	0.84	6.86	0.57	21.78	0.41	1.55	0.42
M5	11	4.99	0.49	7.80	0.31	8.83	0.88	7.29	0.59	23.99	0.43	1.58	0.44
M5	12	4.80	0.48	7.68	0.31	8.98	0.90	7.24	0.58	23.83	0.42	1.54	0.43
M5	13	4.86	0.48	7.79	0.31	8.85	0.89	7.07	0.57	23.96	0.42	1.72	0.44
M5	14	4.93	0.48	7.84	0.30	8.96	0.88	7.35	0.57	23.81	0.41	1.59	0.42
M5	15	4.95	0.49	7.75	0.31	8.69	0.87	7.17	0.58	23.85	0.43	1.56	0.43
M5	16	4.81	0.48	7.79	0.31	8.84	0.89	7.14	0.58	23.91	0.43	1.51	0.42
Mean		4.89		7.77		8.87		7.16		23.74		1.58	
2SD		0.17		0.40		0.36		0.23		1.05		0.11	
Run	points	K	2SD	P	2SD	S	2SD	Mn	2SD	In	2SD	Ti	2SD
M5	1	0.14	0.10	0.12	0.01	0.00	0.01	0.14	0.02	0.18	0.03	0.67	0.02
M5	2	0.15	0.10	0.12	0.01	0.00	0.01	0.14	0.02	0.16	0.03	0.67	0.02
M5	3	0.15	0.09	0.12	0.01	0.00	0.01	0.14	0.02	0.18	0.03	0.67	0.02
M5	4	0.13	0.09	0.12	0.01	0.00	0.01	0.14	0.02	0.19	0.03	0.67	0.02
M5	5	0.13	0.09	0.12	0.01	0.00	0.01	0.14	0.02	0.19	0.03	0.67	0.02
M5	6	0.10	0.09	0.12	0.01	0.00	0.01	0.14	0.02	0.21	0.03	0.66	0.02
M5	7	0.12	0.10	0.12	0.01	0.00	0.01	0.14	0.02	0.20	0.03	0.67	0.02
M5	8	0.15	0.10	0.12	0.01	0.00	0.01	0.14	0.02	0.18	0.03	0.66	0.02
M5	9	0.13	0.09	0.12	0.01	0.00	0.01	0.14	0.02	0.17	0.03	0.66	0.02
M5	10	0.14	0.10	0.11	0.01	0.00	0.01	0.13	0.02	0.16	0.03	0.61	0.02
M5	11	0.14	0.10	0.12	0.01	0.00	0.01	0.14	0.02	0.20	0.03	0.66	0.02
M5	12	0.13	0.09	0.12	0.01	0.00	0.01	0.14	0.02	0.23	0.04	0.66	0.02
M5	13	0.13	0.10	0.12	0.01	0.00	0.01	0.14	0.02	0.23	0.04	0.67	0.02
M5	14	0.16	0.10	0.12	0.01	0.00	0.01	0.14	0.02	0.23	0.04	0.67	0.02

M5	15	0.10	0.09	0.12	0.01	0.00	0.01	0.14	0.02	0.20	0.03	0.66	0.02
M5	16	0.13	0.09	0.12	0.01	0.00	0.01	0.14	0.02	0.19	0.03	0.66	0.02
Mean		0.13		0.12		0.00		0.14		0.19		0.66	
2SD		0.03		0.01		0.00		0.01		0.05		0.03	

T=1300°C, logfO_2= -10, 60 min

Run	points	Mg	2SD	Al	2SD	Ca	2SD	Fe	2SD	Si	2SD	Na	2SD
M2_3	1	4.90	0.49	7.86	0.31	8.92	0.89	7.19	0.58	23.94	0.43	1.83	0.46
M2_3	2	4.88	0.47	7.91	0.31	8.85	0.87	7.31	0.57	24.01	0.41	1.65	0.42
M2_3	3	4.77	0.47	7.86	0.30	8.92	0.88	7.38	0.57	23.95	0.41	1.75	0.43
M2_3	4	4.88	0.47	7.75	0.30	8.80	0.87	7.17	0.56	23.97	0.41	1.67	0.43
M2_3	5	4.95	0.47	7.81	0.30	8.95	0.88	7.35	0.57	24.04	0.41	1.54	0.41
M2_3	6	4.92	0.47	7.85	0.30	8.80	0.87	7.35	0.57	24.08	0.41	1.74	0.43
M2_3	7	4.96	0.47	7.92	0.31	8.88	0.88	7.22	0.56	23.97	0.41	1.58	0.42
M2_3	8	4.89	0.47	7.80	0.30	8.86	0.87	7.31	0.57	24.04	0.41	1.63	0.42
M2_3	9	4.81	0.48	7.81	0.31	8.84	0.89	7.15	0.58	24.00	0.43	1.61	0.44
M2_3	10	4.96	0.49	7.74	0.31	8.94	0.89	7.29	0.59	23.96	0.42	1.65	0.43
M2_3	11	4.81	0.48	7.89	0.31	8.76	0.88	7.11	0.58	23.99	0.43	1.63	0.44
M2_3	12	5.01	0.49	7.77	0.31	8.66	0.87	7.16	0.58	24.06	0.43	1.73	0.44
M2_3	13	4.96	0.49	7.82	0.31	8.83	0.88	7.15	0.58	23.99	0.43	1.75	0.45
M2_3	14	4.96	0.49	7.74	0.31	9.00	0.90	7.21	0.58	23.97	0.43	1.61	0.44
M2_3	15	4.95	0.49	7.75	0.31	8.96	0.90	7.15	0.58	24.07	0.43	1.84	0.46
Mean		4.91		7.82		8.86		7.23		24.00		1.68	
2SD		0.14		0.12		0.18		0.18		0.09		0.18	
Run	points	K	2SD	P	2SD	S	2SD	Mn	2SD	In	2SD	Ti	2SD
M2_3	1	0.16	0.10	0.12	0.01	0.01	0.01	0.14	0.02	0.08	0.03	0.67	0.02
M2_3	2	0.14	0.10	0.12	0.01	0.01	0.01	0.14	0.02	0.09	0.03	0.66	0.02
M2_3	3	0.16	0.10	0.12	0.01	0.01	0.01	0.14	0.02	0.09	0.03	0.66	0.02
M2_3	4	0.18	0.10	0.12	0.01	0.01	0.01	0.14	0.02	0.09	0.03	0.67	0.02
M2_3	5	0.17	0.10	0.12	0.01	0.01	0.01	0.14	0.02	0.10	0.03	0.67	0.02

M2_3	6	0.19	0.10	0.12	0.01	0.01	0.01	0.14	0.02	0.09	0.03	0.67	0.02
M2_3	7	0.16	0.09	0.12	0.01	0.01	0.01	0.14	0.02	0.09	0.03	0.66	0.02
M2_3	8	0.15	0.10	0.12	0.01	0.01	0.01	0.14	0.02	0.09	0.03	0.67	0.02
M2_3	9	0.14	0.10	0.12	0.01	0.01	0.01	0.14	0.02	0.10	0.03	0.67	0.02
M2_3	10	0.11	0.10	0.12	0.01	0.01	0.01	0.13	0.02	0.09	0.03	0.67	0.02
M2_3	11	0.17	0.11	0.12	0.01	0.01	0.01	0.14	0.02	0.09	0.03	0.67	0.02
M2_3	12	0.16	0.10	0.12	0.01	0.01	0.01	0.14	0.02	0.08	0.03	0.67	0.02
M2_3	13	0.16	0.10	0.12	0.01	0.02	0.01	0.15	0.02	0.09	0.03	0.66	0.02
M2_3	14	0.16	0.10	0.13	0.01	0.02	0.01	0.15	0.02	0.09	0.03	0.67	0.02
M2_3	15	0.19	0.11	0.13	0.01	0.01	0.01	0.14	0.02	0.06	0.03	0.66	0.02
		0.16		0.12		0.01		0.14		0.09		0.67	
		0.04		0.01		0.01		0.01		0.02		0.01	

Table S6 The elemental abundances of moderately volatile elements in bulk silicate Vesta (BSV) and bulk silicate Moon (BSM)

Element	Vesta	Moon
wt.%		
Mg	19.57[a]	22.68[c]
Fe	11.21 [a]	6.26 [c]
ppm		
Mn	4093[b]	1046 [c]
Li	2.37 [b]	1.2 [c]
Cu	-	7.2 [c]
K	83.0 [b]	56.8 [c]
Ga	0.6 [b]	2.3 [c]
Na	851 [b]	890 [c]
Rb	0.05 [b]	0.15 [c]
Zn	1.37 [b]	7.70 [c]
ppb		
In	0.42 [b]	1.60[c]

The elemental concentration of BSV and BSM used in Fig. 7 are taken from **a**: Dreibus et al. (1977); **b**: Sossi et al. (2022); **c**: Hauri et al. (2015)

Supplementary figures

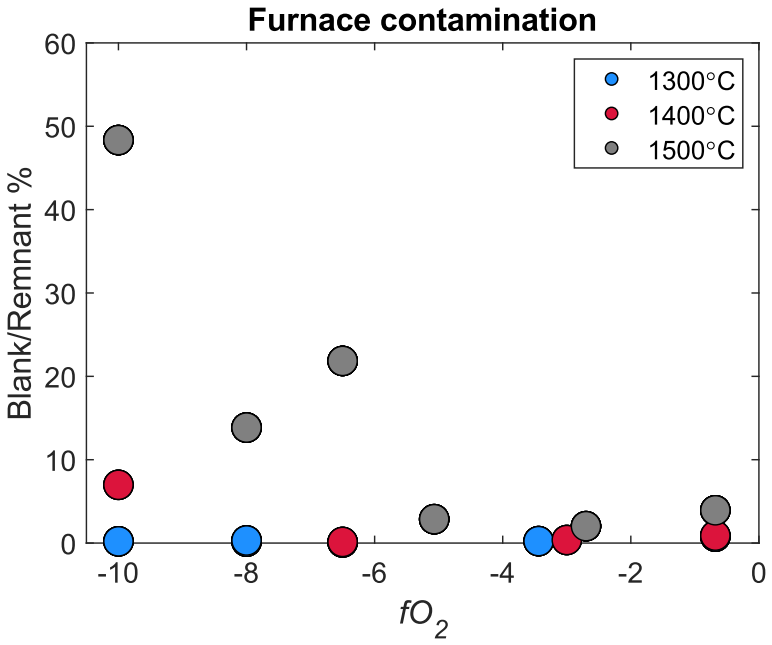

Fig. S1. The furnace contamination contributed In plot against experimental oxygen fugacity. The y-axis represents that the ratio of measured In concentration of blank samples and experimental samples which were performed at the same conditions (T, fO_2 and duration). Proportion of contamination increases with increasing temperature and decreasing oxygen fugacity. The 1500℃ series runs show higher ratio from environmental contamination. The high T and most reducing samples (1500℃ and $logf(O_2) = -10$ and -8) are discarded due to over-high contamination contribution.

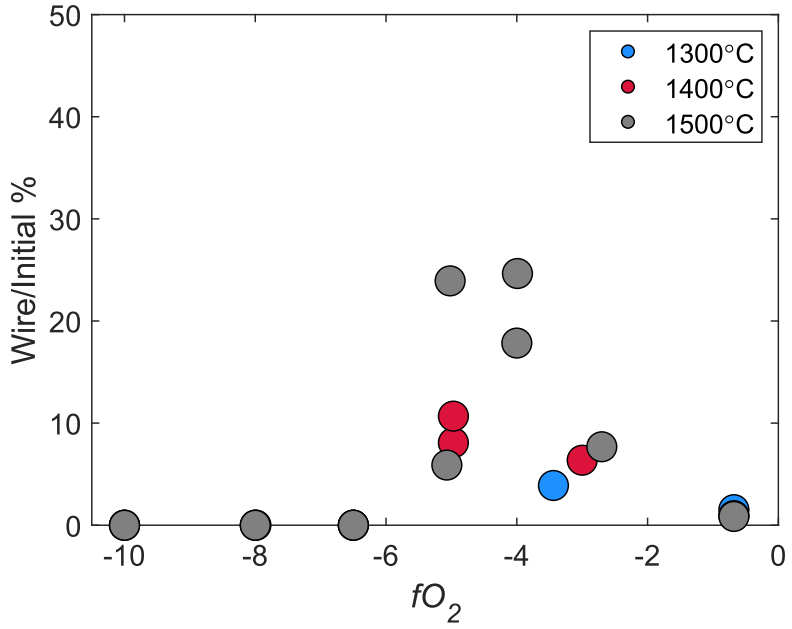

Fig. S2 The proportions of In lost to metal wire relative to initial addition amount plot against experimental oxygen fugacity. The runs that performed at >log$f$(O_2)= -6 used Pt wires, ≤ -6 used Re wires. At 1500℃ and $logf(O_2) = -5$ and -4, there is a significant fraction of In dissolved into Pt wire, for minimizing the additional In loss to wire, these runs are not used to calculate volatility.

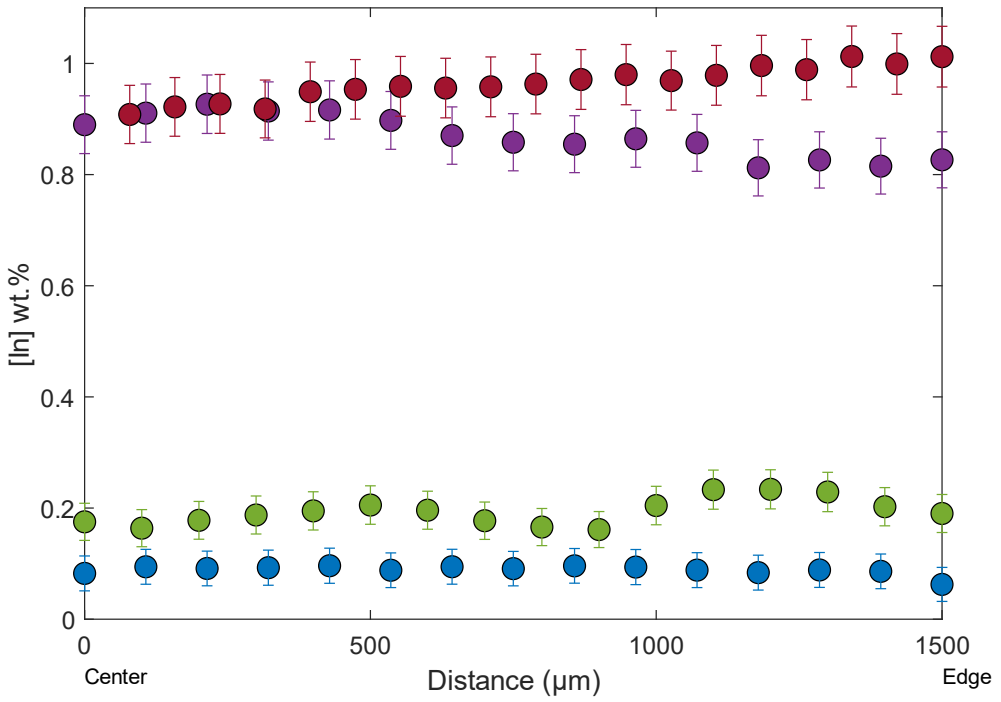

Fig. S3 Elemental zone of In at 1300°C and variable oxygen fugacity ($logf(O_2)$= -0.68 (purple), -3.44 (red), -8 (green) and -10 (blue)) in MORB samples. Measurement points are selected along the radius. Elemental zoning is insignificant within the analytical uncertainty. The fastest evaporation rate sample (log$f$O$_2$ = -10) exhibit near-homogeneous distribution of In.

The comparison of partition coefficients D_{In} and D_{Cd}

As mentioned in main text, the elemental partition coefficient is a function of *P-T-X-*fO_2. Therefore, the relative siderophility of Cd and In can be known by comparing their partition coefficient, D_M, expressed as follow

$$D_M = \frac{X_M^{metal}}{X_{MO_{n/2}}^{silicate}} \quad (1)$$

where X_M^{metal} and $X_{MO_{n/2}}^{silicate}$ are the molar fraction of element M and its oxide in metal and silicate phases, respectively. *n* refers to the valence state of M. For a equilibrium reaction of M between metal and silicate:

$$MO_{n/2}^{silicate} + \frac{n}{2}Fe^{metal} = M^{metal} + \frac{n}{2}FeO^{silicate} \quad (2)$$

The partitioning of element M can be quantified by equilibrium coefficient (*K*), By means of *K*, elemental partitioning can be quantified independently of fO_2. *K* can be expressed as:

$$K = \frac{\left(a_{FeO}^{silicate}\right)^{\frac{n}{2}}(a_M^{metal})}{(a_{MO_{\frac{n}{2}}}^{silicate})(a_{Fe}^{metal})^{n/2}} \quad (3)$$

where a_i refers to the activities of different components, calculated by the multiplying molar fraction of *i* and its activity coefficient, γ_i, $a_i = \gamma_i X_i$. Substitute to Eqn. (3), the equilibrium constant of reaction can be rewritten as follow:

$$logK = log\frac{\left(X_{FeO}^{silicate}\right)^{\frac{n}{2}}(X_M^{metal})}{(X_{MO_{\frac{n}{2}}}^{silicate})(X_{Fe}^{metal})^{n/2}} + log\frac{\gamma_M^{metal}}{(\gamma_{Fe}^{metal})^{n/2}} + log\frac{(\gamma_{FeO}^{silicate})^{n/2}}{\gamma_{MO_{\frac{n}{2}}}^{silicate}} \quad (4)$$

Substitute Eqn. (1) to Eqn. (4), $logK$ can be further expressed to be a function of partition coefficient:

$$logK = log\frac{D_M}{(D_{Fe})^{n/2}} + log\frac{\gamma_M^{metal}}{(\gamma_{Fe}^{metal})^{n/2}} + log\frac{(\gamma_{FeO}^{silicate})^{n/2}}{\gamma_{MO_{\frac{n}{2}}}^{silicate}} \quad (5)$$

The ratio of oxide activity coefficients is neglected due to little influence on the equilibrium constant, particularly for the elements whose valence state below 4+ (In is

3+, Cd is 2+, from Righter et al., 2017 and Kubik et al., 2021). log$K$ is also a function of P-T:

$$logK = a + \frac{b}{T} + \frac{cP}{T} \quad (6)$$

where a, b and c are regression constants corresponding to entropy, enthalpy and volume terms. Combine Eqn. (5) and Eqn. (6), the partition coefficient of M is expressed as:

$$\log(D_i) = a + \frac{b}{T} + \frac{cP}{T} - \frac{n}{2} log \frac{X_{FeO}^{silicate}}{X_{Fe}^{metal}} - log\gamma_M^{metal} + \frac{n}{2} log\gamma_{Fe}^{metal} \quad (7)$$

The oxygen fugacity of metal-silicate reaction can be approximately seen as $\Delta IW = 2log \frac{X_{FeO}^{silicate}}{X_{Fe}^{metal}}$, hence this term in Eqn. 7 can be replaced by $\frac{n}{4}\Delta IW$. Activity coefficients γ_M^{metal} and γ_{Fe}^{metal} are calculated by using the interaction parameter (ε) approach from Ma (2001), for a metallic solution which contains N components, the activity coefficients of Fe and solutes are given by:

$$\begin{aligned} ln\gamma_{Fe}^{metal} = & \sum_{i=1}^{N-1} \varepsilon_i^i (X_i + \ln(1 - X_i)) \\ & - \sum_{j=1}^{N-2} \sum_{k=j+1}^{N-1} \varepsilon_j^k X_j X_k \left(1 + \frac{\ln(1 - X_j)}{X_j} + \frac{\ln(1 - X_k)}{X_k}\right) \\ & + \sum_{i=1}^{N-1} \sum_{k=1}^{N-1} \varepsilon_i^k X_i X_k \left(1 + \frac{\ln(1 - X_k)}{X_k} - \frac{1}{1 - X_i}\right) \\ & + \frac{1}{2} \sum_{j=1}^{N-2} \sum_{k=j+1}^{N-1} \varepsilon_j^k X_j^2 X_k^2 \left(\frac{1}{1 - X_j} + \frac{1}{1 - X_k} - 1\right) \\ & - \sum_{i=1}^{N-1} \sum_{\substack{k=1 \\ k \neq i}}^{N-1} \varepsilon_i^k X_i^2 X_k^2 \left(\frac{1}{1 - X_i} + \frac{1}{1 - X_k} + \frac{X_i}{2(1 - X_i)^2} - 1\right) \quad (8) \end{aligned}$$

and

$$ln\gamma_M^{metal} = ln\gamma_{Fe}^{metal} + ln\gamma_M^0 - \varepsilon_i^i \ln(1-X_i) - \sum_{\substack{j=1 \\ j\neq i}}^{N-1} \varepsilon_i^j X_j \left(1 + \frac{\ln(1-X_j)}{X_j} - \frac{1}{1-X_i}\right)$$

$$+ \sum_{\substack{j=1 \\ j\neq i}}^{N-1} \varepsilon_i^j X_j^2 X_i \left(\frac{1}{1-X_i} + \frac{1}{1-X_j} + \frac{X_i}{2(1-X_i)^2} - 1\right) \quad (9)$$

ε_i^j is a temperature-depend parameter, ε_i^j at 1873 K (T_0) as reference, ε_i^j at given temperature can be calculated by:

$$\varepsilon_i^j(T) = \varepsilon_i^j(T_0)\frac{1873}{T} \quad (10)$$

As mentioned in main text, the light elements abundances in metal (Si and S), particularly Si, play important role on the partitioning of In and Cd. Such light element effect is quantified by the interaction parameter between M and Si and/or S, marked as ε_M^{Si} and ε_M^S. The ε values used here (references at 1873 K) are as follows: ε_{In}^S= -0.24 and ε_{Cd}^S=-3.78 (Wood et al., 2014); ε_{In}^{Si}=18.5 (Righter et al., 2017); ε_{Cd}^{Si}=32 (Righter et al., 2018); ε_S^S=-5.80 and ε_{Si}^{Si}=12.74 from the Steelmaking Data Sourcebook (1988). γ_M^0 is the activity coefficient of M infinitely diluted in liquid Fe, $ln\gamma_{Cd}^0$ for Cd = 0.0015 from Lupis, 1983; $ln\gamma_{In}^0$ is assumed to be 0 due to lack of well-constrained value. For Cd, the value of a_{Cd}= -0.63 ± 0.21, taken from Kubik et al., 2021, they further suggested that the partitioning of Cd is independent from *P*-*T*, i.e., *b* and *c* are negligible. The values of *a*, *b* and *c* of In are regressed from light elements (S, Si, C) absence experimental data from literatures (Mann et al., 2009, Wood et al., 2014, Wang et al., 2016 and Righter et al., 2018). The regressed a_{In}= -0.47 ± 1.35, b_{In}= -449 ± 2535, c_{In}= -31.5 ± 43.3 (Fig. 6).

A simple model is used to compare D_{In} and D_{Cd} between metal and silicate. S is suggested to be the minor light element in the Earth's core with concentration close to 2 wt.%, thus in this model, its concentration is set to be 2 wt.% (Xs≈0.03) (Allègre et al., 1995; Suer et al., 2017); Si concentration is 2 wt.% (X_{Si}≈0.035), 5 wt.% (X_{Si}≈0.09) and 10 wt.% (X_{Si}≈0.16), depending on differing estimations for the Earth's core Si concentration (e.g., Siebert et al., 2013; Badro et al., 2015; Rubie et al., 2015). The

oxygen fugacity is assumed to be constant, IW-2.3, which is corresponding to the current mantle FeO content (8 wt.%). The pressure range is from 0 to 55 GPa, the maximum value is corresponding to *ca.* 40% of mantle's depth (e.g., Siebert et al., 2012). The temperature condition is using the equilibration temperature at the base of magma ocean, which can be estimated by arithmetic mean of mantle liquidus estimated by Fiquet et al. (2010) and Andrault et al. (2011):

$$T_i = \frac{1}{2}\left(2022 + 54.21P_i - 0.34P_i^2 + 9.0747 * 10^{-4}P_i^3 + 1940\left(\frac{P_i}{29} + 1\right)^{\frac{1}{1.9}}\right) \quad (11)$$

Substitute the variables above into Eqn. 7, D_{In} and D_{Cd} across the Earth's core-formation processes can be modelled. Their relative siderophility under these given conditions is expressed with D_{In}/D_{Cd}. The variations of D_{In}/D_{Cd} along with *P-T* and Si abundances are shown in Fig.S5. As mentioned in main text, the normalized abundance of In is nearly three times higher than Cd. In this case, if assuming the bulk budget of In and Cd coming from the late added carbonaceous chondritic materials, $D_{In}/D_{Cd} < 1/3$ is required. However, this is not observed in our model. By contrast, the mean value of D_{In}/D_{Cd} is always higher than 1, which suggests In is more siderophile than Cd regardless of *P-T* and Si effect. If considering the model's uncertainties, i.e., grey area in Fig. S5, $D_{In}/D_{Cd} > 1/3$ is also observed across the different core-formation conditions. Therefore, the relative depletion between In and Cd cannot be explained by late added volatile-rich materials only, precursor materials with In/Cd >1 is required as discussed in main text.

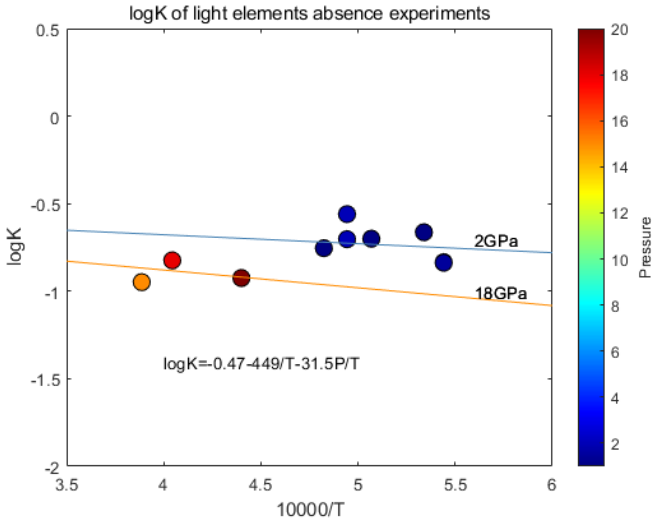

Fig. S4 equilibrium constant (*K*) is plotted as a function of 10000/T. Literature data is taken from Mann et al., 2009, Wood et al., 2014, Wang et al., 2016 and Righter et al., 2018. To avoid the effect of light elements, only S- and Si- free and MgO capsule (avoid C effect from graphite capsule) experimental results are used to regress the parameters.

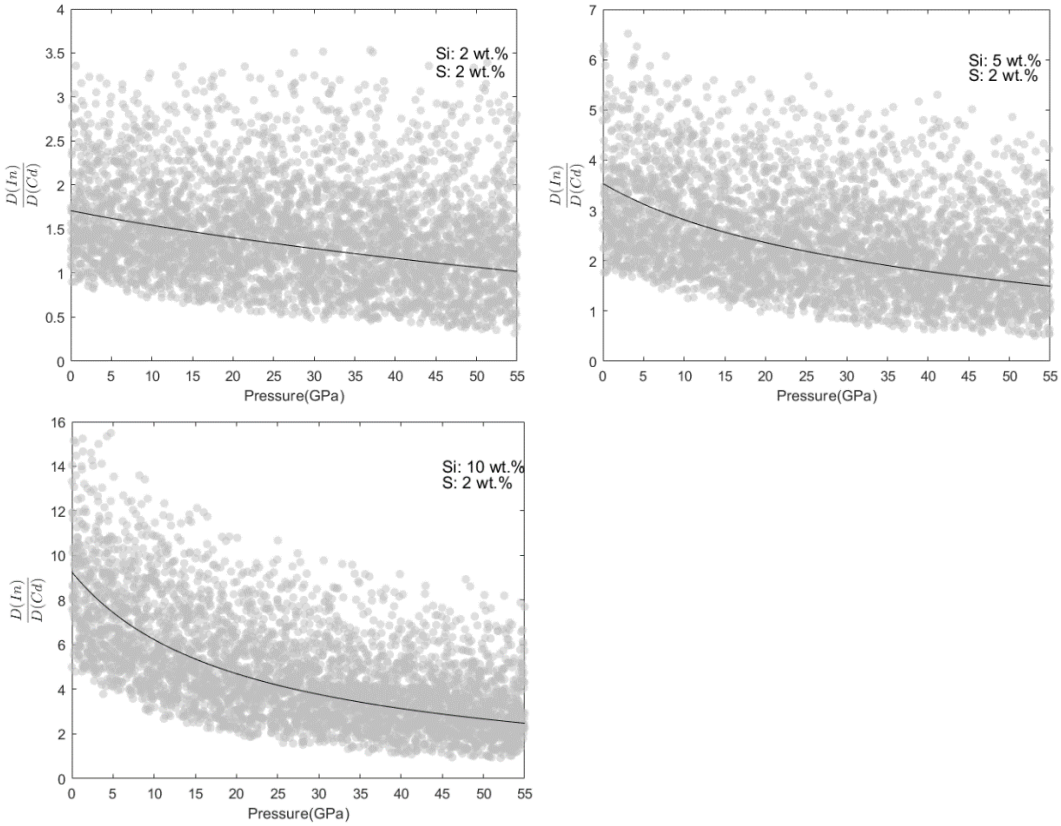

Fig. S5 D_{In}/D_{Cd} is plotted against pressure. The black solid line is the mean value of D(In)/D(Cd) along with pressure and grey area represents its uncertainty given by Monte-Carlo simulation (10,000 times simulations). The S concentration in Earth's core is set as 2 wt.% (e.g., Suer et al., 2017), and variable Si concentration (2 wt.%, 5 wt.% and 10 wt.%) are used in this model, the range are selected based on different estimations (e.g., Siebert et al., 2013; Badro et al., 2015; Rubie et al., 2015).

References

Allègre, C.J., Poirier, J.-P., Humler, E. and Hofmann, A.W. (1995) The chemical composition of the Earth. Earth and Planetary Science Letters 134, 515-526.

Andrault, D., Bolfan-Casanova, N., Nigro, G.L., Bouhifd, M.A., Garbarino, G. and Mezouar, M. (2011) Solidus and liquidus profiles of chondritic mantle: Implication for melting of the Earth across its history. Earth and Planetary Science Letters 304, 251-259.

Badro, J., Brodholt, J.P., Piet, H., Siebert, J. and Ryerson, F.J. (2015) Core formation and core composition from coupled geochemical and geophysical constraints. Proceedings of the National Academy of Sciences 112, 12310-12314.

Dreibus, G., Kruse, H., Spettel, B. and Wänke, H. (1977) The bulk composition of the moon and the eucrite parent body, Lunar and Planetary Science Conference Proceedings, pp. 211-227.

Fiquet, G., Auzende, A., Siebert, J., Corgne, A., Bureau, H., Ozawa, H. and Garbarino, G. (2010) Melting of peridotite to 140 gigapascals. Science 329, 1516-1518.

Hauri, E.H., Saal, A.E., Rutherford, M.J. and Van Orman, J.A. (2015) Water in the Moon's interior: Truth and consequences. Earth and Planetary Science Letters 409, 252-264.

Kubik, E., Siebert, J., Blanchard, I., Agranier, A., Mahan, B. and Moynier, F. (2021) Earth's volatile accretion as told by Cd, Bi, Sb and Tl core–mantle distribution. Geochimica et Cosmochimica Acta 306, 263-280.

Lupis, C.H. (1983) Chemical thermodynamics of materials. Elsevier Science Publishing Co., Inc., 1983, 581.

Mann, U., Frost, D.J. and Rubie, D.C. (2009) Evidence for high-pressure core-mantle differentiation from the metal–silicate partitioning of lithophile and weakly-siderophile elements. Geochimica et Cosmochimica Acta 73, 7360-7386.

Righter, K., Nickodem, K., Pando, K., Danielson, L., Boujibar, A., Righter, M. and Lapen, T. (2017) Distribution of Sb, As, Ge, and In between metal and silicate during accretion and core formation in the Earth. Geochimica et Cosmochimica Acta 198, 1-16.

Righter, K., Pando, K., Marin, N., Ross, D.K., Righter, M., Danielson, L., Lapen, T.J. and Lee, C. (2018) Volatile element signatures in the mantles of Earth, Moon, and Mars: Core formation fingerprints from Bi, Cd, In, and Sn. Meteorit. Planet. Sci. 53, 284-305.

Rubie, D.C., Jacobson, S.A., Morbidelli, A., O'Brien, D.P., Young, E.D., de Vries, J., Nimmo, F., Palme, H. and Frost, D.J. (2015) Accretion and differentiation of the terrestrial planets with implications for the compositions of early-formed Solar System bodies and accretion of water. Icarus 248, 89-108.

Siebert, J., Badro, J., Antonangeli, D. and Ryerson, F.J. (2012) Metal-silicate

partitioning of Ni and Co in a deep magma ocean. Earth and Planetary Science Letters 321, 189-197.

Siebert, J., Badro, J., Antonangeli, D. and Ryerson, F.J. (2013) Terrestrial accretion under oxidizing conditions. Science, 1227923.

Sossi, P.A., Stotz, I.L., Jacobson, S.A., Morbidelli, A. and O'Neill, H.S.C. (2022) Stochastic accretion of the Earth. Nature Astronomy, 1-10.

Steelmaking, J. (1988) Steelmaking data sourcebook. Gordon and Breach Science Publishers, Montreux.

Suer, T.-A., Siebert, J., Remusat, L., Menguy, N. and Fiquet, G. (2017) A sulfur-poor terrestrial core inferred from metal–silicate partitioning experiments. Earth and Planetary Science Letters 469, 84-97.

Wang, Z., Laurenz, V., Petitgirard, S. and Becker, H. (2016) Earth's moderately volatile element composition may not be chondritic: Evidence from In, Cd and Zn. Earth and Planetary Science Letters 435, 136-146.

Wood, B.J., Kiseeva, E.S. and Mirolo, F.J. (2014) Accretion and core formation: The effects of sulfur on metal-silicate partition coefficients. Geochimica Et Cosmochimica Acta 145, 248-267.

Ma, Z. (2001) Thermodynamic description for concentrated metallic solutions using interaction parameters. Metallurgical and Materials Transactions B 32, 87-103.

Chapter 3. The indium isotopic composition of the bulk silicate Earth

Deze Liu[1]*, Frederic Moynier[1], Paolo A. Sossi[1,2], Raphael Pik[3], Sæmundur Ari Halldórsson[4], Edward Inglis[1], Julien Siebert[1,5]

1. Université Paris Cité, Institut de Physique du Globe de Paris, 1 Rue Jussieu, 75005 Paris, France
2. Institute of Geochemistry and Petrology, ETH Zürich, Sonneggstrasse 5, CH-8092 Zürich, Switzerland
3. Centre de Recherches Pétrographiques et Géochimiques, Université de Lorraine, CNRS UMR 7358, 54501 Vandoeuvre, France
4. Nordic Volcanological Center, Institute of Earth Sciences, University of Iceland, Reykjavík, Iceland
5. Institut Universitaire de France, Paris, France.

This chapter is presented as submitted to be peer reviewed by Geochimica et Cosmochimica Acta journal.

Abstract

Indium (In) behaves as a moderately volatile metal during nebular and planetary processes, and its volatility depends strongly on oxygen fugacity. The In isotopic composition of the bulk silicate Earth (BSE) could provide a critical constraint on the nature of Earth's building blocks and its volatile depletion mechanisms. However, accurately and precisely determining the isotopic composition of In of the silicate Earth is challenging due to its low abundance in igneous rocks and the presence of significant isobaric interferences on its isotopes (e.g., $^{113}Cd^{+}$ on $^{113}In^{+}$ and $^{115}Sn^{+}$ on $^{115}In^{+}$). Here, we present a purification procedure for In from rock matrices and report the first dataset of In isotopic compositions of 17 terrestrial igneous rocks measured on a Nu Sapphire collision-cell equipped multi-collector inductively-coupled-plasma mass-spectrometer (CC-MC-ICP-MS) with an external reproducibility of 0.12‰ (2SD). At this level of precision, we find no statistically significant difference in the In isotopic compositions of mid-ocean-ridge basalts (MORBs), oceanic island basalts (OIBs), and continental flood basalts (CFBs). Furthermore, Iceland and Afar magmatic suites display no

analytically resolvable In isotopic variations from basalts to rhyolites. Therefore, In isotope fractionation during igneous processes is smaller than our analytical uncertainty and the In isotopic compositions of basalts are shown to be representative samples of their mantle sources. The ten terrestrial basalts from diverse geological settings have an average δ^{115}In of -0.03 ± 0.18 ‰ (2SD). This value represents the current best estimate of the In isotopic composition of the mantle as well as of the bulk silicate Earth due to the small contribution of the continental crust in the In budget (< 5%), and provides a baseline to compare with chondrites and differentiated planetary bodies in future studies.

1. Introduction

Indium (In) has a 50% condensation temperature (T_c^{50}) of 492 K (Wood et al., 2019), and its nebular volatility lies at the transition between moderately volatile and highly volatile elements. Its CI, -Mg normalized abundance plots above the volatility trend defined by other lithophile volatile elements, indicating that In is overabundant in the Earth's mantle (Palme and O'Neill, 2014). This overabundance has been explained by either i) late accretion of CI-like volatile-rich materials to the Earth; or ii) an over estimation of the In volatility, implying that In would be significantly less volatile during planetary evaporation compared to what is suggested based on its T_c^{50} (Braukmüller et al., 2019; Norris and Wood, 2017; Witt-Eickschen et al., 2009). These mechanisms could result in different In isotopic compositions for the Earth, as planetary evaporation processes can kinetically fractionate In isotopes, leading to a heavy isotope enrichment in residue (*e.g.,* Richter, 2004). Conversely, if late-added CI-like volatile-rich materials have constituted the dominant portion of Earth's In budget, the Earth would have inherited an In isotopic composition similar to that of chondrites. Therefore, the isotopic composition of In could be used to test the origin of the In overabundance in the mantle, and as a tracer for the nature of volatile depletion and the building blocks of the Earth more generally.

Indium is an incompatible element with a higher concentration in the crust (~ 0.05 ppm in the continental crust, and ~ 0.08 ppm in the oceanic crust) than in the mantle (~

0.01 ppm) (Arevalo Jr and McDonough, 2010; Palme and O'Neill, 2014; Rudnick et al., 2003). Although In is a moderately chalcophile element, it is preferentially hosted in silicate minerals such as pyroxene, olivine (in mafic rocks) and biotite, and amphibole (in felsic rocks), rather than sulfide (Wager et al., 1958; Witt-Eickschen et al., 2009). Indium has two naturally occurring isotopes, ^{113}In (~ 4.28 %) and ^{115}In (~ 95.72 %). ^{113}In is a stable isotope, ^{115}In is a radioactive isotope (β-decay to ^{115}Sn) with a very long half-life of 4.41×10^{14} years (Pfeiffer et al., 1979) , and can be approximately considered as a stable isotope.

The In isotopic composition in natural samples is presently poorly constrained, while the effect of igneous differentiation on its isotopic composition remains unstudied. In this study, we have developed the first method capable of determining the In isotopic composition of igneous rock samples to a high precision. We present the In isotopic composition of a widely available geostandards (BHVO-2, BCR-2, and GSP-2) as well rocks from the Afar, and Iceland and Mid-ocean ridge basalts from Atlantic Ocean and Indian Ocean in order to examine the effect of igneous differentiation on In isotopic fractionation and potential spatial heterogeneities in their mantle sources.

2. Samples and methods

2.1 Samples

Seventeen samples were analyzed in this study, including three widely available geostandards that could be used for future inter-laboratory comparison and fourteen samples which are collected from different geological settings. The geostandards include BHVO-2 (basalt, United States Geological Survey, USGS), BCR-2 (basalt, USGS), GSP-2 (granodiorite, USGS). The other samples comprise rocks from two magmatic suites (Hekla/Iceland, and the Afar hotspot in East Africa) and three mid-ocean ridge basalts (MORB), from Atlantic and Indian Oceans. Afar (Ethiopia, East Africa) is located at the triple junction between main Ethiopian rift, the Gulf of Aden and the Red Sea, and is known for a series of volcanoes, which is thought to have formed by melting of a mantle plume beneath the Afar region (Barberi et al., 1980; Field et al., 2008; Pik et al., 1999; Pik et al., 2006). The eruption products of the Afar

rift volcanoes cover a range from basalt to rhyolite. Five Afar samples are analyzed in this study, including two basalts (AF12-01, AF13-46), one trachyandesite (Boha) and two rhyolites (AF-15-10, AF-12-15), collected from the groups of Stratoid Series, Gulfs Acide and Manda Hararo/ Dabahu, with a MgO range of ~ 0.1 to 5.3 wt.%. Most of these samples are Quaternary volcanic rocks except AF-12-15 (late Miocene-Pliocene), and the isotopes of Sr - Nd - Pb and Zr/Nb ratio of the corresponding geographic groups indicate that Quaternary volcanic rocks in Afar region have a common source and are not contaminated by crustal assimilation (Ayalew et al., 2019). The rhyolites in this region are thought to be formed by fractional crystallization of basaltic magma (Ayalew et al., 2002; Ayalew et al., 2019). Therefore, Afar hotspot rocks are well suited for studying the elemental and isotopic behaviors during fractional crystallization (Field et al., 2008). The Icelandic samples also span a wide chemical range, from basalt to rhyolite, permitting examination of the potential effect of magma differentiation on isotopic fractionation. Moreover, some Icelandic rocks with high $^{3}He/^{4}He$ ratio are suggested to represent magmas least affected by crustal assimilation (Craig and Lupton, 1976; Harðardóttir et al., 2018). Six Icelandic samples are analyzed, including three basalts (MID-1, A24, B-ALK), one obsidian rhyolitic glasses (A-THO), one andesite (I-ICE) and one dacite (I-DAC). These samples were collected from the currently active on-land rift zones (Northern and Eastern Rift Zones) and active volcanic zone (The South Iceland volcanic zone, propagation rift). Their MgO concentrations (~0.1 to 10 wt.%) cover the typical geochemical variability shown in Icelandic magma series (Ranta et al., 2022). The MORB samples analyzed in this study were collected from Atlantic (EW9309-3D-19, ARP74 column) and Indian Oceans (MD57-D13) and were selected to study the In isotopic composition of the upper mantle. The detailed information of the samples is reported in Table S1, Table S2 and Figure S1.

2.2 Sample dissolution and chemical purification

All samples were ground to fine powders with an agate mortar, and then 200 ~ 250 mg of sample powders (containing 5 ~ 35 ng of In) were dissolved in mixed acids by 2 mL of HNO_3 (16 mol/L) and 6 ml of HF (28 mol/L) in Savillex® standard PFA Teflon

vials. The Teflon vials were closed and heated on a hotplate at 130 ℃ for 48 hours, then evaporated to dryness at 100 ℃ and re-dissolved in 8 mL of aqua regia at 130℃ for 24 hours to break down the potential insoluble fluorides. The samples were dried down again at 100 ℃ and then re-dissolved in 6 ml of 6 mol/L HCl to prevent formation of insoluble residues and dried down.

Approximately 0.4 mL of pre-cleaned (3 ml 0.5 mol/L HNO_3 and 3 ml Mili-Q water, repeat three times) and pre-conditioned (3 ml 1.5 mol/L HBr) anion exchange resin AG 1X8 (200-400 mesh) were loaded on homemade heat-shrink Teflon columns (size: length 1.5 cm; diameter: 0.5 cm), then the dried samples were re-dissolved in 3 mL of 1.5 mol/L HBr and loaded on the resin. Under these conditions, the major matrix elements (Ca, Mg, Fe, Al) pass through the columns directly and are separated from In, which remains bound to the anion exchange sites of the resin. Then 12 mL of 0.1 mol/L HBr were used to further separate In from Cd, and In was eluted and collected during this step. Additionally, Cd can be collected by adding 12 mL 0.1 mol/L HNO_3 at the end of this step. To further remove matrix elements from In, the collected In aliquots were dried down and re-dissolved with 0.5 mL 1.5 mol/L HBr, and then loaded on the same resin and columns. Following this, 2.5 mL 1.5 mol/L HBr was added to remove matrix elements, and then the In-collection step with 12mL of 0.1 mol/L HBr was repeated. This procedure was repeated four times to ensure matrix elements were removed nearly complete and achieve the concentration ratio M/In < 3, where M refers to the typical matrix elements (e.g., Mg, Ca, Fe, Al, Na and K), which cannot result in resolvable deviation for isotopic composition analysis (see section 3.5.2). An elution curve diagram is provided in supplementary materials (Figure S2).

A third column chromatography procedure is used to further separate Sn from In. To do so, the same columns and resin volume and type as described above were used. The collected In aliquots were evaporated to dryness, re-dissolved in 1 mL of 0.1 mol/L HF and then loaded on pre-cleaned and pre-conditioned resins. Six mL of 0.1 mol/L HF are used to collect In. This step was repeated twice to achieve In/Sn > 100. The recovered percentage of In relative to the amount loaded over the whole procedure was always >

92%.

Isotopic measurement on Sapphire

The In isotopic composition measurements were performed with a Nu Sapphire CC-MC-ICP-MS (collision-cell multi-collectors inductively-coupled-plasma mass-spectrometer) at the Institut de Physique du Globe de Paris (IPGP). Instrumental mass bias was corrected using a standard-sample-bracketing (SSB) method. An In standard solution (Sigma-Aldrich, Lot number: BCBS0171V, named IPGP-In standard hereafter) was used as the bracketing standard. Both samples and standard solution were dissolved in 0.5 mol/L HNO_3 and further diluted to 3 ppb.

Samples were introduced into the plasma source via an APEX Omega desolvating system combined with a 100 μL/min PFA nebulizer (MicroFlow nebulizer, Elemental Scientific, Omaha, NE, USA) and a standard Ni dry cone ('dry plasma'). A 0.5 mol/L HNO_3 solution was measured at the beginning of each sequence and interspersed several times during the sequence and applied as a blank correction. The 3 ppb solutions used for analysis yielded an intensity of ^{115}In between 3 and 5 V in low resolution mode. The variations of intensity were likely induced by variations of nebulizer uptake rate and/or aging of cones. Faraday cups equipped with $10^{11}\Omega$ resistors were used to monitor ^{110}Cd, ^{111}Cd, ^{112}Cd, ^{113}In, ^{115}In, ^{117}Sn, ^{118}Sn and ^{119}Sn. Each analysis contains a block of 40 cycles with 5 s integration time, followed by a 120 s wash procedure performed in 0.5 mol/L HNO_3. Peak centering was done before each analysis.

3. Results

In this study, the isotopic compositions of samples are reported as δ^{115}In, which is expressed as below:

$$\delta^{115}In\ (‰) = \left[\frac{(^{115}In/^{113}In)_{sample}}{(^{115}In/^{113}In)_{IPGP-In}} - 1\right] \times 1000$$

The In isotopic composition of samples are reported in Tables S1 and S2. Their errors are reported as the two standard-deviation (2SD) of replicate measurements. For

samples that were measured only once due to the very low amount of In, their errors are reported with the largest 2SD of the other samples/standards that were analyzed in the same batch.

3.1 Reproducibility and accuracy of the method

Three geostandards, BHVO-2, BCR-2 and GSP-2 were fully processed (including digestion) multiple times to evaluate the external reproducibility for the whole procedure. A total of nine BHVO-2, five BCR-2 and three GSP-2 were processed for the test, and exhibit consistent results. The obtained average value of nine BHVO-2 is -0.03 ± 0.12‰, five BCR-2 is -0.05 ± 0.11‰, three GSP-2 is + 0.01 ± 0.11‰ (2SD). The largest error is 0.12‰ (for the nine external replicates of BHVO-2) and therefore used as our value for the external reproducibility. Furthermore, a BHVO-2 and a BCR-2 were used to further determine the potential isotopic fractionation during column chromatography by passing them one more time through the full column procedure, and their isotopic data are indistinguishable compared with the same solution that did not go through the additional column purification (results are shown in Table S2). Therefore, both the replicates for the same geostandard and additional column processes support an accuracy and reproducibility for the total procedure of ~0.12‰ (2SD). Additionally, another In standard solution (Plasma-Cal) was used to estimate the intermedia precision for the analyses results from different sessions across nearly one-year, giving the In isotopic composition of 0.15 ± 0.09‰ (2SD), which is close to the external reproducibility.

Since the isotopic compositions of these geostandards are not known *a priori*, another chemical purification was also performed for an IPGP In-standard solution to further confirm the absence of isotopic fractionation occurred during column chromatography, and assess the accuracy of the method. The IPGP In-standard was processed following the same dissolution procedure as for the samples, and then performed twice HBr- and once HF- column chemistry on it and saved the aliquot after each step. The δ^{115}In values for the solutions after first and second HBr-column and HF-column are 0.00 ± 0.05‰

(n=4, 2SD), 0.03 ± 0.06‰ (n=4, 2SD), 0.01 ± 0.02‰ (n=4, 2SD), respectively, indicating there is no isotopic fractionation occurring on the columns. The results are listed in Table S2.

3.2 Effects of In concentration

A test of the effect of In concentration on accuracy and precision was performed with pure IPGP-In standard. The concentration of In standards of 1 ppb, 2 ppb, 3 ppb, 5 ppb, and 10 ppb (intensity of ^{115}In from ~ 1 to 15V), were analyzed. As shown in Figure. 1, although the results of different concentration solutions give consistent accuracy, their precision vary significantly with concentration: 1 ppb: δ^{115}In = 0.00 ± 0.29‰ (n = 16), 2 ppb: δ^{115}In = -0.01 ± 0.15‰ (n = 8), 3 ppb: δ^{115}In = -0.01 ± 0.07‰ (n = 8), 5 ppb: δ^{115}In = 0.00 ± 0.03‰ (n = 8), 10 ppb: δ^{115}In = 0.00 ± 0.02‰ (10 ppb, n = 8). Herein, the solution at 3 ppb provides an acceptable compromise between precision and amount of sample needed for measurement so that low In samples could be analyzed. Therefore, the samples in this study are all analyzed with a 3 ppb solution.

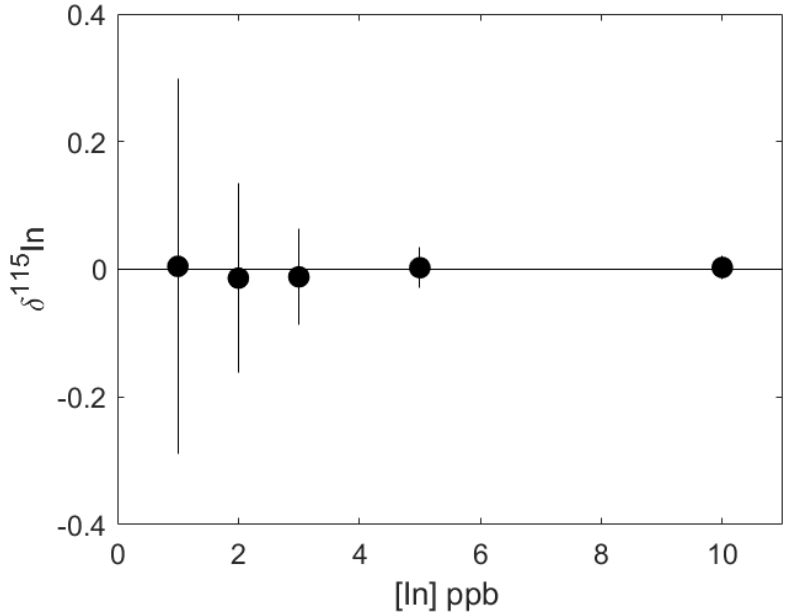

Figure. 1. δ^{115}In is plotted as a function of In concentration for pure IPGP-In standard. The tested In standard concentration varies from 1 ppb to 10 ppb. The accuracy of all concentration tests are consistent, while precision of 1 ppb and 2 ppb runs is significantly low.

3.3 Effect of concentration mismatch between standard and sample

The effect of a concentration mismatch on the precision and accuracy of the isotopic measurements was tested by using a 3 ppb IPGP In standard as the bracketing standard, and a series of IPGP standards of varying concentration measured as samples. The samples' concentration varies from ~ 50 % to 160 % relative to the bracketing standard. The variations of δ^{115}In values obtained with this range of concentration are insignificant within the uncertainty except the most extreme case where the samples were analyzed at 1.8 ppb (52 % relative to the bracketing standard) (Figure 2). Although the mismatch does not result in significant shift on measured values, the samples are analyzed with concentrations within 10 % that of the standard to minimize this effect.

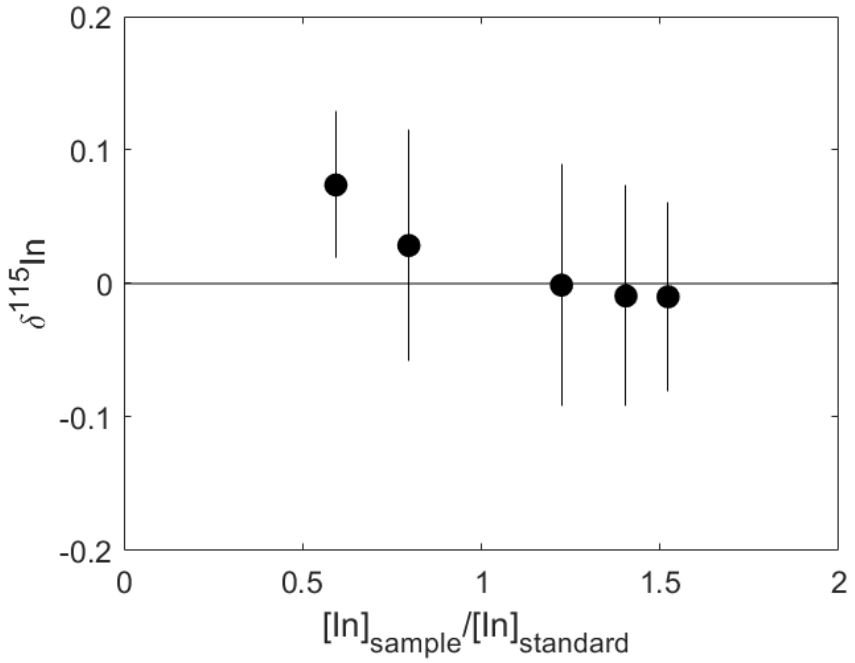

Figure. 2. The effect of concentration mismatch between sample and standard on δ^{115}In. Both sample and bracketing standard are IPGP-In standard solutions, and bracketing standard is diluted to 3 ppb. The x-axis is the ratio of In concentration of sample and bracketing standard.

3.4 Effect of the mismatch between the nitric concentration

A mismatch between the HNO_3 concentration of the standard and the samples can

have an effect on mass bias and affect the measured isotope ratio (e.g., Moynier et al., 2021 for K isotopes). To test this effect, we used the IPGP-In standard run at 3 ppb with a solution dissolved in 3% (v/v) HNO_3, and a series of solutions dissolved in variable HNO_3 concentration (1%, 2%, 4%, and 5%). The results show a linear correlation between $\delta^{115}In$ and HNO_3 concentration ($R^2 = 0.96$), with variations from -0.05 ± 0.08‰ (n = 6, 1% HNO_3) to 0.07 ± 0.16‰ (n = 6, 5% HNO_3) (Figure. 3). Therefore, in the following, all samples and standards were dissolved in 3% HNO_3 from the same bottle during each session.

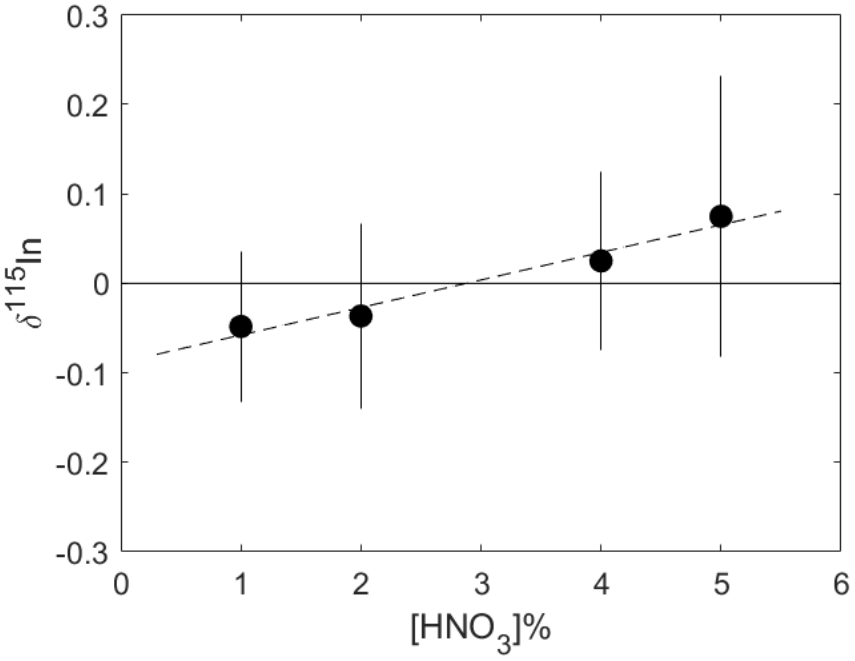

Figure. 3. The effect of HNO_3 concentration mismatch. Both tested samples and bracketing standard are 3 ppb IPGP-In standard solutions. HNO_3 concentrations for samples vary from 1% to 5%, and bracketing standard is in 3% HNO_3.

3.5 Isobaric interferences and matrix effect

3.5.1 Cd and Sn isobaric interferences

The isotopes ^{113}In and ^{115}In have isobaric interferences from ^{113}Cd and ^{115}Sn, respectively. Although Cd and Sn can be removed near completely with our purification protocol (In/Cd and In/Sn ratios always lower than 0.0003 and 0.15 respectively),

isotopes of Cd, particularly ^{113}Cd (12.22 %), may potentially affect the measured ratio due to the low abundance of ^{113}In (4.28 %). To correct for the interferences, the intensities of ^{110}Cd, ^{111}Cd, ^{112}Cd, ^{117}Sn, ^{118}Sn and ^{119}Sn were monitored during each analysis. However, the ratios of ^{110}Cd/^{111}Cd, ^{112}Cd/^{111}Cd are observed to vary between samples and sessions from < 10 to more than 100, which deviates from the natural ratios (~ 0.97 and 1.88, respectively). This suggests potential isobaric interferences on the measured intensity of ^{112}Cd and ^{110}Cd, likely ^{110}Pd, ^{112}Sn and/or other poly-atomic interferences, due to the very low abundance of Cd in the In fractions. Therefore, ^{111}Cd is used to calculate the interference due to its lack of isobaric interferences from nearby isotopes. The abundance of ^{113}Cd is then calculated using the natural abundances of ^{111}Cd and ^{113}Cd.

The correction of interference of ^{115}Sn was made by assuming the instrumental fractionation of isotopes following an exponential law:

$$R_T = R_M \times (m_1/m_2)^{\beta} \quad (1)$$

where R_T and R_M refer to the true and measured isotope ratios, m_1 and m_2 are the masses of measured isotopes, and β refers to the fractionation factor. Hence, the above equation can be written as below:

$$^{115}Sn_M = {}^{118}Sn_M \times \left(\frac{^{115}Sn}{^{118}Sn}\right)_T / \left(\frac{114.90}{117.90}\right)^{\beta} \quad (2)$$

The fractionation factor β between ^{115}Sn and ^{118}Sn is assumed to approximately equal to β between ^{117}Sn and ^{118}Sn during a session, and can be calculated by the equation below:

$$\beta = \frac{\ln\left(\frac{(^{118}Sn/^{117}Sn)_T}{(^{118}Sn/^{117}Sn)_M}\right)}{\ln(117.9/116.9)} \quad (3)$$

Then the corrections of ^{113}In and ^{115}In are made by subtracting the intensity of ^{113}Cd and ^{115}Sn from monitored mass on 113 and 115. The δ^{115}In values before and after correction are shown in Table S6. As the Sn/In ratio of the sample increases, it returns an isotopically heavy composition due to contribution on mass 115 from ^{115}Sn. Applying the ^{115}Sn interference correction method above, the δ^{115}In values of samples

can be corrected to be near-zero within the Sn/In range from 0.003 ($\delta^{115}In_{measured}$ = 0.01 ± 0.11‰ and $\delta^{115}In_{corrected}$ =-0.01 ± 0.10‰) to 0.33 ($\delta^{115}In_{measured}$ = 0.99 ± 0.05‰ and $\delta^{115}In_{corrected}$ = 0.03 ± 0.11‰), indicative of a robust correction method (Figure. 4). Furthermore, our purification protocol can effectively remove Sn, generally yielding Sn/In < 0.15, suggesting that Sn interferences can be well corrected by our chemical protocol and correction method. By contrast, the isobaric interference of ^{113}Cd can result in considerable deviation of $\delta^{115}In$ from its true value due to the relatively low abundance of ^{113}In (4.28 %). Indeed, even a small fraction of Cd (2.5 ppt of Cd, i.e., Cd/In = 0.0008) can cause an apparent deviation ($\delta^{115}In$ = -1.54 ± 0.06‰ before correction). Among the three Cd doping tests, only 0.25 ppt and 2.5 ppt Cd doping samples can be corrected to be near-zero ($\delta^{115}In_{corrected}$ = 0.05 ± 0.10‰, 0.25 ppt; $\delta^{115}In_{corrected}$ = 0.01 ± 0.06‰, 2.5 ppt; Figure. 4 and Table S6). While, for higher Cd doping sample (25 ppt Cd, Cd/In=0.008), the artificial deviation of $\delta^{115}In$ cannot be completely corrected (-0.37 ± 0.19‰, Figure. 4) that may be caused by the measured uncertainty of ^{111}Cd and/or instrumental mass bias. Therefore, we consider this Cd/In ratio of 0.0008 (2.5 ppt Cd doping test) to be the upper limit for effectively applying Cd interference correction method. After chemical purification, the Cd/In is typically lower than 0.0003 ensuring an adequate correction of the isobaric interference of ^{113}Cd in ^{113}In.

3.5.2 Effect of major elements

For the measurement of In isotopes, the instrumental mass bias on bracketed standards is assumed to be equal to that on bracketed samples. However, matrix effect from major elements may also affect the measurement of isotopic composition (e.g., Archer and Vance, 2004; Chaussidon et al., 2017; Mason et al., 2004). These matrix effects could be brought about by different phenomena, for example, space-charge effects displacing the In ions from the axis of the plasma, the production of spectral interferences through poly-atomic molecules to create isobaric interferences, or these elements can affect the ionization efficiency of the plasma and result in a non-linear

shift on the instrumental mass bias (e.g., Pietruszka and Reznik, 2008). For example, the effect of major elements on the isotopic measurements on the Nu Sapphire have

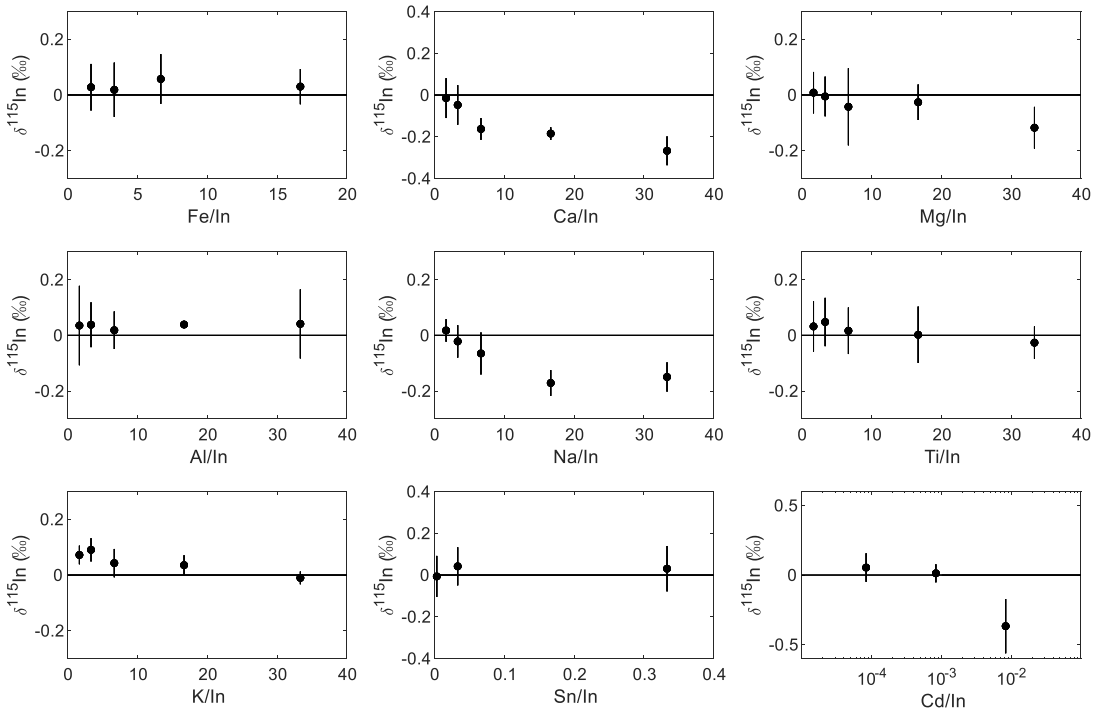

Figure. 4. Tests for matrix effect (Fe, Ca, Mg, Al, Na, Ti and K) and isobaric interferences (Sn and Cd). The plots of isobaric interferences shows the isotopic results after performing the Sn/Cd correction. The x-axis represents the concentration ratio of matrix element and In. Ca and Na are oberserved to have influences on the measurement of In isotopes, while other matrix elements do not have resolvable effect on the measured In isotopic data within the current precision and doping concentration. Isobaric interferences from Sn and Cd can vary the measured results significantly, the measured results before corretion are given in Table. S-7. Sn interference can be well corrected with out correction method due to higher abundance of ^{115}In. However, Cd correction only effectively when Cd concentration is Cd/In is less than 0.001. Therefore, samples with higher Cd amount require a further Cd purification step.

been previously demonstrated on K and Ca for possibly isobaric interferences, e.g., $^{23}Na^{16}O^{+}$, $^{40}CaH^{+}$ and $^{39}KH^{+}$) (Dai et al., 2022; Moynier et al., 2021). To determine the potential matrix effect from major elements on In isotopes measurement, a series of doping tests, including Fe, Ca, Al, Mg, Na, K, and Ti with variable concentrations

(between ~ 150 % and 3500 % relative to a 3 ppb IPGP-In standard) were performed.

The results of doping tests of multi elements are shown in Table S7. Most matrix elements are not found to strongly affect the isotope ratio measurement within the doping range, with the exception of Na and Ca. The presence of both Na and Ca in the In solution result in isotopically light In isotopic compositions for Na/In and Ca/In ratios above 6 (Figure 4). Although the cause for the effect of Ca and Na is presently unknown, possible isobaric interferences of poly-atomic molecules on the mass 113 such as $^{40}Ca_2{}^{16}O_2{}^{1}H^+$, which has been observed as a spectral interference on the measurement of ^{113}Cd (May and Wiedmeyer, 1998), are likely. In any case, the chemical purification protocol effectively removes these matrix elements from In (Ca/In and Na/In always <3), and these elemental ratios are tested after chemical purification and additional pass through the column chemistry would be repeated if needed.

3.6 Natural samples

The In concentration and isotopic composition of natural samples are reported in Table S1 and Table S2. The In concentration of natural samples in this study spread from 59 ppb (A24, basalt) to 208 ppb (A-THO, rhyolite), exhibiting a negative correlation with MgO (wt.%), which is consistent with the moderately incompatibility of In during igneous differentiation as observed in previous studies (e.g., Yi et al., 2000) (Figure. 5). Three MORB's In concentration varies from 66 to 170 ppb, falling in the range of oceanic floor basaltic glasses reported by Jenner and O'Neill (2012). Three Icelandic basalts are observed to be with In concentration from 59 to 124 ppb, which are similar as Yi et al (2000) reported OIB In concentration (~ 70 to 95 ppb).

The δ^{115}In values of three geostandards, BHVO-2, BCR-2 and GSP-2 are -0.03 ± 0.12‰ (n = 9), -0.05 ± 0.11‰ (n = 5), and 0.01 ± 0.11‰ (n=3), respectively. Three MORB samples yield similar isotopic compositions: 0.07 ± 0.04‰ (MD57-D13, n=8), 0.03 ± 0.14‰ (EW9309-3D-19), and -0.01 ± 0.11‰ (APR74 column, n=14), which are indistinguishable from our analytical precision. More isotopic variability is observed for Afar and Iceland samples, but with no clear correlation with rock types and

concentration of In. For Afar samples, AF-12-01 (δ^{115}In = -0.12 ± 0.11‰, n= 5, 127ppb of In, basalt) is isotopically similar to AF-15-10 (δ^{115}In = -0.17 ± 0.17‰, n= 9, 170 ppb of In, rhyolite). Most Afar samples have the δ^{115}In values from -0.02 to -0.17, which are not resolvable within our analytical uncertainty. The In isotopic composition of the analyzed Icelandic samples, including basalts (-0.16 ± 0.11‰ to +0.13 ± 0.11‰), andesite (-0.09 ± 0.13‰,), dacite (-0.04 ± 0.11‰) and rhyolite (+ 0.03 ± 0.08‰) do not exhibit significant isotopic variations along with rock types either.

4. Discussion

4.1 Limited In isotopic fractionation during fractional crystallization

The Afar volcanic rocks were collected from the geographic groups of the Stratoid Series, Gulf and Manda Hararo and formed during the Quaternary (AF15-10, AF12-01, AF13-46, Boha) and late Miocene-Pliocene (AF12-15) (Ayalew et al., 2019; Field et al., 2008). The δ^{115}In values of the Afar samples do not exhibit systematic variations related to differentiation indices such as MgO (Figure 5a) nor with indium content (Figure. 5b). This is also confirmed by the Icelandic samples which also cover a range from basalts to rhyolites and for which δ^{115}In does not vary with MgO nor In content. Therefore, igneous differentiation does not exert a major effect on In isotopes within our analytical resolution.

This insignificant isotopic fractionation could be explained by the limited variations of bond strength of In among different phases during fractional crystallization, in addition to its moderately incompatible behavior. Equilibrium isotope fractionation is controlled by the differences of zero-point energies of molecules between different isotopes (e.g., Urey, 1947). Zero-point energy is related to the bond strength, which is generally correlated with the coordination number and valence of an ion (Sossi and O'Neill, 2017; Young et al., 2015), which will be discussed below. Whether this fractionation is expressed in magmas differentiated along their liquid line of descent in a closed system depends upon the fraction of In remaining in the melt, f_{In}, which can be

approximated as a Rayleigh process. Thus, should the In remain in moderate concentration in the melt, f_{In} remains high, and the isotopic composition of the melt evolves little.

The oxidation state of In is suggested to be trivalent (In^{3+}) in Earth's mantle (Witt-Eickschen and O'Neill, 2005), and metal-silicate partition experiments that carried out under more reducing conditions ΔIW-3, where IW is the iron-wüstite buffer (Righter et al., 2018b) further confirms that In remains as In^{3+} . This implies that the oxidation state of In is unchanged during igneous processes on Earth, during which the fO_2 is rarely below the IW buffer. Indium rarely forms discrete mineral phases. Instead, and despite its close chemical association with Ga^{3+} and Y^{3+} (Yi et al., 2000), its host minerals are thought to be ferromagnesian silicates, including garnet, pyroxene and olivine in mafic systems, biotite and amphibole in felsic systems (Gion et al., 2018; Van Westrenen et al., 1999; Wager et al., 1958; Witt-Eickschen et al., 2009). The ionic radius of VI-coordinated In^{3+} is 0.8 Å, which is similar to VI-coordinated Fe^{2+} (0.78 Å), and therefore In^{3+} is thought to enter these ferromagnesian phases (*e.g.,* by substituting for Fe^{2+} in the M1 site of clinopyroxene) (Gion et al., 2018; Schroll et al., 1999; Shannon, 1976; Witt-Eickschen et al., 2009), even if this requires a charge compensator (*e.g.,* Na^{+}). Although In is a chalcophile element, and can be concentrated in some ore deposit sulfide minerals such as sphalerite, stannite (Gion et al., 2018; Schwarz-Schampera and Herzig, 2002; Shannon, 1976), its contents in accessory sulfides are observed to be significantly lower than the above ferromagnesian minerals in mantle xenoliths and felsic magmatic systems, suggesting sulfides not being the major carriers (Gion et al., 2018; Witt-Eickschen et al., 2009). Additionally, the low In concentration in oxides (e.g., magnetite and ilmenite) also indicates negligible influence of oxides during magmatic crystallization (e.g., Gion et al., 2018).

The two pyroxenes together host ~80 % of the In budget in fertile mantle peridotites (Witt-Eickschen et al. 2009). The bulk partition coefficient for In during mantle melting is roughly 0.2 to 0.3, based on assessment of In contents of oceanic basalts (Yi et al. 2000) and mantle peridotites (Witt-Eickschen et al. 2009). The In contents of basalts

reported herein span a limited range (a factor 3 from basalt to rhyolite; Fig. 5), indicative of mildly incompatible behavior, though sample AF-12-15, a rhyolite, has a significantly lower In content (88 ppb) than basaltic samples from the same series (AF-12-01 and AF-13-46), 127 ppb and 207 ppb, respectively.

The structural and electronic environment of In in silicate glasses has not been well characterized. However, the lower-*Z* Group XIII elements, Al and Ga, tend to exist in IV-fold co-ordination at ambient pressure (Cormier et al., 2007; Mare et al., 2021; Mysen and Richet, 2018), though Ga shows a transition to 50% VI-fold coordination by 10 GPa (Mare et al. 2021). Owing to the systematic increase in cationic radius down the group, it is likely that at least some In is in VI-fold coordination, even at ambient pressure. Therefore, the insignificant In isotopic fractionation among our basalt-rhyolite sample set, likely arises from *i)* its mildly incompatible behavior, *ii)* constant oxidation state and *iii)* possibly limited variations of coordination number during fractional crystallization of basaltic magma, but this last point remains to be tested.

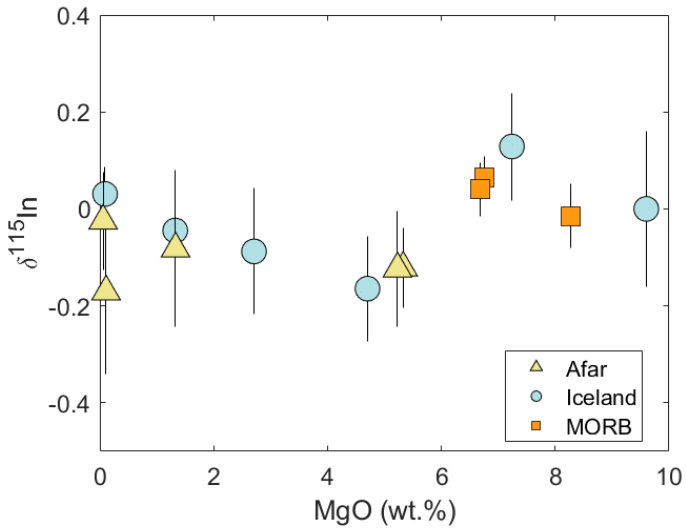

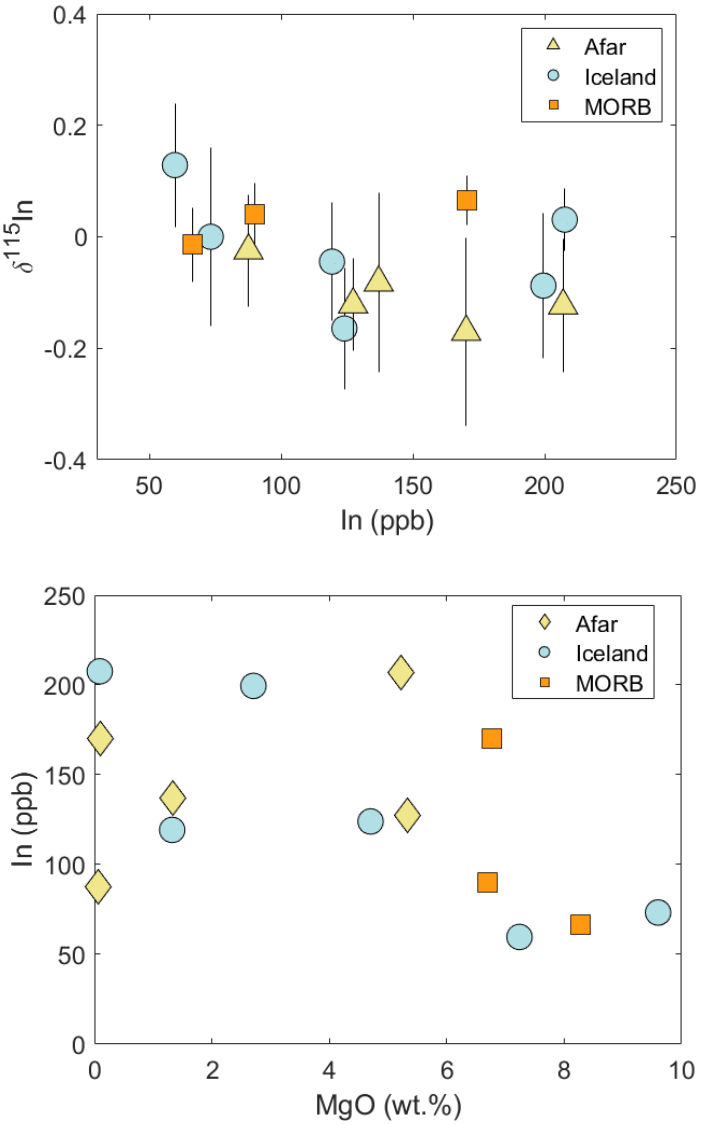

Figure. 5 In isotopic composition, In concentration and MgO concentration in Iceland, Afar and MORB samples. a) In isotopic composition plotted against MgO concentration. There is no clear correlation between In isotopic composition and MgO concentration observed. b) In isotopic composition plotted against In concentration. There is no significant correlation of In isotopic composition and concentration observed within the current precision. c) In concentration plotted against MgO concentration. In concentration can be observed to decrease with the increasing MgO concentration, supporting In as a moderately incompatible element during igneous differentiation.

4.2 Implications for the In isotopic composition in the mantle

As already discussed in section 4.1, the isotopic fractionation of In is not resolvable during fractional crystallization process within the analytical precision. Moreover, the potential isotopic fractionation during mantle's partial melting is also thought to be minor as well due to the same oxidation state of In and potential limited variations of coordination numbers between melt and major host phases in peridotites (i.e., VI-fold in pyroxene and olivine, Witt-Eickschen et al. (2009)). Therefore, magmatic differentiation process is considered not to fractionate In isotopes significantly, and the In isotopic composition in mantle-derived mafic and ultramafic rocks can be used as representative of mantle's composition. Given mantle metasomatism and/or interaction between melt and peridotite are ubiquitous in the mantle, which may alter the primitive isotopic compositions of incompatible elements in peridotites (e.g., Ionov and Wang, 2021) and the difficulties of analysis on peridotite for its low In content (~5 to 18 ppb, Witt-Eickschen et al. (2009)), basalts from different settings and with various partial melting degrees are used to provide clues as to the In isotopic composition of the mantle.

We analyzed ten basalts from different geological settings, including Ocean Island Basalts (Icelandic basalts and BHVO-2), Continental flood basalts (Afar basalts and BCR-2) and MORB from Atlantic and Indian Ocean. These basalts, show similar In isotopic composition within the limit of the 2SD uncertainties, with an average δ^{115}In = -0.03 ± 0.19 ‰, 2SD, which is our best estimate for the Earth's mantle In isotopic composition (Figure. 6). This clustering of samples from different magmatic settings and localities, suggest a relatively homogenous In isotopic composition in the mantle and/or limited influences from assimilation of crustal materials due to lack of isotopic fractionation during fractional crystallization. Furthermore, In has a concentration of ~0.05 ppm in continental crust (Rudnick et al., 2003), ~0.06 ppm in primitive MORB (approximately representing oceanic crust) (Jenner and O'Neill, 2012) and has ~ 0.017 ppm in mantle (Witt-Eickschen et al. 2009), meaning the proportion of In residing in the crust is < 5% that of its bulk budget in silicate Earth. Therefore, the In isotopic composition of the mantle is an excellent proxy for the composition for bulk silicate

Earth (BSE). Additionally, the limited In isotopic fractionation during magmatic processes implies that crustal extra-terrestrial samples could be used to estimate the isotopic composition of the mantle of the parent body.

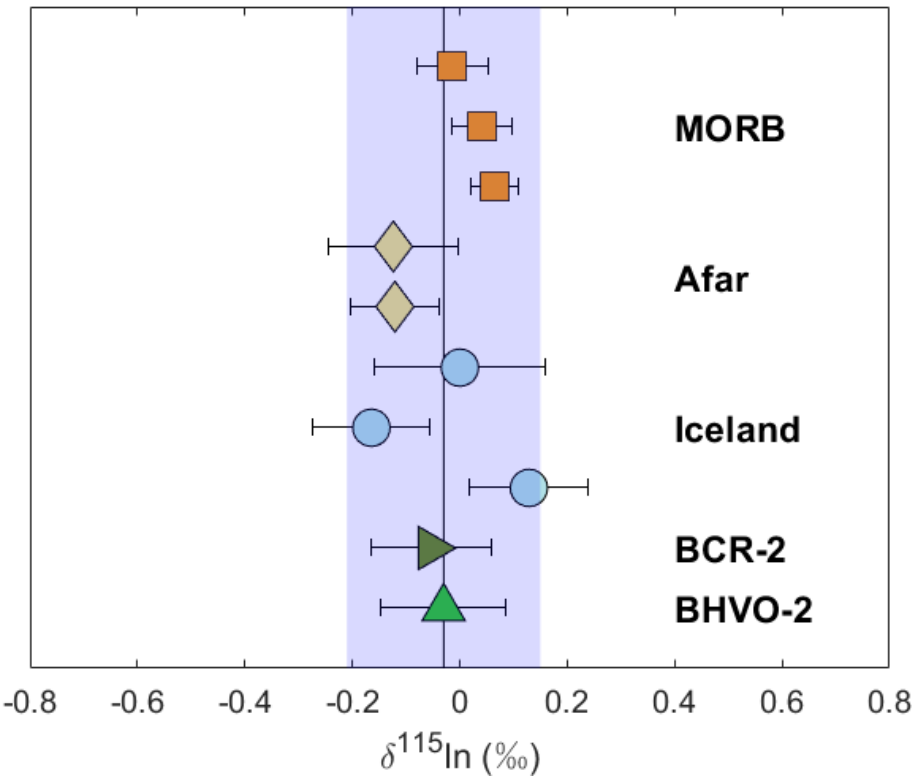

Figure. 6 The Indium isotopic composition of basalts. The black solid line represents the average value of δ^{115}In of these basalts, and light blue shaded area shows the 2SD range of average value based on the available data.

4.3 Implications for the In overabundance in BSE

Relative to the volatility trend defined by the abundances of the moderately lithophile volatile elements in the BSE as a function of their nebular T_c^{50}, In falls off this trend. Given its estimated volatility under solar nebula conditions (Lodders, 2003; Wood et al. 2019), In is apparently overabundant in the BSE. Moreover, the change in volatility of In relative to other moderately volatile elements between nebular and post-nebular environments means its abundance can be used to discriminate between nebular- and post-nebular scenarios for the volatile depletion history of the Earth (Braukmüller et al.,

2019; Norris and Wood, 2017; Righter et al., 2017; Witt-Eickschen et al., 2009). Elemental volatility is a function of the physical-chemical conditions (*P-T-fO₂*) under which gas-condensed phase equilibrium occurs (Sossi et al., 2019). As opposed to a nebular environment, in which In is thought to condense into FeS as InS (Lodders, 2003; Wood et al. 2019), it is forced to evaporate/condense into silicate melts in a planetary, post-nebular environment at higher fO_2, fundamentally changing its volatility relative to elements that condense into silicates in the solar nebula (*e.g.,* the alkalis, Zn and Cd). Such behavior led Norris and Wood (2017) to propose that volatile loss occurred on precursor materials of the Earth by evaporation of silicate material (*e.g.,* planetesimals). Alternatively, the In budget of the Earth may have been delivered by late-added CI-like volatile-rich materials with 10 ~ 20 wt.% of the Earth's mass (Braukmüller et al., 2019), noting that the resulting hockey-stick pattern implies no overabundance of In, but significant core sequestration of other moderately volatile elements, notably Cd and Sn. Whether the In overabundance in the BSE is originated from evaporation on precursor materials or late additions from CI-like materials, or both, their signatures can be recorded by the isotopic composition of In. The possible In isotopic composition of the Earth and chondrites of corresponding models are shown in the Figure 7 and further discussed below.

Evaporation processes can result in the enrichment of the heavy isotope in the residue, via kinetic isotopic fractionation, with the magnitude of this effect being sensitive to the dynamical environment under which evaporation occurs (Richter, 2004; Sossi et al., 2020; Young et al., 2019). Therefore, if partial evaporation occurred on the precursor materials of the Earth and/or the proto-Earth, the isotopic composition of the Earth may be heavier than those of chondrites, as suggested for Mg (Hin et al., 2017), Si isotopes (Moynier et al., 2020; Pringle et al., 2014). However, these heavier isotopic compositions are not observed in the moderately volatile elements like K, Rb and Zn (Luck et al., 2005; Pringle and Moynier, 2017; Pringle et al., 2017; Sossi et al., 2018b; Wang and Jacobsen, 2016), suggesting that the majority of the budget of these elements in the BSE was delivered by late-added volatile-rich materials. Alternatively, in the

scenario envisaged by Braukmüller et al. (2019), the CI-like materials that delivered the majority of the In to the BSE would have also imparted an In isotopic composition indistinguishable from those of carbonaceous chondrites (light blue area in Figure.7). Otherwise, the mixing of In isotopes from precursor materials with potential evaporative loss and chondritic volatile-rich materials could result in a heavier bulk Earth's In isotopic composition than carbonaceous chondrites (Figure 7, light grey area).

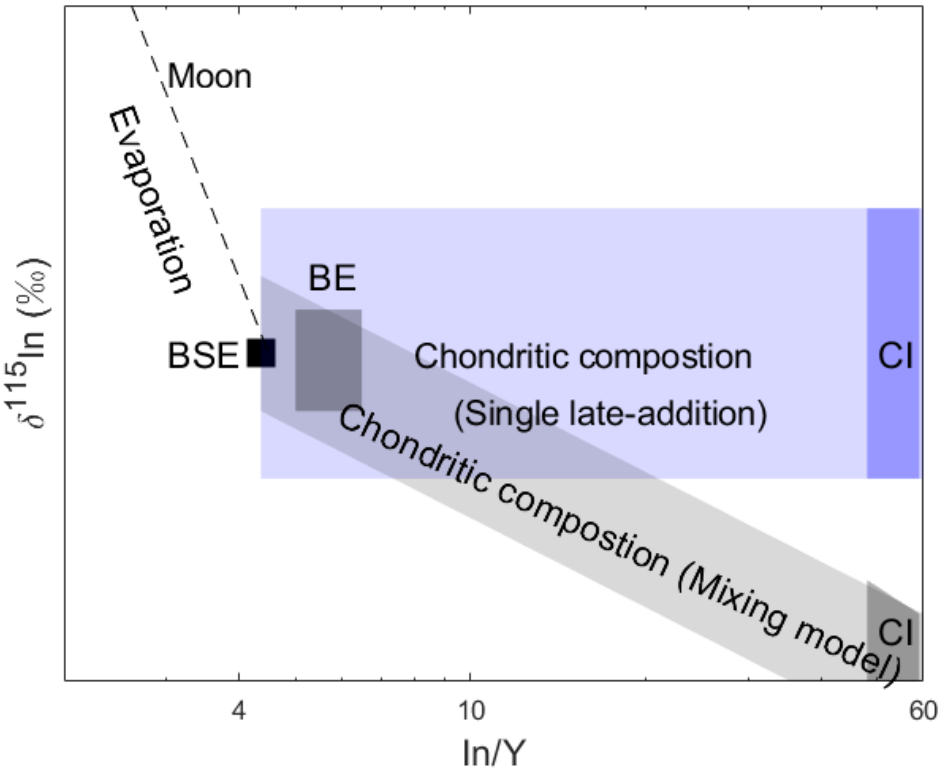

Figure.7 Schematic diagram for the possible In isotopic composition of materials of planets and chondrites. The light blue area shows the possible In isotopic composition of chondrites, overlapping with the In isotopic composition of BSE. In this case, the major budget of Earth's In is constituted by late-added volatile-rich chondritic materials, and therefore inherited the chondritic In isotopic composition. Light grey area represents another possible model for the origin of In: the present In budget of the Earth is the results of mixing sources from both precursor materials and late-added volatile-rich materials. Dark grey area represents the In isotopic composition of the bulk Earth (BE). This area only shows a rough boundary of BE composition due to lack of well-constrained estimation of In content in the core and isotopic fractionation during metal-silicate segregation. Dash line points to the evaporation trend to the Moon that has the precursor materials with BSE composition.

5. Conclusions

We have developed a chemical column chromatography method to separate In from rock samples and its isotopic measurement on a MC-ICPMS Nu Sapphire. Our chemical method can effectively remove matrix elements and isobaric interferences (Sn and Cd) nearly completely, and can return In isotopic composition of rock samples with an external reproducibility of ~0.12‰ (2SD).

We used this method on a few terrestrial samples, including geostandards BHVO-2, BCR-2, GSP-2, and Afar/Iceland samples whose rock types from basalt to rhyolite. Their In isotopic composition show insignificant isotopic fractionations within our analytical uncertainty, which can be attributed to constant oxidation sate and limited variations of coordination number of In during fractional crystallization. Our results show basalts analyzed so far with a nearly homogenous In isotopic composition within the current level of analytical uncertainty, and therefore, we further make the first estimation for the In isotopic composition of the mantle (δ^{115}In = -0.02 ± 0.19‰, 2SD, n = 10) based on the basalts from a variety of tectonic settings. We show that by using this method, In isotopes can be potential tools to study the origin of volatile elements in planetary systems.

Acknowledgements

We thank Pascale Lovat, Julien Moureau, Yan Hu, Wei Dai, Pierre Burckel for the help on the analysis on MC-ICP-MS and Q-ICP-MS. D.L thanks the support of CSC scholarship. This work was partly supported by the IPGP analytical platform PARI, Ile-de-France SESAME Grants 12015908, DIM ACAV+, the ERC grant 101001282 (METAL), and Labex UnivEarth (FM).

References

Archer, C. and Vance, D. (2004) Mass discrimination correction in multiple-collector

plasma source mass spectrometry: an example using Cu and Zn isotopes. Journal of Analytical Atomic Spectrometry 19, 656-665.

Arevalo Jr, R. and McDonough, W.F. (2010) Chemical variations and regional diversity observed in MORB. Chem. Geol. 271, 70-85.

Ayalew, D., Barbey, P., Marty, B., Reisberg, L., Yirgu, G. and Pik, R. (2002) Source, genesis, and timing of giant ignimbrite deposits associated with Ethiopian continental flood basalts. Geochimica et Cosmochimica Acta 66, 1429-1448.

Ayalew, D., Pik, R., Bellahsen, N., France, L. and Yirgu, G. (2019) Differential fractionation of rhyolites during the course of crustal extension, Western Afar (Ethiopian rift). Geochemistry, Geophysics, Geosystems 20, 571-593.

Barberi, F., Civetta, L. and Varet, J. (1980) Sr isotopic composition of Afar volcanics and its implication for mantle evolution. Earth and Planetary Science Letters 50, 247-259.

Braukmüller, N., Wombacher, F., Funk, C. and Münker, C. (2019) Earth's volatile element depletion pattern inherited from a carbonaceous chondrite-like source. Nature Geoscience 12, 564-568.

Chaussidon, M., Deng, Z., Villeneuve, J., Moureau, J., Watson, B., Richter, F. and Moynier, F. (2017) In Situ Analysis of Non-Traditional Isotopes by SIMS and LA–MC–ICP–MS: Key Aspects and the Example of Mg Isotopes in Olivines and Silicate Glasses. Reviews in Mineralogy and Geochemistry 82, 127-163.

Cormier, L., Ferlat, G., Itie, J.-P., Galoisy, L., Calas, G. and Aquilanti, G. (2007) Amorphous-amorphous transformation at high pressure in gallo-germanosilicate tetrahedral network glasses. Physical Review B 76, 134204.

Craig, H. and Lupton, J. (1976) Primordial neon, helium, and hydrogen in oceanic basalts. Earth and Planetary Science Letters 31, 369-385.

Dai, W., Moynier, F., Paquet, M., Moureau, J., Debret, B., Siebert, J., Gerard, Y. and Zhao, Y. (2022) Calcium isotope measurements using a collision cell (CC)-MC-ICP-MS. Chem. Geol. 590, 120688.

Field, L., Blundy, J. and Yirgu, G. (2008) The magmatic evolution of Dabbahu volcano,

Afar, Ethiopia, AGU Fall Meeting Abstracts, pp. V21B-2103.

Gion, A.M., Piccoli, P.M. and Candela, P.A. (2018) Partitioning of indium between ferromagnesian minerals and a silicate melt. Chem. Geol. 500, 30-45.

Harðardóttir, S., Halldórsson, S.A. and Hilton, D.R. (2018) Spatial distribution of helium isotopes in Icelandic geothermal fluids and volcanic materials with implications for location, upwelling and evolution of the Icelandic mantle plume. Chem. Geol. 480, 12-27.

Hin, R.C., Coath, C.D., Carter, P.J., Nimmo, F., Lai, Y.-J., Pogge von Strandmann, P.A.E., Willbold, M., Leinhardt, Z.M., Walter, M.J. and Elliott, T. (2017) Magnesium isotope evidence that accretional vapour loss shapes planetary compositions. Nature 549, 511-515.

Ionov, D.A. and Wang, K. (2021) Potassium distribution and isotope composition in the lithospheric mantle in relation to global Earth's reservoirs. Geochimica et cosmochimica acta 309, 151-170.

Jenner, F.E. and O'Neill, H.S.C. (2012) Analysis of 60 elements in 616 ocean floor basaltic glasses. Geochemistry, Geophysics, Geosystems 13.

Luck, J.-M., Othman, D.B. and Albarède, F. (2005) Zn and Cu isotopic variations in chondrites and iron meteorites: early solar nebula reservoirs and parent-body processes. Geochimica et Cosmochimica Acta 69, 5351-5363.

Mare, E.R., O'Neill, H.S.C., Berry, A.J., Frigo, C. and Glover, C.J. (2021) Coordination change of Ge4+ and Ga3+ in silicate melt with pressure. Geochimica et Cosmochimica Acta 303, 184-204.

Mason, T.F., Weiss, D.J., Horstwood, M., Parrish, R.R., Russell, S.S., Mullane, E. and Coles, B.J. (2004) High-precision Cu and Zn isotope analysis by plasma source mass spectrometry Part 2. Correcting for mass discrimination effects. Journal of Analytical Atomic Spectrometry 19, 218-226.

May, T.W. and Wiedmeyer, R.H. (1998) A table of polyatomic interferences in ICP-MS. ATOMIC SPECTROSCOPY-NORWALK CONNECTICUT- 19, 150-155.

Moynier, F., Deng, Z., Lanteri, A., Martins, R., Chaussidon, M., Savage, P. and Siebert,

J. (2020) Metal-silicate silicon isotopic fractionation and the composition of the bulk Earth. Earth and Planetary Science Letters 549, 116468.

Moynier, F., Hu, Y., Wang, K., Zhao, Y., Gérard, Y., Deng, Z., Moureau, J., Li, W., Simon, J.I. and Teng, F.-Z. (2021) Potassium isotopic composition of various samples using a dual-path collision cell-capable multiple-collector inductively coupled plasma mass spectrometer, Nu instruments Sapphire. Chem. Geol. 571, 120144.

Mysen, B. and Richet, P. (2018) Silicate glasses and melts. Elsevier.

Norris, C.A. and Wood, B.J. (2017) Earth's volatile contents established by melting and vaporization. Nature 549, 507.

Palme, H. and O'Neill, H. (2014) Cosmochemical Estimates of Mantle Composition. Planets, Asteriods, Comets and The Solar System, Volume 2 of Treatise on Geochemistry . Edited by Andrew M. Davis. Elsevier.

Pfeiffer, L., Mills Jr, A.P., Chandross, E. and Kovacs, T. (1979) Beta spectrum of In 115. Physical Review C 19, 1035.

Pietruszka, A.J. and Reznik, A.D. (2008) Identification of a matrix effect in the MC-ICP-MS due to sample purification using ion exchange resin: An isotopic case study of molybdenum. International Journal of Mass Spectrometry 270, 23-30.

Pik, R., Deniel, C., Coulon, C., Yirgu, G. and Marty, B. (1999) Isotopic and trace element signatures of Ethiopian flood basalts: evidence for plume–lithosphere interactions. Geochimica et Cosmochimica Acta 63, 2263-2279.

Pik, R., Marty, B. and Hilton, D.R. (2006) How many mantle plumes in Africa? The geochemical point of view. Chem. Geol. 226, 100-114.

Pringle, E.A. and Moynier, F. (2017) Rubidium isotopic composition of the Earth, meteorites, and the Moon: Evidence for the origin of volatile loss during planetary accretion. Earth and Planetary Science Letters 473, 62-70.

Pringle, E.A., Moynier, F., Beck, P., Paniello, R. and Hezel, D.C. (2017) The origin of volatile element depletion in early solar system material: Clues from Zn isotopes in chondrules. Earth and Planetary Science Letters 468, 62-71.

Pringle, E.A., Moynier, F., Savage, P.S., Badro, J. and Barrat, J.-A. (2014) Silicon isotopes in angrites and volatile loss in planetesimals. Proceedings of the National Academy of Sciences 111, 17029-17032.

Ranta, E., Gunnarsson-Robin, J., Halldórsson, S.A., Ono, S., Izon, G., Jackson, M.G., Reekie, C.D.J., Jenner, F.E., Guðfinnsson, G.H., Jónsson, Ó.P. and Stefánsson, A. (2022) Ancient and recycled sulfur sampled by the Iceland mantle plume. Earth and Planetary Science Letters 584, 117452.

Richter, F.M. (2004) Timescales determining the degree of kinetic isotope fractionation by evaporation and condensation. Geochimica et Cosmochimica Acta 68, 4971-4992.

Righter, K., Nickodem, K., Pando, K., Danielson, L., Boujibar, A., Righter, M. and Lapen, T. (2017) Distribution of Sb, As, Ge, and In between metal and silicate during accretion and core formation in the Earth. Geochimica et Cosmochimica Acta 198, 1-16.

Righter, K., Pando, K., Marin, N., Ross, D.K., Righter, M., Danielson, L., Lapen, T.J. and Lee, C. (2018) Volatile element signatures in the mantles of Earth, Moon, and Mars: Core formation fingerprints from Bi, Cd, In, and Sn. Meteorit. Planet. Sci. 53, 284-305.

Rudnick, R., Gao, S., Holland, H. and Turekian, K. (2003) Composition of the continental crust. The crust 3, 1-64.

Schroll, E., Bea, F., Butler, E.C.V., van Calsteren, P., Shimizu, N., Griffen, D.T., Barefoot, R.R., Williamson, M.A., Montgomery, C.W. and Clark, I.D. (1999) I, in: Marshall, C.P., Fairbridge, R.W. (Eds.), Encyclopedia of Geochemistry. Springer Netherlands, Dordrecht, pp. 339-357.

Schwarz-Schampera, U. and Herzig, P.M. (2002) Indium: Geology, mineralogy, and economics. Springer Science & Business Media.

Shannon, R.D. (1976) Revised effective ionic radii and systematic studies of interatomic distances in halides and chalcogenides. Acta crystallographica section A: crystal physics, diffraction, theoretical and general crystallography 32, 751-767.

Sossi, P.A., Klemme, S., O'Neill, H.S.C., Berndt, J. and Moynier, F. (2019) Evaporation of moderately volatile elements from silicate melts: Experiments and theory. Geochimica et Cosmochimica Acta.

Sossi, P.A., Moynier, F., Treilles, R., Mokhtari, M., Wang, X. and Siebert, J. (2020) An experimentally-determined general formalism for evaporation and isotope fractionation of Cu and Zn from silicate melts between 1300 - 1500 °C and 1 bar. Geochimica et Cosmochimica Acta.

Sossi, P.A., Nebel, O., O'Neill, H.S.C. and Moynier, F. (2018) Zinc isotope composition of the Earth and its behaviour during planetary accretion. Chem. Geol. 477, 73-84.

Sossi, P.A. and O'Neill, H.S.C. (2017) The effect of bonding environment on iron isotope fractionation between minerals at high temperature. Geochimica et Cosmochimica Acta 196, 121-143.

Urey, H.C. (1947) The thermodynamic properties of isotopic substances. Journal of the Chemical Society (Resumed), 562-581.

Van Westrenen, W., Blundy, J. and Wood, B. (1999) Crystal-chemical controls on trace element partitioning between garnet and anhydrous silicate melt. American Mineralogist 84, 838-847.

Wager, L.R., Smit, J.v.R. and Irving, H. (1958) Indium content of rocks and minerals from the Skaergaard intrusion, East Greenland. Geochimica et Cosmochimica Acta 13, 81-86.

Wang, K. and Jacobsen, S.B. (2016) An estimate of the Bulk Silicate Earth potassium isotopic composition based on MC-ICPMS measurements of basalts. Geochimica et Cosmochimica Acta 178, 223-232.

Witt-Eickschen, G. and O'Neill, H.S.C. (2005) The effect of temperature on the equilibrium distribution of trace elements between clinopyroxene, orthopyroxene, olivine and spinel in upper mantle peridotite. Chem. Geol. 221, 65-101.

Witt-Eickschen, G., Palme, H., O'neill, H.S.C. and Allen, C.M. (2009) The geochemistry of the volatile trace elements As, Cd, Ga, In and Sn in the Earth's mantle: new evidence from in situ analyses of mantle xenoliths. Geochimica et

Cosmochimica Acta 73, 1755-1778.

Wood, B.J., Smythe, D.J. and Harrison, T. (2019) The condensation temperatures of the elements: A reappraisal. American Mineralogist 104, 844-856.

Yi, W., Halliday, A.N., Alt, J.C., Lee, D.C., Rehkämper, M., Garcia, M.O., Langmuir, C. and Su, Y. (2000) Cadmium, indium, tin, tellurium, and sulfur in oceanic basalts: Implications for chalcophile element fractionation in the Earth. Journal of Geophysical Research: Solid Earth 105, 18927-18948.

Young, E.D., Manning, C.E., Schauble, E.A., Shahar, A., Macris, C.A., Lazar, C. and Jordan, M. (2015) High-temperature equilibrium isotope fractionation of non-traditional stable isotopes: Experiments, theory, and applications. Chem. Geol. 395, 176-195.

Young, E.D., Shahar, A., Nimmo, F., Schlichting, H.E., Schauble, E.A., Tang, H. and Labidi, J. (2019) Near-equilibrium isotope fractionation during planetesimal evaporation. Icarus 323, 1-15.

Supplementary materials

Table. S-1 Indium isotopic composition of 16 natural samples from different geological settings. The In isotopic composition are reported with notion '$\delta^{115/113}$In', which is described in main text. The IPGP-In standard is used for all isotopic data in this study.

Sample name	Rock type	$\delta^{115/113}$In (‰)	2SD	n	In (ppb)	MgO (wt. %)
Iceland						
A24	Basalt	0.13	0.11	5	59	7.2
B-ALK	Basalt	-0.16	0.11	8	124	4.7
M1D	Basalt	0.00	0.16	1	73	9.6
I-ICE	Andesite	-0.09	0.13	5	200	2.7
I-DAC	Dacite	-0.04	0.11	5	119	1.3
A-THO	Rhyolite	0.03	0.08	7	208	0.1
Afar						
AF-12-01	Basalt	-0.12	0.12	5	127	5.3
AF-13-46	Basalt	-0.12	0.12	4	207	5.2
Boha	Trachyandesite	-0.08	0.16	9	137	1.3
AF-15-10	Rhyolite	-0.17	0.17	9	170	0.1
AF-12-15	Rhyolite	-0.02	0.10	7	88	0.1
MORB						
MD57-D13	Basalt	0.07	0.04	8	170	6.7
EW9309-3D-19	Basalt	0.04	0.06	8	90	6.7
ARP74 column	Basalt	-0.01	0.07	15	66	8.3

Table. S-2 Indium isotopic composition of geostandards and chemical reproducibility for the In purification step.

Sample	δ^{115}In	2SD	n
BHVO-2	-0.02*	0.06	3
	-0.01	0.03	3
	-0.12	0.01	2
	-0.10	0.03	4
	-0.03	0.08	4
	0.00	0.14	4
	-0.04	0.14	4
	-0.04	0.17	5
	0.08	0.11	2
Average	-0.03	0.12	
Third pass chemistry	-0.06	0.06	3
BCR-2	0.01*	0.09	3
	-0.12	0.01	3
	-0.02	0.09	3
	-0.10		1
Average	-0.05	0.11	
Third pass chemistry	-0.04		1
GSP-2	0.07		1
	-0.03	0.11	3
	-0.02	0.17	2
Average	0.01	0.11	
Column yield			
First HBr column	0.00	0.05	4
First HBr column[d]	-0.01	0.08	4
Second HBr column	0.03	0.06	4
Second HBr column[d]	0.03	0.03	4
HF column	0.01	0.02	4
HF column[d]	-0.05	0.04	4

Mark * refers to the sample used to pass the additional column chemistry and the 'Third pass chemistry' represents the results of these additional chemistry samples. 'd' refers to duplicate sample.

Table. S-3 Tests for influence of different IPGP-In standard concentrations on precision and accuracy.

Concentration	δ^{115}In	2SD	n
1 ppb	0.00	0.29	16
2 ppb	-0.01	0.15	8
3 ppb	-0.01	0.07	8
5 ppb	0.00	0.03	8
10 ppb	0.00	0.02	8

Table. S-4 Intensity mismatch tests on IPGP-In standards. A 3 ppb IPGP-In standard is used as the bracketing standard.

$[In]_{sample}/[In]_{standard}$	δ^{115}In	2SD	n
0.52	-0.05	0.06	5
0.80	0.03	0.09	5
1.25	0.00	0.09	5
1.43	-0.01	0.08	5
1.52	-0.01	0.07	5

Table. S-5 Tests on the nitric concentration mismatch. The bracketing IPGP-In standard is dissolved in 3% HNO_3.

[HNO3] %	δ^{115}In	2SD	n
1% HNO3	-0.05	0.08	6
2% HNO3	-0.04	0.10	6
4% HNO3	0.03	0.10	6
5% HNO3	0.07	0.16	6

Table. S-6 Tests on isobaric interferences of Sn and Cd. The measured solutions are 3 ppb IPGP-In standards doping with variable amounts of Sn and Cd. The bracketing standard is a 3 ppb pure IPGP-In standard. The isotopes result before and after isobaric interferences correction are shown below.

Element	concentration	$\delta^{115}In_{measured}$ (‰)	2SD	$\delta^{115}In_{corrected}$ (‰)	2SD	n
Sn	0.01 ppb	0.01	0.11	-0.01	0.10	4
	0.1 ppb	0.14	0.14	0.04	0.09	4
	1 ppb	0.99	0.05	0.03	0.11	4
Cd	0.25 ppt	-0.11	0.08	0.05	0.10	3
	2.5 ppt	-1.54	0.06	0.01	0.06	3
	25 ppt	-15.21	0.18	-0.37	0.19	3

Table. S-7 Tests of matrix effect, including Fe, Ca, Mg, Al, Na, Ti and K. A series of 3 ppb IPGP-In standards doped with various amounts of matrix elements are used as samples, and another pure 3 ppb IPGP-In standard is used as bracketing standard for all the matrix effect tests.

Element	Concentration (ppb)	δ^{115}In (‰)	2SD	n
Fe	5	0.03	0.08	4
	10	0.02	0.10	5
	20	0.06	0.09	5
	50	0.03	0.06	5
Ca	5	-0.01	0.10	5
	10	-0.05	0.10	5
	20	-0.16	0.05	5
	50	-0.18	0.03	5
	100	-0.27	0.07	4
Mg	5	0.01	0.07	5
	10	-0.01	0.07	5
	20	-0.04	0.14	5
	50	-0.03	0.06	5
	100	-0.12	0.07	5
Al	5	0.04	0.14	5
	10	0.04	0.08	5
	20	0.02	0.07	5
	50	0.04	0.01	5
	100	0.04	0.12	5
Na	5	0.02	0.04	5
	10	-0.02	0.06	5
	20	-0.06	0.08	4

	50	-0.17	0.05	5
	100	-0.15	0.05	5
Ti	5	0.03	0.09	5
	10	0.05	0.09	4
	20	0.02	0.08	5
	50	0.00	0.10	5
	100	-0.03	0.06	5
K	5	0.07	0.03	6
	10	0.09	0.04	7
	20	0.04	0.05	7
	50	0.04	0.04	6
	100	-0.01	0.02	5

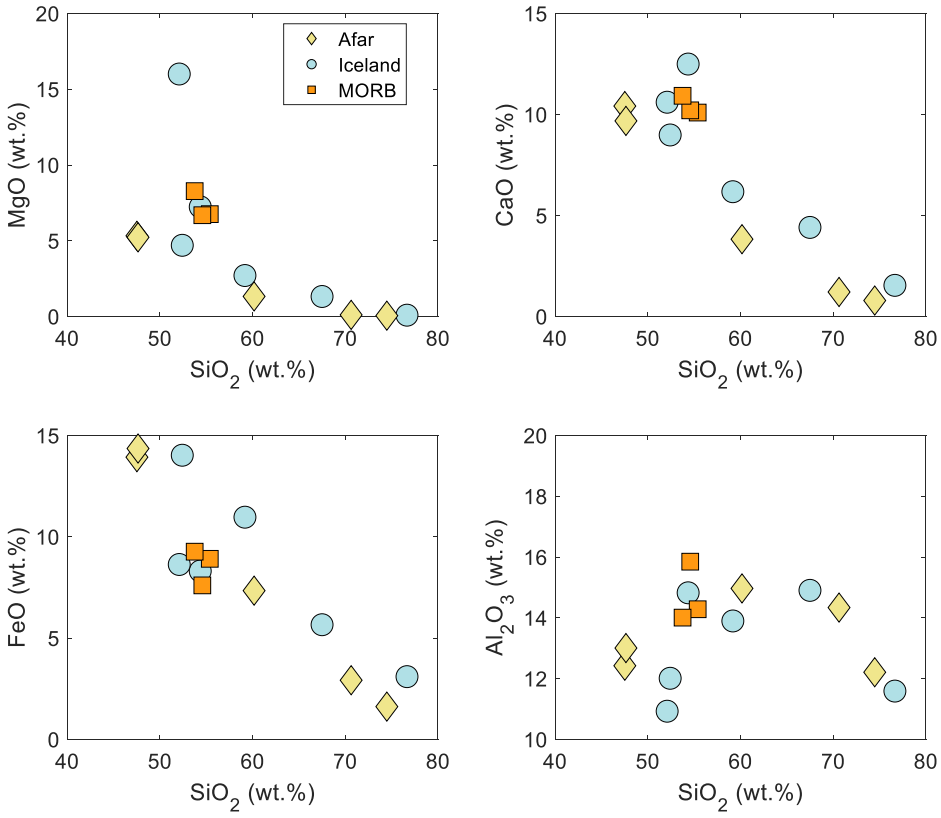

Figure.S1 Harker diagram for typical major elements vs. SiO_2 wt.% of analyzed Afar, Iceland and MORB samples. With increasing SiO_2 content, MgO, CaO and FeO exhibit negative correlation implying fractionation of olivine and pyroxene. The later decreasing concentration may reflect the fractionation of clinopyroxene and feldspar.

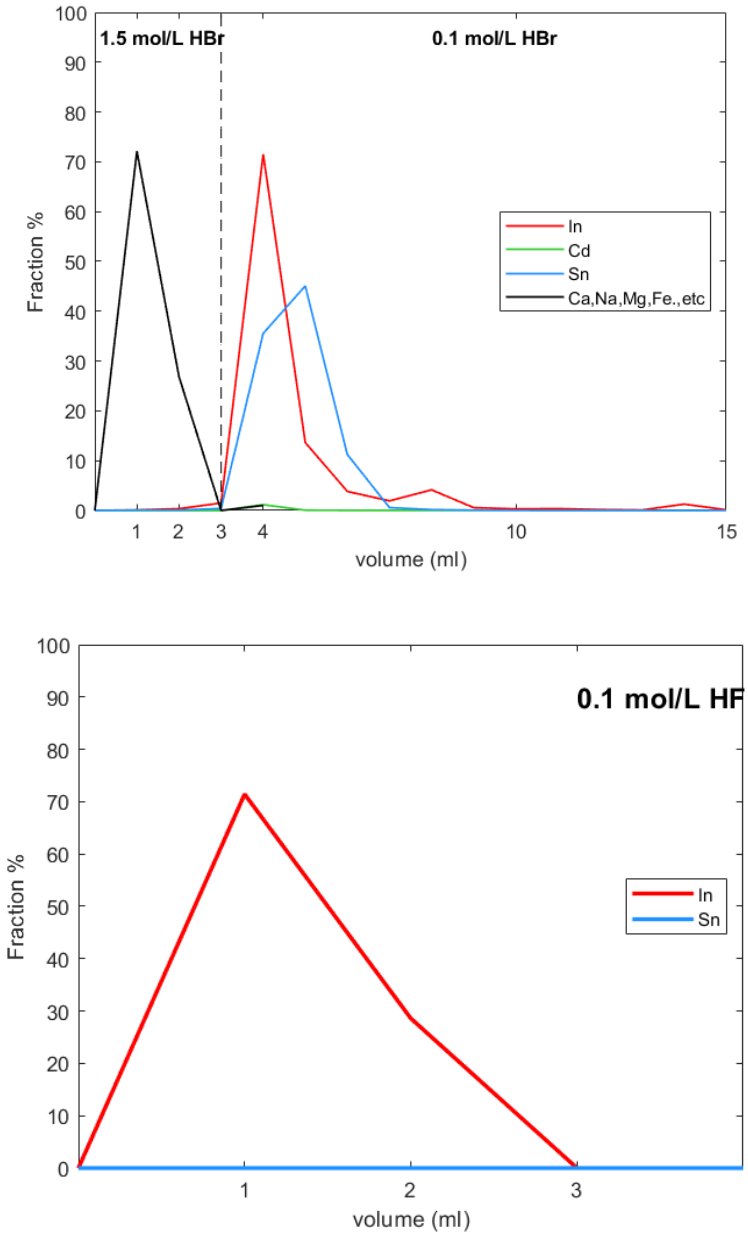

Figure.S2 A two-step elution profiles for separating In from matrix elements based on BHVO-2. The top panel a) shows the separation of In from typical major elements and Cd. Typical matrix elements include Ca, Na, Mg, Fe, K, Mn etc., which have almost completely overlapped elution curve here and hence are represented by the black solid line. The bottom panel b) shows the elution curve for separating In from Sn.

Chapter 4. Metal and silicate partitioning of indium up to P-T conditions of a deep magma ocean: implications for the origin of volatile depletions on Earth

Deze Liu[1*] , Edith Kubik[1,4], Julien Siebert[1,2], Paolo A. Sossi[1, 3], Ingrid Blanchard[4], Frédéric Moynier[1]

1. Université Paris Cité, Institut de Physique du Globe de Paris, 1 Rue Jussieu, 75005 Paris, France
2. Institut Universitaire de France, Paris, France.
3. Institute of Geochemistry and Petrology, ETH Zürich, Sonneggstrasse 5, CH-8092 Zürich, Switzerland
4. Bayerisches Geoinstitut, University of Bayreuth, Bayreuth, Germany

The chapter is in preparation for submission to Geochimica et Cosmochimica Acta journal.

Abstract

Indium (In) is considered overabundant in the bulk silicate Earth. This overabundance has been explained as the results of either over-estimated In volatility or late-accretion of CI-like volatile-rich materials delivered during the final-stage of core-formation process. Therefore, In can be expected to provide insights to the volatility processes occurring on Earth's building blocks and/or the timing and origin of the volatile elements accreted to the Earth. However, the partitioning behavior of In between metal and silicate and its potential isotopic fractionation during this process are still poorly constrained which hamper the understanding of the volatile depletion history of the Earth. In this work, we have performed a series of experiments under a wide range of pressure (~ 2 to 50 GPa) and temperature (~ 1500 to 4000 K) using different high pressure and high temperature devices such as piston cylinder, multi-anvil presses and diamond anvil cell. Experimental results indicate that both temperature and pressure have limited effect on the partitioning of In, while composition, in particular the effect of S and Si in metal can be significant and is likely pressure-dependent. Using parameterization of In partitioning, we modelled a final In

partition coefficient ranging in between 3 to 5, depending on the different accretion models and oxygen fugacity path considered. These results suggest that the budget of In the BSE requires the combination of both the late accretion of ~ 10% Earth mass volatile-rich materials delivered to the Earth before core-formation ceased and the precursor materials accreted during main stage of proto-Earth containing In to some extent. We also find a resolvable isotopic fractionation of In between silicate and metal in the S-free experiments, while the presence of S can decrease this fractionation. Extrapolating the regressed parameter to final temperature condition at the base of magma ocean, we provide a current best estimation of bulk Earth indium isotopic composition of -0.03 ± 0.18 ‰ as the upper limit and -0.08 ± 0.15 ‰ as the lower limit according to the variable effects of S.

1. Introduction

Volatile elements are significantly depleted in the Earth in comparison with CI chondrites, which are commonly used to represent the bulk chemical composition of rocky materials in the solar system (McDonough and Sun, 1995; Palme and O'Neill, 2014). However, the origin of the volatile depletion in the Earth is still unclear. The CI, -Mg normalized abundances of moderately volatile elements (MVEs) in the bulk silicate Earth (BSE) are observed to follow a decreasing trend with decreasing 50% condensation temperature (T_C^{50}), a temperature scale that is generally used to represent elemental volatility under solar nebular conditions (e.g., 10^4bar and logfO_2 = -14) (Lodders, 2003; Wood et al., 2019). The CI, -Mg normalized abundances of lithophile MVEs exhibit a near log-linear correlation with their T_C^{50}, suggesting that their depletion is correlated with the volatility-relevant processes, e.g., condensation and/or evaporation (Albarede, 2009; Moynier et al., 2020; Ringwood, 1966; Vollstaedt et al., 2020). The siderophile/chalcophile MVEs falls below this 'volatility trend' defined by lithophile MVEs, indicating an additional sequestration due to the core-formation process. Moreover, the depletion extent of these siderophile/chalcophile MVEs are governed by both volatility-relevant events and the physical/chemical conditions during

Earth's core-formation process, including pressure, temperature, chemical composition of melt, light elements in the metallic core (e.g., S, Si, C etc.) and oxygen fugacity (fO_2), and therefore can provide a constraint on the timing of the volatile elements delivered to the Earth, as well as the implications of the origin of volatile depletion of the Earth.

Although the abundance of most of MVEs in the BSE follows the 'volatility trend' and further core-mantle partitioning according to their siderophility, indium (In) is an exception. In is a both volatile and siderophile element, however, its CI, -Mg normalized abundance falls over the 'volatility trend', and hence is considered to be over-abundant in the BSE (Palme and O'Neill, 2014; Wang et al., 2016a; Witt-Eickschen et al., 2009). This feature allows In to have a potential to give an unique insight to the origin of the Earth's volatile depletion, in particular the 'late accretion' model, which suggested that the volatile budget of the Earth was largely contributed by the late-delivery of volatile-rich materials during the last 10 - 20 % roughly of Earth's accretion (Rubie et al., 2011; Rubie et al., 2015; Schönbächler et al., 2010; Wänke and Dreibus, 1988; Wänke et al., 1984). Wänke et al. (1984) and Wänke and Dreibus (1988) proposed that the Earth accreted from reduced, volatile-free materials (~ 85% of Earth mass), followed by the addition of oxidized, volatile-rich materials (~ 15% of Earth mass), and the budget of Earth's MVEs whose volatility higher than Na were also all from these late-accreted materials. Similar conclusion was also reached in a recent study from Braukmuller et al. (2019), they further proposed a 'hockey-stick' model of the Earth's volatile trend of depletions, and suggested that the MVEs whose T_C^{50} are lower than Zn should all have a similar volatility. Here, the source of volatile elements was a 10 -15 % Earth mass CI-like materials delivered to the Earth before core-formation process ceased. A key point in this model, as they stated, is the partitioning of In between core and mantle, which requires In to behave as a lithophile element under the conditions of Earth's core formation. Otherwise, the Earth would require i) either a larger fraction of the late-accreted CI-like materials delivered to the Earth before core-formation ceased to achieve the present In abundance in the BSE. or ii) That In was present in some extent in the precursor materials of the proto-Earth to

supplement the deficit caused by core-formation process (see Chapter 2). Therefore, In partitioning between metal and silicate needs to be investigated to estimate precisely the effect of core formation on the budget of In in the BSE and precise the origin of its observed overabundance.

Some previous experimental works have studied the metal-silicate partitioning behavior of In (Ballhaus et al., 2013b; Mann et al., 2009; Righter et al., 2017; Righter et al., 2018a; Steenstra et al., 2020; Wang et al., 2016a; Wood et al., 2014a). The results of these experiments recognized In as a moderately siderophile element and further provided some regressed parameters to model the possible partitioning behavior of In under core-formation conditions, corresponding to P-T conditions of ~ 40 to 60 GPa, ~ 3200 – 4000 K (e.g., Siebert et al., 2012; Siebert et al., 2013). However, this P-T condition is significantly higher than most of previous In partitioning experiments, which were generally performed at 1 ~ 3 GPa, 1500 ~ 2000 K, and the experiments that were conducted at higher pressure (e.g., > 10 GPa) are very scarce (Mann et al., 2009; Wang et al., 2016a). Moreover, some recent studies have observed a pressure-dependent interaction parameter of S/Si for some MVEs such as Cd, Sn, Bi, Tl and In, indicating a variable S/Si effect of metal composition on the partitioning of these MVEs for variable pressure (Kubik et al., 2021a; Kubik et al., 2021b; Steenstra et al., 2020). Accordingly, extrapolation of parameters regressed from low P-T conditions may result in a significant deviation at higher P-T conditions relevant to core formation in a deep magma ocean, and therefore, additional experiments performed under high P-T conditions are required.

The In isotopic composition of the Earth is also a crucial tracer for tracking the origin of In of the Earth. The possible building blocks (i.e., meteorite-like materials) of the Earth may have distinct isotopic compositions (e.g., Ku and Jacobsen, 2020; Luck et al., 2005; Moynier et al., 2007; Savage et al., 2015), and hence, the Earth's isotopic composition can be expected to provide an insight to the source of its building blocks. However, the estimation of the bulk Earth (BE) isotopic composition of a siderophile element is hindered by the core-formation process, which may fractionate isotopes

during metal-silicate segregation (Kubik et al., 2021b; Mahan et al., 2017; Moynier et al., 2020; Shahar et al., 2015; Shahar et al., 2009). Therefore, the knowledge of In isotopic fractionation between metal and silicate during core formation is critical for the application of In isotope system to the Earth.

Here, we report a series of metal-silicate segregation experiments performed in between 2 to ~ 50 GPa and 1500 to ~ 4000 K, which covers most of the predicted the P-T range of core-mantle equilibration. Based on the experimental results, we regressed the parameters that apply to the partitioning of In between metal and silicate, and further discuss the effects of light elements, S and Si, and their dependency with pressure. Combined with these regressed parameters, we model the possible evolution of the partitioning behavior of In between core and mantle, and discus the origin of indium's overabundance in the BSE. Furthermore, the In isotopic fractionation between silicate and metallic phases was also analyzed with the piston-cylinder synthesized samples. According to the In isotopic fractionation under low P-T conditions (2 GPa, ~ 1500 to 2000 K), as well as light elements-free and S/Si – bearing samples, we discuss the effects of light elements on the In isotopic fractionation, in particular S effect, and further regress a temperature-dependent parameter, which allow to provide a current best estimation of the In isotopic composition of the bulk Earth.

2. Method

2.1 Starting materials

The starting materials of metal-silicate partitioning experiments are mixtures of silicate and metallic powders. For the piston-cylinder and multi-anvil experiments, the silicate part uses mid-ocean-ridge basalt (MORB) powders, while metal part is a mixture of pure Fe and In powders with/without additional doping of FeS or Si metal. Some other MVEs (Sn, Cd, Sb, Bi) were doped in the starting materials of multi-anvil experiments and the compositions can be found in Kubik et al. (2021a) and Kubik et al. (2021b). Two additional experiments performed with the diamond anvil cell (DAC)

uses a starting material made of pyrolite powders and a metallic mixture of In, Cd, Bi, Sn, Tl, Fe and or FeS. All the starting material powders were grounded homogeneously in an agate mortar. The chemical compositions of these starting materials are listed in Table. 1.

Table. 1 The chemical composition of starting materials

Mixture	mixture	silicate	In	Fe	FeS	Si
MFI-S1	MORB+Fe+In+FeS	63.7	1.3	25.4	9.6	-
MFI-S2	MORB+Fe+In+FeS	63.7	1.3	15.8	19.2	-
MFI1	MORB+Fe+In	63.7	1.3	35	-	-
MFI-Si1	MORB+Fe+In+Si	63.7	1.3	31.5	-	3.5
MFI-Si2	MORB+Fe+In+Si	63.7	1.3	33.25	-	1.75
MFI-Si3	MORB+Fe+In+Si	63.7	1.3	34.3	-	0.7
MFI-Si4	MORB+Fe+In+Si	63.7	1.3	28	-	7
A-MF1	MORB+Fe+In+Sn,Cu,Tl,Cd,Bi,Sb	64.4	1	27.6	-	-
B-MFS1	MORB+Fe+FeS+In+Sn,Cu,Tl,Cd,Bi,Sb	64.4	1	12.4	15.18	-
D-Pm1	Pyrolite+Fe+In+Sn,Cd,Bi, S,Tl					
D-PSm2	Pyrolite+Fe+FeS+In+Sn,Cd,Bi, S,Tl					

High pressure experiments

The experimental pressure and temperature conditions span a wide range from 2 GPa to 50 GPa and 1623 K to ~ 4000 K, which covers the typical P-T conditions of planetary core-formation process in small differentiated asteroids and larger terrestrial bodies such as the Earth. There are 22 experiments conducted in a piston-cylinder apparatus at Institut de Physique du Globe de Paris (IPGP). These piston-cylinder experiments were performed at 2 GPa and variable temperature (1450℃ to 2000℃). All piston-cylinder experiments used MgO capsule for placing and sealing powders of starting materials, then these capsules were put into talc-pyrex (⩽1700 ℃) or $BaCO_3$ assembly (> 1700 ℃) for the following high P-T experiments. An element equilibrium test between molten metal and surrounding silicate was performed at the lowest temperature 1623 K and variable durations (10 min, 30 min and 60 min) to determine the efficiency of metal-silicate equilibrium of In.

Twelve experiments were conducted in a multi anvil apparatus at the Bayerisches

Geoinstitut. These experiments span a P-T range from 7 to 20 GPa, and ~ 1960 K to 2573 K. MgO single crystal capsule and MgO + Cr_2O_3 pressure media were used in these experiments. More details of these experiments can be found in Kubik et al. (2021a). Two experiments were performed with a diamond anvil cell (DAC) apparatus at IPGP, whose pressure and temperature are corresponding to ~ 50 GPa and 4000 K. The experimental conditions of these two experiments allow to estimate the partitioning behavior of In at the direct P-T conditions of Earth's core-formation, and allow to better constrain the extrapolated parameters from low P-T experiments (e.g., Huang et al., 2021; Huang and Badro, 2018; Siebert et al., 2012).

2.2 Composition analysis

Large pieces of metal and silicate are picked out and mounted in epoxy, and then polished to the largest cross section for the following analysis. The micro probe analysis was conducted with a CAMECA SX Five electron probe micro-analysis (EPMA) at CAMPARIS service, Sorbonne University. The chemical compositions of most of silicate and metal samples performed with piston-cylinder and multi-anvil were analyzed with electron micro probe analysis (EPMA), and the silicate samples conducted with multi-anvil were also analyzed with laser-ablation inductively coupled plasma mass spectrometry (LA-ICP-MS) as a comparison. For the EPMA analyses, the operation voltage and current are 20 keV and 10 nA for Na, Mg, Si, Al, K, Ca and Fe; 20 keV and 200 nA for S, Mn, In, P and Ti. The standards used for Na is albite, diopside for Mg, Si and Ca; orthopyroxene for K and Al; Mn-Ti oxide for Mn and Ti; an alloy of In and P (InP) for In; pyrite for S. For the silicate samples, the standard for Fe is pyrite, while for metal samples, Fe_2O_3 is used for the analysis of Fe and O. The beam size is 30 microns for all EPMA analyses. The detection limit of In is ~ 160 ppm in silicate and ~ 1100 ppm in metal.

The LA-ICP-MS analyses were performed on an Element XR high-resolution mass spectrometer that coupled with a 193 nm Compex Pro 102 Coherent laser system at Université de Brest. Analyses were conducted under the operating conditions of 15

J/cm^2 laser and 10 Hz frequency with a beam size of 90 microns. The data calibration was made by using the Mg concentration measured on EPMA. Only multi-anvil silicate samples were analyzed with LA-ICP-MS in this study.

2.4 Chemical purification

The samples that synthesized with piston-cylinder were used for the further analyses of isotopic compositions to determine the potential isotopic fractionation between metal and silicate phase. The silicate and metal part of each sample were carefully separated from each other and further checked under microscope to ensure no visible metal particles bearing in silicate phase and *vice versa*. Then the silicate samples were crushed to tiny pieces, and a magnet was placed over these silicate pieces to remove potential metal particles. This step was repeat a few times until there was no magnetically attracted metal particles observed and afterwards, the silicate pieces were grounded to fine powders.

These sorted samples were then dissolved for the following chemical purification. The silicate samples were dissolved with a mixed acids of HNO_3 (3 ml, 16 mol/L) and HF (1 ml, 28 mol/L) under 130℃ for 48 hours. Then these samples were evaporated to dryness at 100℃, and were re-dissolved with 3 ml 6 mol/L HCl for 24 hours and dried down. This step was designed to remove the potential insoluble fluorides. Then these samples were dissolved in 1 ml 1.5 mol/L HBr for further column chemistry. The metal samples were dissolved in 3 ml 6 mol/L HCl at 130℃ for 48 hours, and then evaporated to dryness and re-dissolved in 1 ml 1.5 mol/L HBr.

The chemical purification procedure is a two-step column chemistry. The columns for both steps are homemade heat-shrink Teflon columns with a size of 1.5 cm length and 0.5 cm diameter. 0.4 mL of AG1X8 resin (200-400 meshes) was used for the purification. The resins were cleaned with 3 mL 18.2 Ω Mili-Q water and 0.5 mol/L HNO_3 for three times before the following pre-condition step. For the first step column chemistry, 3 mL 1.5 mol/L HBr was used for the pre-condition of resin, and then 1 mL of sample solution was loaded on column and then 2 mL of 1.5 mol/L HBr was added

on column to further remove matrix elements. Then 12 mL of 0.1 mol/L HBr was used to collect In. This step was repeated three times to ensure that most of matrix effect (Fe, Mg, Ca, Al etc.) and Cd (isobaric) interference have been removed. The second column chemistry is designed to separate Sn from In. The collected samples from the last column were evaporated to dryness and dissolved in 1 mL 0.1 mol/L HF. The same pre-cleaned resin and column were also used for the second column chemistry. 3 mL 0.1 mol/L HF is used for the pre-condition, and then sample solution is loaded on column and followed with 6 mL 0.1 mol/L HF to collect In.

2.5 Isotopic analysis on MC-ICP-MS

The isotopic compositions of indium were analyzed on a Neptune plus multi-collector inductively coupled plasma mass spectrometer (MC-ICP-MS) at IPGP. The instrumental mass bias is calibrated by the sample-standard-bracketing (SSB) method. The standard is an ICP-MS indium standard solution produced by Sigma-Aldrich (lot number: BCBS0171V, named as IPGP-In standard). Both samples and standards were dissolved in 0.5 mol/L HNO_3 and diluted to 50 ppb for the following analyses.

The solutions were introduced into plasma source via an APEX IR desolvating system that combined with a 100 μL/min PFA nebulizer (Micro-Flow nebulizer, Elemental Scientific, Omaha, NE, USA) and Jet + H cones. The 50-ppb solution can yield a sensitivity of ~ 20 V for mass 115 and ~ 0.9 V for mass 113. A blank test (0.5 mol/L HNO_3, from the same bottle that used for dissolving samples, standards and washing procedure) was performed at the beginning and then interspersed for a few times during each sequence, and its value was used as blank correction (~ 0.04 V for mass 115 and ~ 0.002 V for mass 113). Faraday cups equipped with $10^{11}\Omega$ resistors were used to monitor ^{110}Cd, ^{111}Cd, ^{112}Cd, ^{113}In, ^{115}In, ^{117}Sn, ^{118}Sn and ^{119}Sn. Each analysis contains a block of 25 cycles with 8 s integration time, followed by a 120 s wash procedure performed in 0.5 mol/L HNO_3.

3. Results

3.1 Textures of run products

All of the run products consist of Fe-rich alloy embedded in silicate phases due to the immiscibility of metal and silicate phases. The textures of silicate and metal phases after quenching are influenced by the experimental temperature and starting materials (e.g., the presence of S). For the run products performed at a temperature below1823 K, the silicate textures are typically glassy (Figure. 1a), or only with minor skeletal mineral crystals (olivine and/or pyroxene) along with the MgO capsule, while the other run products conducted at higher temperature are commonly observed with the spinifex-textured silicate phases (Figure. 1b) that result from the dissolution and saturation of MgO from capsule.

The textures of metallic phases depend on the concentration of light elements (S and Si) in the starting materials. For the S- bearing run products, their metallic phases exhibit typical quench textures with the exsolution of FeS-rich phases (Figure. 1c). The metallic phases of most of light elements-absence and Si- bearing run products are cryptocrystalline and/or with near-homogeneously distributed bright spots (Figure. 1d), which may be exsolved In. Given the quench-induced heterogeneity of elemental distribution in silicate and metallic phases, we used a broad de-focused beam (30 μm on EPMA, 90 μm on LA-ICP-MS) and a large number of measurements (15 to 30 analyses for each silicate/metal sample) to minimize the influence of quench textures.

3.2 Elemental compositions

The chemical compositions of silicate and metal of experimental products are listed in Table 2. The initial silicate (MORB) was analyzed with EPMA and has the following composition in major elements: SiO_2 (50.18 ± 0.29 wt.%), MgO (7.99 ± 0.29 wt.%), Al_2O_3 (14.61± 0.16 wt.%), CaO (12.20 ± 0.25 wt.%), FeO (9.18 ± 0.25 wt.%), Na_2O (2.17 ± 0.18 wt.%), K_2O (0.18 ± 0.29 wt.%). The elemental compositions of silicate and metal phases in run products are influenced by experimental conditions (T, fO_2),

starting materials (for example, S and Si) and dissolution of MgO capsule, and can result in compositional variations: SiO_2 (32 to 50 wt.%), FeO (< 1 to ~ 10 wt.%), MgO (~ 15 to 35 wt.%) in silicate phases; Fe (60 to 98 wt.%), S (~ 0.1 to 20 wt.%), and Si (~ 0.01 to 4 wt.%) in metallic phases. The MgO content in silicate phases is observed to be relevant with temperature, as the increase of temperature can lead to more MgO dissolved in silicate melt. The concentration of SiO_2 and FeO in silicate are governed

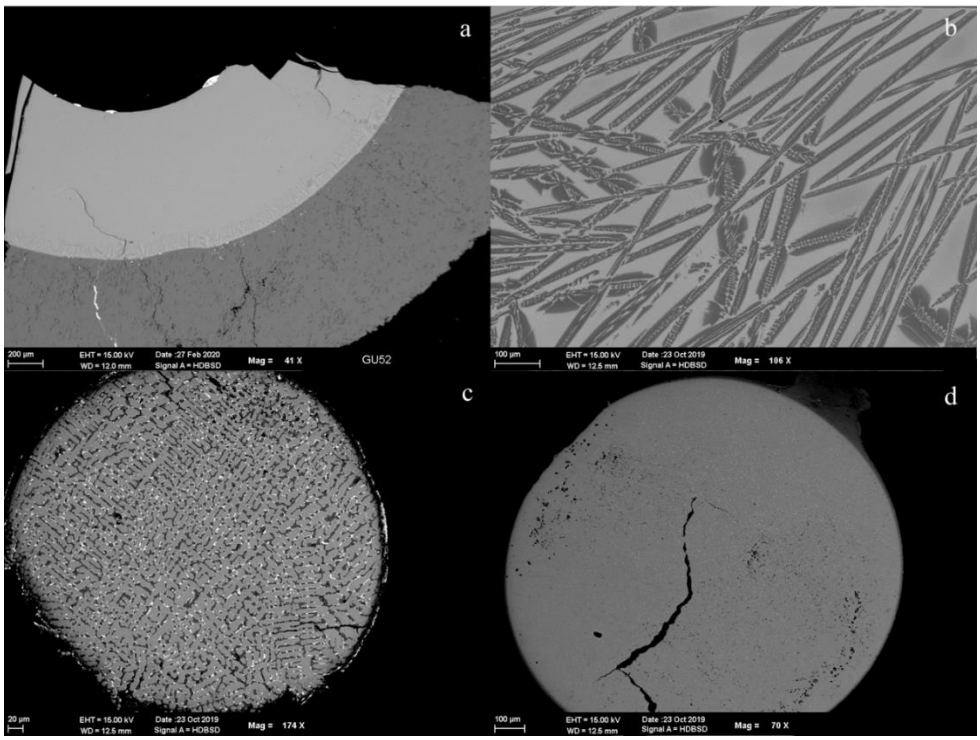

Figure. 1 Back-scatter images of typical textures of silicate and metal phases. a) image of silicate phase of E335 (2 GPa, 1823 K), well-glassy silicate texture can be observed. The surrounded silicate phase is MgO capsule. b) image of silicate phase of E349 (2 GPa, 1973 K). Typical spinifex-textured crystals distributed in silicate phases. c) image of metallic phase in E350 (2 GPa, 2273 K). Metallic phase with the exsolution of FeS-rich phases. d) image of metallic phase in E355 (2 GPa, 1823 K). Near-homogeneously distributed bright points. All the EPMA measurments were conducted with a 30 microns defocused beam and calculated their average value to the following metal-silicate partitioning calculation.

by the doped Si, which follows the reaction: Si + FeO = SiO_2 +Fe, and hence the addition of Si can lead to an enrichment of SiO_2 in silicate and increase the Fe content of metallic phases, and further decrease the experimental oxygen fugacity. The concentrations of In_2O_3 in silicate phases vary from ~ 0.1 to 0.35 wt.%, which is much higher than the detection limit of In in silicate (~ 160 ppm on EPMA); In concentration

in metallic phases vary from ~ 1.4 to 4 wt.% with a detection limit ~ 1000 ppm in metallic phases on EMPA. The In concentration in silicate and metal is a function of experimental conditions and compositions, which a further description is given in section 3.3.

Table 2. The experimental conditions and chemical compositions of run products.

Run	E335	σ	E336	σ	E337	σ	E338	σ	E339	σ
Starting material	MFI-S1		MFI-S1		MFI-S1		MFI-S1		MFI-S1	
Temperature (°C)	1450		1550		1600		1450		1450	
Pressure (Gpa)	2		2		2		2		2	
Duration (min)	10		7		4		30		60	
Pressure media	Talc-pyrex		Talc-pyrex		Talc-pyrex		Talc-pyrex		Talc-pyrex	
Capsule	MgO		MgO		MgO		MgO		MgO	
ΔIW	-2.1		-2.4		-2.0		-2.1		-2.4	
Silicate composition (wt.%)										
Na_2O	1.93	0.11	2.58	0.13	1.96	0.88	2.02	0.11	2.35	0.18
MgO	14.56	0.87	22.84	1.75	25.07	11.94	15.97	0.27	20.48	2.51
Al2O3	13.27	0.16	7.90	0.86	9.45	3.95	12.84	0.35	12.80	0.85
SiO2	45.84	0.72	47.92	0.54	43.25	10.30	44.62	1.12	41.93	0.97
K2O	0.17	0.02	0.29	0.03	0.21	0.11	0.17	0.02	0.25	0.03
CaO	11.13	0.20	7.55	0.47	7.29	3.67	10.99	0.19	10.90	0.91
FeO	10.57	0.12	6.80	0.37	10.56	3.06	10.56	0.14	7.70	0.33
P2O5	0.16	0.01	0.11	0.01	0.12	0.06	0.14	0.02	0.13	0.02
SO2	0.08	0.01	0.11	0.01	0.15	0.08	0.09	0.01	0.11	0.02
MnO	0.17	0.00	0.11	0.01	0.11	0.03	0.17	0.00	0.13	0.01
In2O3	0.29	0.01	0.22	0.02	0.28	0.13	0.25	0.01	0.17	0.02
TiO2	0.94	0.01	0.51	0.05	0.61	0.28	0.91	0.02	0.87	0.06
Total	99.12	0.97	96.94	0.58	99.07	3.14	98.72	1.68	97.84	0.82

n	23		20		24		21		24	
Metal composition (wt.%)										
Si	0.03	0.01	0.04	0.01	0.03	0.01	0.03	0.00	0.03	0.00
Continued										
Fe	86.80	1.12	83.27	1.79	85.26	1.37	88.00	1.07	87.90	0.68
P	0.09	0.01	0.09	0.01	0.08	0.01	0.10	0.01	0.10	0.01
S	7.15	0.58	7.95	0.90	7.72	0.90	5.74	0.59	6.28	0.40
1n	2.61	0.37	3.37	0.65	3.32	0.63	2.72	0.31	2.99	0.33
O	-	-	-	-	-	-	-	-	-	-
Total	96.69	0.65	94.79	0.99	96.41	0.46	96.61	0.53	97.32	0.41
n	28		22		25		20		26	
$logK_D^{In}$	-0.48	0.13	-0.44	0.18	-0.54	0.22	-0.44	0.10	-0.41	0.10
D_{In}	10.99	3.24	19.73	7.42	9.46	3.20	13.04	3.02	22.75	5.27
Run	E340	σ	E341	σ	E343	σ	E344	σ	E346	σ
Starting material	MFI-S2		MFI1		MFI1		MFI-Si1		MFI1	
Temperature (°C)	1450		1550		2000		1550		1800	
Pressure (Gpa)	2		2		2		2		2	
Duration (min)	10		7		1.5		7		2	
Pressure media	Talc-pyrex		Talc-pyrex		$BaCO_3$		Talc-pyrex		$BaCO_3$	
Capsule	MgO		MgO		MgO		MgO		MgO	
ΔIW	-1.9		-2.2		-2.6		-5.1		-2.3	
Silicate composition (wt.%)										
Na_2O	2.17	0.24	1.89	0.10	1.70	0.78	1.79	0.13	2.35	1.05
MgO	15.53	0.56	17.73	0.64	37.37	5.44	19.67	1.44	27.38	10.23

Al2O3	12.52	0.83	11.75	0.73	9.81	2.68	13.35	1.07	13.85	3.85
SiO2	46.71	0.84	38.25	3.68	34.37	1.87	50.72	5.10	33.83	2.53
K2O	0.23	0.05	0.17	0.02	0.17	0.07	0.17	0.02	0.22	0.09
CaO	10.64	0.46	9.98	0.64	9.57	2.82	11.41	0.94	12.87	4.66
FeO	9.87	0.71	9.69	0.22	7.58	0.92	0.34	0.04	9.91	1.90
P2O5	0.14	0.01	0.24	0.07	0.10	0.02	0.13	0.05	0.14	0.06
SO2	0.20	0.01	0.01	0.00	0.03	0.01	0.08	0.01	0.02	0.01
MnO	0.16	0.01	0.15	0.01	0.12	0.01	0.16	0.01	0.14	0.02
In2O3	0.21	0.01	0.34	0.02	0.16	0.03	0.19	0.02	0.21	0.07
TiO2	0.88	0.07	0.86	0.06	0.76	0.17	0.98	0.08	0.91	0.32
Total	99.25	0.70	91.07	5.66	101.76	0.84	99.00	8.10	101.84	1.18
n	27		24		24		26		26	
Metal composition (wt.%)										
Si	0.03	0.00	0.03	0.01	0.03	0.01	4.17	0.10	0.02	0.00
Fe	76.43	1.31	98.61	1.22	97.38	0.82	92.78	0.61	98.31	0.51
P	0.08	0.01	0.12	0.02	0.03	0.01	0.08	0.01	0.09	0.01
S	20.74	1.37	0.19	0.10	0.17	0.07	0.12	0.02	0.19	0.05
1n	3.15	0.50	2.47	1.07	2.37	0.64	2.26	0.17	2.45	0.29
O	-	-	-	-	-	-	-	-	-	-
Total	100.44	0.49	101.47	0.48	99.92	0.67	99.41	0.68	101.06	0.42
n	24		19		19		19		19	
$\log K_D^{In}$	-0.25	0.08	-0.85	0.19	-0.59	0.14	-2.66	0.25	-0.35	0.16
D_{In}	16.17	2.54	8.68	2.84	20.19	5.77	14.96	1.86	15.80	5.61
Run	E347	σ	E348	σ	E349	σ	E350	σ	E353	σ
Starting material	MFI-Si1		MFI-S1		MFI-S1		MFI-S1		MFI1	

Temperature (°C)	1550		1800		1700		2000		1550	
Pressure (Gpa)	2		2		2		2		2	
Duration (min)	15		2		3		1		7	
Pressure media	Talc-pyrex		$BaCO_3$		$BaCO_3$		$BaCO_3$		Talc-pyrex	
Capsule	MgO		MgO		MgO		MgO		MgO	
ΔIW	-5.2		-2.1		-2.2		-2.3		-2.4	
Silicate composition (wt.%)										
Na_2O	2.01	0.07	2.47	1.00	1.85	0.45	1.80	0.91	1.92	0.05
MgO	26.64	0.19	26.51	8.38	25.20	5.78	34.37	6.22	20.10	0.34
Al2O3	10.50	0.10	13.77	3.18	14.21	2.39	10.49	2.37	12.16	0.24
SiO2	48.78	0.61	32.00	2.40	37.27	0.94	32.21	2.74	43.95	0.67
K2O	0.21	0.02	0.22	0.08	0.17	0.04	0.17	0.07	0.15	0.02
CaO	8.84	0.14	13.23	3.68	11.06	2.24	10.44	3.39	9.75	0.14
FeO	0.32	0.09	10.73	1.86	9.14	0.65	8.28	1.84	8.57	0.13
P2O5	0.12	0.01	0.22	0.06	0.16	0.03	0.15	0.05	0.13	0.01
SO2	0.06	0.01	0.73	0.26	0.35	0.06	0.71	0.25	0.01	0.00
MnO	0.11	0.00	0.16	0.03	0.15	0.01	0.13	0.02	0.14	0.00
In2O3	0.10	0.03	0.20	0.04	0.18	0.03	0.14	0.05	0.25	0.02
TiO2	0.73	0.02	1.04	0.26	0.92	0.17	0.77	0.19	0.83	0.01
Total	98.42	0.59	101.29	1.01	100.66	0.90	99.66	1.09	97.95	0.77
n	28.00		23.00		23		23.00		15	
Metal composition (wt.%)										
Si	3.11	0.06	0.01	0.00	0.01	0.00	0.01	0.00	0.01	0.00
Fe	91.59	0.54	85.49	2.27	83.31	1.42	85.67	1.79	97.50	0.55

P	0.08	0.00	0.07	0.01	0.07	0.01	0.07	0.01	0.09	0.01
S	0.12	0.01	9.38	1.73	9.51	0.61	8.68	1.12	0.16	0.07
1n	2.68	0.18	3.07	0.60	4.14	0.92	3.07	0.75	2.05	0.40
O	0.39	0.10	0.63	0.12	0.98	0.26	0.89	0.14	0.22	0.05
Total	98.16	0.47	98.79	0.68	98.16	0.64	98.53	0.59	100.18	0.28
n	20.00		21		21		20		21	
$logK_D^{In}$	-2.36	0.22	-0.26	0.17	-0.16	0.13	-0.27	0.23	-0.76	0.09
D_{In}	33.86	8.93	19.01	5.58	28.42	7.89	28.02	11.76	10.20	2.20
Run	E354	σ	E355	σ	E356	σ	E389	σ	E392	σ
Starting material	MFI1		MFI-Si2		MFI-Si3		MFI-Si1		MFI-Si4	
Temperature (°C)	1600		1550		1550		1550		1550	
Pressure (Gpa)	2		2		2		2		2	
Duration (min)	6		15		15		18		18	
Pressure media	Talc-pyrex		Talc-pyrex		Talc-pyrex		Talc-pyrex		Talc-pyrex	
Capsule	MgO		MgO		MgO		MgO		MgO	
ΔIW	-2.3		-4.1		-2.8		-5.3		-6.2	
Silicate composition (wt.%)										
Na_2O	2.15	0.23	1.88	0.06	1.95	0.09	2.12	0.34	2.09	0.09
MgO	15.13	3.76	23.15	1.70	18.72	0.46	20.76	1.22	20.17	0.53
Al2O3	15.01	1.61	11.68	1.65	12.71	0.30	13.77	0.25	13.79	0.24
SiO2	42.23	0.53	48.67	0.66	44.63	0.62	49.68	1.25	49.81	0.98
K2O	0.20	0.03	0.23	0.03	0.20	0.01	0.20	0.07	0.21	0.03
CaO	12.94	1.52	10.19	0.61	10.89	0.15	11.21	0.33	11.49	0.14
FeO	9.27	0.32	1.10	0.08	5.28	0.09	0.29	0.13	0.09	0.03
P2O5	0.10	0.01	0.08	0.00	0.08	0.01	0.09	0.02	0.09	0.01

SO2	0.01	0.00	0.01	0.00	0.01	0.00	0.04	0.01	0.08	0.01
MnO	0.08	0.01	0.08	0.00	0.08	0.01	0.08	0.02	0.06	0.01
In2O3	0.16	0.02	0.13	0.03	0.16	0.02	0.07	0.03	0.07	0.02
TiO2	0.54	0.07	0.44	0.05	0.45	0.06	0.52	0.10	0.48	0.05
Total	97.81	0.70	97.65	1.22	95.16	1.38	98.83	1.74	98.42	1.09
n	19		20		15		18		19	
Metal composition (wt.%)										
Si	0.01	0.00	0.32	0.01	0.02	0.00	2.79	0.06	6.37	0.10
Fe	96.94	0.56	96.15	0.31	93.08	0.87	92.33	0.60	86.75	0.48
P	0.09	0.00	0.08	0.00	0.16	0.03	0.07	0.00	0.09	0.01
S	0.18	0.05	0.15	0.02	0.53	0.15	0.11	0.02	0.05	0.01
1n	2.87	0.50	2.71	0.18	5.48	0.84	2.53	0.38	1.65	0.22
O	0.24	0.06	0.22	0.04	0.22	0.05	0.55	0.17	0.34	0.08
Total	100.47	0.36	99.78	0.33	99.62	0.55	98.53	0.36	95.44	0.53
n	17		19		10		21		20	
$\log K_D^{In}$	-0.35	0.09	-1.69	0.10	-0.78	0.11	-2.33	0.19	-3.21	0.24
D_{In}	22.39	4.66	26.18	5.14	19.49	4.92	43.20	9.80	28.93	7.42
Run	Z1824	σ	H4950	σ	Z1959	σ	Z1823	σ	H4951	σ
Starting material	A-MF1		A-MF1		A-MF1		A-MF1		A-MF1	
Temperature (K)	2200		2000		2200		2300		2100	
Pressure (Gpa)	18		12		16		14		14	
Duration (min)	4		2		1		1		2	
Pressure media	$MgO+Cr_2O_3$		$MgO+Cr_2O_3$		$MgO+Cr_2O_3$		$MgO+Cr_2O_3$		$MgO+Cr_2O_3$	
Capsule	MgO SC		MgO SC		MgO SC		MgO SC		MgO SC	
ΔIW	-2.8		-2.7		-2.7		-2.6		-2.6	

silicate wt.%										
In_2O_3	0.23	0.00	0.11	0.00	0.13	0.01	0.13	0.00	0.12	0.00
n	9		13		15		13		14	
metal wt.%										
In	2.26	0.03	1.91	0.08	2.22	0.06	2.23	0.05	2.10	0.09
n	33		14		9		39		11	
$logK_D^{In}$	-0.94	0.03	-0.60	0.03	-0.58	0.03	-0.54	0.01	-0.55	0.03
D_{In}	13.73	0.19	26.11	1.62	25.74	1.39	25.92	0.62	25.68	1.39
Run	Z1956	σ	Z1821	σ	Z1820	σ	Z1825	σ	H4735	σ
Starting material	A-MF1		A-MF1		B-MFS1		B-MFS1		B-MFS1	
Temperature (K)	2300		1750		1706		2200		2000	
Pressure (Gpa)	20		7		7		18		10	
Duration (min)	1		1		10		4		10	
Pressure media	$MgO+Cr_2O_3$		$MgO+Cr_2O_3$		$MgO+Cr_2O_3$		$MgO+Cr_2O_3$		$MgO+Cr_2O_3$	
Capsule	MgO SC		MgO SC		MgO SC		MgO SC		MgO SC	
ΔIW	-2.5		-2.3		-1.9		-2.1		-2.1	
silicate wt.%										
In_2O_3	0.18	0.04	0.20	0.07	0.28	0.01	1.07	0.08	0.21	0.02
n	15		19		13		22		30	
metal wt.%										
In	2.16	0.06	1.41	0.06	1.50	0.10	2.52	0.12	1.36	0.08
n	19		18		10		43		28	
$logK_D^{In}$	-0.65	0.11	-0.75	0.15	-0.55	0.04	-1.08	0.04	-0.67	0.04
D_{In}	16.98	4.13	9.16	3.20	7.10	0.57	2.89	0.25	7.70	0.74
Run	Z1957	σ	H4952	σ	EK-02-X17	σ	EK-03-JS1	σ		

Starting material	B-MFS1		B-MFS1		D-Pm1		D-PSm2	
Temperature (K)	2300		2100		4100		4200	
Pressure (Gpa)	20		12		51		47.5	
Duration (min)	1		2					
Pressure media	$MgO+Cr_2O_3$		$MgO+Cr_2O_3$					
Capsule	MgO SC		MgO SC					
ΔIW	-2.2		-2.0		-1.46		-1.36	
silicate wt.%								
In_2O_3	0.46	0.08	0.36	0.02	0.60	0.03	0.28	0.01
n	13		10					
metal wt.%								
In	1.66	0.16	1.95	0.12	1.18	0.01	0.50	0.01
n	16		15					
$\log K_D^{In}$	-1.01	0.09	-0.68	0.04	-0.73		-0.73	
D_{In}	4.47	0.88	6.36	0.54	2.29		1.97	

3.3 The partitioning of In between metal and silicate

The partitioning of In between metal and silicate can be described by the exchange reaction:

$$InO_{n/2}^{silicate} + \frac{n}{2}Fe^{metal} = \frac{n}{2}FeO^{silicate} + In^{metal} \quad (3.3.1)$$

Where n refers to the valence state of In in silicate melt and its value can be determined by fO_2 and partition coefficient (defined as $D_M^{metal} = X_M^{metal}/X_{MO_{n/2}}^{silicate}$), and is discussed below. When the reaction 3.3.1 reaches equilibrium, its equilibrium constant (K) can be expressed as:

$$K = \frac{\left(a_{FeO}^{silicate}\right)^{n/2}(a_{In}^{metal})}{(a_{InO_{n/2}}^{silicate})(a_{Fe}^{metal})^{n/2}} \quad (3.3.2)$$

a represents the activity of each component and can be calculated with $a_i=\gamma_i X_i$, in which γ_i is activity coefficient and X_i is the molar fraction of component i. Substitute γ_i and X_i to Eqn.3.3.2, the equilibrium constant in log-scale can be written as:

$$logK = \log\left(\frac{X_{In}^{metal}}{X_{In}^{metal}}\right) + \log\left(\frac{\gamma_{In}^{metal}}{\gamma_{InO_{n/2}}^{silicate}}\right) + \frac{n}{2}log\frac{X_{FeO}^{silicate}\gamma_{FeO}^{silicate}}{X_{Fe}^{metal}\gamma_{Fe}^{metal}} \quad (3.3.3)$$

In which the third term can be replaced with oxygen fugacity relative to iron-wüstite (ΔIW) buffer:

$$\Delta IW = 2\log\left(\frac{a_{FeO}}{a_{Fe}}\right) = 2\log\left(\frac{X_{FeO}^{silicate}\gamma_{FeO}^{silicate}}{X_{Fe}^{metal}\gamma_{Fe}^{metal}}\right) \approx 2\log\left(\frac{X_{FeO}}{X_{Fe}}\right) \quad (3.3.4)$$

We used a simplified approach by assuming an ideal model with the activities of Fe and FeO in metal and silicate approximately equal to their molar fractions, and the experimental fO_2 can be expressed as:

$$\Delta IW \approx 2\log\left(\frac{X_{FeO}}{X_{Fe}}\right) \quad (3.3.5)$$

Although this simplified calculation may have some deviation to non-ideal situation (~ 0.4 log units at most, as suggested in Siebert et al. (2013)), it can be used as a convenient way to calculate fO_2. The fO_2 of our experiments vary from ΔIW -1.9 to ΔIW -5.3 (Table. 2). Most of experiments fall in the range ΔIW -2 to -3, only the Si

metal doped run products have a significant reduced redox state (down to ~ ΔIW -5) due to the reaction of Si and FeO.

At given *P-T* condition and melt composition, the value of logK can be seen as a constant. Furthermore, following Wade and Wood (2005), the oxide activity coefficients of low charge cations (< +4) can also be approximately considered as a constant as they should not highly depend on the silicate composition. If assuming that activity coefficients of metal are also near constants at these given conditions, and then substituting D_{In}^{metal} to Eqn.3.3.3, a function of D_{In}^{metal} and oxygen fugacity can be obtained:

$$logD_{In}^{metal} = -\frac{n}{4}\Delta IW + constant \quad (3.3.6)$$

According to Eqn.3.3.6, the valence state (n) of indium in silicate melt can be determined by the slope of $\log D_{In}^{metal}$ vs. ΔIW. However, Vogel et al. (2018) observed that the effect of Si can significantly vary the elemental activity coefficients in metal phase, and deviate the linear relationship of $\log D_{In}^{metal}$ and ΔIW. Therefore, the run products with significant amount of Si partitioned into metal should be avoided for determining elemental valence state. The relationship of partitioning coefficient of In and oxygen fugacity is shown in Figure.2, in which the slope is -0.61 ± 0.07, approaching a valence state of 3+, indicating In as a trivalent cation in silicate melt during metal-silicate experiments. This valence state is consistent with the estimated results from the recent literatures (Righter et al., 2017; Righter et al., 2018a; Steenstra et al., 2020), and therefore In^{3+} is favored in the following calculations and discussions of this study.

The Eqn.3.3.3 can also be written as following:

$$logK = log\frac{\left(X_{FeO}^{silicate}\right)^{n/2}(X_{In}^{metal})}{(X_{InO_{n/2}}^{silicate})(X_{Fe}^{metal})^{n/2}} + log\frac{\gamma_{In}^{metal}}{(\gamma_{Fe}^{metal})^{n/2}} + log\frac{(\gamma_{FeO}^{silicate})^{n/2}}{\gamma_{InO_{n/2}}^{silicate}} \quad (3.3.7)$$

Where the first term of Eqn.3.3.7 is named as the exchange coefficient (K_D), which is a function of temperature and pressure. It can also be expressed as $K_D^M = D_{In}^{metal}/(D_{Fe}^{metal})^{n/2}$, which can be directly determined from experimentally measured molar fractions of In and Fe. The partition coefficient of In is normalized here to the

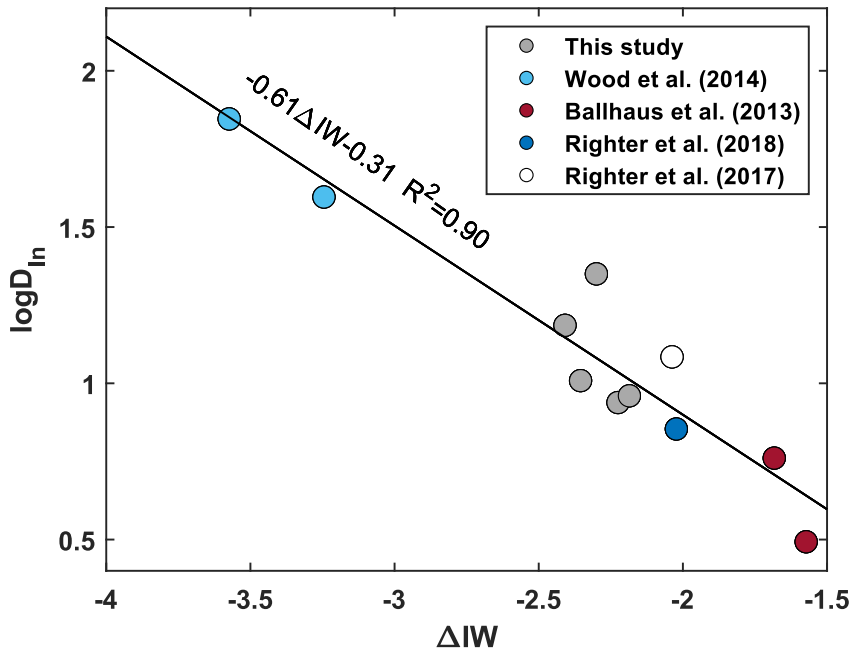

Figure. 2. The partitioning coefficient of In is plotted as a function of variable oxygen fugacity relative to ΔIW buffer. The slope is corresponding to $-n/4$, which is -0.61 ± 0.07, approaching a valence state of 3+. The data points are taken from this study and literatures (see legend in figure), in which experiments were performed at similar P-T conditions (1773 to 1873 K, 1 to 2 GPa), and absence of light elements (sulfur, silicon and carbon, whose molar fraction ≤ 0.01).

partitioning of Fe, and therefore allows to compare elemental siderophile behavior independently of oxygen fugacity. The relationship of K_D and the reciprocal of temperature is shown in Figure 3 where K_D is not observed with a clear relationship with both temperature and pressure conditions. The effects of light elements are also observed. S has either a positive or negative effect along with pressure variations, and Si displays a strong negative effect on the partitioning of In as observed in previous work (e.g., Righter et al., 2017; Steenstra et al., 2020), which can decrease the value of K_D by several orders of magnitude. The effect of S and Si can be corrected with interaction parameter approach (ε_M^S and ε_M^{Si}) described in Ma (2001), and a detailed discussion can be found in section 4.2.

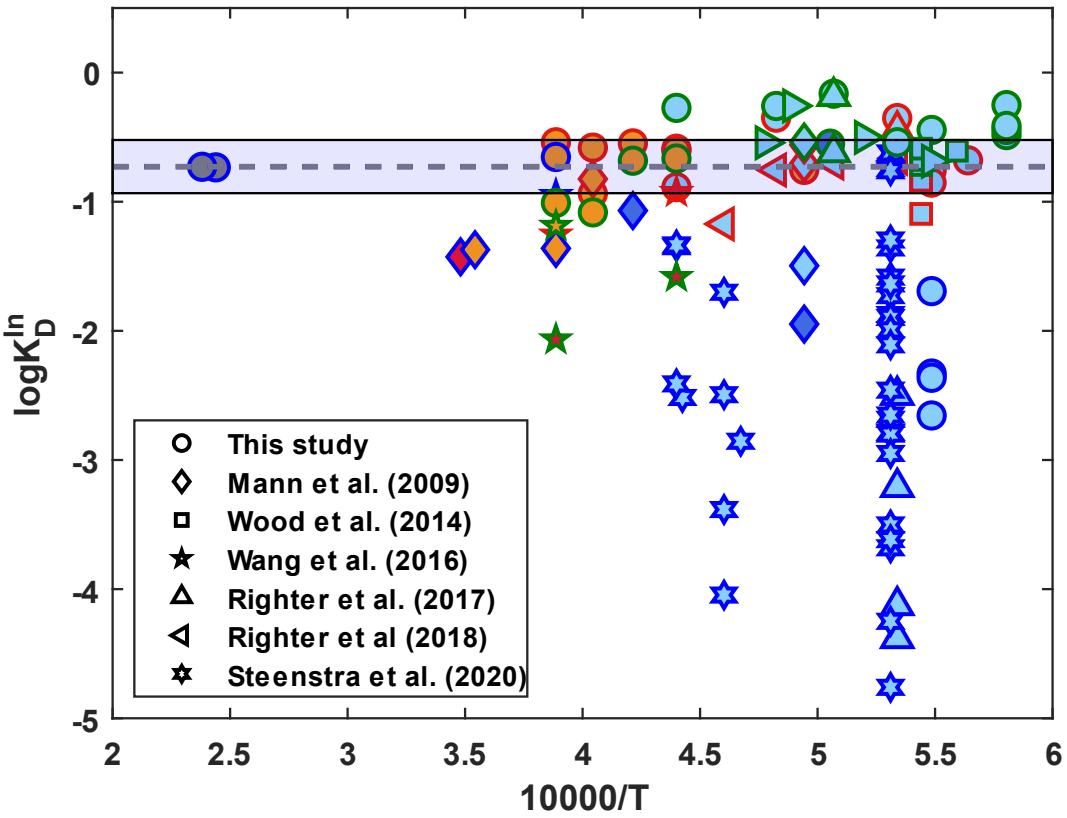

Figure. 3. Exchange coefficient (K_D) in log-scale is plotted as a function of reciprocal temperature. These plotted data are taken from this study and literatures which have been shown in legend. The experimental conditions cover a wide P-T range: 1823 K to 4200 K for temperature and 1 GPa to 51 GPa for pressure. The variable pressure is displayed with different colors: light blue: 1-5 GPa; blue: 6-10 GPa; orange: 11-19 GPa; red: 20-25 GPa; grey: 47-51 GPa. All the experiments are carbon-free experiments, and light elements only include S and Si, which have been marked in this figure: the symbols with blue circles are Si-bearing run products; the symbols with green circles are S-bearing run products; the other symbols with red circles are the light elements absence samples. The light blue area shows the range of regressed parameter *a*.

3.4 The In isotopic composition of metal and silicate phase

The In isotopic composition of measured silicate and metal samples are reported as δ^{115}In, which is expressed following:

$$\delta^{115}In\ (‰) = \left[\frac{(^{115}In/^{113}In)_{sample}}{(^{115}In/^{113}In)_{IPGP-In}} - 1\right] \times 1000 \quad (3.4.1)$$

The isotopic fractionation between silicate and metal can be calculated as follows:

$$\Delta^{115}In_{silicate-metal}\ (‰) = \delta^{115}In_{silicacte} - \delta^{115}In_{metal} \quad (3.4.2)$$

The In isotopic compositions and fractionations are reported in Table.3. The errors are reported as two standard-deviation (2SD) of replicate measurements. The measured samples can be divided into three groups: Fe-In series, Fe-In-S series and Fe-In-Si series. Both Fe-In series and Fe-In-Si series show resolvable In isotopic fractionation between silicate and metal, in which the heavier In isotopes are enriched in the silicate part, corresponding to a $\Delta^{115}In_{metal\text{-}silicate}$ varying from 0.15 ± 0.08 to 0.25 ± 0.02 ‰ (Fe-In series) and 0.17 ± 0.06 to 0.39 ± 0.07 ‰ (Fe-In-Si series). The isotopic fractionations for Fe-In-S series samples are less significant with a $\Delta^{115}In_{metal\text{-}silicate}$ range of 0.02 ± 0.09 to 0.14 ± 0.10‰.

4. Discussion

4.1 Chemical equilibrium and potential evaporation/diffusion loss of In

The efficiency of In to reach equilibrium was tested on three samples (E335, E338 and E339), which were performed with the same starting materials (MFI-S1) and pressure (2 GPa), the lowest temperature (1623 K) and variable durations (10 min, 30 min and 60 min). The partitioning results obtained with their $\log K_D$ correspond to -0.48 ± 0.13 (E335), -0.44 ± 0.10 (E338) and -0.41 ± 0.10 (E339), which do not show any resolvable difference within uncertainties, indicating chemical equilibrium between liquid metal and silicate can be reached in less than 10 min for these run products conducted at the lowest temperature. With increasing temperature, equilibrium between metal and silicate is likely be achieved even much faster as observed in Thibault and Walter (1995) and Corgne et al. (2008) , who found that equilibrium could be reached within a few seconds at ~ 2000°C. These observations allow us to keep the duration within a relative short time (1 min to 10 min, depending on experimental temperature) to minimize potential metal diffusion into surrounding MgO capsule.

The potential isotopic fractionation induced by unexpected evaporation and/or diffusion loss of In is required to be taken into account. Given that In is a moderately volatile element, the metal-silicate experiment performed at high temperature may

Table 3. The In isotopic composition of metal-silicate experimental run products.

Run	δ^{115}In	2SD	Δ^{115}In $_{silicate-metal}$	2SD	T(K)	Xs (mol.%)	Xsi (mol.%)	ΔIW	$\delta^{115}In_{bulk}$	2SD
E348 silicate	0.13	0.05	0.08	0.08	2073.00	0.15	0.00	-2.05	-0.03	0.09
E348 metal	0.06	0.05								
E349 silicate	0.13	0.03	0.03	0.07	1973.00	0.16	0.00	-2.16	0.01	0.07
E349 metal	0.11	0.06								
E335 silicate	0.23	0.03	0.03	0.07	1723.00	0.12	0.00	-2.05	0.11	0.07
E335 metal	0.20	0.07								
E337 silicate	0.18	0.07	0.10	0.07	1873.00	0.13	0.00	-2.02	0.00	0.09
E337 metal	0.08	0.01								
E350 silicate	0.12	0.08	0.14	0.10	2273.00	0.14	0.00	-2.29	-0.10	0.12
E350 metal	-0.02	0.06								
E336 silicate	0.06	0.08	0.02	0.09	1823.00	0.14	0.00	-2.43	-0.06	0.12
E336 metal	0.04	0.05								
E340 silicate	0.11	0.04	0.06	0.09	1723.00	0.32	0.00	-1.90	-0.04	0.09
E340 metal	0.05	0.08								
E355 silicate	0.38	0.05	0.21	0.08	1828.00	0.00	0.01	-4.15	0.10	0.09
E355 metal	0.17	0.06								
E389 silicate	0.40	0.04	0.26	0.05	1823.00	0.00	0.05	-5.29	0.07	0.06
E389 metal	0.14	0.03								
E344 silicate	0.26	0.05	0.17	0.06	1827.00	0.00	0.08	-5.11	0.02	0.07
E344 metal	0.10	0.03								
E347 silicate	0.35	0.06	0.39	0.07	1823.00	0.00	0.06	-5.20	-0.13	0.09
E347 metal	-0.04	0.03								

E353 silicate	0.33	0.04	0.24	0.05	1833.00	0.00	0.00	-2.35	0.04	0.06
E353 metal	0.09	0.04								
E354 silicate	0.26	0.03	0.16	0.04	1873.00	0.00	0.00	-2.27	0.02	0.04
E354 metal	0.10	0.02								
E356 silicate	0.23	0.05	0.04	0.10	1818.00	0.01	0.00	-2.80	0.10	0.09
E356 metal	0.19	0.08								
E346 silicate	0.26	0.02	0.25	0.02	2073.15	0.00	0.00	-2.31	-0.06	0.03
E346 metal	0.02	0.02								
E343 silicate	0.14	0.05	0.15	0.08	2273.00	0.00	0.00	-2.56	-0.09	0.09
E343 metal	-0.01	0.07								
Starting material	0.10	0.01								

result in an additional evaporative loss of In and/or leave the evaporated residue with a heavier In isotopic composition as observed in previous evaporation experiments despite the experiments were conducted in controlled atmosphere furnace at 1 bar (e.g., Sossi et al., 2020; Wimpenny et al., 2019; Yu et al., 2003). Most MVEs are observed to have a higher volatility with increasing temperature and reduced oxygen fugacity conditions (e.g., Norris and Wood, 2017; Sossi et al., 2019). Therefore, if evaporation-induced In loss and isotopic fractionation occurred, a correlation between In isotopic composition of bulk run products and temperature/oxygen fugacity/duration should be observed. The In isotopic composition of bulk samples are calculated with the mass-balance approach using the metal and silicate fraction reported in Table.1. Although this metal and silicate fractions may have some deviation to their initial fraction due to the dissolution of MgO capsule, this approach is considered as a simplified and convenient way to provide the bulk In isotopic composition at our best.

The correlation of bulk In isotopic compositions along with duration/temperature/oxygen fugacity are shown in Figure 4, in which most data fall into the $\delta^{115}In_{bulk}$ range of -0.1 to +0.1‰ regardless of the variations of experimental conditions. This observation indicates that no evaporative loss of In occurred during heating process or that evaporation process did not significantly fractionate In isotopes due to the high pressure condition where mass transport rate from liquid to gas can be strongly suppressed and limit the potential isotopic fractionation (Sossi et al., 2020; Young et al., 2019). The same conclusion can also be given on the diffusive loss of In to MgO capsule. If diffusion process would have fractionated In isotopes, the samples with longer durations and higher temperature should have the most fractionated isotopic composition, which is not observed within analytical precision.

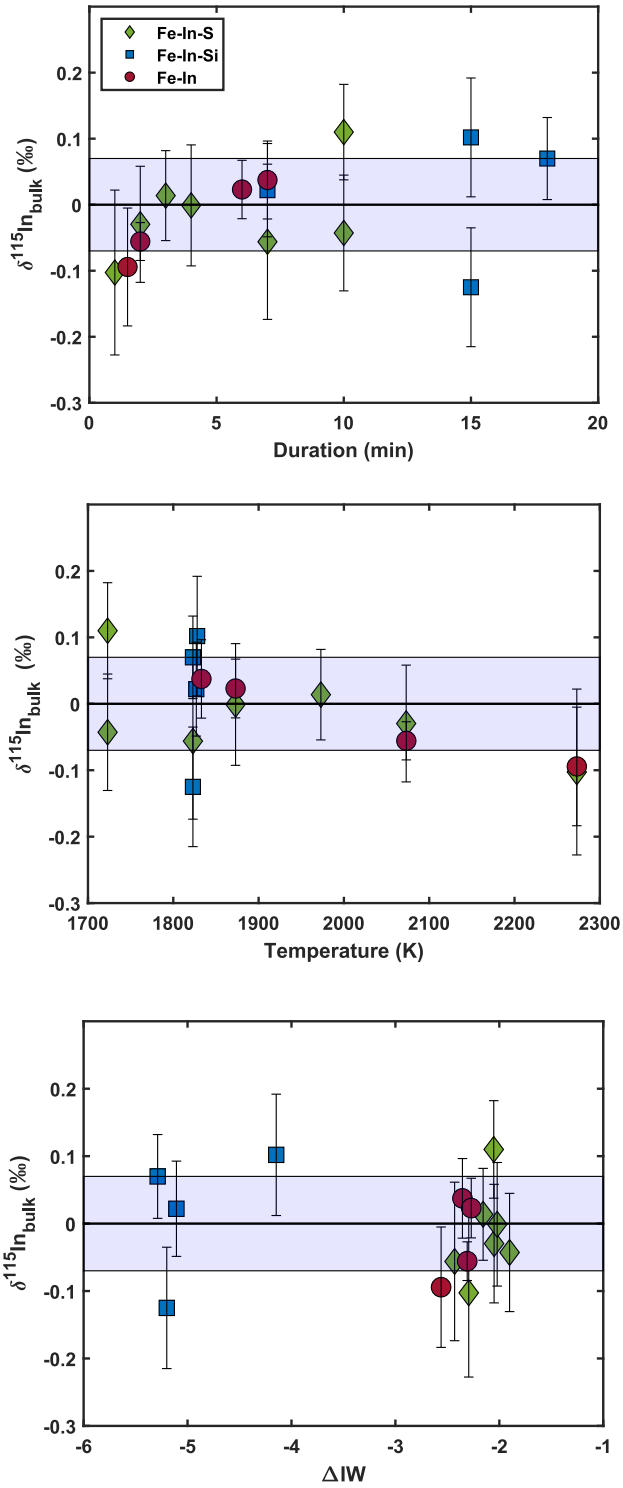

Figure. 4. The In isotopic composition of bulk metal-silicate samples plotted vs. variable duration, temperature and oxygen fugacity. The bulk In isotopic composition was normalized to their starting materials and calculated by a mass-balance approach and described in section 4.1. The shaded area represents the two-standard deviation (2SD = 0.07 ‰) of the whole batch of samples estimated from the bracketing standard of different sequences in this batch of analyses.

4.2 Metal-silicate partitioning of In and its budget in the Earth

4.2.1 The parameterization of metal-silicate partitioning of In

For the exchange reaction 3.3.1 that describes the partitioning behavior of In between metal and silicate, the equilibrium constant *K* can be expressed as a function of temperature, pressure and melt structure following:

$$logK = a + \frac{b}{T} + \frac{cP}{T} + d\frac{nbo}{t} \quad (4.2.1)$$

Where *a, b, c* and *d* are constants that can be regressed by least-square multi-variable approach with the experimental dataset. *nbo/t* represents the molar ratio of non-bridging oxygens over tetrahedral cations in the silicate melt. For low-charge cations (≤3+), the effect of silicate melt structure can be assumed negligible (e.g., Siebert et al., 2011) and therefore, this equation can be simplified as:

$$logK = a + \frac{b}{T} + \frac{cP}{T} \quad (4.2.2)$$

In which *log K* can be considered as a function of *P-T* conditions, and the values of *a*, *b* and *c* can be regressed using results of experiments free of light elements (S, Si, C, etc.) in the metal phase. Combining the results of the present work and results from previous studies of In partitioning (Ballhaus et al., 2013b; Mann et al., 2009; Righter et al., 2017; Righter et al., 2018a; Wang et al., 2016a; Wood et al., 2014a), it can be observed that the effects of temperature and pressure are negligible, and therefore only *a* value is regressed (*a* = -0.79 ± 0.21). Using Eqn 3.3.7, the exchange coefficient can be expressed as:

$$logK_D = a + \frac{b}{T} + \frac{cP}{T} - log\gamma_{In}^{metal} + \frac{n}{2}log\gamma_{Fe}^{metal} \quad (4.2.3)$$

For the S- and Si- bearing samples, the activity coefficients of Fe and In in metal phases can be calculated with the interaction parameter approach described by Ma (2001). γ_{Fe}^{metal} and γ_{In}^{metal} can be approximately expressed as:

$$ln\gamma_{Fe}^{metal} = \varepsilon_S^S(X_S + \ln(1 - X_S)) + \varepsilon_{Si}^{Si}(X_{Si} + \ln(1 - X_{Si})) \quad (4.2.4)$$

and

$$ln\gamma_{In}^{metal} = ln\gamma_{Fe}^{metal} + ln\gamma_{In}^{0} - \varepsilon_{In}^{In}\ln(1 - X_{In}) - \varepsilon_{In}^{S}X_S\left(1 + \frac{\ln(1-X_S)}{X_S} - \frac{1}{1-X_{In}}\right) -$$

$\varepsilon_{In}^{Si} X_{Si} \left(1 + \frac{\ln(1-X_{Si})}{X_{si}} - \frac{1}{1-X_{In}}\right)$ (4.2.5)

The values of ε_i^j (i and j refer to the solutes in metal including S, Si and In) have a relationship with temperature following:

$$\varepsilon_i^j(T) = \varepsilon_i^j(T_0)\frac{T_0}{T} \quad (4.2.6)$$

A reference temperature T_0 = 1873 K is used in this study. The values of ε_S^S and ε_{Si}^{Si} are taken from Steelmaking (1988). The values of ε_{In}^S and ε_{In}^{Si} are estimated and discussed in the following section 4.2.2.

4.2.2 The pressure-dependent interaction parameter $\boldsymbol{\varepsilon_{In}^S}$ and $\boldsymbol{\varepsilon_{In}^{Si}}$

The estimation of ε_{In}^S and ε_{In}^{Si} follows the approach described in Wood et al. (2014a), at given temperature and pressure, the Eqn.4.2.3 can be re-arranged as below:

$$lnK_D - \left(\frac{n}{2} - 1\right) ln\gamma_{Fe}^{metal} = constant - ln\gamma_{In}^0 + \varepsilon_{In}^j \ln\left(1 - X_j\right) \quad (4.2.7)$$

Where j refers to S or Si. At given temperature, $ln\gamma_{In}^0$ is also constant. Therefore, the value of ε_{In}^S and ε_{In}^{Si} can be estimated with the slope of this linear-relationship (Figure. 5). It is notable that both ε_{In}^S and ε_{In}^{Si} are observed to show a pressure-dependent behavior, which is consistent with previous studies from Wang et al. (2016a) and Steenstra et al. (2020). ε_{In}^S exhibits an opposite behavior in between low pressure (2 GPa) and high pressure (≥ 14 GPa), indicating that the presence of sulfur may increase the partitioning of In under low pressure, and decrease its partitioning under high pressure conditions. ε_{In}^{Si} likely decreases with increasing pressure, although the high-pressure data points containing Si in the metal phase are limited. The estimated values of ε_{In}^S and ε_{In}^{Si} are listed in Table. 4.

Table 4. Regressed parameters used in this study

a	b	c	ε_{In}^{S} (1873 K)	ε_{In}^{Si} (1873 K)
- 0.79±0.21	-	-	-2.87±0.74 (2 GPa)	38.09±3.75 （1 Gpa)
			0.86±0.18 （14 GPa）	28.05±2.87 (2 Gpa)
			1.16±0.39 (18 Gpa)	17.85±3.13 (>18 Gpa)

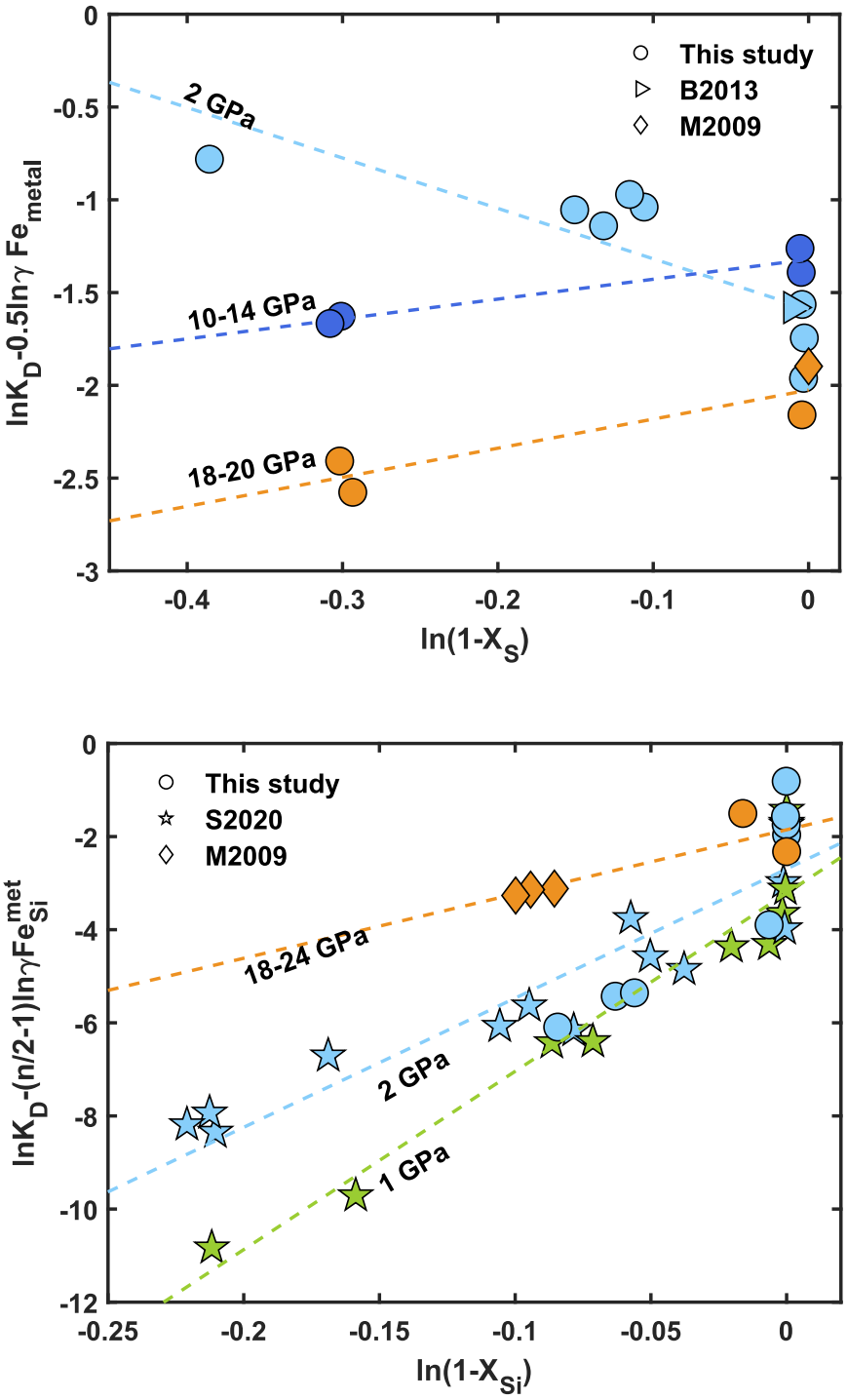

Figure. 5. The metal-silicate partitioning behavior plotted as a function of S and Si content in metal. The different colors represent experimental conditions: Green: 1 GPa, 1883 K; Light blue: 2 GPa, 1723 to 1823 K; Dark blue: 10- 14 GPa, 2273 to 2373 K Orange: a) S:18-20 GPa, 2473-2573 K; b) Si:18-24 GPa, 2573-2873 K; The fitted interaction parameters ε_{ln}^{S} and ε_{ln}^{Si} are normalized to the reference temperature 1873 K and listed in Table. 4.

This pressure-dependent effect can be explained as the results of the structural transitions occurring in the alloy of iron and light elements, e.g., Fe-C, Fe-Si and Fe-S alloys (Fei et al., 1997; Fei et al., 2000; Morard et al., 2007; Sanloup et al., 2011; Shibazaki et al., 2015). These studies reported a discontinuous evolution of compact structure along with pressure with a significant structural change at ~5 GPa, which is consistent with the observed relationship variations between pressure and partitioning coefficients of Ni, Co and W(Sanloup et al., 2011 and references therein). In addition, the structural transition can also take place under higher pressure (~ 13 - 15 GPa) in Fe-S alloy (Morard et al., 2007). Such pressure-dependent interaction parameters for MVEs (Sn, Tl, In, Zn and Cd) have also been recently reported in some metal-silicate partitioning experimental works (Kubik et al., 2021a; Kubik et al., 2021b; Steenstra et al., 2020; Wang et al., 2016a), and the present work on In partitioning further confirms the existence of this effect.

Given that interaction parameters of In are pressure-dependent, the extrapolated values from low pressure experiments may result in erroneous assessment of the partitioning of In at conditions of Earth's core formation. Therefore, we examined the applicability of these extrapolated ε_{In}^{S} and ε_{In}^{Si} values on the experiments with a wide range of pressure (2 ~ 51 GPa), spanning from approaching planetesimals size to the final P-T conditions of the base of deep magma ocean (~ 40-60 GPa, e.g., Bouhifd and Jephcoat, 2003; Gessmann and Rubie, 2000; Siebert et al., 2012; Wade and Wood, 2005). The results of log *K* are shown in Figure. 6, in which it can be observed that the S- and Si- bearing samples in this study can be corrected to the similar partitioning behaviors obtained with light elements-free samples. Moreover, the highest P-T conditions samples (~ 50 GPa and ~ 4000 K) performed with DAC are approaching the regressed results, indicating a proper applicability for the values of ε_{In}^{S} and ε_{In}^{Si} estimated from medium pressure (18 to 24 GPa). This observation suggests that the usage of the low pressure-derived interaction parameters, in particular ε_{In}^{Si} which has a very strong effect on In partitioning between metal and silicate, may result in an underestimation of the Earth's core In content.

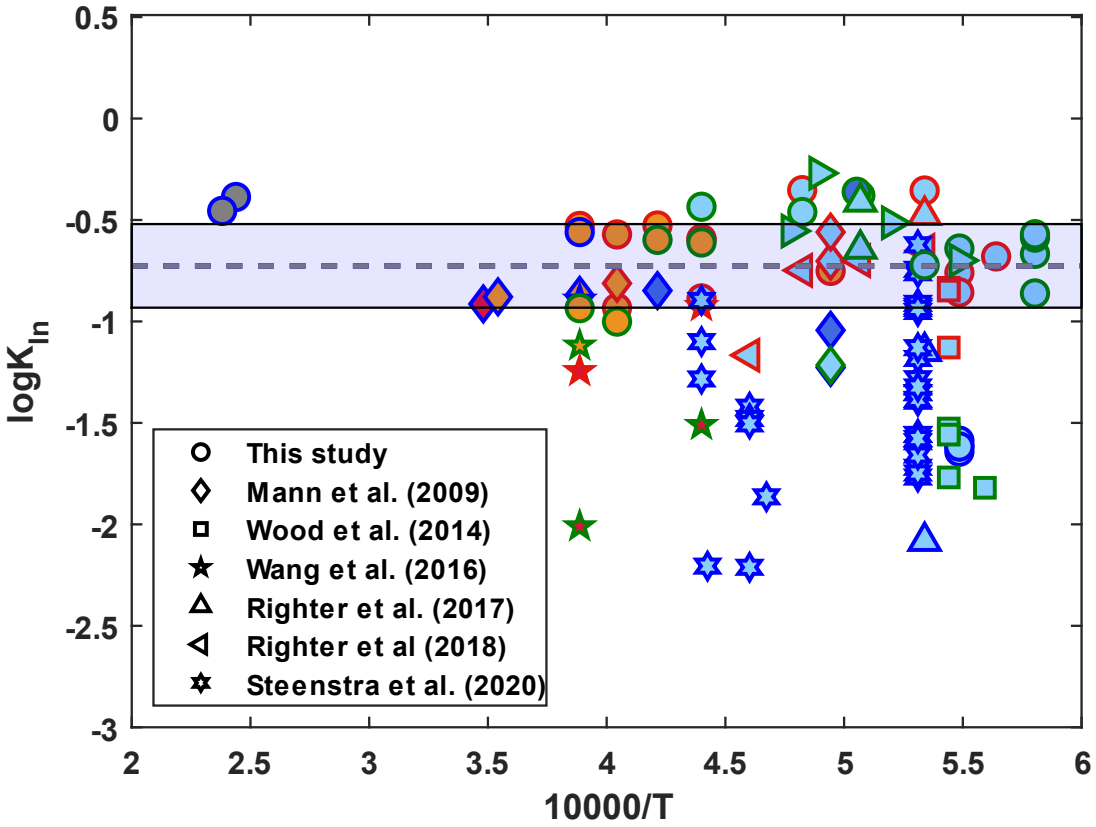

Figure. 6. The values of log$K$ plotted as function of reciprocal temperature. The plotted data are from this study and literatures shown in figure. The symbols and colors are the same as described in Figure. 3. The log$K$ values of S- and Si-bearing samples have been corrected with the interaction parameters that fitted in this study. These corrected samples exhibit similar partitioning behaviors as light elements free samples. The highest P-T samples (grey points) applied the ε_{In}^{S} and ε_{In}^{Si} values extrapolated from 18-24 GPa experiments from this study and literatures.

4.2.3 The Earth's In budget

In comparison with the canonical volatility trend, indium is over-abundant in the Earth's present mantle (Lodders, 2003; Witt-Eickschen et al., 2009; Wood et al., 2019; Yi et al., 2000). In order to explain its over-abundance in the BSE, the origin of In on Earth was attributed to the late-delivery of volatile-rich materials during the last stages of Earth's accretion before core-formation ceased (e.g., Braukmüller et al., 2019). In this hypothesis, the Earth is considered to accrete from highly volatile depleted materials and the major elemental budgets of MVEs whose T_c^{50} are lower than Zn were

brought to the Earth by a late delivery of carbonaceous-like volatile-rich materials, resulting in the 'hockey-stick' volatile depletion pattern reported by (Braukmüller et al., 2019). This hypothesis relies on the assumption that In must behave as a lithophile element under the conditions of Earth's core formation. However, our experimental results demonstrate that In does not behave as lithophile element during Earth's core-formation.

In this study, we used our regressed parameters to model the evolution of In partitioning coefficient during core-formation. The partitioning coefficient of In, D_{In}, can be expressed as a function of P-T and compositions by re-arranging the Eqn.4.2.3:

$$\log(D_{In}) = a + \frac{b}{T} + \frac{cP}{T} - \frac{n}{2} log \frac{X_{FeO}^{silicate}}{X_{Fe}^{metal}} - log\gamma_{In}^{metal} + \frac{n}{2} log\gamma_{Fe}^{metal} \quad (4.2.7)$$

Where a, b, c, ε_{In}^{S} and ε_{In}^{Si} used the values listed in Table. 3, ε_{s}^{S} and ε_{Si}^{Si} are taken from Steelmaking (1988). The In partitioning behaviors in both homogeneous and heterogeneous accretion scenarios are modelled and shown in Figure. 7. The homogenous accretion model assumed a continuous accretion process with a constant oxygen fugacity (ΔIW = -2.3), which corresponds to the present mantle concentration of FeO (~ 8 wt.%, Palme and O'Neill (2014)). There is an issue on the equilibration efficiency between impactor's core and surrounding mantle silicate. According to Deguen et al. (2011), the impactor's core may not fully equilibrate with the surrounding mantle silicate, and only limited fraction of metal can achieve chemical equilibration. Based on this observation, we followed the approach for quantifying equilibration efficiency in Deguen et al. (2014) with an assumption of the value of k, which describes the fraction of metal phase equilibrium with silicate, as 1 and 0.5, respectively, which means full equilibration and half equilibration, and our results do not exhibit significant discrepancy on the evolution curves for both equilibration efficiencies (Figure. 7a). Therefore, we made a simplification for the following calculations by assuming that the metallic cores of impactors can be fully emulsified as they sink into the base of magma ocean, and the equilibrated fraction of impactor's metallic core is 100%.

Several potential accretion paths were modelled in Figure 7. As mentioned above, the Figure 7a displays the evolution of indium partitioning along with a homogenous

accretion model, in which the Earth was assumed to accrete at fixed oxygen fugacity (ΔIW = -2.3). As a comparison, an area of 'apparent partitioning coefficient' is also shown in figures. The 'apparent partitioning coefficient' is estimated by comparing its abundance in the BSE and CI with a lithophile element of similar volatility. Assuming that they have a similar CI -Mg normalized abundance in the bulk Earth, it is possible to estimate the partitioning coefficient that should produce the observed depletion of In in the BSE. In Chapter 2, we have suggested that In has a similar or is even less volatile than Zn under non-nebular environment. Therefore, fluorine (F), which has a volatility in between Zn and Rb, and is a strong lithophile element, is selected to estimate the apparent partitioning coefficient. F has a T_C^{50} of 674 K (Wood et al., 2019) or 734 K (Lodders, 2003), similar to the estimates of T_C^{50} of Zn of 704 K (Wood et al., 2019) or 726 K (Lodders, 2003).

Three heterogeneous accretion models were shown in Figure 7. In these models, the Earth is assumed to accrete and grow step-by-step with 0.1% Earth's mass volatile depleted embryos at the beginning, followed by the addition of a 10 % Earth's mass CI-like materials at the end to simulate the late accretion hypothesis (e.g., Braukmuller et al., 2019). The late delivered volatile-rich material is set to 10% Earth's mass according to some constraints from previous metal-silicate experiments and isotopic studies on MVEs (e.g., Braukmuller et al., 2019; Kubik et al., 2021a; Kubik et al., 2021b; Schönbächler et al., 2010). This proportion approaches the mass of Theia (Mars-size) considered to have cause the Moon forming impact (Hartmann and Davis, 1975). The evolution path of fO_2 is set as:

i) fixed fO_2 at ΔIW = -2.3, assuming the FeO concentration in Earth's mantle is constant during Earth's accretion;

ii) highly reduced model, which assume an increased FeO concentration in Earth's mantle along with the core-formation process (Rubie et al., 2011; Wade and Wood, 2005; Wood et al., 2006). The fO_2 varies from reduced to oxidized condition (ΔIW-4.3 to ΔIW-2.3), following the path described in Siebert et al. (2013);

iii) oxidized model. This model assumes that the FeO concentration in magma ocean

gradually decreases during core-formation process as the mantle's iron partition into the core (e.g., Badro et al., 2015). The fO_2 path evolves from ΔIW-1.4 to ΔIW-2.3 (corresponding to an initial FeO concentration of 17 mol% to 5.9 mol%), and lead to a core composition in agreement with seismological observables of density and sound velocity (Badro et al., 2015). The S concentration in Earth's core in all models is set to 2 wt.%; Si concentration was modelled following the approach in Siebert et al. (2013), and combined with the fO_2 models in this study.

Although the initial values of D_{In} of different models exhibit significant variations, in particular the highly reduced model with an initial $D_{In} > 150$, their final D_{In} values are all approaching the range of apparent partitioning coefficients within respective uncertainties. The homogenous accretion model yields a final D_{In} value of 4.8 ± 2.5; The heterogeneous accretion models yield final D_{In} values of 3.4 ± 2.2 (fixed fO_2 model), 4.8 ± 2.9 (reduced model) and 2.4 ± 1.5 (oxidized model). Considering that the heterogeneous accretion model was observed to better explain the depletions of other MVEs such as Cu, Zn, Sn, Cd, Bi, Tl in previous partitioning studies of these elements (Kubik et al., 2021a; Kubik et al., 2021b; Mahan et al., 2018c; Mahan et al., 2018d; Mahan et al., 2017), the heterogeneous accretion model is favored as well in this study.

Regardless of which fO_2 path the Earth accreted from, our results suggest that indium does not behave as a lithophile element under any Earth's core-formation conditions and accretion scenario. Consequently, the Earth's core is expected to be an important reservoir of Earth's In. According to these partitioning coefficients from different models, the possible In abundance of the bulk Earth (BE) can be estimated. In addition, a late veneer of ~ 0.5% of Earth mass CI-like materials, which was delivered to the Earth mantle after core-formation process ceased, can also be taken into account (O'Neill et al., 1995; Wang and Becker, 2013). Using a recent estimate of In concentration in the BSE of ~ 12 ± 2 ppb (Wang et al. (2016a)), we predict a In concentration in the bulk Earth (BE) of 22 ± 13 ppb (constant fO_2), 27 ± 15 ppb (reduced model) and 18 ± 8 ppb (oxidized model).

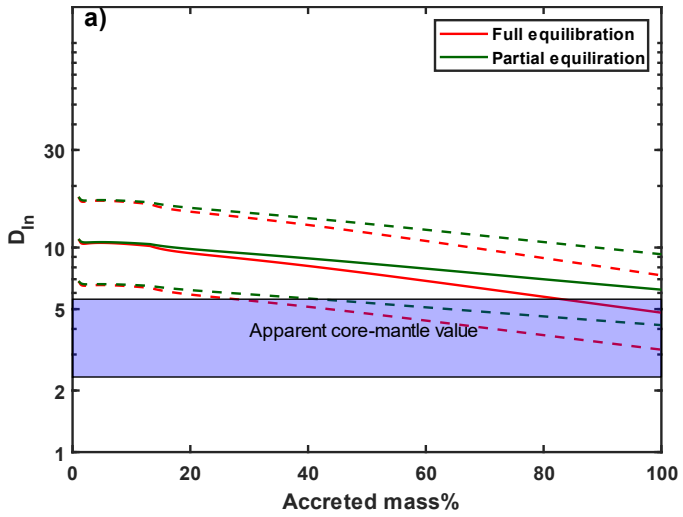
a)
Full equilibration
Partial equiliration
30
10
5
2
1
D_{In}
Apparent core-mantle value
0
20
40
60
80
100
Accreted mass%

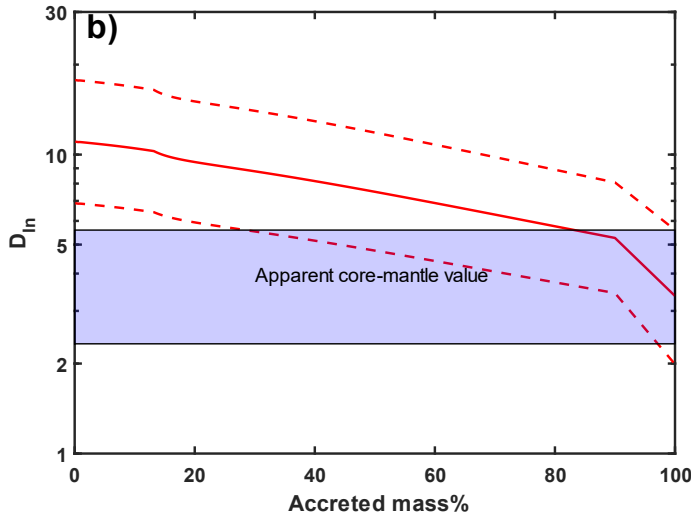
b)
30
10
5
2
1
D_{In}
Apparent core-mantle value
0
20
40
60
80
100
Accreted mass%

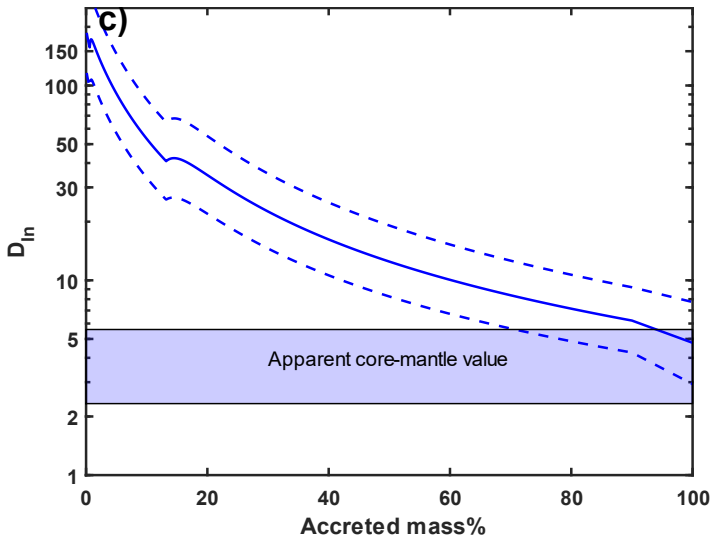
c)
150
100
50
30
10
5
2
1
D_{In}
Apparent core-mantle value
0
20
40
60
80
100
Accreted mass%

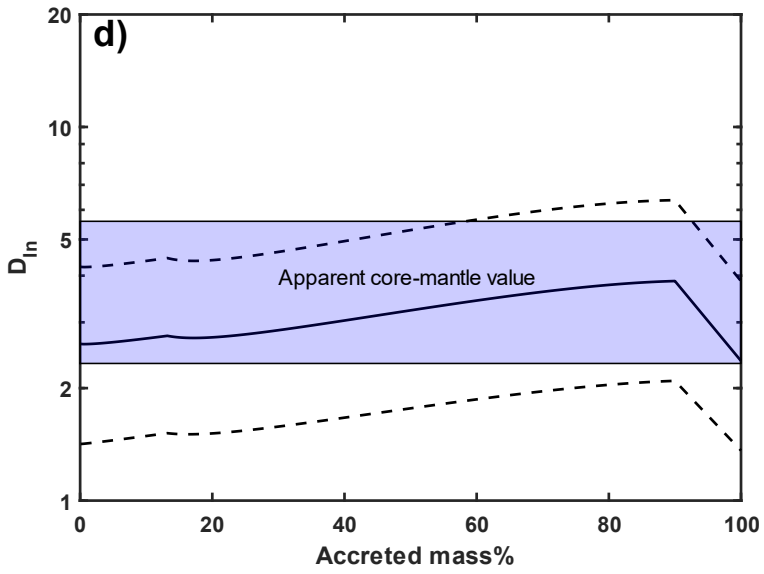

Figure. 7 The evolution of partitioning coefficient of In during the accretion of the Earth. a) shows the scenarios of full equilibration and partial equilibration for a homogeneous accretion (ΔIW = -2.3), where the equilibration efficiency was set to 1 and 0.5, respectively. Each accretion step is set as 0.1% of Earth mass b-d) show the scenarios that the Earth accreted from the first 90 % Earth mass volatile depleted materials and followed with 10 % CI-like volatile rich materials. Three accretion paths are taken into account: b) oxygen fugacity (ΔIW-2.3); c) reduced accreted path and d) oxidized accreted path. The first 90 % accretion is set as 0.1 % of Earth mass, and the last 10 % is set as 10% of Earth mass.

4.3 The origin of the Earth's indium

Our experimental results indicate that the Earth's core must contain a significant fraction of the Earth's In budget. Therefore, assuming that volatile loss occurred under reducing nebular conditions on precursor materials of the proto-Earth (e.g., logfO_2=10^{-14}), the remaining amount of In should be approximately nil due to its high volatility, and the budget of In should be dominated by late delivery of volatile-rich materials (e.g., Braukmuller et al., 2019). However, using this late 10% Earth mass addition of CI-like materials as the source of In yields a final In abundance in the BSE of ~ 3 - 5 ppb significantly lower than the estimated In abundance (12 to 18 ppb) of the BSE (Palme and O'Neill, 2014; Wang et al., 2016a; Witt-Eickschen et al., 2009; Yi et al., 2000). Moreover, in comparison with Cd an element with similar T_C[50] (502 K, In is 492 K; Wood et al. (2019)), In stays always more siderophile than Cd even in Si-bearing

experiments (Kubik et al., 2021a; Steenstra et al., 2020; Wang et al., 2016a and this study), except the extremely high S-bearing experiments (up to 50 mol% of S) (Wood et al., 2014a), which are not realistic in Earth's core. The D_{In}/D_{Cd} values under different fO_2 models are shown in Figure. 8. Moreover, the CI, -Mg normalized abundance of In is ~ three times higher than Cd (Palme and O'Neill, 2014; Wang et al., 2016a). Thus, adding a higher mass of late delivered volatile-rich material (e.g., Braukmuller et al., 2019; Wänke et al., 1984) to fully explain the Earth's In budget would still not allow to produce the relative abundances of In and Cd due to the In higher siderophility predicted at any conditions of Earth's core formation and accretion. These observations argue against the late-delivered CI-like materials as the only source of Earth's In and suggest instead that the precursor materials of the proto-Earth should also carry a considerable amount of In. The Earth's In budget is likely the product of the mixing of these two sources.

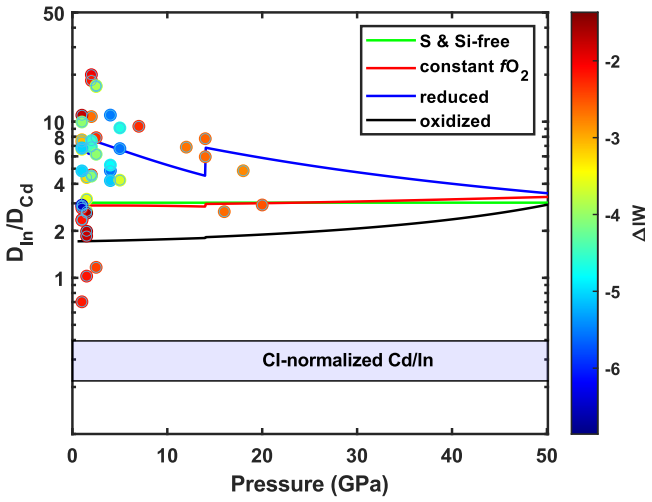

Figure. 8 The ratio of partition coefficients of In and Cd plotted against pressure. The plotted data points are from Ballhaus et al. (2013), Wood et al. (2014), Righter et al. (2018), Steenstra et al. (2020), Kubik et al (2021a) and this study. Only the experiments with S (< 4 mol%) and Si (< 15 mol%) content are used because they are closer to the realistic light element contents in Earth's core. The green curve represents the D_{In}/D_{Cd} values under which the sulfur and silicon absence in the metallic phases and constant fO_2 (ΔIW-2.3); red, blue and black curves represent the different fO_2 evolution (constant model, reduced model and oxidized model), which are described in section 4.2.3. The fluctuation of curve is from the various values of interaction parameters applied to different pressure conditions (see section 4.2.2). The values of ε_{In}^{S} and ε_{In}^{Si}, and ε_{Cd}^{S} and ε_{Cd}^{Si} are taken from Kubik et al (2021a), Steenstra (2020) and this study. The blue area represents the ratio of CI-normalized of Cd and In, calculated from recently estimated In and Cd abundances from Wang et al. (2016).

The precursor materials of the proto-Earth have the potential to preserve a certain amount of In after volatile-depletion event (s). Although In is highly volatile under nebular environment, its volatility is sensitive to the environmental conditions (e.g., fO_2). Under oxidized conditions, In is predicted to be significantly less volatile than the elements with similar T_C^{50}, allowing the evaporation residue to preserve some In (Norris and Wood, 2017 and Chapter 2). Such higher oxygen fugacity conditions can prevail in the silicate vapor-melt system due to the high partial pressure of SiO, O_2 and O gas species in the silicate vapor (Visscher and Fegley Jr (2013)). Even considering more reduced material such as enstatite chondrites as Earth's building blocks, the interface between vapor and melt would be still more oxidized. Therefore, evaporation loss on precursor materials of the proto-Earth may has the potential to prevent the complete loss of In, which has been observed on the smaller differentiated bodies like Moon and Vesta as discussed in Chapter 2.

Isotopic evidences from Mg (Hin et al., 2017), Si (Moynier et al., 2020) and Fe (Sossi et al., 2016) suggest that the precursor materials of the Earth underwent volatile depletion during planetary accretion with the heavier isotopic composition of the Earth being attributed to isotopic fractionation between melt and vapor. Although heavier MVE isotopic compositions of the Earth have not been clearly evidenced to date (e.g., Pringle and Moynier, 2017; Savage et al., 2015; Schönbächler et al., 2010; Sossi et al., 2018a), a new view from indium isotopes is expected as both sources of In, the precursor materials of proto-Earth and late-added carbonaceous materials, should carry isotopic evidences of evaporative loss.

4.4 Indium isotopic fractionation between metal and silicate and implications for the In isotopic composition of the bulk Earth

The isotopic fractionation of In between silicate and metal is a function of $1/T^2$ (Urey, 1947). This relationship can be quantified with our experimental results as shown in Figure 9. A resolvable isotopic fractionation is observed for the light elements free and Si-bearing samples, while insignificant fractionation is observed in the S-bearing

samples. Similar results were also observed for Fe isotopes (Shahar et al., 2015) and Sn isotopes (Kubik et al., 2021b). Shahar et al. (2015) explained this as the result of stronger Fe-S covalent bond than Fe-Fe metallic bond, where the stiffer covalent bond can promote the enrichment in heavy isotopes. Similar explanation may be given for the Fe-In-S system but the In-S and In-Fe bonds in alloy need to be characterized properly to confirm this hypothesis.

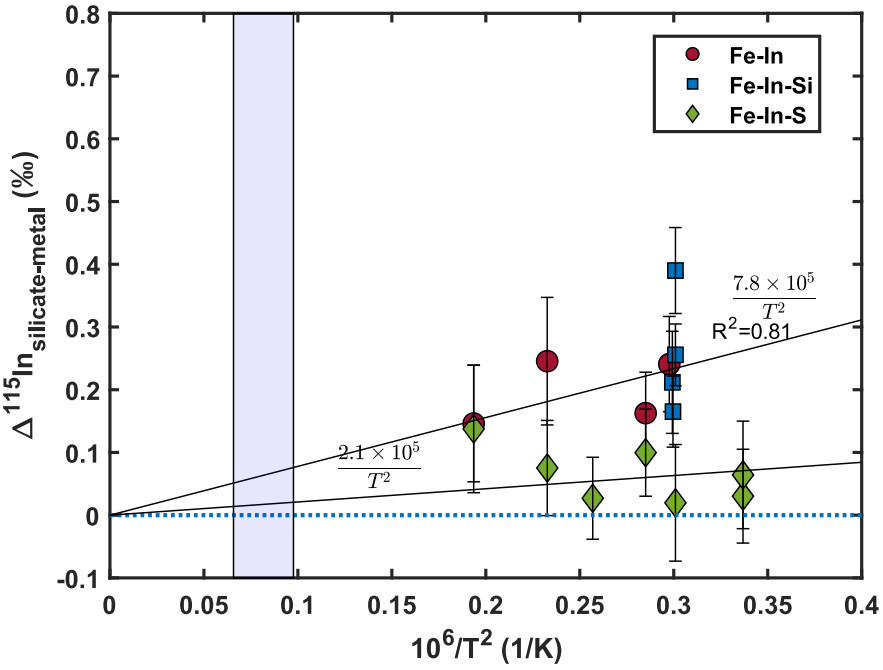

Figure. 9 The In isotopic fractionation between silicate and metal. The light elements-free sample and Si-bearing samples have the similar isotopic fractionation. The isotopic fractionation in S-bearing samples is insignificant. The function of their isotopic fractionation and $1/T^2$ are shown in figure. The blue area represents the temperature range corresponding to the peridotite liquidus under 40 – 60 GPa, approximately seen as the P-T conditions under the base of magma ocean.

Here we used the parameters regressed from both light elements free and S-bearing samples as the upper and lower limits to estimate the isotopic fractionation of In between silicate and metal. All the S-bearing samples in our experiments exhibit lower isotopic fractionation than S-free samples, however, the isotopic fractionation of S-bearing samples do not show a clear correlation with increasing sulfur concentration, for example, the $\Delta^{115}In_{silicate-metal}$ of E337 (~ 8 wt.% of S in metallic phases) is 0.10 ± 0.07 ‰, while E340 (~ 20 wt.% of S in metallic phases) is 0.06 ± 0.09 ‰, there is no

resolvable difference within analytical precision. Nonetheless, considering the significantly higher S concentration in experimental samples (~ 8 to 20 wt.%) than the Earth's core (~ 2 wt.%) (McDonough, 2003; Suer et al., 2017b), the S-bearing samples regressed value must be seen as a lower bound value for In fractionation. The Si-bearing samples do not show a systematic variation as S-bearing samples, and are almost overlapped with the light elements-free samples, thus the Si effect is not further considered in this study. The function of In isotopic fractionation between silicate and metal and $1/T^2$ can be expressed as:

$$\Delta^{115}In_{silicate-metal} = \frac{7.8(\pm 2.4)\times 10^5}{T^2} \text{ (S-free)}$$

$$\Delta^{115}In_{silicate-metal} = \frac{2.1(\pm 1.5)\times 10^5}{T^2} \text{ (S-bearing)}$$

The reported uncertainties are 95% confidence interval. Extrapolating these equations to the temperature condition of the base of magma ocean (~ 3200 to 3900 K, estimated from the average value of peridotite liquidus at the pressure range 40 to 60 GPa, as suggested in Siebert et al. (2013)), the In isotopic fractionation between mantle and core can be expected within the range of ~ 0.05 - 0.07 ‰ (S-free) to 0.01 - 0.02 ‰ (S-bearing), while the latter can be approximately seen as the same isotopic composition as BSE, which is estimated to be -0.03 ± 0.18 ‰ in Chapter 3. The In isotopic composition of the bulk Earth depends on the fraction of In in the core and (i.e., the partitioning coefficient between core and mantle) modelled in Figure 10. Although the final partitioning coefficients of the three tested models are different, the modelled In final isotopic compositions are similar due to the limited isotopic fractionation under relevant temperature conditions of Earth's core-formation. We predict bulk Earth In isotopic compositions of -0.07 ± 0.15 ‰ (oxidized model), -0.08 ± 0.15 ‰ (constant fO_2) and -0.08 ± 0.16 ‰ (reduced model), given these indistinguishable results, an average value of -0.08 ± 0.15 ‰ can be considered as the lower bound of In isotopic composition of the bulk Earth.

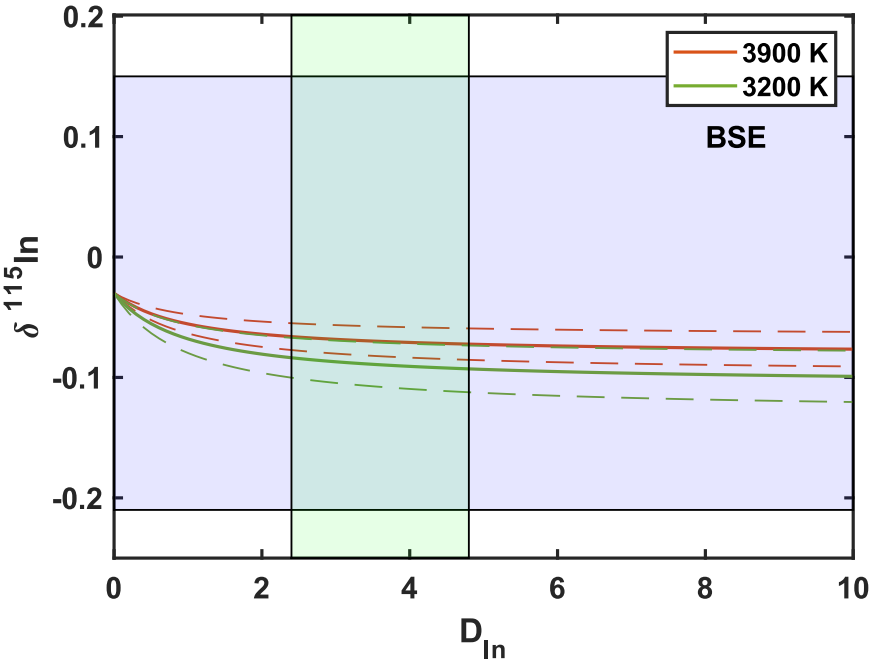

Figure. 10 The In isotopic composition of the bulk Earth plotted against the partitioning coefficient of In between core and mantle. The different redox state models are shown in the figure, however, their differences are small and can be negligible due to the limited isotopic fractionation when extrapolating to the core-formation temperature conditions as shown marked in figure. The blue area represents the estimated In isotopic composition in BSE (see Chapter 3). Green and red solid lines represent different temperature conditions, and the uncertainties of regressed parameter are shown with their respective dash lines.

5. Conclusion

A series of metal-silicate partitioning experiments were conducted in this study to constrain the elemental partitioning and isotopic fractionation of In between metal and silicate. According to our experiments, as well as previous studies, we suggest that temperature and pressure have negligible effects on the partitioning of In, while light elements, in particular Si has a strong effect on partitioning. However, these metal composition effects are both temperature- and pressure- dependent. Using the regressed parameters of In partitioning with different heterogenous accretion models, we show that the partitioning coefficient of In varies from 3.4 ± 2.2 (fixed fO_2 model), 4.8 ± 2.9 (reduced model) and 2.4 ± 1.5 (oxidized model), indicating that the Earth's core is an important reservoir for In. The origin of the Earth's In budget is suggested to be the

result of the mixing of both late-accreted CI-like materials and precursor materials of the proto-Earth. Precursor materials of the proto-Earth likely experienced volatile loss in a vapor-melt system under non-nebular conditions, allowing to preserve some amount of In. A resolvable isotopic fractionation is observed on the S-free samples and we show that the presence of S can significantly suppress the In isotopic fractionation between silicate and metal. However, an identical isotopic composition of core and mantle is predicted when modeling core formation at relevant temperature conditions of the base of a deep magma ocean. Based on this observation, we propose a bulk Earth In isotopic composition of -0.03 ± 0.18 ‰ as the upper limit and -0.08 ± 0.15 ‰ as the lower limit according to the potential effect of sulfur on In metal silicate isotopic fractionation.

Acknowledgements

The authors thank Nicolas Wehr for the technical assistance on the high-pressure experiments. We thank Stephan Borensztajn for the help on SEM. We also thank Michel Fialin and Nicolas Rividi for technical support on EPMA in CAMPARIS platform. We thank Pascale Louvat for the help on the isotope analyses. D.L thanks the financial support of China Scholarship Council. This work was partly supported by the IPGP analytical platform PARI, Ile-de-France SESAME Grants 12015908, DIM ACAV+, the ERC grant 101001282 (METAL), and Labex UnivEarth (FM).

References

Albarede, F. (2009) Volatile accretion history of the terrestrial planets and dynamic implications. Nature 461, 1227-1233.

Albarede, F., Ballhaus, C., Blichert-Toft, J., Lee, C.-T., Marty, B., Moynier, F. and Yin, Q.-Z. (2013) Asteroidal impacts and the origin of terrestrial and lunar volatiles. Icarus 222, 44-52.

Allègre, C.J., Poirier, J.-P., Humler, E. and Hofmann, A.W. (1995) The chemical composition of the Earth. Earth and Planetary Science Letters 134, 515-526.

Archer, C. and Vance, D. (2004) Mass discrimination correction in multiple-collector plasma source mass spectrometry: an example using Cu and Zn isotopes. Journal of

Analytical Atomic Spectrometry 19, 656-665.
Arevalo Jr, R. and McDonough, W.F. (2010) Chemical variations and regional diversity observed in MORB. Chem. Geol. 271, 70-85.
Ayalew, D., Barbey, P., Marty, B., Reisberg, L., Yirgu, G. and Pik, R. (2002) Source, genesis, and timing of giant ignimbrite deposits associated with Ethiopian continental flood basalts. Geochimica et Cosmochimica Acta 66, 1429-1448.
Ayalew, D., Pik, R., Bellahsen, N., France, L. and Yirgu, G. (2019) Differential fractionation of rhyolites during the course of crustal extension, Western Afar (Ethiopian rift). Geochemistry, Geophysics, Geosystems 20, 571-593.
Badro, J., Brodholt, J.P., Piet, H., Siebert, J. and Ryerson, F.J. (2015) Core formation and core composition from coupled geochemical and geophysical constraints. Proceedings of the National Academy of Sciences 112, 12310-12314.
Ballhaus, C., Laurenz, V., Münker, C., Fonseca, R.O.C., Albarède, F., Rohrbach, A., Lagos, M., Schmidt, M.W., Jochum, K.-P., Stoll, B., Weis, U. and Helmy, H.M. (2013a) The U/Pb ratio of the Earth's mantle—A signature of late volatile addition. Earth and Planetary Science Letters 362, 237-245.
Ballhaus, C., Laurenz, V., Munker, C., Fonseca, R.O.C., Albarede, F., Rohrbach, A., Lagos, M., Schmidt, M.W., Jochum, K.P., Stoll, B., Weis, U. and Helmy, H.M. (2013b) The U/Pb ratio of the Earth's mantle-A signature of late volatile addition. Earth and Planetary Science Letters 362, 237-245.
Barberi, F., Civetta, L. and Varet, J. (1980) Sr isotopic composition of Afar volcanics and its implication for mantle evolution. Earth and Planetary Science Letters 50, 247-259.
Barin, I. and Platzki, G. (1989) Thermochemical data of pure substances. Wiley Online Library.
Bouhifd, M.A. and Jephcoat, A.P. (2003) The effect of pressure on partitioning of Ni and Co between silicate and iron-rich metal liquids: a diamond-anvil cell study. Earth and Planetary Science Letters 209, 245-255.
Braukmüller, N., Wombacher, F., Funk, C. and Münker, C. (2019) Earth’s volatile element depletion pattern inherited from a carbonaceous chondrite-like source. Nature Geoscience 12, 564-568.
Braukmüller, N., Wombacher, F., Hezel, D.C., Escoube, R. and Münker, C. (2018) The chemical composition of carbonaceous chondrites: Implications for volatile element depletion, complementarity and alteration. Geochimica et Cosmochimica Acta 239, 17-48.
Braukmuller, N., Wombacher, F., Funk, C. and Munker, C. (2019) Earth's volatile element depletion pattern inherited from a carbonaceous chondrite-like source. Nature Geoscience 12, 564-+.

Budde, G., Burkhardt, C. and Kleine, T. (2019) Molybdenum isotopic evidence for the late accretion of outer Solar System material to Earth. Nature Astronomy 3, 736-741.
Burkhardt, C., Kleine, T., Bourdon, B., Palme, H., Zipfel, J., Friedrich, J.M. and Ebel, D.S. (2008) Hf–W mineral isochron for Ca, Al-rich inclusions: age of the solar system and the timing of core formation in planetesimals. Geochimica et Cosmochimica Acta 72, 6177-6197.
Chaussidon, M., Deng, Z., Villeneuve, J., Moureau, J., Watson, B., Richter, F. and Moynier, F. (2017) In Situ Analysis of Non-Traditional Isotopes by SIMS and LA–MC–ICP–MS: Key Aspects and the Example of Mg Isotopes in Olivines and Silicate Glasses. Reviews in Mineralogy and Geochemistry 82, 127-163.
Cieza, L.A., Casassus, S., Tobin, J., Bos, S.P., Williams, J.P., Perez, S., Zhu, Z., Caceres, C., Canovas, H., Dunham, M.M., Hales, A., Prieto, J.L., Principe, D.A., Schreiber, M.R., Ruiz-Rodriguez, D. and Zurlo, A. (2016) Imaging the water snow-line during a protostellar outburst. Nature 535, 258-261.
Clayton, D. (1982) Cosmic chemical memory-a new astronomy. Quarterly Journal of the Royal Astronomical Society 23, 174.
Clayton, D. (2003) Handbook of Isotopes in the Cosmos.
Clayton, R.N., Onuma, N. and Mayeda, T.K. (1976) A classification of meteorites based on oxygen isotopes. Earth and Planetary Science Letters 30, 10-18.
Connelly, J.N., Bizzarro, M., Krot, A.N., Nordlund, Å., Wielandt, D. and Ivanova, M.A. (2012) The absolute chronology and thermal processing of solids in the solar protoplanetary disk. Science 338, 651-655.
Corgne, A., Keshav, S., Wood, B.J., McDonough, W.F. and Fei, Y.W. (2008) Metal-silicate partitioning and constraints on core composition and oxygen fugacity during Earth accretion. Geochimica Et Cosmochimica Acta 72, 574-589.
Cormier, L., Ferlat, G., Itie, J.-P., Galoisy, L., Calas, G. and Aquilanti, G. (2007) Amorphous-amorphous transformation at high pressure in gallo-germanosilicate tetrahedral network glasses. Physical Review B 76, 134204.
Craig, H. and Lupton, J. (1976) Primordial neon, helium, and hydrogen in oceanic basalts. Earth and Planetary Science Letters 31, 369-385.
Dai, W., Moynier, F., Paquet, M., Moureau, J., Debret, B., Siebert, J., Gerard, Y. and Zhao, Y. (2022) Calcium isotope measurements using a collision cell (CC)-MC-ICP-MS. Chem. Geol. 590, 120688.
Dalou, C., Füri, E., Deligny, C., Piani, L., Caumon, M.-C., Laumonier, M., Boulliung, J. and Edén, M. (2019) Redox control on nitrogen isotope fractionation during planetary core formation. Proceedings of the National Academy of Sciences 116, 14485-14494.
Dalou, C., Hirschmann, M.M., von der Handt, A., Mosenfelder, J. and Armstrong, L.S. (2017) Nitrogen and carbon fractionation during core-mantle differentiation at shallow

depth. Earth and Planetary Science Letters 458, 141-151.
Dauphas, N. and Chaussidon, M. (2011) A perspective from extinct radionuclides on a young stellar object: the Sun and its accretion disk. arXiv preprint arXiv:1105.5172.
Dauphas, N., Chen, J.H., Zhang, J., Papanastassiou, D.A., Davis, A.M. and Travaglio, C. (2014) Calcium-48 isotopic anomalies in bulk chondrites and achondrites: Evidence for a uniform isotopic reservoir in the inner protoplanetary disk. Earth and Planetary Science Letters 407, 96-108.
Deguen, R., Landeau, M. and Olson, P. (2014) Turbulent metal–silicate mixing, fragmentation, and equilibration in magma oceans. Earth and Planetary Science Letters 391, 274-287.
Deguen, R., Olson, P. and Cardin, P. (2011) Experiments on turbulent metal-silicate mixing in a magma ocean. Earth and Planetary Science Letters 310, 303-313.
Dreibus, G., Kruse, H., Spettel, B. and Wänke, H. (1977) The bulk composition of the moon and the eucrite parent body, Lunar and Planetary Science Conference Proceedings, pp. 211-227.
Faure, G. and Mensing, T. (2007) Introduction to planetary science. Springer.
Fei, Y., Bertka, C.M. and Finger, L.W. (1997) High-pressure iron-sulfur compound, Fe3S2, and melting relations in the Fe-FeS system. Science 275, 1621-1623.
Fei, Y., Li, J., Bertka, C.M. and Prewitt, C.T. (2000) Structure type and bulk modulus of Fe3S, a new iron-sulfur compound. American Mineralogist 85, 1830-1833.
Field, L., Blundy, J. and Yirgu, G. (2008) The magmatic evolution of Dabbahu volcano, Afar, Ethiopia, AGU Fall Meeting Abstracts, pp. V21B-2103.
Fogel, R.A., Hess, P.C. and Rutherford, M.J. (1989) Intensive parameters of enstatite chondrite metamorphism. Geochimica et Cosmochimica Acta 53, 2735-2746.
Gessmann, C.K. and Rubie, D.C. (2000) The origin of the depletions of V, Cr and Mn in the mantles of the Earth and Moon. Earth and Planetary Science Letters 184, 95-107.
Gion, A.M., Piccoli, P.M. and Candela, P.A. (2018) Partitioning of indium between ferromagnesian minerals and a silicate melt. Chem. Geol. 500, 30-45.
Harðardóttir, S., Halldórsson, S.A. and Hilton, D.R. (2018) Spatial distribution of helium isotopes in Icelandic geothermal fluids and volcanic materials with implications for location, upwelling and evolution of the Icelandic mantle plume. Chem. Geol. 480, 12-27.
Hartmann, W.K. and Davis, D.R. (1975) Satellite-sized planetesimals and lunar origin. Icarus 24, 504-515.
Hauri, E.H., Saal, A.E., Rutherford, M.J. and Van Orman, J.A. (2015) Water in the Moon's interior: Truth and consequences. Earth and Planetary Science Letters 409, 252-264.
Hin, R.C., Coath, C.D., Carter, P.J., Nimmo, F., Lai, Y.-J., Pogge von Strandmann,

P.A.E., Willbold, M., Leinhardt, Z.M., Walter, M.J. and Elliott, T. (2017) Magnesium isotope evidence that accretional vapour loss shapes planetary compositions. Nature 549, 511-515.
Huang, D., Siebert, J. and Badro, J. (2021) High pressure partitioning behavior of Mo and W and late sulfur delivery during Earth's core formation. Geochimica et Cosmochimica Acta 310, 19-31.
Huang, D.Y. and Badro, J. (2018) Fe-Ni ideality during core formation on Earth. American Mineralogist 103, 1707-1710.
Ionov, D.A. and Wang, K. (2021) Potassium distribution and isotope composition in the lithospheric mantle in relation to global Earth's reservoirs. Geochimica et cosmochimica acta 309, 151-170.
Javoy, M., Kaminski, E., Guyot, F., Andrault, D., Sanloup, C., Moreira, M., Labrosse, S., Jambon, A., Agrinier, P. and Davaille, A. (2010) The chemical composition of the Earth: Enstatite chondrite models. Earth and Planetary Science Letters 293, 259-268.
Jenner, F.E. and O'Neill, H.S.C. (2012) Analysis of 60 elements in 616 ocean floor basaltic glasses. Geochemistry, Geophysics, Geosystems 13.
Johansen, A., Low, M.-M.M., Lacerda, P. and Bizzarro, M. (2015) Growth of asteroids, planetary embryos, and Kuiper belt objects by chondrule accretion. Science Advances 1, e1500109.
Johansen, A., Ronnet, T., Bizzarro, M., Schiller, M., Lambrechts, M., Nordlund, Å. and Lammer, H. (2021) A pebble accretion model for the formation of the terrestrial planets in the Solar System. Science Advances 7, eabc0444.
Kennedy, G.M. and Kenyon, S.J. (2008) Planet formation around stars of various masses: the snow line and the frequency of giant planets. The Astrophysical Journal 673, 502.
Kruijer, T.S., Kleine, T. and Borg, L.E. (2020) The great isotopic dichotomy of the early Solar System. Nature Astronomy 4, 32-40.
Ku, Y. and Jacobsen, S. (2020) Potassium isotope anomalies in meteorites inherited from the protosolar molecular cloud. Science advances 6, eabd0511.
Kubik, E., Siebert, J., Blanchard, I., Agranier, A., Mahan, B. and Moynier, F. (2021a) Earth's volatile accretion as told by Cd, Bi, Sb and Tl core–mantle distribution. Geochimica et Cosmochimica Acta 306, 263-280.
Kubik, E., Siebert, J., Mahan, B., Creech, J., Blanchard, I., Agranier, A., Shcheka, S. and Moynier, F. (2021b) Tracing Earth's Volatile Delivery With Tin. Journal of Geophysical Research: Solid Earth 126, e2021JB022026.
Lloyd, E.C. (1971) Accurate Characterization of the High-pressure Environment: Proceedings. US National Bureau of Standards.
Lodders, K. (2003) Solar system abundances and condensation temperatures of the

elements. The Astrophysical Journal 591, 1220.
Luck, J.-M., Othman, D.B. and Albarède, F. (2005) Zn and Cu isotopic variations in chondrites and iron meteorites: early solar nebula reservoirs and parent-body processes. Geochimica et Cosmochimica Acta 69, 5351-5363.
Ma, Z. (2001) Thermodynamic description for concentrated metallic solutions using interaction parameters. Metallurgical and Materials Transactions B 32, 87-103.
Mahan, B., Moynier, F., Beck, P., Pringle, E.A. and Siebert, J. (2018a) A history of violence: Insights into post-accretionary heating in carbonaceous chondrites from volatile element abundances, Zn isotopes and water contents. Geochimica et Cosmochimica Acta 220, 19-35.
Mahan, B., Moynier, F., Siebert, J., Gueguen, B., Agranier, A., Pringle, E.A., Bollard, J., Connelly, J.N. and Bizzarro, M. (2018b) Volatile element evolution of chondrules through time. Proceedings of the National Academy of Sciences 115, 8547-8552.
Mahan, B., Siebert, J., Blanchard, I., Badro, J., Kubik, E., Sossi, P. and Moynier, F. (2018c) Investigating Earth's Formation History Through Copper and Sulfur Metal-Silicate Partitioning During Core-Mantle Differentiation. Journal of Geophysical Research-Solid Earth 123, 8349-8363.
Mahan, B., Siebert, J., Blanchard, I., Borensztajn, S., Badro, J. and Moynier, F. (2018d) Constraining compositional proxies for Earth's accretion and core formation through high pressure and high temperature Zn and S metal-silicate partitioning. Geochimica et Cosmochimica Acta 235, 21-40.
Mahan, B., Siebert, J., Pringle, E.A. and Moynier, F. (2017) Elemental partitioning and isotopic fractionation of Zn between metal and silicate and geochemical estimation of the S content of the Earth's core. Geochimica et Cosmochimica Acta 196, 252-270.
Mann, U., Frost, D.J. and Rubie, D.C. (2009) Evidence for high-pressure core-mantle differentiation from the metal–silicate partitioning of lithophile and weakly-siderophile elements. Geochimica et Cosmochimica Acta 73, 7360-7386.
Mare, E.R., O'Neill, H.S.C., Berry, A.J., Frigo, C. and Glover, C.J. (2021) Coordination change of Ge4+ and Ga3+ in silicate melt with pressure. Geochimica et Cosmochimica Acta 303, 184-204.
Marty, B. (2012) The origins and concentrations of water, carbon, nitrogen and noble gases on Earth. Earth and Planetary Science Letters 313, 56-66.
Marty, B. and Yokochi, R. (2006) Water in the early Earth. Reviews in Mineralogy and Geochemistry 62, 421-450.
Mason, T.F., Weiss, D.J., Horstwood, M., Parrish, R.R., Russell, S.S., Mullane, E. and Coles, B.J. (2004) High-precision Cu and Zn isotope analysis by plasma source mass spectrometry Part 2. Correcting for mass discrimination effects. Journal of Analytical Atomic Spectrometry 19, 218-226.

May, T.W. and Wiedmeyer, R.H. (1998) A table of polyatomic interferences in ICP-MS. ATOMIC SPECTROSCOPY-NORWALK CONNECTICUT- 19, 150-155.
McDonough, W. (2003) 2.15–Compositional model for the earth's core. Treatise on geochemistry, 547-568.
McDonough, W.F. and Sun, S.-S. (1995) The composition of the Earth. Chem. Geol. 120, 223-253.
Morard, G., Sanloup, C., Fiquet, G., Mezouar, M., Rey, N., Poloni, R. and Beck, P. (2007) Structure of eutectic Fe–FeS melts to pressures up to 17 GPa: implications for planetary cores. Earth and Planetary Science Letters 263, 128-139.
Moynier, F., Blichert-Toft, J., Telouk, P., Luck, J.-M. and Albarède, F. (2007) Comparative stable isotope geochemistry of Ni, Cu, Zn, and Fe in chondrites and iron meteorites. Geochimica et Cosmochimica Acta 71, 4365-4379.
Moynier, F., Deng, Z., Lanteri, A., Martins, R., Chaussidon, M., Savage, P. and Siebert, J. (2020) Metal-silicate silicon isotopic fractionation and the composition of the bulk Earth. Earth and Planetary Science Letters 549, 116468.
Moynier, F., Hu, Y., Wang, K., Zhao, Y., Gérard, Y., Deng, Z., Moureau, J., Li, W., Simon, J.I. and Teng, F.-Z. (2021) Potassium isotopic composition of various samples using a dual-path collision cell-capable multiple-collector inductively coupled plasma mass spectrometer, Nu instruments Sapphire. Chem. Geol. 571, 120144.
Mysen, B. and Richet, P. (2018) Silicate glasses and melts. Elsevier.
Nanne, J.A., Nimmo, F., Cuzzi, J.N. and Kleine, T. (2019) Origin of the non-carbonaceous–carbonaceous meteorite dichotomy. Earth and Planetary Science Letters 511, 44-54.
Norris, C.A. and Wood, B.J. (2017) Earth's volatile contents established by melting and vaporization. Nature 549, 507.
O'Neill, H.S.C., Dingwell, D., Borisov, A., Spettel, B. and Palme, H. (1995) Experimental petrochemistry of some highly siderophile elements at high temperatures, and some implications for core formation and the mantle's early history. Chem. Geol. 120, 255-273.
O'Neill, H.S.C. and Palme, H. (2008) Collisional erosion and the non-chondritic composition of the terrestrial planets. Philosophical Transactions of the Royal Society A: Mathematical, Physical and Engineering Sciences 366, 4205-4238.
Palme, H. and O'Neill, H. (2014) Cosmochemical Estimates of Mantle Composition. Planets, Asteriods, Comets and The Solar System, Volume 2 of Treatise on Geochemistry . Edited by Andrew M. Davis. Elsevier.
Perkins, D. and Newton, R. (1981) Charnockite geobarometers based on coexisting garnet—pyroxene—plagioclase—quartz. Nature 292, 144-146.
Pfeiffer, L., Mills Jr, A.P., Chandross, E. and Kovacs, T. (1979) Beta spectrum of In 115.

Physical Review C 19, 1035.
Piani, L., Marrocchi, Y., Rigaudier, T., Vacher, L.G., Thomassin, D. and Marty, B. (2020) Earth's water may have been inherited from material similar to enstatite chondrite meteorites. Science 369, 1110-1113.
Pietruszka, A.J. and Reznik, A.D. (2008) Identification of a matrix effect in the MC-ICP-MS due to sample purification using ion exchange resin: An isotopic case study of molybdenum. International Journal of Mass Spectrometry 270, 23-30.
Pik, R., Deniel, C., Coulon, C., Yirgu, G. and Marty, B. (1999) Isotopic and trace element signatures of Ethiopian flood basalts: evidence for plume–lithosphere interactions. Geochimica et Cosmochimica Acta 63, 2263-2279.
Pik, R., Marty, B. and Hilton, D.R. (2006) How many mantle plumes in Africa? The geochemical point of view. Chem. Geol. 226, 100-114.
Pringle, E.A. and Moynier, F. (2017) Rubidium isotopic composition of the Earth, meteorites, and the Moon: Evidence for the origin of volatile loss during planetary accretion. Earth and Planetary Science Letters 473, 62-70.
Pringle, E.A., Moynier, F., Beck, P., Paniello, R. and Hezel, D.C. (2017) The origin of volatile element depletion in early solar system material: Clues from Zn isotopes in chondrules. Earth and Planetary Science Letters 468, 62-71.
Pringle, E.A., Moynier, F., Savage, P.S., Badro, J. and Barrat, J.-A. (2014) Silicon isotopes in angrites and volatile loss in planetesimals. Proceedings of the National Academy of Sciences 111, 17029-17032.
Ranta, E., Gunnarsson-Robin, J., Halldórsson, S.A., Ono, S., Izon, G., Jackson, M.G., Reekie, C.D.J., Jenner, F.E., Guðfinnsson, G.H., Jónsson, Ó.P. and Stefánsson, A. (2022) Ancient and recycled sulfur sampled by the Iceland mantle plume. Earth and Planetary Science Letters 584, 117452.
Richter, F.M. (2004) Timescales determining the degree of kinetic isotope fractionation by evaporation and condensation. Geochimica et Cosmochimica Acta 68, 4971-4992.
Richter, F.M., Davis, A.M., Ebel, D.S. and Hashimoto, A. (2002) Elemental and isotopic fractionation of Type B calcium-, aluminum-rich inclusions: experiments, theoretical considerations, and constraints on their thermal evolution. Geochimica et Cosmochimica Acta 66, 521-540.
Richter, F.M., Janney, P.E., Mendybaev, R.A., Davis, A.M. and Wadhwa, M. (2007) Elemental and isotopic fractionation of Type B CAI-like liquids by evaporation. Geochimica et Cosmochimica Acta 71, 5544-5564.
Righter, K., Nickodem, K., Pando, K., Danielson, L., Boujibar, A., Righter, M. and Lapen, T. (2017) Distribution of Sb, As, Ge, and In between metal and silicate during accretion and core formation in the Earth. Geochimica et Cosmochimica Acta 198, 1-16.

Righter, K., Pando, K., Marin, N., Ross, D., Righter, M., Danielson, L., Lapen, T. and Lee, C. (2018a) Volatile element signatures in the mantles of Earth, Moon, and Mars: Core formation fingerprints from Bi, Cd, In, and Sn. Meteorit. Planet. Sci. 53, 284-305.
Righter, K., Pando, K., Marin, N., Ross, D.K., Righter, M., Danielson, L., Lapen, T.J. and Lee, C. (2018b) Volatile element signatures in the mantles of Earth, Moon, and Mars: Core formation fingerprints from Bi, Cd, In, and Sn. Meteorit. Planet. Sci. 53, 284-305.
Righter, K., Sutton, S.R., Danielson, L., Pando, K. and Newville, M. (2016) Redox variations in the inner solar system with new constraints from vanadium XANES in spinels. American Mineralogist 101, 1928-1942.
Ringwood, A.E. (1966) Chemical evolution of the terrestrial planets. Geochimica et Cosmochimica Acta 30, 41-104.
Rubie, D. (1999) Characterising the sample environment in multianvil high-pressure experiments. Phase Transitions 68, 431-451.
Rubie, D.C., Frost, D.J., Mann, U., Asahara, Y., Nimmo, F., Tsuno, K., Kegler, P., Holzheid, A. and Palme, H. (2011) Heterogeneous accretion, composition and core-mantle differentiation of the Earth. Earth and Planetary Science Letters 301, 31-42.
Rubie, D.C., Jacobson, S.A., Morbidelli, A., O'Brien, D.P., Young, E.D., de Vries, J., Nimmo, F., Palme, H. and Frost, D.J. (2015) Accretion and differentiation of the terrestrial planets with implications for the compositions of early-formed Solar System bodies and accretion of water. Icarus 248, 89-108.
Rudnick, R., Gao, S., Holland, H. and Turekian, K. (2003) Composition of the continental crust. The crust 3, 1-64.
Sanloup, C., Van Westrenen, W., Dasgupta, R., Maynard-Casely, H. and Perrillat, J.-P. (2011) Compressibility change in iron-rich melt and implications for core formation models. Earth and Planetary Science Letters 306, 118-122.
Savage, P.S., Moynier, F. and Boyet, M. (2022) Zinc isotope anomalies in primitive meteorites identify the outer solar system as an important source of Earth's volatile inventory. Icarus 386, 115172.
Savage, P.S., Moynier, F., Chen, H., Shofner, G., Siebert, J., Badro, J. and Puchtel, I.S. (2015) Copper isotope evidence for large-scale sulphide fractionation during Earth's differentiation. Geochem. Perspect. Lett. 1, 53-63.
Schönbächler, M., Carlson, R., Horan, M., Mock, T. and Hauri, E. (2010) Heterogeneous accretion and the moderately volatile element budget of Earth. Science 328, 884-887.
Schiller, M., Bizzarro, M. and Fernandes, V.A. (2018) Isotopic evolution of the protoplanetary disk and the building blocks of Earth and the Moon. Nature 555, 507-510.

Schiller, M., Bizzarro, M. and Siebert, J. (2020) Iron isotope evidence for very rapid accretion and differentiation of the proto-Earth. Science advances 6, eaay7604.
Schroll, E., Bea, F., Butler, E.C.V., van Calsteren, P., Shimizu, N., Griffen, D.T., Barefoot, R.R., Williamson, M.A., Montgomery, C.W. and Clark, I.D. (1999) I, in: Marshall, C.P., Fairbridge, R.W. (Eds.), Encyclopedia of Geochemistry. Springer Netherlands, Dordrecht, pp. 339-357.
Schwarz-Schampera, U. and Herzig, P.M. (2002) Indium: Geology, mineralogy, and economics. Springer Science & Business Media.
Shahar, A., Hillgren, V.J., Horan, M.F., Mesa-Garcia, J., Kaufman, L.A. and Mock, T.D. (2015) Sulfur-controlled iron isotope fractionation experiments of core formation in planetary bodies. Geochimica et Cosmochimica Acta 150, 253-264.
Shahar, A., Ziegler, K., Young, E.D., Ricolleau, A., Schauble, E.A. and Fei, Y. (2009) Experimentally determined Si isotope fractionation between silicate and Fe metal and implications for Earth's core formation. Earth and Planetary Science Letters 288, 228-234.
Shannon, R.D. (1976) Revised effective ionic radii and systematic studies of interatomic distances in halides and chalcogenides. Acta crystallographica section A: crystal physics, diffraction, theoretical and general crystallography 32, 751-767.
Shibazaki, Y., Kono, Y. and Fei, Y. (2015) Microscopic structural change in a liquid Fe-C alloy of~ 5 GPa. Geophysical Research Letters 42, 5236-5242.
Siebert, J., Badro, J., Antonangeli, D. and Ryerson, F.J. (2012) Metal-silicate partitioning of Ni and Co in a deep magma ocean. Earth and Planetary Science Letters 321, 189-197.
Siebert, J., Badro, J., Antonangeli, D. and Ryerson, F.J. (2013) Terrestrial accretion under oxidizing conditions. Science, 1227923.
Siebert, J., Corgne, A. and Ryerson, F.J. (2011) Systematics of metal–silicate partitioning for many siderophile elements applied to Earth’s core formation. Geochimica et Cosmochimica Acta 75, 1451-1489.
Siebert, J., Sossi, P.A., Blanchard, I., Mahan, B., Badro, J. and Moynier, F. (2018) Chondritic Mn/Na ratio and limited post-nebular volatile loss of the Earth. Earth and Planetary Science Letters 485, 130-139.
Sossi, P.A. and Fegley, B. (2018) Thermodynamics of Element Volatility and its Application to Planetary Processes, in: King, P., Fegley, B., Seward, T. (Eds.), High Temperature Gas-Solid Reactions in Earth and Planetary Processes. Mineralogical Soc Amer & Geochemical Soc, Chantilly, pp. 393-459.
Sossi, P.A., Klemme, S., O'Neill, H.S.C., Berndt, J. and Moynier, F. (2019) Evaporation of moderately volatile elements from silicate melts: Experiments and theory. Geochimica et Cosmochimica Acta.

Sossi, P.A., Moynier, F., Treilles, R., Mokhtari, M., Wang, X. and Siebert, J. (2020) An experimentally-determined general formalism for evaporation and isotope fractionation of Cu and Zn from silicate melts between 1300 - 1500 °C and 1 bar. Geochimica et Cosmochimica Acta.

Sossi, P.A., Nebel, O. and Foden, J. (2016) Iron isotope systematics in planetary reservoirs. Earth and Planetary Science Letters 452, 295-308.

Sossi, P.A., Nebel, O., O'Neill, H.S. and Moynier, F. (2018a) Zinc isotope composition of the Earth and its behaviour during planetary accretion. Chem. Geol. 477, 73-84.

Sossi, P.A., Nebel, O., O'Neill, H.S.C. and Moynier, F. (2018b) Zinc isotope composition of the Earth and its behaviour during planetary accretion. Chem. Geol. 477, 73-84.

Sossi, P.A. and O'Neill, H.S.C. (2017) The effect of bonding environment on iron isotope fractionation between minerals at high temperature. Geochimica et Cosmochimica Acta 196, 121-143.

Sossi, P.A., Stotz, I.L., Jacobson, S.A., Morbidelli, A. and O'Neill, H.S.C. (2022) Stochastic accretion of the Earth. Nature Astronomy, 1-10.

Steelmaking, J. (1988) Steelmaking data sourcebook. Gordon and Breach Science Publishers, Montreux.

Steenstra, E.S., Seegers, A.X., Putter, R., Berndt, J., Klemme, S., Matveev, S., Bullock, E.S. and van Westrenen, W. (2020) Metal-silicate partitioning systematics of siderophile elements at reducing conditions: A new experimental database. Icarus 335, 113391.

Steller, T., Burkhardt, C., Yang, C. and Kleine, T. (2022) Nucleosynthetic zinc isotope anomalies reveal a dual origin of terrestrial volatiles. Icarus 386, 115171.

Suer, T.-A., Siebert, J., Remusat, L., Menguy, N. and Fiquet, G. (2017a) A sulfur-poor terrestrial core inferred from metal–silicate partitioning experiments. Earth and Planetary Science Letters 469, 84-97.

Suer, T.A., Siebert, J., Remusat, L., Menguy, N. and Fiquet, G. (2017b) A sulfur-poor terrestrial core inferred from metal-silicate partitioning experiments. Earth and Planetary Science Letters 469, 84-97.

Thibault, Y. and Walter, M.J. (1995) The influence of pressure and temperature on the metal-silicate partition coefficients of nickel and cobalt in a model C1 chondrite and implications for metal segregation in a deep magma ocean. Geochimica et Cosmochimica Acta 59, 991-1002.

Trinquier, A., Birck, J.-L. and Allegre, C.J. (2007) Widespread 54Cr heterogeneity in the inner solar system. The Astrophysical Journal 655, 1179.

Trinquier, A., Elliott, T., Ulfbeck, D., Coath, C., Krot, A.N. and Bizzarro, M. (2009) Origin of nucleosynthetic isotope heterogeneity in the solar protoplanetary disk.

Science 324, 374-376.
Urey, H.C. (1947) The thermodynamic properties of isotopic substances. Journal of the Chemical Society (Resumed), 562-581.
Van Kooten, E., Schiller, M., Moynier, F., Johansen, A., Haugbølle, T. and Bizzarro, M. (2021) Hybrid accretion of carbonaceous chondrites by radial transport across the Jupiter barrier. The Astrophysical Journal 910, 70.
Van Westrenen, W., Blundy, J. and Wood, B. (1999) Crystal-chemical controls on trace element partitioning between garnet and anhydrous silicate melt. American Mineralogist 84, 838-847.
Visscher, C. and Fegley Jr, B. (2013) Chemistry of impact-generated silicate melt-vapor debris disks. The Astrophysical Journal Letters 767, L12.
Vogel, A.K., Jennings, E.S., Laurenz, V., Rubie, D.C. and Frost, D.J. (2018) The dependence of metal-silicate partitioning of moderately volatile elements on oxygen fugacity and Si contents of Fe metal: Implications for their valence states in silicate liquids. Geochimica Et Cosmochimica Acta 237, 275-293.
Vollstaedt, H., Mezger, K. and Alibert, Y. (2020) Carbonaceous chondrites and the condensation of elements from the Solar Nebula. The Astrophysical Journal 897, 82.
Wänke, H. and Dreibus, G. (1988) Chemical composition and accretion history of terrestrial planets. Philosophical Transactions of the Royal Society of London. Series A, Mathematical and Physical Sciences 325, 545-557.
Wänke, H., Dreibus, G. and Jagoutz, E. (1984) Mantle chemistry and accretion history of the Earth, Archaean geochemistry. Springer, pp. 1-24.
Wade, J. and Wood, B. (2005) Core formation and the oxidation state of the Earth. Earth and Planetary Science Letters 236, 78-95.
Wager, L.R., Smit, J.v.R. and Irving, H. (1958) Indium content of rocks and minerals from the Skaergaard intrusion, East Greenland. Geochimica et Cosmochimica Acta 13, 81-86.
Wang, H., Weiss, B.P., Bai, X.-N., Downey, B.G., Wang, J., Wang, J., Suavet, C., Fu, R.R. and Zucolotto, M.E. (2017) Lifetime of the solar nebula constrained by meteorite paleomagnetism. Science 355, 623-627.
Wang, K. and Jacobsen, S.B. (2016) An estimate of the Bulk Silicate Earth potassium isotopic composition based on MC-ICPMS measurements of basalts. Geochimica et Cosmochimica Acta 178, 223-232.
Wang, Z. and Becker, H. (2013) Ratios of S, Se and Te in the silicate Earth require a volatile-rich late veneer. Nature 499, 328.
Wang, Z., Becker, H. and Wombacher, F. (2015) Mass Fractions of S, Cu, Se, Mo, Ag, Cd, In, Te, Ba, Sm, W, Tl and Bi in Geological Reference Materials and Selected Carbonaceous Chondrites Determined by Isotope Dilution ICP-MS. Geostandards and

Geoanalytical Research 39, 185-208.
Wang, Z., Laurenz, V., Petitgirard, S. and Becker, H. (2016a) Earth's moderately volatile element composition may not be chondritic: Evidence from In, Cd and Zn. Earth and Planetary Science Letters 435, 136-146.
Wang, Z.C., Laurenz, V., Petitgirard, S. and Becker, H. (2016b) Earth's moderately volatile element composition may not be chondritic: Evidence from In, Cd and Zn. Earth and Planetary Science Letters 435, 136-146.
Warren, P.H. (2011) Stable-isotopic anomalies and the accretionary assemblage of the Earth and Mars: A subordinate role for carbonaceous chondrites. Earth and Planetary Science Letters 311, 93-100.
Wasson, J.T. and Kallemeyn, G.W. (1988) Compositions of chondrites. Phil. Trans. R. Soc. Lond. A 325, 535-544.
Wimpenny, J., Marks, N., Knight, K., Rolison, J.M., Borg, L., Eppich, G., Badro, J., Ryerson, F.J., Sanborn, M. and Huyskens, M.H. (2019) Experimental determination of Zn isotope fractionation during evaporative loss at extreme temperatures. Geochimica et Cosmochimica Acta 259, 391-411.
Witt-Eickschen, G. and O'Neill, H.S.C. (2005) The effect of temperature on the equilibrium distribution of trace elements between clinopyroxene, orthopyroxene, olivine and spinel in upper mantle peridotite. Chem. Geol. 221, 65-101.
Witt-Eickschen, G., Palme, H., O'neill, H.S.C. and Allen, C.M. (2009) The geochemistry of the volatile trace elements As, Cd, Ga, In and Sn in the Earth's mantle: new evidence from in situ analyses of mantle xenoliths. Geochimica et Cosmochimica Acta 73, 1755-1778.
Wood, B.J., Kiseeva, E.S. and Mirolo, F.J. (2014a) Accretion and core formation: The effects of sulfur on metal-silicate partition coefficients. Geochimica Et Cosmochimica Acta 145, 248-267.
Wood, B.J., Kiseeva, E.S. and Mirolo, F.J. (2014b) Accretion and core formation: The effects of sulfur on metal–silicate partition coefficients. Geochimica et Cosmochimica Acta 145, 248-267.
Wood, B.J., Smythe, D.J. and Harrison, T. (2019) The condensation temperatures of the elements: A reappraisal. American Mineralogist 104, 844-856.
Wood, B.J., Walter, M.J. and Wade, J. (2006) Accretion of the Earth and segregation of its core. Nature 441, 825.
Yagi, T., Akaogi, M., Shimomura, O., Suzuki, T. and Akimoto, S.I. (1987) In situ observation of the olivine-spinel phase transformation in Fe2SiO4 using synchrotron radiation. Journal of Geophysical Research: Solid Earth 92, 6207-6213.
Yagi, T. and Akimoto, S.-I. (1976) Direct determination of coesite-stishovite transition by in-situ X-ray measurements. Tectonophysics 35, 259-270.

Yi, W., Halliday, A.N., Alt, J.C., Lee, D.C., Rehkämper, M., Garcia, M.O., Langmuir, C. and Su, Y. (2000) Cadmium, indium, tin, tellurium, and sulfur in oceanic basalts: Implications for chalcophile element fractionation in the Earth. Journal of Geophysical Research: Solid Earth 105, 18927-18948.

Young, E.D., Manning, C.E., Schauble, E.A., Shahar, A., Macris, C.A., Lazar, C. and Jordan, M. (2015) High-temperature equilibrium isotope fractionation of non-traditional stable isotopes: Experiments, theory, and applications. Chem. Geol. 395, 176-195.

Young, E.D., Shahar, A., Nimmo, F., Schlichting, H.E., Schauble, E.A., Tang, H. and Labidi, J. (2019) Near-equilibrium isotope fractionation during planetesimal evaporation. Icarus 323, 1-15.

Yu, Y., Hewins, R.H., Alexander, C.M.O.D. and Wang, J. (2003) Experimental study of evaporation and isotopic mass fractionation of potassium in silicate melts. Geochimica et Cosmochimica Acta 67, 773-786.

Chapter 5. Conclusions

The origin of the depletion of the moderately volatile elements (MVEs) of the Earth is the major research subject in this PhD dissertation. The mechanisms that induced the volatile depletion of the Earth, as well as the origin and timing of volatile elements delivered to the Earth are highly debated topics. In this dissertation, the sight is placed on a unique element, indium (In), which is both moderately volatile and siderophile (VSE) but was considered as 'overabundant' in BSE. This unique characteristic allows the elemental and isotopic composition of In to be shaped by both 'volatility-relevant' processes and core-formation process, and the knowledge of the origin of the In's overabundance can therefore provide an insight to the origin of the Earth's volatile depletion. Combining the volatility and siderophility of In, a series of evaporation experiments and metal-silicate partitioning experiments were performed in this dissertation to better understand the geochemical behaviors of In during the volatile loss on the Earth's building materials and core-formation process. In order to further apply the In isotope system for tracking the origin of volatile depletion and the potential building materials of the Earth, a high precision In isotopes determination method on rocks was firstly developed in this dissertation, and the In isotopic fractionation during igneous differentiation was further discussed. According to the measured In isotopic composition of terrestrial rocks, the isotopic composition of the bulk silicate Earth, as well as the bulk Earth extrapolated from the metal-silicate experimental results, are estimated based on the current best analytical results.

The volatility of In was studied via a series of evaporation experiments performed under variable temperature (1573 to 1773 K) and fO_2 (-10 to -0.68 in log units). The experimental results indicated a lower volatility of In compared to other MVEs with neighboring 50% condensation temperature, suggested 1% evaporation temperature (i.e., 1% of a specified element evaporated from condensed phase to vapor phase and reached equilibrium) as a more proper temperature scale in a vapor-melt system during

evaporation. Using this new temperature scale, In is actually not 'over-abundant' in the BSE, and further allows an additional deficit by core-formation process, indicating that the building materials of the Earth most have lost their MVEs under oxidative 'non-nebular' conditions, and hence preserved more In than typical expected from nebular conditions.

A range of metal-silicate partitioning experiments were conducted to study the partitioning behavior of In as a function of temperature, pressure, melt composition, oxygen fugacity and light elements in metallic phases. Experimental conditions covered a wide range of pressure (2 ~ 51 GPa) and temperature (1600 ~ 4000 K), spanning from approaching planetesimals size to the final P-T conditions of the base of deep magma ocean. The effects of S and Si on the partitioning of In were further examined by their respective doping experiments. Our experimental results suggested a negligible effects of pressure and temperature on the partitioning of In, while the effects of light elements, S and Si, were observed, in particular Si, whose presence in metallic phases can significantly decrease the partitioning of In. Moreover, S and Si effects on In were observed to be both temperature and pressure-dependent, and the validity of the regressed interaction parameters of ε_{In}^{S} and ε_{In}^{Si} were examined with the highest P-T experiments. Homogeneous accretion and three possible heterogeneous accretion (based on the different oxygen fugacity evolution path) scenarios were modelled, and their results all yielded a final partition coefficient D_{In} from 3 ~ 5, indicating the core as an important reservoir of Earth's In budget. This estimation is consistent with the previous 'late-accretion' models that suggested late delivered CI-like volatile-rich materials to the Earth before core-formation ceased. Furthermore, the modelled results also indicated a higher siderophility of In compared to Cd throughout core-formation conditions, which was contrary to the CI-normalized In/Cd ratio in BSE, arguing against the late accreted CI-like materials that have the identical relative abundance of In and Cd as the only source of Earth's In budget. Instead, the Earth's In budget is more likely from the mixing of two sources: (1) the late-accreted CI-like materials (last 10% Earth mass); (2) the precursor materials of the proto-Earth accreted during the main

stage accretion (i.e., first 90% Earth mass), which should contain substantial amounts of In and much less Cd. This assumption is consistent with the significantly low volatility of In under oxidative 'non-nebular' conditions, implying the volatile depletion of the early accreted precursor materials occurred under such conditions.

The first In isotopes determination method, as well as the In isotopic compositions of terrestrial rocks are reported in this dissertation. The In isotopic determination method, including the purification of In with column chromatography and isotopic measurement on mass spectrometer were developed at IPGP. This chemical method can effectively remove matrix elements and isobaric interferences (Sn and Cd) nearly completely, and can return In isotopic composition of rock samples with an external reproducibility of ~0.12‰ (2SD). The In isotopic compositions of a series of rock samples, including geostandards BHVO-2, BCR-2, GSP-2, and Afar/Iceland samples whose rock types from basalt to rhyolite were reported here. The indium isotopic compositions of these samples show insignificant isotopic fractionations within the current analytical uncertainty, which can be explained as the results of a constant oxidation sate and limited variations of coordination number of In during fractional crystallization. The analyzed basalts from different geological settings were observed with a nearly homogenous In isotopic composition within the current level of analytical uncertainty, and therefore, the first estimation for the In isotopic composition of the mantle (δ115In = -0.02 ± 0.19‰, 2SD, n = 10) is suggested. Furthermore, the In isotopic composition of the samples of metal-silicate partitioning experiments were also analyzed to study the In isotopic fractionation during metal-silicate segregation. The analytical results show a resolvable isotopic fractionation in the sulfur-free samples, where the heavier In isotope is enriched in silicate phases. In addition, the presence of sulfur in metallic phases can decrease the In isotopic fractionation, possibly due to the stronger In-S covalent bond than In-Fe metallic bond, in which the former can enrich more heavier isotopes. Given the discrepancy of the isotopic fractionation on S-bearing/free samples, as well as the estimated partition coefficients D_{In}, the upper and lower bound of the In isotopic composition of the bulk Earth (BE) can be assessed.

Extrapolating the regressed parameters to the base of the magma ocean (~ 40 – 50 GPa, 3200 ~ 3900 K), the upper bound of BE is identical with BSE, and the lower bound is ~ -0.08 ± 0.15‰, which is overlapped with the In isotopic composition in the BSE within the current analytical precision.

These research works carried out at IPGP moved forward our knowledge of the geochemical behavior of indium, and allowed us to better understand the origin of the 'overabundance' of indium in the BSE, and further provided implication to the origin of the Earth's volatile depletion and the timing of the volatiles delivered to the Earth.